INVESTIGATING THE ROLES OF THE C-TERMINAL TAIL AND THE METAL-DEPENDENT C2 DOMAIN IN PKCα REGULATION

A Dissertation

by

YUAN YANG

Submitted to the Office of Graduate and Professional Studies of
Texas A&M University
in partial fulfillment of the requirements for the degree of

DOCTOR OF PHILOSOPHY

Chair of Committee,	Tatyana I. Igumenova
Committee Members,	Pingwei Li
	Hays S. Rye
	Matthew S. Sachs
Head of Department,	Gregory D. Reinhart

August 2016

Major Subject: Biochemistry

ABSTRACT

Protein kinase C (PKC) isoenzymes sit in the crossroad of numerous signaling pathways involved in cellular functions such as proliferation, differentiation, migration and survival. The dysregulation of PKCs have been shown to associate with human diseases including cancers, cardiovascular diseases and neurodegenerative diseases. However, the knowledge of PKC regulation is still limited. The objective of this dissertation is to determine the roles of the PKCα C-terminal tail and the C2 regulatory domain in its maturation, activation and down-regulation.

The C-terminal V5 domain of PKC contains the least conserved sequence among the isoenzymes. In this study, nuclear magnetic resonance (NMR) and circular dichroism are used to show that the isolated V5 domain is intrinsically disordered in solution. A detailed characterization is provided for the V5 domain's secondary structural preference, dynamic properties and propensity to interact with a hydrophobic environment.

NMR techniques are used to demonstrate that the PKCα C2 domain interacts with the V5 domain. A structural model for the C2–V5 complex is determined. In addition, NMR-detected binding studies reveal that V5 and calcium interact with C2 cooperatively. Mutations that disrupt the C2–V5 interface altered both the conformation of full-length PKCα and the kinetics of membrane translocation. These results indicate that C2-V5 interaction plays an essential role in PKC regulation, through its contribution to both autoinhibition and activation. Furthermore, the V5 domain is shown to directly

interact with the peptidyl-prolyl isomerase Pin1. The V5–Pin1 interaction is observed to be highly specific, non-catalytic, and is enhanced by the avidity from bivalent binding. These data provide insights into a novel mechanism for the Pin1-mediated down-regulation process of PKCs.

The metal-dependent membrane interactions of the C2 domain are studied with cadmium as structural surrogate and the results compared to other divalent metals. Conformational dynamics change induced by calcium binding is detected for regions connecting to other PKC domains. These results reveal specific roles of calcium ion during membrane interaction and conformational rearrangement of PKC.

Together, these data contribute to our understanding of PKC regulation with concerted intramolecular contacts and complex intermolecular interactions, which can help to develop isoenzyme-specific agents to modulate PKC activity.

ACKNOWLEDGEMENTS

I would like to thank my principal investigator and committee chair, Dr. Tatyana Igumenova, and members of my graduate committee, Dr. Matthew Sachs, Dr. Hays Rye and Dr. Pingwei Li, for their training, guidance, and helpful suggestions throughout my graduate research and studies.

I would also like to thank the amazing friends, colleagues, faculty and staff at Texas A&M University: Dr. Ratna Ghosh and Dr. Vytas Bankaitis for collaboration on the nodulin project; Dr. Mauricio Lasagna and Dr. Gregory Reinhart for the training and fluorometer time; Dr. Chang Shu and Dr. Pingwei Li for their help with insect cell expression and discussions for protein crystal screening; Dr. Hsiaoling Huang and Dr. James Sacchettini for their training in X-ray crystallography; Dr. Gregory Martin and Dr. Friedhelm Schroeder for their training and time usage of circular dichroism spectrometer; Dr. Lawrence Dangott for training in both MALDI and ESI mass spectrometry and Dr. Mandar Naik for helpful input in structural calculations. Thanks also go to my collaborators Julia Callender and Dr. Alexandra Newton at University of California, San Diego for conducting functional experiments of PKCα. I also want to thank Dr. Alexander Taylor and Dr. P. John Hart at the University of Texas Health Science Center, San Antonio for C2 structural refinement.

Special thanks go to the faculty and staff in the Department of Biochemistry and Biophysics for making my time in graduate school a great experience. I also want to extend my gratitude to the Department of Biochemistry and Biophysics at Texas A&M

University, the Welch Research Foundation, and American Heart Association for funding this research.

Thanks to the former and present members of the Igumenova laboratory, especially Mikaela, Krystal and Taylor, for their kind support, scientific input, lively discussions and concerted research efforts. Also thanks to the rotation students and undergraduate students over the years who contributed to my projects.

Finally, thanks to my family, boyfriend and friends for their encouragement and love, especially my mother who told me chemistry is really cool when I was young.

NOMENCLATURE

ATP	adenosine triphosphate
βME	β-mercaptoethanol
CD	circular dichroism
CFP	cyan fluorescent protein
CM	center of mass
CMBL	calcium membrane binding loop
CN	coordination number
CNBr	cyanogen bromide
CSP	chemical shift perturbation
DAG	diacylglycerol
DM	double mutant
DPC	dodecylphosphocholine
EDTA	ethylenediaminetetraacetic acid
EGTA	ethyleneglycoltetraacetic acid
ER	endoplasmic reticulum
ESI	electrospray ionisation
FRET	Föster resonance energy transfer
GPCR	G-protein coupled receptor
GST	Glutathione S-transferase
HE	Hahn-Echo

HEPES	4-(2-hydroxyethyl)-1-piperazineethanesulfonic acid
HM	hydrophobic motif
HPLC	high-performance liquid chromatography
HSQC	heteronuclear single quantum coherence
IDP	intrinsically disordered protein
IPTG	isopropyl-D-1-thiogalactopyranoside
KIE	kinetic isotope effect
KSI	ketosteroid isomerase
LRC	lysine-rich cluster
LUV	large unilamellar vesicle
MALDI-TOF	matrix-assisted laser desorption/ionization time-of-flight
MES	2-(N-morpholino)ethanesulfonic acid
MWCO	molecular weight cut-off
mTORC	mammalian target of rapamycin complex
NLS	nuclear localization signal
NMR	nuclear magnetic resonance
NOE	nuclear Overhauser effect
PCS	pseudocontact shift
PDB	protein data bank
PDB ID	protein data bank identification number
PDBu	phorbol 12,13-dibutyrate
PDK-1	phosphatidylinositide-dependent kinase-1

pHM	phosphorylated hydrophobic motif
Pin1	peptidyl-prolyl cis-trans isomerase NIMA-interacting 1
PIP_2	phosphatidylinositol 4,5-bisphosphate
PKA	protein kinase A
PKC	protein kinase C
PKG	protein kinase G
PLC	phospholipase C
PMA	phorbol 12-myristate 13-acetate
PMSF	phenylmethylsulfonyl fluoride
POPC	1-palmitoyl-2-oleoyl-sn-glycero-3-phosphocholine
POPS	1-palmitoyl-2-oleoyl-sn-glycero-3- phospho-L-serine
PRE	paramagnetic relaxation enhancement
PS	pseudosubstrate
PtdSer	phosphatidylserine
PtdIns(4,5)P_2	phosphatidylinositol 4,5-bisphosphate
PtdIns(3,4,5)P_3	phosphatidylinositol 3,4,5-trisphosphate
pTM	phosphorylated turn motif
pV5	bisphosphorylated V5
RACK	receptor for activated C-kinase
RMSD	root-mean-square deviation
SEM	standard error of the mean
SDS-PAGE	sodium dodecyl sulfate polyacrylamide gel electrophoresis

SH3	SRC Homology 3
SSP	secondary structure propensity
STD	standard deviation
SUMO	small ubiquitin-like modifier
TCEP	tris(2-carboxyethyl)phosphine
TM	turn motif
WT	wild-type
YFP	yellow fluorescent protein

TABLE OF CONTENTS

Page

Page

Page

Page

LIST OF FIGURES

Page

Page

Page

Page

LIST OF TABLES

Page

CHAPTER I

INTRODUCTION

Introduction to protein kinase C and objectives

Protein kinase C (PKC) was first identified in 1977 by Nishizuka and colleagues as a cyclic nucleotide-independent protein that phosphorylates histone and protamine.[1] A few years later, PKC was discovered to be directly activated by tumor-promoting phorbol esters.[2] Since then, accumulated research efforts have revealed that PKC controls a multitude of signaling cascades controlling cell proliferation, differentiation, migration and survival.[3,4] Because of its central role in cell signaling, the up- and down-regulation of PKC is associated with numerous diseases including cancers,[4-6] cardiovascular diseases[6-9] and neurodegenerative diseases.[10-13]

The isoenzymes of the PKC family have overlapping tissue distributions with distinct and sometimes opposing roles.[4,14] Therefore, therapeutic strategies targeting PKCs require isoenzyme-specific modulation. However, a lack of knowledge about the function and regulation of individual PKC isoenzymes is currently preventing the development of isoenzyme-specific regulatory agents.[12] In addition, a detailed molecular mechanism of PKC action in cells is not yet fully understood. Driven by a motivation to provide atomic-level understanding of the PKC function, this dissertation is focused on investigating the roles of the PKC C-terminal tail and the metal ion-dependent C2 regulatory domain in PKC's maturation, activation and down-regulation.

This chapter provides an overview of the structural components of PKC isoenzymes, regulation of PKC, the C-terminal V5 domain and the C2 regulatory domain.

Structural components of PKC

The PKC family of isoenzymes is a member of the AGC (PKA, PKG and PKC) superfamily of protein kinases. These protein kinases share a highly conserved catalytic core fold, and a regulatory region that keeps the enzyme inactive prior to signaling events. The regulatory region of PKC is located at the N-terminal half of the polypeptide, and the catalytic region is in the C-terminal half. At least 10 mammalian PKC isoenzymes are traditionally divided into three subfamilies: conventional PKCs (cPKCs: α, βI, βII, and γ), novel PKCs (nPKCs: δ, ε, η, and θ) and atypical PKCs (aPKCs: ζ, ι/λ).

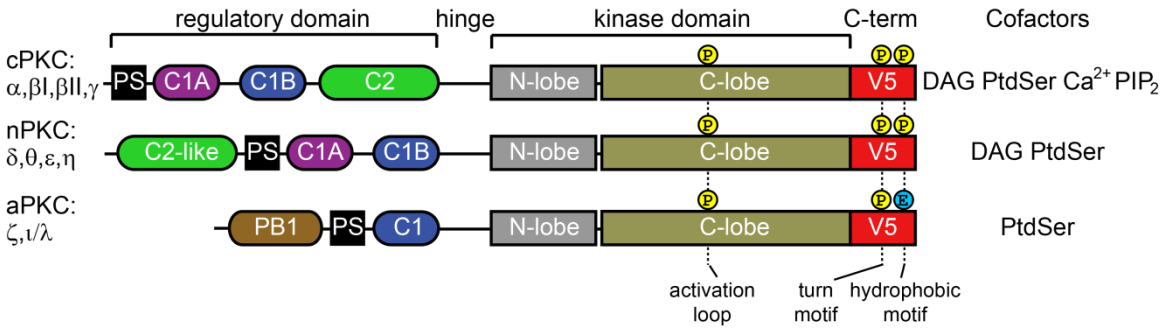

Figure 1. Structural components of PKC isoenzymes and their cofactors. 10 isoenzymes of PKC are divided into three subfamilies: conventional (cPKC), novel (nPKC) and atypical (aPKC). The functional domain diagram and their cofactors are shown for each subfamily. PS, DAG, PtdSer and PIP_2 stand for the pseudosubstrate region, diacylglycerol, phosphatidylserine and phosphatidylinositol 4,5-bisphosphate, respectively. Phosphorylation sites are shown as yellow spheres and annotated at the bottom. The glutamic acid in the blue sphere is shown for the aPKC subfamily.

The three subfamilies are categorized based on their differences in the N-terminal regulatory region and the cofactors they bind as shown in Figure 1.

All PKCs are multi-modular serine/threonine kinases with a single polypeptide chain. Domains in PKC are named based on their degree of conservation. For example, conventional PKCs have four conserved domains (C1 through C4) and five variable domains (V1 through V5). The C1 and C2 domains belong to the N-terminal regulatory region, whereas the C3, C4 and V5 domains comprise the C-terminal catalytic region. The C3 and C4 domains are often referred to as the N-lobe and C-lobe of the kinase core. The C1 and C2 domains in the N-terminal regulatory region are independently folded functional modules that interact with cofactors both in cytosol and on cell membranes.

As illustrated in Figure 1, the three subfamilies of PKC have different cofactor requirements. This is due to differences in modular compositions for the N-terminal regulatory region of each subfamily. Conventional PKCs (α, βI, βII, and γ) require both diacylglycerol and increased cellular calcium level for activation. There are two tandem C1 domains (C1A and C1B) and a C2 domain in their N-terminal regulatory region. C1 domains are responsible for diacylglycerol association. The C2 domain binds to anionic membranes in a calcium-dependent manner. The lipid specificity of C2-membrane binding includes phosphatidylserine (PtdSer) and phosphatidylinositol 4,5-bisphosphate (PtdIns(4,5)P_2). PtdSer is also shown to interact with C1 domains.[15]

Novel PKCs (δ, ε, η, and θ) have an altered arrangement of regulatory regions, with a C2-like domain that does not bind calcium ions followed by two tandem C1

domains. As a result, nPKCs are activated by diacylglycerol, but not by calcium. Atypical PKCs (ζ, ι/λ) are activated through protein-protein interactions with a PB1 (Phox and Bem 1) domain.[16,17] The atypical C1 domain does not bind diacylglycerol. However, aPKCs can be activated or regulated by PtdSer, PtdIns(3,4,5)P_3, ceramide and other lipid components.[18-20]

To date, moderate structural data obtained by NMR and crystallography are available for individual domains of PKC, including C1 domains, C2 domain and the kinase core.[21,22] However, there currently exists no structural model of any full-length PKC. In the only structure available from a full-length construct of PKCβII (PDB ID 3PFQ), multiple domains and linkers are still missing electron densities.[23] This is largely because of the intrinsic flexibility of PKC due to its multi-modular structure and potential promiscuous modes of intramolecular interaction. Another challenge to a full-length structure determination lies in the post-translational phosphorylation events (*vide infra*) required for the maturation of these enzymes. These phosphorylation events add to complexity and limitations of the expression systems needed to acquire a structural sample of PKC.

Regulation of PKC

PKC isoenzymes are regulated through four specific aspects: (1) maturation through phosphorylation, (2) activation by association with cofactors, (3) spatial localization through interaction with proteins and (4) down-regulation. All of these

regulatory mechanisms are combined to determine the life cycle and activity at any given cellular state of PKC.

PKC maturation through phosphorylation

Newly synthesized PKC is unphosphorylated, inactive and partitions into an unidentified membrane cellular compartment.[24] For conventional PKCs in the cells, the unphosphorylated precursor is fully released into the cytosol upon completion of three ordered phosphorylation events located at the activation loop, the turn motif and the hydrophobic motif, respectively (Figure 1).[25] The first step of phosphorylation is characterized to be at the activation loop located in the C-lobe of the kinase domain and is mediated by the upstream kinase phosphoinositide-dependent kinase-1 (PDK-1).[24] For PKCα and PKCβII this phosphorylation is on T497 and T500, respectively. This is followed by two additional phosphorylation events at the turn motif and hydrophobic motif at the C-terminal V5 region.[24,26]

For novel and atypical PKCs, although phosphorylations at the three conserved sites occur, regulation by phosphorylation remains controversial.[22,27-29] Notable differences from cPKCs are summarized in the following observations: (1) a glutamic acid substitutes for the phosphorylated residue in the hydrophobic motif for aPKCs, (2) PKCδ (an nPKC isoenzyme) can function without activation loop phosphorylation, and (3) alternative regulatory mechanisms have been suggested for PKCδ and PKCι/λ.[17,22]

The reason why the three phosphorylation events are required for releasing the newly synthesized cPKCs into the cytosol appears to be that these events trigger a

conformational change from an "open" form (with the psdeudosubstrate region exposed) to a "closed" form (with the psdeudosubstrate tucked in the active site of the kinase domain). This process is illustrated schematically in Figure 2. The mature, closed form of PKC in the cytosol is catalytically competent, but it remains inactive until activated by corresponding cofactors in cell signaling events. For this reason, the mature cytosolic PKC is also referred to as the latent form. The driving forces behind the conformational changes that occur upon PKC maturation are not yet fully understood. The specific roles of the two phosphorylation sites at the C-terminal tail are also only partially elucidated (*vide infra*).

By treating the mature PKCβII with specific phosphatases and testing the kinase activity of the resulting dephophosphorylated species, it has been illustrated previously that once PKC becomes mature in the cells, only the phosphorylation at the turn motif is required for PKC catalytic activity; activation loop and hydrophobic motif phosphorylation sites are not essential for the activity of the mature kinase.[26] The mutations at the hydrophobic motif phosphorylation site affect mainly the thermal stability and cytosolic population of the enzyme, but a mutation to Ala in PKCβII does not abolish the kinase activity of the soluble half population from the cell lysate.[30-32] On the other hand, the T641AAA mutations of PKCβII, which abolishes the turn motif phosphorylation, resulted in completely unphosphorylated and inactive kinase with half of the population remained in the detergent-insoluble fraction of the cell.[30] However, the newly-synthesized wild-type and the T641AAA mutant of PKCβII (both are unphosphorylated) are soluble when expressed in cell-free translation system shown in

the same study.[30] From the above discussions, the turn motif and hydrophobic motif phosphorylation events play important roles in the cytosolic population of PKC in cells. However, there seem to be unknown steps that remain to be elucidated between the PKC phosphorylation events and its final cytosolic localization. These steps probably include protein-membrane and protein-protein interactions.

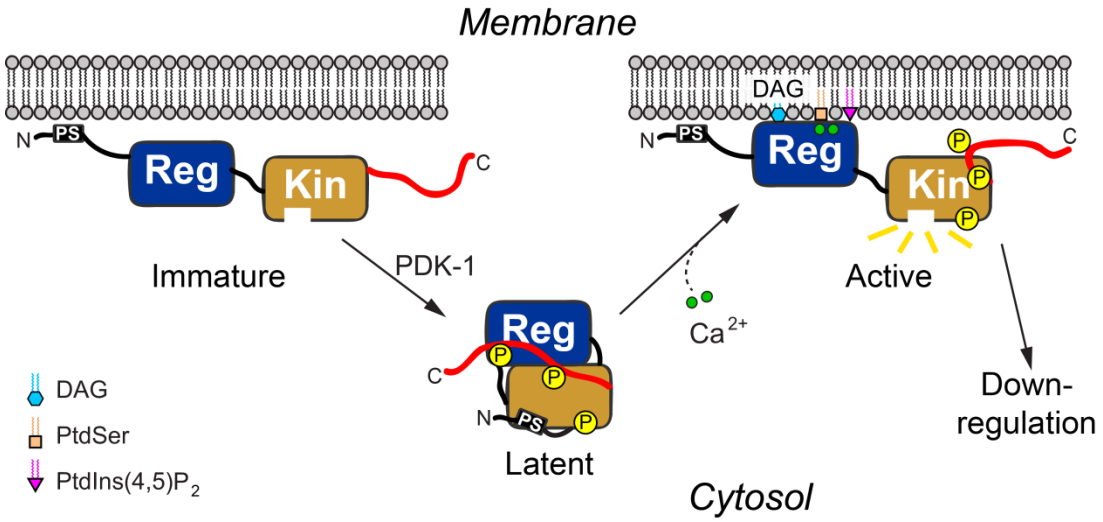

Figure 2. A schematic view illustrating the regulation of conventional PKC isoenzymes. Phosphorylation sites are shown as yellow spheres. Calcium ions are shown as green spheres, and lipid cofactors are annotated at the left bottom. The C-terminal V5 domain is colored in red. Regulatory domain (Reg) and kinase domain (Kin) are colored blue and brown, respectively. Their modular compositions can be found in Figure 1.

PKC activation by association with cofactors

There are three conditional peripheral membrane-binding domains in conventional PKCs: C1A, C1B and C2 (Figure 1). The activation of mature cPKC requires the binding of second messengers diacylglycerol and calcium ions to C1 and C2

domains, respectively. The association of second messengers releases the "closed", latent form of cPKC and translocates the enzyme from cytosol to cell membrane. The membrane associated cPKC then becomes fully active to phosphorylate target proteins downstream in the signaling pathways. The signaling events triggering increased levels of both membrane diacylglycerol and cytosolic calcium lead to membrane translocation and activation of PKCα (first isoenzyme in cPKC subfamily), which can be visualized in Figure 3. The extracellular signaling agonists simulates phospholipase Cβ through G-proteins, which leads to hydrolysis of PtdIns(4,5)P_2. The hydrolysis of one PtdIns(4,5)P_2 molecule results in one molecule of diacylglycerol remaining in the plasma membrane and one molecule of cytosolic messenger Ins(1,4,5)P_3. Ins(1,4,5)P_3 binds to receptor calcium channels and releases calcium ions from the calcium reservoir of endoplasmic reticulum to the cytosol. Now both diacylglycerol and calcium levels are elevated in the cell for effective activation of PKCα.

The order of cofactor binding events is generally thought to begin with calcium binding to the C2 domain. This is supported by a few studies showing that the calcium binding event causes much faster membrane translocation kinetics of PKCγ in cells than that triggered by diacylglycerol alone and that cPKC membrane translocation synchronizes very well with cellular calcium spikes.[33-35] The calcium spike causes a transient membrane association of cPKC, which reduces the dimensions required for a diacylglycerol search from the three-dimensional cytosolic space to the two-dimensional membrane surface. C1 domain binding to diacylglycerol then provides enough energy accumulative with the energy contributed by C2 membrane binding to pull the

pseudosubstrate out of the active site, leading to full activation of cPKCs.[36] For cPKCs, the C1B domain provides a weaker diacylglycerol site than that found in their C1A domain. Replacement of a conserved Tyr with a Trp alone increases the diacylglycerol affinity of the conventional C1B domain.[37,38] High diacylglycerol affinity applies to both C1A and C1B domains of novel PKCs, potentially compensating the reduced membrane binding ability of the C2-like domain when comparing to the conventional calcium-binding C2 domain.

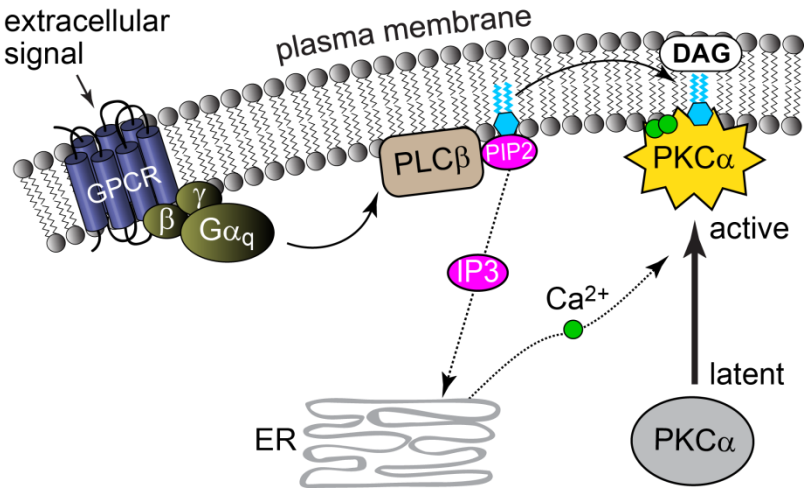

Figure 3. A model of signaling events leading to activation of PKCα. GPCR, PLCβ and ER denote the G-protein coupled receptor, phospholipase Cβ and endoplasmic reticulum, respectively. Figure adapted with permission from T. I. Igumenova. *Biochemistry* 2015, 54, 4953.[21]

It is worth noting that tumor promoting phorbol esters, first discovered to directly activate PKC in 1982,[2] associate with significantly higher affinity to the C1 domains than their natural agonist diacylglycerol. As stated previously, the structural information regarding the activation process of PKC is still largely unknown. This is due to a lack of

a full-length PKC structure in either latent or membrane associated form. Thus, it is difficult to delineate the detailed structural changes that occur during PKC activation, other than the global change of activated PKC possessing no pseudosubstrate in the active site and the N-terminal regulatory domain associated with the membrane (Figure 2).

PKC spatial localization through interaction with proteins and PKC down-regulation

PKC isoenzymes are rather generic kinases in regard to their substrate specificity. It is suggested that spatial localization through protein interactions is an important pathway to deliver PKC isoenzymes to the appropriate cellular compartments and microdomains so that substrate specificity can be achieved.[22,39] A broad range of substrates, receptors, cytoskeletal proteins and scaffold proteins have been shown to interact with PKC in an isoenzyme-specific manner, as discussed in detail in the review of Jaken and Parker.[39] A notable example related to this dissertation is the receptors for activated C kinase (RACKs) scaffold proteins. The RACK interaction sites are mapped to the C2 domain and V5 domain on PKCβ, δ and ε.[22] Peptides with sequences based on RACK binding sites have been shown by Mochly-Rosen and colleagues to effectively modulate subcellular localizations of PKC isoenzymes.[40-43]

Down-regulation of PKC is an integral part of PKC regulation, so that the PKC activities can be accurately controlled by cofactors and other signaling molecules. The most basic down-regulation mechanism of PKC is through decreasing cofactor concentrations as a result of calcium oscillations and metabolism of lipid cofactors such

as diacylglycerol. When cofactor concentrations are decreased in the cells, PKC dissociates from the membrane and become latent again. However, when PKC is stimulated with phorbol esters, it is down regulated through dephosphorylation and degradation, since phorbol esters cannot be metabolized.[44] Recent studies suggest the presence of both ubiquitination/proteasome dependent and endolysosome dependent degradation mechanisms for cPKCs.[45,46]

V5 domain

The C-terminal V5 (Variable 5) domains are 60 to 80 amino acid segments containing two highly conserved turn and hydrophobic phosphorylation motifs (Figure 1). These two phosphorylation sites in the V5 domain are among the three ordered phosphorylation events required for newly-synthesized cPKC isoenzymes to become mature and catalytically competent. Due to its variability among PKC isoenzymes (*vide infra*), the V5 domain is an ideal candidate for isoenzyme-specific targeting.

It was not until recently that the V5 domain has received significant attention from researchers who were trying to unveil the molecular mechanism of PKC regulation. Collectively, V5 domains are involved in (1) priming the maturation of newly-synthesized PKCs (*vide supra*), (2) intramolecular interactions to maintain the latent form of PKCs until activation,[23,47] and (3) intermolecular interactions with upstream or downstream proteins and kinases.[22,32,45,48-50] However, the intrinsic properties of V5 domains have caused difficulties for traditional structural techniques and for elucidating detailed information of protein-protein interactions involving the V5 domain. The lack

of atomic level information is currently the missing link between the functional importance of V5 domain and a broader usage of V5 properties to modulate PKC activities. Driven by this motivation, this dissertation seeks to understand the role of V5 domain and focuses on characterization of the isolated V5 domain from PKCα and probing its intramolecular and intermolecular interactions.

The variability of V5 and its isoform specific properties

As shown in Figure 4 for the sequence alignment of V5 domains from PKC isoenzymes, V5 domains have large variations in amino acid compositions outside of the three conserved motifs and an N-terminal PPXXP site. The sequence at the extreme C-terminus beyond the hydrophobic motif is the least conserved sequence with varying lengths (7–22 amino acids) among all PKC isoenzymes. These highly variable terminal sequences of V5 can be used to identify each isoenzyme through specific antibodies.

More importantly, V5 domains modulate the individual subcellular localization of each isoenzyme. For example, PKCβI and βII are alternatively spliced products of the same gene and they only differ in their V5 sequences. However, PKCβII localizes to the juxtanuclear region in addition to plasma membrane upon sustained PMA stimulation. But PKCβI only localizes to plasma membrane under the same conditions potentially due to a different V5 domain from PKCβII.[51,52] For another example, expression of a chimeric PKCα with the last 13 amino acids from PKCβII resulted in a PKCβII-type nuclear localization of the chimeric protein upon prolonged PMA stimulation.[53] In

addition, V5 domain from PKCδ contains a nuclear localization signal (NLS) sequence from residues 611–623.[54]

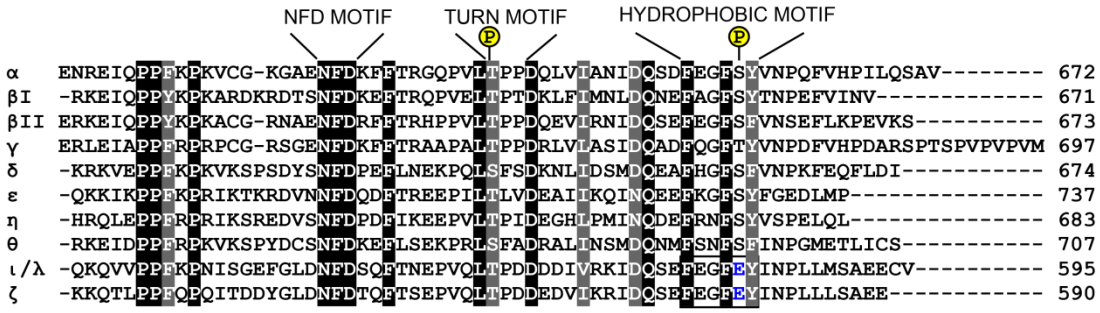

Figure 4. Sequence alignment of V5 domains from PKC isoenzymes. Identical residues are shaded in black, and similar residues are shaded in grey. Conserved motifs of V5 domains are annotated at the top of each motif. Phosphorylation sites are highlighted with yellow spheres, with blue Glu residues shown for aPKCs at the conserved hydrophobic motif phosphorylation site. The amino acid sequences are from *Mus musculus* and are highly similar to those of *Homo sapiens*.

Conserved motifs and their proposed function

There are three conserved motifs in the V5 domains of PKC isoenzymes: NFD, turn and hydrophobic (Figure 4). The NFD motif contains three highly conserved amino acids Asn (N), Phe (F), and Asp (D) as it is named, and another conserved Phe residue following the NFD trio. This motif forms a short helix segment as observed in various crystal structures of PKC kinase domains. The exact function of this motif is not known, but it is proposed to interact with C1B domain within the same PKC molecule judging from the contact observed from PKCβII crystal structure (PDB ID 3PFQ) (Figure 5).[23] However, the function of this proposed interaction remains controversial since a recent

study did not observe any difference in PKCβII activation by mutating the conserved Phe629.[55]

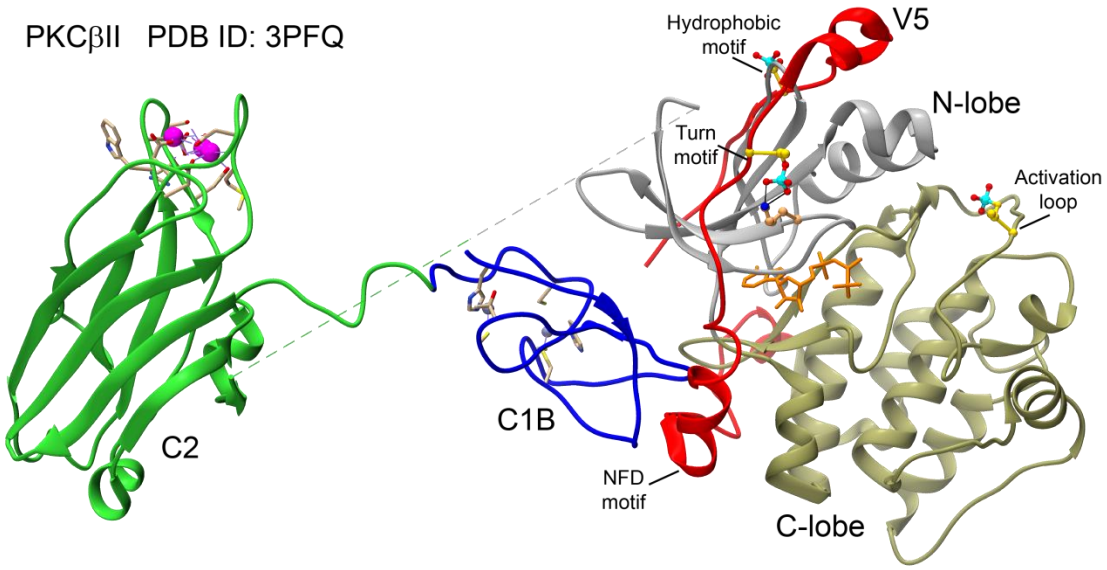

Figure 5. Crystal structure of PKCβII (PDB ID 3PFQ) showing the structural elements. The color coding of individual domains are the same as in Figure 1. Pseudosubstrate, C1A domain, and the hinge are missing in this structure. Activation loop and the conserved motifs (NFD, turn and hydrophobic) of the V5 domain are labeled with black annotations, with the three phosphorylation sites shown in ball and stick representations for the phosphate moiety. The ANP molecule is shown in orange stick, which is a non-hydrolysable ATP analog located between the N- and C-lobes.

The conserved turn motif and hydrophobic motif contain two out of the three phosphorylation sites required for the maturation of cPKCs (*vide supra*). The turn motif is named because it contains at least one proline residue immediately following the phosphorylated Thr residue for cPKCs and aPKCs. However, three out of four nPKC isoenzymes do not share this property. As described previously, the turn motif is most critical among the three phosphorylation sites for the catalytic competence of the mature

PKC enzyme but the reason for this is not fully understood. It is possibly due to formation of a salt bridge between the phosphate group and a Lys residue on the N-lobe of the kinase domain (Figure 5). The turn motif also appears to be important for at least two other functions. The V5 domain of PKCβII is implicated in a direct interaction with the heat shock protein HSP70 potentially via the unphosphorylated turn motif and the invariant Leu residue preceding the Thr phosphorylation site.[50,56] Most recently, the turn motif was proposed to be important for peptidyl-proyl isomerase Pin1-mediated down-regulation of cPKCs.[45]

The hydrophobic motif was shown to be the docking site for the upstream kinase PDK-1 during the maturation process of PKC.[32] Due to the trans-activating property of PDK-1, the hydrophobic motif of PKC potentially functions in both recruitment and activation of PDK-1.[57] The phosphorylation of the hydrophobic motif appears to happen after PDK-1 is disassociated from PKC.[32] Interestingly, PDK-1 has a higher affinity for the phosphorylated isolated C-terminus (GST-V5 fusion protein) than the unphosphorylated mutants of GST-V5.[32] On the contrary, PDK-1 interacts preferably with unphosphorylated full-length PKCβII.[32] These data indicate that the hydrophobic motif becomes masked upon phosphorylation. The phosphorylation of hydrophobic motif, on the other hand, is not as critical as the phosphorylation of the turn motif for the catalytic competence of mature PKCs. However, the hydrophobic motif appears to affect the thermostability and calcium binding efficiency of PKCβII.[30-32] In addition, negatively charged residues in the hydrophobic motif are important for the

diacylglycerol insensitivity of PKCα possibly due to intramolecular interactions that stabilize the closed conformation of latent PKCα.[47]

The function of the conserved PPXXP site at the N-terminal part of the V5 domain is less well studied. Although overlapping with the NLS, it has been suggested to be important for nuclear exclusion of PKCδ.[58] This proline rich site contains an SH3 domain binding consensus PXXP, but the function has not yet been addressed to our knowledge.

C2 domain

C2 (Conserved region 2) domains are calcium dependent lipid binding modules that are currently found in about 140 different human proteins.[59,60] Conventional PKCs all have one calcium-binding C2 domain, whereas novel PKCs have a C2-like domain insensitive to calcium, and atypical PKCs lack a C2 domain. The C2 domains of cPKCs are implicated in modulating their PtdSer and PtdIns(4,5)P_2 specific membrane translocation.[61]

Structural elements of C2

C2 domains share a common fold consisting of an eight-stranded β-sandwich interconnected with three calcium membrane binding loops (CMBLs) to provide metal coordination. The sequence alignment and crystal structure of the C2 domain from cPKCs are shown in Figure 6, with the functional elements highlighted.

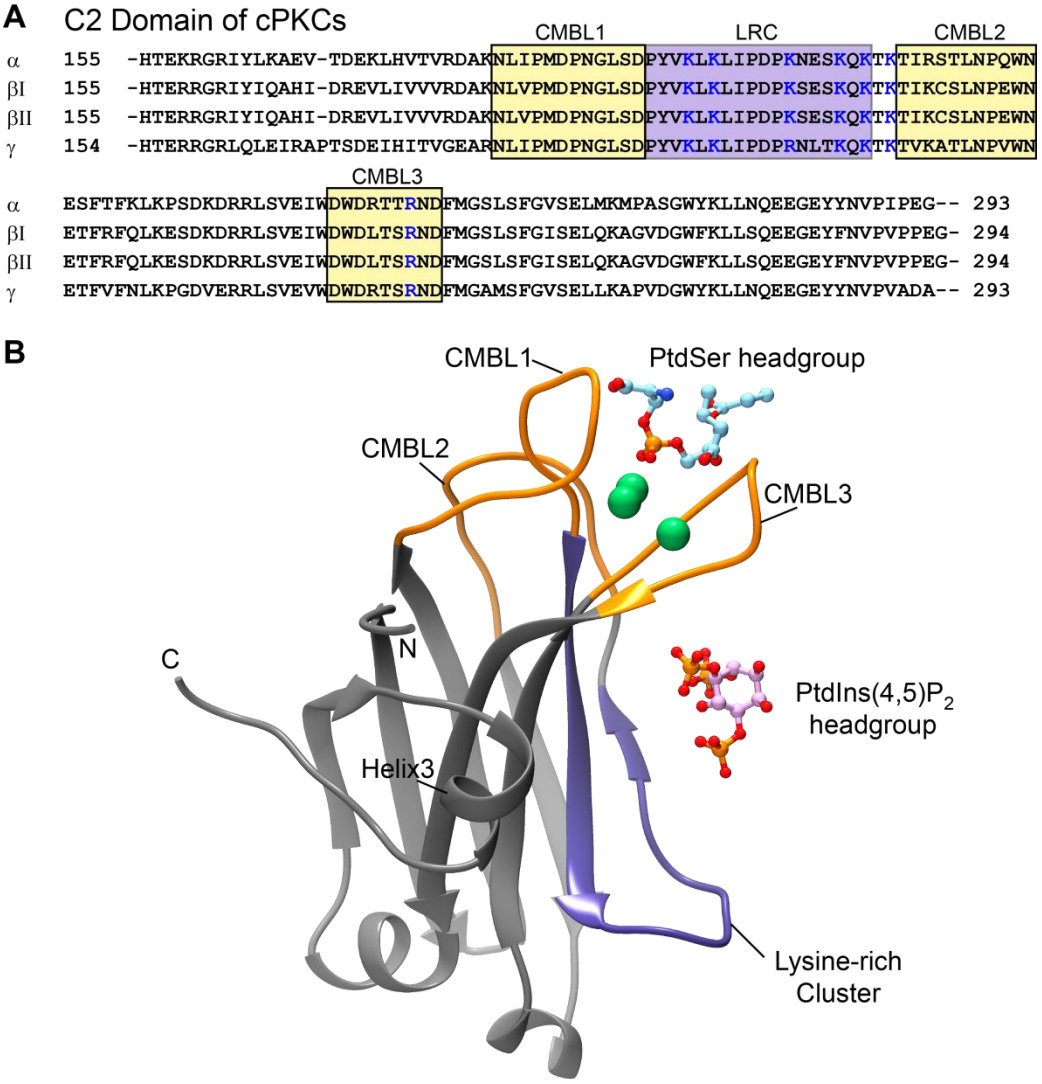

Figure 6. The calcium and lipid binding C2 domains from conventional PKC isoenzymes. (A) Sequence alignment of C2 domains from cPKCs. Conserved Lys residues are highlighted with blue fonts. The amino acid sequences are from *Rattus norvegicus* and are highly similar to those of *Homo sapiens*. **(B)** Crystal structure of C2 domain from PKCα indicating the structural and functional elements. PDB entries used to generate this figure are 1DSY, 3RDJ and 3GPE. In both panels, calcium membrane binding loops (CMBLs) are colored orange, and the lysine-rich cluster (LRC) is colored purple. Calcium ions are shown as green spheres, and the lipid headgroups are shown as ball and stick representations.

The three CMBLs of conventional C2 domains bind two to three calcium ions, and interact with the PtdSer lipid headgroups in a calcium-dependent manner. In addition to the CMBLs, the C2 domain from cPKCs has a polybasic lysing-rich cluster (LRC) located at the β3-β4 groove. The LRC was indicated by the crystal structure and functional studies to interact with PtdIns(4,5)P_2 headgroups at the plasma membrane.[62-64] LRC was also suggested by a mutagenesis study to contribute to the diacylglycerol insensitivity together with the hydrophobic motif of V5 domain from PKCα.[47] Another unique structural element for PKC C2 domains is the C-terminal Helix3, which does not exist in C2 domains from synaptotagmins or phospholipase C proteins. Residues in this helix have been suggested to play a role in intramolecular C2–C1A interaction by mutagenesis and computational modeling.[65,66]

Metal coordination and membrane interactions

The CMBLs of C2 domains coordinate calcium ions using their conserved Asp side-chain carboxyl groups in combination with several backbone carbonyl groups. The coordination ligand environment is oxygen based. The calcium binding properties of C2 domain is proposed to regulate C2 function in three ways: (1) modulation of the electrostatic potential of C2 domain by neutralizing the negative charges at the loop region, i.e., an electrostatic switch;[67] (2) provision of a potential bridge with the lipid headgroups during membrane association[68] and (3) initiation of large conformational changes in the host enzyme presumably by destabilizing the intramolecular interactions.[33,65,69] Another important metal-coordination related aspect of C2 domains

is that it is one of the molecular targets for heavy metal toxicity in the cell, with representative evidences for C2A domain from synaptotagmin-I[70] and C2 domain from PKCα[71,72] as targets for lead toxicity.

The C2 domain together with C1 domain from PKC were the first described conditional peripheral membrane protein domains.[59] Numerous studies have provided insights into the mechanisms of C2 membrane binding. As mentioned previously, the C2 domain interacts with PtdSer-containing membrane in a calcium dependent manner, with LRC rendering a PtdIns(4,5)P_2 specificity for the plasma membrane. However, it was suggested that the electrostatic switch mechanism does not fully explain the membrane binding behavior of C2 since CMBL mutations that increase the electrostatic potential decreased the membrane binding affinity of PKCβII.[73] On the other hand, the "bridging" mechanism is only supported by the crystal structure of C2 in complex with calcium and a PtdSer analog. Further investigation is needed to elucidate the molecular mechanism of C2 membrane interactions, and relate the two electrostatic switch and "bridging" mechanisms.

Organization of dissertation

In this dissertation, I further address the mechanisms regulating PKC activity with a focus on acquiring structural and dynamic information about the ligand binding, intramolecular and intermolecular interactions involving the C-terminal V5 domain and the C2 regulatory domain. Given the functional importance of and sparse structural information about the C-terminal V5 domain of PKC, our main question is centered on

this highly variable V5 domain, with the C2 regulatory domain as a starting point to address the interplay between V5 domain and other PKC regulatory domains. Furthermore, I address questions about the role of the V5 domain in the down-regulation of conventional PKC. The calcium dependent membrane binding mechanism of C2 regulatory domain is also investigated.

Specifically, in Chapter II, I address the intrinsically disordered nature of the isolated C-terminal V5 domain from PKCα. In addition, an unexpected membrane interacting propensity of V5 domain is also investigated. In Chapter III, I study the intramolecular interaction between V5 and C2 domains with both structural and functional approaches. In Chapter IV, I examine the intermolecular interaction between V5 domain and the peptidyl-prolyl isomerase Pin1. A "divide-and-conquer" strategy is used to demonstrate the specific interaction mode. In Chapter V, metal coordination of the C2 domain is related to the membrane interaction mechanism using cadmium as a calcium surrogate. The weak binding of a third calcium ion to C2 domain is also investigated. The last chapter summarizes the results and suggests further studies to understand PKC regulations involving the C-terminal V5 domain.

CHAPTER II

THE C-TERMINAL V5 DOMAIN IS INTRINSICALLY DISORDERED AND HAS MEMBRANE ASSOCIATING PROPENSITY*

Background

In order to develop therapeutic strategies for diseases involving PKCs, the first step is to achieve modulation of PKC activity in an isoform-specific manner. This is one of the current challenges in the PKC field.[74,75] A promising target for this purpose is the most C-terminal region of PKCs comprising 60-80 amino acids, due to its variability.[76-80] In this chapter, we describe the experiments designed for (i) the first solution-state characterization of the C-terminal region from PKCα; (ii) probing the conformational differences between the unphosphorylated sequence and a phosphorylation-mimicking variant; (iii) investigating the potential membrane associating propensity with two different membrane mimetics.

The most C-terminal region of PKCs is termed the "Variable 5", or V5 domain. This domain contains two highly conserved turn and hydrophobic phosphorylation motifs, while the extreme C-terminal residues beyond the hydrophobic motif are the least conserved sequence both in length and amino acid composition among all PKC isozymes (Figure 7B). Analysis of the existing literature prior to this study suggests that V5 plays multiple roles within its parent protein:

(i) it serves as a docking site for the upstream phosphoinositide-dependent kinase-1(PDK-1) to initiate the maturation process of newly-synthesized kinase[24,32]; (ii) the two phosphorylation events of V5 domain are required for the catalytic competency and thermal stability;[30,81] (iii) it participates in the auto-inhibitory interactions for the latent conformation of the enzyme;[23,47,75,82] and (iv) it mediates sub-cellular localization of different PKC isoforms by interacting with the isoform-specific adaptor proteins, receptors for activated C kinases (RACKs).[49]

Newly synthesized ("immature") PKC partitions into an unidentified membrane cellular compartment, from which it is released into cytosol upon completion of three ordered phosphorylation events.[24] This is necessary for the conventional PKC isoforms to reach their full catalytic competence, or maturity.[83] The first phosphorylation, catalyzed by phosphoinositide-dependent kinase, PDK-1, occurs at a conserved Thr residue on the activation loop that is located at the C-lobe of the kinase core. However, V5 likely serves as an interaction site between the newly synthesized PKC and PDK-1.[32] Two other phosphorylation sites among the three belong to the V5 domain and include the Thr residue of the turn motif (TM) and the Ser residue of the hydrophobic motif (HM) in the case of PKCα and PKCβI/II, as shown in Figure 7B. Both of these phosphorylation reactions occur after V5 is released from PDK-1.[32] The identity of the kinase(s) responsible for the V5 phosphorylation is still under debate. Experimental evidence supports the essential role of mTORC2 (mammalian target of rapamycin complex 2) in the phosphorylation of the TM for conventional and novel PKCs[84,85] and auto-phosphorylation of the HM for conventional PKC.[86]

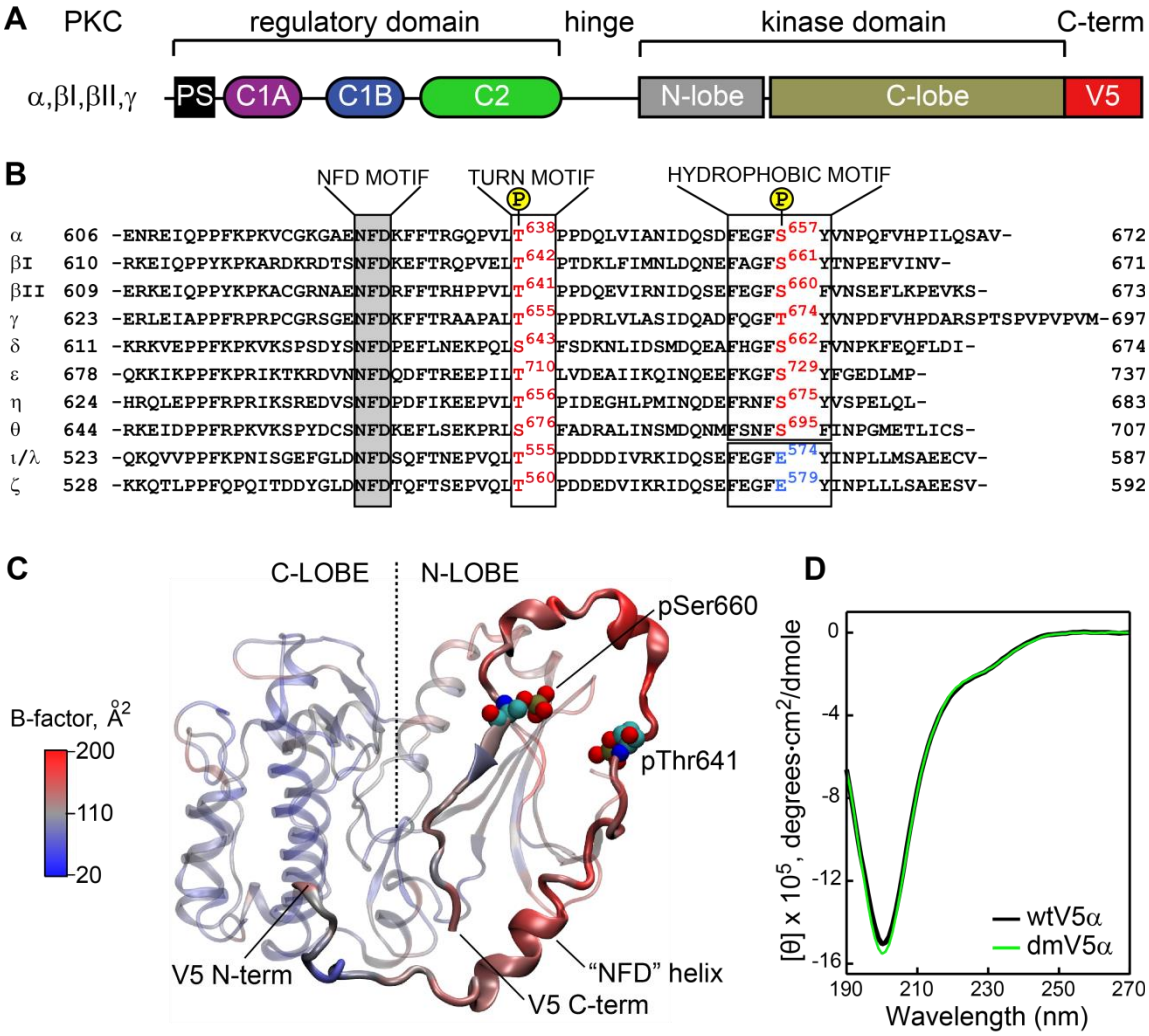

Figure 7. V5 domain is a variable C-terminal region of PKCs. (A) Linear diagram of conventional PKC isoforms illustrating the multi-modular structure of the enzyme. **(B)** Alignment of V5 primary structures of PKC isoforms from *M. musculus*. The conserved NFD motif is highlighted in gray; HM and TM motifs are boxed. The Ser/Thr residue of the HM is a Glu residue (blue) in atypical isoforms. **(C)** Catalytic domain (residues 339-679) taken from the crystal structure of the PKCβII "intermediate", PDB ID 3PFQ. The B-factors of backbone atoms are mapped onto the structure as a color gradient. The N-/C-lobes of the kinase domain and V5 are shown with transparent and opaque representations, respectively. **(D)** Circular dichroism spectra of micelle-free wtV5α and dmV5α domains.

Despite the pivotal role of V5 in the maturation and regulation of the parent enzymes, little is known about its structure in the extended conformation of PKCs that is associated either with immature (i.e. un-phosphorylated) or with activated kinase (mature and membrane-bound). The existing structural information about V5 domains comes exclusively from crystal structures of five isolated catalytic domains[87-91] and of PKCβII that represents an intermediate state in the activation process.[23] All crystal structures are of mature, fully-phosphorylated protein species. In some structures, the elctron density of the V5 domain is either missing or poorly defined.[89-91] In others,[23,87,88] the V5 domain wraps around the N-lobe of the kinase sub-domain, as shown in Figure 7C. Even in those structures, the B-factors of the V5 region are significantly elevated comparing to other regions pf the protein. This indicates that V5 domain has certain degree of either static or dynamic disorder (Figure 8).

In this work, we seek to understand the conformational preferences of the V5 domain from PKCα, a conventional PKC isoform. The obtained structural information enabled us to evaluate the effect of negative charges introduced into V5 upon the phosphorylation of TM and HM, and to assess the extent of the V5 conformational changes during maturation process. Unexpectedly, we found that V5 associates with micelles serving as a membrane mimetic. The domain acquires partial helical structure upon association with micelles. In order to assess the strength of interaction and relevance to physiological lipid bilayer, we also used large unilamellar vesicles (LUV) as a membrane mimetic. We incorporated paramagnetic components into the LUVs as sensitive probes for interaction by NMR.

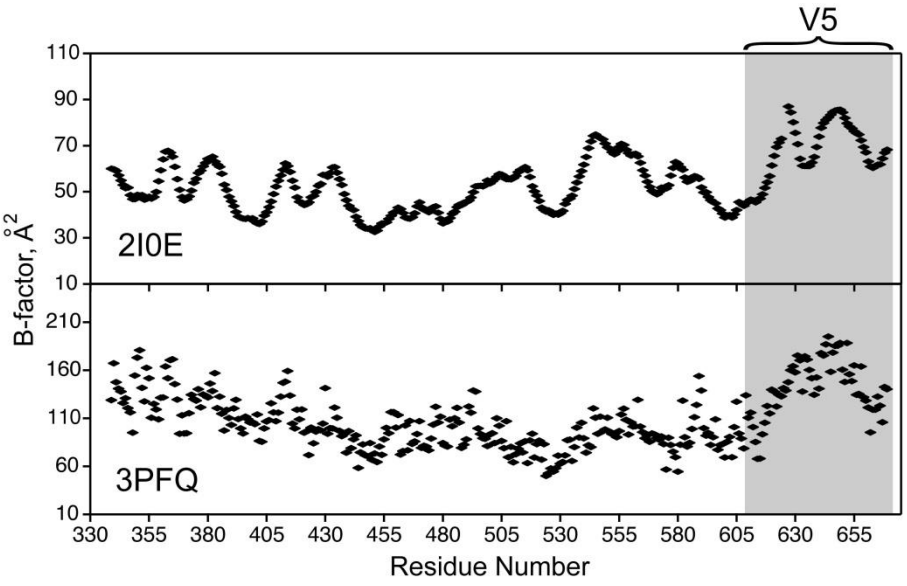

Figure 8. The B-factors of Cα atoms extracted from the crystal structures of isolated PKCβII catalytic domain (2I0E[88]) and the PKCβII intermediate (3PFQ[23]). The residues corresponding to the C-terminal V5 domain (609-669) are shaded. V5 has elevated B-factors in both structures, indicating some degree of either static or dynamic disorder.

Experimental procedures

Materials

1-palmitoyl-2-oleoyl-sn-glycero-3-phosphocholine (POPC), 1-palmitoyl-2-oleoyl-sn-glycero-3- phospho-L-serine (POPS), L-α-phosphatidylinositol-4,5-bisphosphate (Brain, Porcine) (ammonium salt) (brain PtdIns(4,5)P_2) and 1-palmitoyl-2-stearoyl-(5-doxyl)-sn-glycero-3-phosphocholine (5-Doxyl PC) were obtained from Avanti Polar Lipids (Alabaster, AL).

Preparation of V5α samples

V5α (residues 606–672 of Protein Kinase Cα, M. musculus) was cloned into a pET31b(+) vector (Novagen) as a C-terminal fusion with ketosteroid isomerase (KSI) using the following protocol. A codon-optimized DNA sequence of V5α in a pUC57 vector was obtained from Genscript. Two identical AlwNI restriction sites with Met codons, 5'-CAGATGCTG-V5α-CAGATGCTG-3', were engineered into the sequence. In addition, C619S mutation was introduced into the gene to prevent V5α dimerization via the formation of disulfide bonds. The source plasmid, pUC57, was digested with the AlwNI restriction enzyme (NEB) at 37 ℃ for 4 hours. The DNA fragment containing V5α was purified from the 2% agarose gel using the Gel Extraction Kit (Qiagen). The target vector, pET31b(+), was linearized by treatment with AlwNI restriction enzyme at 37 °C for 4 hours and dephosphorylated with alkaline phosphatase (NEB). The V5α DNA insert was ligated into the pET31b(+) vector using T4 DNA ligase (NEB). As a result, the V5α sequence was placed downstream of the 125 amino acids KSI gene and upstream of a His•tag sequence. QuikChange™ protocol (Agilent Technologies) was used to (i) delete three extra nucleotides from each AlwNI restriction site; and (ii) introduce the phosphorylation-mimicking T638E/S657E mutations into the newly constructed wtV5α plasmid. In this manuscript, we refer to the T638E/S657E mutant as dmV5α.

The fusion proteins KSI–(wtV5α or dmV5α)–His•tag, with KSI, V5α, and His•tag separated by Met residues, were expressed in BL21(DE3) pLysS *E. coli* cells. For natural abundance preparations, the expression was induced by adding isopropyl β-

D-1-thiogalactopyranoside (IPTG) to a final concentration of 0.5 mM to the cell cultures at OD_{600} of 0.5. The induction period was 5 hours at 37 ℃. For uniformly [^{15}N, ^{13}C] (or [^{15}N]-enriched) proteins, we used the re-suspension method of Marley et al.[92] with M9 minimal media containing 3 g/L of [^{13}C-6]-D-glucose (or natural abundance glucose) and 1 g/L of $^{15}NH_4Cl$ (Cambridge Isotopes). In this case, the protein expression was induced for 4 hours at 37 ℃.

The cells were harvested by centrifugation (30 min, 4,000 rpm at 4 ℃) and lysed by sonication in a buffer containing 20 mM Tris-HCl, 0.5 M NaCl, and 5 mM imidazole at pH 7.9 (Buffer A). The inclusion bodies containing KSI-V5-His•tag fusion protein were pelleted by centrifugation (15 min at 14,000 rpm, 4 ℃) and washed once with 1 M urea in Buffer A. The pellet was then solubilized in Buffer B (8 M urea dissolved in Buffer A) and incubated with Ni-Sepharose resin (GE Healthcare) for 1 hour at room temperature. The resin was washed four times with 16 mM imidazole in Buffer B, followed by the elution of the fusion protein by 300 mM imidazole in the same buffer.

The eluted fraction was acidified by adding HCl to a final concentration of 0.5 M. The fusion protein was cleaved at Met residues with CNBr (Acros Organics). CNBr was dissolved in acetonitrile and added to the acidified fusion protein to obtain a ~100-fold molar excess. The reaction was carried out in the dark under N_2 at room temperature with constant stirring. After 18 hours, the solvent was removed from the reaction mixture using a rotary evaporator at 28 ℃. The solid residue containing the target protein was dissolved in deionized water and neutralized with 10 M KOH. The mixture contained V5α, its fusion partner KSI, His•tag, and un-cleaved fusion protein.

All species containing a His•tag moiety were removed from solution by an extra incubation step with Ni-Sepharose resin.

To remove urea, the protein solution was dialyzed into a buffer containing 20 mM Tris-HCl and 0.1 mM EDTA at pH 7.0. The precipitated KSI was spun down at 8,000 rpm for 10 min at 4 °C. The supernatant containing V5α was further purified on a HiTrap Q HP anion exchange column (GE Healthcare) using a linear gradient from 0 to 0.4 M NaCl. The purified V5α protein was dialyzed into deionized water, freeze-dried, and stored at –80 ℃. Molecular weights of wtV5α and dmV5α were verified by MALDI-TOF mass spectrometry.

Protein stock solutions were prepared by dissolving lyophilized V5α in the NMR buffer containing 20 mM MES at pH 6.0, 100 mM KCl, 8% D_2O, and 0.02% NaN_3. The protein concentration was determined using the bicinchoninic acid protein assay reagent (Thermo Scientific Pierce) with Bovine Serum Albumin (Sigma-Aldrich) as a standard. NMR samples were prepared by diluting the stock solutions to 250 μM [U-^{13}C,^{15}N] enriched V5α and [U-^{15}N] enriched V5α for assignment and relaxation experiments, respectively.

Natural abundance n-dodecylphosphocholine (DPC) and [U-$^{2}H_{38}$, 98%] DPC were purchased from Avanti Polar Lipids and Cambridge Isotopes, respectively. Aliquots of DPC stock solutions in chloroform were dried under a slow stream of N_2 gas and then under vacuum for 2 hours. The DPC film was re-suspended in NMR buffer by vortexing for 1 min to form a clear micelle solution. The micelle and protein stock solutions were then mixed to produce a final concentration of 316 μM [U-^{13}C,^{15}N] V5α

and 100 mM DPC. Natural abundance DPC and [U-$^{2}H_{38}$, 98%] DPC were used to prepare the wtV5α and dmV5α samples, respectively.

Spectroscopy

The circular dichroism spectra were collected using the Jasco J-815 CD instrument on samples containing either 10 μM V5α or 10 μM V5α/10 mM DPC, both in 10 mM potassium phosphate buffer at pH 7.0.

NMR experiments were performed on Varian spectrometers at magnetic field strengths of 11.7 Tesla or 14.1 Tesla, corresponding to the ^{1}H Larmor frequencies of 500 and 600 MHz, respectively. The assignment of cross-peaks to the specific residues was carried out using the following triple-resonance NMR experiments: HNCACB[93], CBCA(CO)NH[93], HNCO[93], HN(CA)CO[94] (micelle-free sample only), and C(CO)NH[95] on the V5α samples uniformly enriched with ^{15}N and ^{13}C. The NMR resonance assignments are deposited in BioMagResBank under accession numbers: 18927 (wtV5α), 18928 (dmV5α), 18929 (micelle-associated wtV5α), and 18930 (micelle-associated dmV5α). The chemical shift perturbation Δ was calculated according to the following equation[96]:

$$\Delta = [(\Delta\delta_H)^2 + (0.152 \times \Delta\delta_N)^2 + (0.288 \times \Delta\delta_{C\alpha})^2 \\ (0.288 \times \Delta\delta_{C\beta})^2 + (0.329 \times \Delta\delta_{CO})^2]^{1/2} \quad \textbf{2.1}$$

where $\Delta\delta_H$, $\Delta\delta_N$, $\Delta\delta_{C\alpha}$, $\Delta\delta_{C\beta}$, and $\Delta\delta_{CO}$ are the chemical shift differences between the $^{1}H_N$, ^{15}N, $^{13}C\alpha$, $^{13}C\beta$ and ^{13}CO nuclei. In the conformational analysis of Pro-containing segments of V5α, the populations of cis- and trans- conformers were determined from

the peak intensities normalized to the combined intensity of all cross-peaks observed for a given residue.

There are wtV5α/DPC and dmV5α/DPC residues that do not have a complete set of shifts for CSP analysis, and they are listed as following. The missing chemical shifts are indicated in parentheses. wtV5α: Q611 (^{13}CO), P612, P613 ($^{1}H_N$, ^{15}N), K615 (^{13}CO), P616 ($^{1}H_N$, ^{15}N), G620 (^{13}Cβ), G622 (^{13}Cβ), G633 (^{13}Cβ), Q634 (^{13}CO), P635 ($^{1}H_N$, ^{15}N), T638 (^{13}CO), P639, P640 ($^{1}H_N$, ^{15}N), G655 (^{13}Cβ), N660 (^{13}CO), P661 ($^{1}H_N$, ^{15}N), F663 (^{13}CO), V664, H665, P666, I667 ($^{1}H_N$, ^{15}N). dmV5α: Q611 (^{13}CO), P612, P613 ($^{1}H_N$, ^{15}N), K615 (^{13}CO), P616 ($^{1}H_N$, ^{15}N), G620 (^{13}Cβ), G622 (^{13}Cβ), G633 (^{13}Cβ), Q634 (^{13}CO), P635 ($^{1}H_N$, ^{15}N), E638 (^{13}CO), P639, P640 ($^{1}H_N$, ^{15}N), G655 (^{13}Cβ), V659 (^{13}Cα, ^{13}Cβ, ^{13}CO), N660, P661 ($^{1}H_N$, ^{15}N), Q662 (^{13}Cβ, ^{13}CO), F663, V664, H665, P666, I667 (^{1}HN, ^{15}N, ^{13}Cα, ^{13}Cβ).

Longitudinal relaxation rate constants (R_1), transverse relaxation rate constants (R_2), and {^{1}H}-^{15}N Nuclear Overhauser Enhancement (NOE) were measured for all spectrally resolved N-H groups of wtV5α and dmV5α using standard method.[97] The measurements were carried out at a magnetic field strength of 11.7 Tesla corresponding to the ^{1}H Larmor frequency of 500 MHz. Twelve time points ranging from 0.008 to 0.200 s (R_2) and 0.020 to 0.700 s (R_1) were collected, three of which were duplicates. The NOE data were acquired in an interleaved manner, with a 3 s saturation period and a 5 s recycle delay. Cross-peak intensities were used to quantify relaxation, and the uncertainties of these intensities were estimated either from the root-mean-square noise level of the base plane (NOE) or from the duplicate measurements (R_1 and R_2). The

reduced[98,99] spectral density mapping[100,101] approach was used to calculate the values of spectral density at 0, ω_N, $0.87\omega_H$, and $0.92\omega_H$ MHz. ω_N = 50 MHz and ω_H = 500 MHz are the ^{15}N and ^{1}H Larmor frequencies, respectively.

Interaction of wtV5α with membranes probed by paramagnetic relaxation enhancement with NMR spectroscopy

To determine if V5α interacts with bilayer type of membrane mimetics, we used paramagnetic nitroxyl radical group doxyl covalently modified at 5-carbon position of POPC (5-doxyl-PC) incorporated into LUVs, as well as Mn(II) coated PtdSer containing LUVs. The doxyl-LUVs were made by mixing lipid stocks to homogeneity of POPC:POPS:PtdIns(4,5)P_2:5-doxyl-PC in a molar ratio of 88.5:10:1:0.5. The diamagnetic control sample contained separately prepared LUVs with POPC:POPS:PtdIns(4,5)P_2 (89:10:1). Total lipid concentrations in NMR samples were 20mM. For the Mn(II) coated LUVs, $MnCl_2$ stock solution was added to the diamagnetic LUV containing sample to a final concentration of 0.4mM. Since total concentration of POPS and PtdIns(4,5)P_2 components was 2.2mM, all Mn^{2+} ions were associated with LUVs in the sample. For the control sample in which Mn^{2+} was directly added to V5 in the absence of LUVs, final Mn^{2+} concentration was 35μM. Protein concentrations of wtV5α used in all samples were 140μM.

The ^{1}H transverse paramagnetic relaxation enhancement experiments were measured as Γ_2 rates with methods from Iwahara et al..[102] Experiments were performed on Bruker AvanceIII spectrometer equipped with a cryogenic probe at magnetic field

strengths of 14.1 Tesla, corresponding to the ^{1}H Larmor frequencies of 600 MHz. The Γ_2 rates are calculated for each residue according to the following equation:

$$\Gamma_2 = R_{2,para} - R_{2,dia} \qquad \textbf{2.2}$$

where the paramagnetic ($R_{2,\text{para}}$) and diamagnetic ($R_{2,\text{dia}}$) states were measured with the pairs of two samples containing the paramagnetic 5-doxyl-PC LUVs or Mn(II) coated LUVs and the diamagnetic LUVs, respectively. The relaxation delay ΔT was optimized to be 40ms by minimizing the error of Γ_2 rates as described in Iwahara et al..[102]

Results

Recombinant V5α can be prepared in quantities sufficient for structural work

Structural studies using NMR spectroscopy require milligram quantities of highly purified isotopically enriched proteins. Heterologous expression of the full-length 67-residue V5α by itself or with soluble fusion partners in E. coli produced a protein that was either un-inducible or severely proteolyzed. Therefore, we directed the expression of V5α into inclusion bodies using the approach pioneered by Walsh's laboratory.[103] The codon-optimized DNA sequence corresponding to the polypeptide sequence of V5 domain from PKCα (*M. musculus* and identical in *H. sapiens*) was cloned as a fusion with ketosteroid isomerase (KSI) gene into a pET31b(+) expression vector, in which Met codons are inserted between the KSI, the V5 gene, and the $(His)_6$ cassette. The fusion protein was extracted from the inclusion bodies, purified using Ni-NTA affinity resin, and cleaved with CNBr. V5 was separated from KSI using dialysis against an aqueous buffer solution and subsequently purified using anion-exchange chromatography. We

obtained ~6-12 mg of >95% pure protein per 1 Liter of cell culture, depending on the expression medium. The detailed expression and purification protocol is given in Experimental procedures (*vide supra*).

We prepared two variants of V5: one is the unphosphorylated construct named wild type (wtV5α) and the other is a double mutant mimicking the fully phosphorylated state (dmV5α). The C619S mutation was introduced into both constructs to prevent carbamylation of the Cys residue under the acidic conditions of the CNBr cleavage reaction. The dmV5α contains two mutations: T638E and S657E, where the Glu residue at each position mimics the phosphorylated states of TM and HM (see Figure 7B). These or equivalent phosphorylation-mimicking mutations were shown to preserve the catalytic competency of both PKCα[104,105] and PKCβII.[30,31]

V5α is intrinsically disordered with a propensity to form α-helical and β structures

We first used circular dichroism (CD) spectroscopy to evaluate the conformational preferences of the V5α variants. The spectra shown in Figure 7D are essentially identical for the wtV5α and dmV5α, indicating that the introduction of two negative charges at the TM and HM does not appreciably influence the secondary structure content of the domain. The spectra have a pronounced minimum at 200 nm that is typical for intrinsically disordered proteins.[106,107] There is also a small shoulder at 230 nm suggesting that V5α may have some secondary structure content. Estimation of the secondary structure by the CONTIN[108,109] software package revealed 4.0% and 8.9% content of the regular α-helical and β-structures, respectively, for wtV5α. The estimated

secondary structure convents are 4.1% and 9.2% of the regular α-helical and β-structures, respectively, for dmV5α. One could see that the estimated secondary structure contents are also essentially identical between the two constructs.

The ^{15}N-^{1}H hetero-nuclear single-quantum coherence (HSQC) spectra of the [U-^{15}N] enriched V5α variants are superimposed in Figure 9A. The cross-peaks in the spectra correspond to the amide ^{15}N-^{1}H groups of the protein backbone. The assignment of cross-peaks to the specific residues was carried out using the triple-resonance NMR experiments on the V5α samples uniformly enriched with ^{15}N and ^{13}C as described in the Experimental procedures. The HSQC spectra of Figure 9A are characterized by small chemical shift dispersion in the amide ^{1}H region from 7.8 to 8.6 ppm, which is a spectroscopic signature of intrinsically disordered proteins.[110] To evaluate the influence of phosphorylation-mimicking mutations, we carried out a chemical shift perturbation (CSP) analysis for the dmV5α-wtV5α pair using the $^{1}H_N$, ^{15}N, ^{13}CO, $^{13}C\alpha$, and $^{13}C\beta$ chemical shifts. Significant perturbations are observed at the mutation sites, Ser657 and Thr638, due to the change in amino acid identities. In addition, the residues adjacent to the phosphorylation-mimicking mutations experienced minor chemical shift changes. We attribute those to the changes in the local electrostatic environment caused by the introduction of two negative charges at the TM and HM.

To evaluate the conformational preferences of V5 variants, we calculated secondary structure propensity (SSP) scores[111] using the Cα and Cβ chemical shifts (Figure 9C). The sign and magnitude of SSP scores, which range from -1 to +1, reflect the propensity of a given residue in the polypeptide to form β- or α-structures.

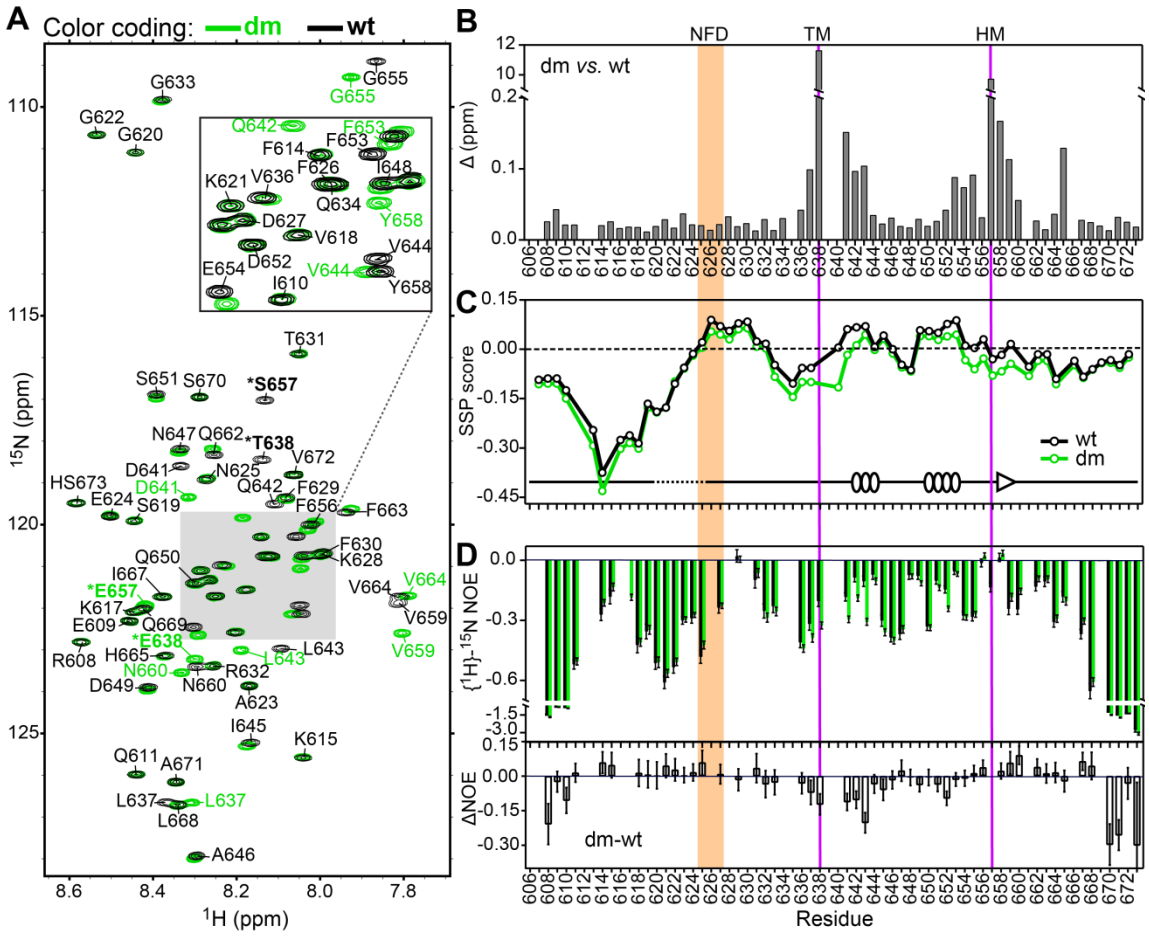

Figure 9. **Conformational preferences and sub-nanosecond dynamics of wtV5α and dmV5α.** **(A)** Overlay of the ^{15}N-^{1}H HSQC spectra of wtV5α (black) and dmV5α (green). The asterisks indicate the mutation sites, Thr638 (TM) and Ser657 (HM). HS673 stands for homoserine lactone, which is the C-terminal residue generated upon CNBr cleavage of the $(His)_6$-tag from V5α. **(B)** Chemical shift perturbation analysis of the dmV5α-wtV5α pair. Purple vertical lines mark the mutation sites; the NFD motif is shaded. **(C)** SSP scores plotted as a function of the primary structure. The secondary structure elements of the V5 domain in the structure of the catalytic domain from PKCα (PDB ID 3IW4) are shown for comparison. **(D)** Comparison of the hetero-nuclear {^{1}H} -^{15}N NOE values obtained for wtV5α (black) and dmV5α (green). The NOE values and their difference are plotted against the V5 primary structure in the top and bottom panels, respectively.

The SSP scores vary significantly across the V5α domain. The N-terminal quarter of both V5α variants has a rather high propensity to form β-structures, with a minimum SSP score reaching -0.43. A region with weak α-helical propensity that contains a conserved NFD motif follows the β segment. In three crystal structures of PKC catalytic domains, the NFD motif forms part of the 8-12 residue helical region. The interaction partners of the NFD motif in the crystalline state vary depending on the PKC isoform/construct and include the adenine ring of ATP (catalytic domain of PKCι in complex with ATP, 3A8W[87]), the N-terminal lobe of the kinase (catalytic domain of PKCβII, 2I0E[88]), and the regulatory C1B domain (PKCβII intermediate, 3PFQ[23]). Another V5α segment with weak α-helical propensity is located between the TM and HM, which are marked with purple lines in Figure 9B-D. The secondary structure elements of V5α taken from the crystal structure of the catalytic domain of PKCα (PDB ID 3IW4[91]) are plotted on the SSP graph. In this crystal structure, most of V5α is unstructured, and the segment preceding the NFD motif is missing. However, there are two short helical regions between the TM and HM that correlate with our positive SSP scores. Taken together, these data suggest that the association of V5α with the N-terminal lobe of the kinase domain during the final step of maturation may include both "conformational selection" and "folding upon binding" mechanisms.[112]

To assess the conformational flexibility of the V5α backbone, we measured three relaxation parameters: longitudinal relaxation rate constants (R_1), transverse relaxation rate constants (R_2), and $\{^1H\}$-^{15}N Nuclear Overhauser Enhancement (NOE) for all spectrally resolved N-H groups (Figure 9 and Figure 10). As shown in Figure 9D, the

NOE values are negative throughout most of the primary structure. The negative NOE values indicate a large contribution of high frequency, i.e. sub-nanosecond, motions to the dynamics of the V5 backbone. The NOE profile of V5 is non-uniform with lower values for the N- and C-termini, and higher values for the short N-terminal segment with high β-structure propensity; the region following the NFD motif; the region upstream of the TM; and the HM. Overall, there is moderate correlation between the regions of lower conformational flexibility, manifested in elevated NOE values, and the regions with a propensity to form secondary structure. The NOE difference graph of Figure 9D shows that phosphorylation-mimicking mutations increase the conformational flexibility of V5 at the N- and C-termini, as well as between the TM and HM.

To determine the relative contribution of high- and low-frequency motions to the V5 dynamics, we carried out the reduced[98,99] spectral density mapping[100,101] analysis of the relaxation data (Figure 11). The contributions of high-frequency components are reflected in two spectral density values, J(435 MHz) and J(460 MHz). Both values are rather uniform throughout the V5 backbone but increase towards the N- and C-termini. The contributions of low-frequency motions are reflected in the J(0) and J(50 MHz) terms that show moderate variations across most of the V5 backbone but decrease significantly towards the terminal regions. Overall, the relative average values of spectral densities for both V5 variants are given by $J(0):J(\omega_N):J(0.87\omega_H):J(0.92\omega_H)$ =17:9:1:1. These data are consistent with an extended spectral density frequency profile characteristic of unstructured proteins[113], in which the values of low- and high-frequency

components are smaller and larger, respectively, than those of globular proteins of comparable size[98]. The extended spectral density profile, along with the low average values of J(0) (0.60 ns for wtV5α and 0.55 ns for dmV5α), indicate that N-H groups in V5α undergo large-amplitude motions.[114]

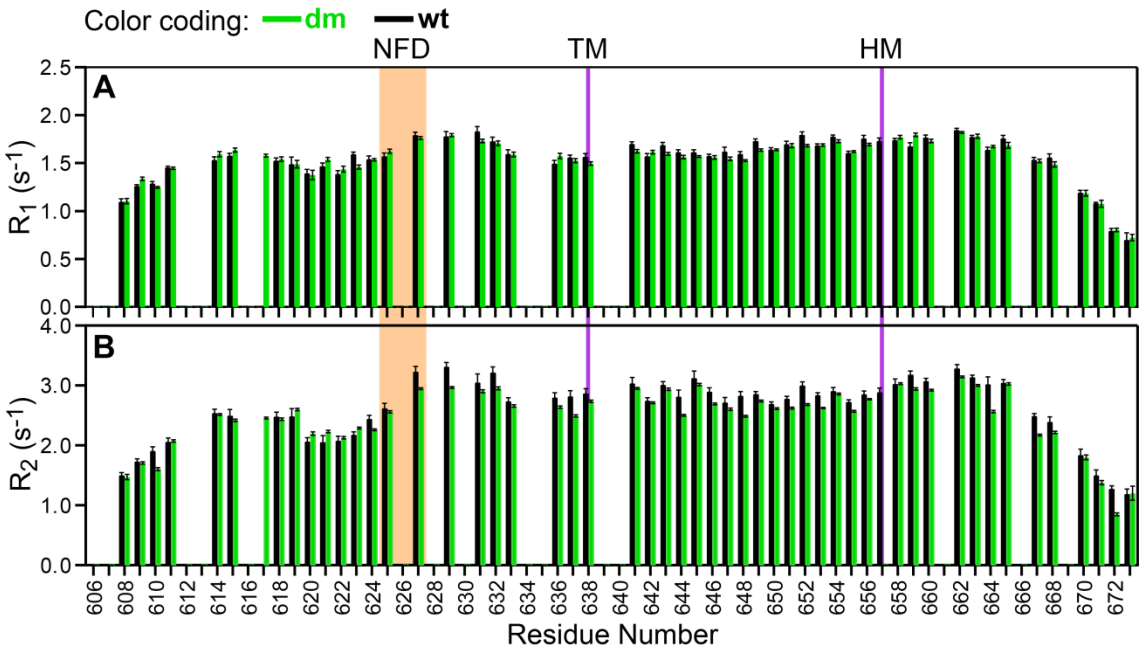

Figure 10. (A) R_1 and (B) R_2 relaxation rate constants versus the primary structure of V5α. The NFD motif is shaded. The hydrophobic motif (HM) and turn motif (TM) are marked with purple lines.

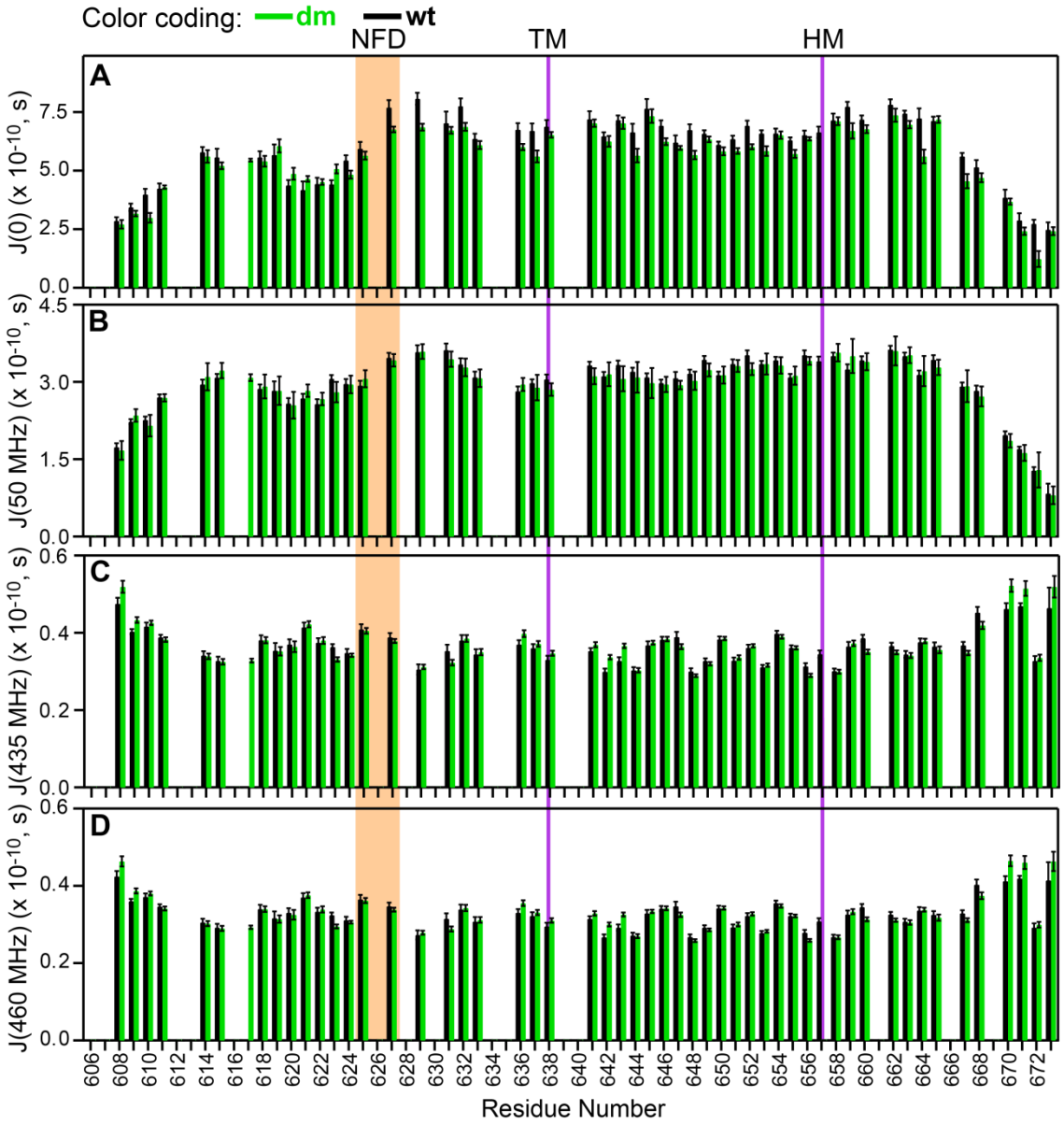

Figure 11. (A) J(0), (B) J(50 MHz), (C) J(435 MHz), and (D) J(460 MHz) versus the primary structure of V5*α*. The NFD motif is shaded. The hydrophobic motif (HM) and turn motif (TM) are marked with purple lines.

In summary, high-frequency large-amplitude motions dominate the backbone dynamics of both V5α variants. Regions with weak propensity towards α-helical structure formation, such as the region upstream of the NFD motif and the TM-HM segment, show a higher degree of motional restriction than the rest of the protein residues. Phosphorylation-mimicking mutations increase the conformational flexibility of V5α in the region between the TM and HM, and at the N- and C-termini.

V5α samples multiple conformations due to cis-trans isomerization of the peptidyl-prolyl bonds

The ^{15}N-^{1}H HSQC spectra of both wtV5α and dmV5α showed a subset of cross-peaks with minor intensities. We were able to assign these peaks using three-dimensional NMR experiments. These peaks correspond to the residues that bracket specific prolines in the primary structure of V5α. Given that our V5α preparations are homogeneous, we concluded that both wtV5α and dmV5α sample multiple conformations due to the cis-trans isomerization of Xaa-Pro bonds, where Xaa is the preceding amino acid. These conformations are in slow exchange on the NMR chemical shift timescale. A distinct spectroscopic signature of trans- and cis- conformations of the Xaa-Pro bonds is the difference between Pro Cβ and Cγ chemical shifts, Δ(Cβ-Cγ): 4.5 ± 1.2 ppm and 9.6 ± 1.3 ppm, respectively.[115] This is most conveniently detected in the ^{15}N strips of the three-dimensional C(CO)NH spectra that correlate the chemical shifts of the N-H amide group of the residue following Pro to the ^{13}C resonances of the Pro sidechain.

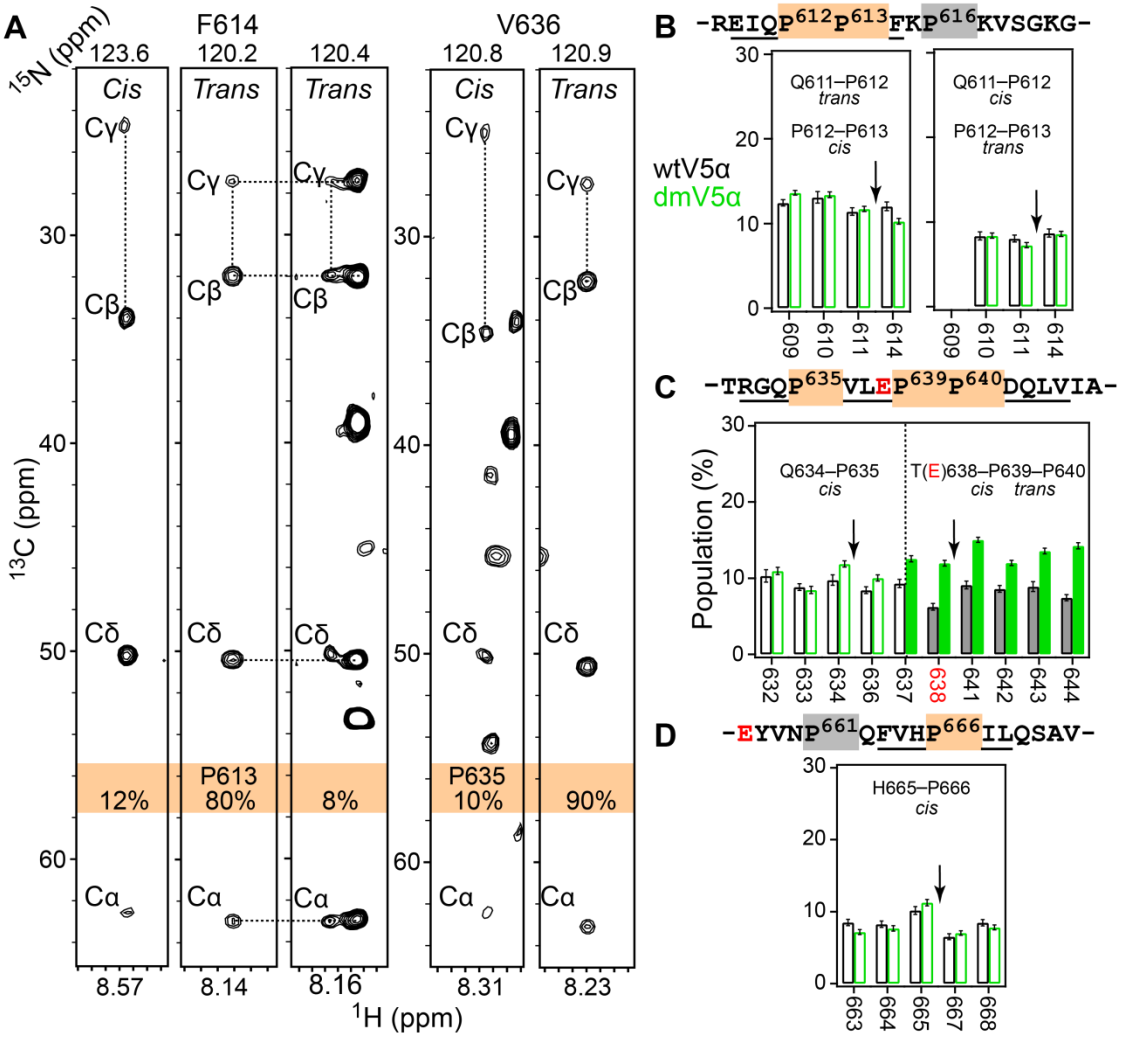

Figure 12. Cis-trans isomerization of Pro residues modulates the conformation of V5α. **(A)** The C(CO)NH strip plots of the F614 and V636 ^{1}H-^{15}N amide planes showing the characteristic spectroscopic pattern of cis- and trans- Pro^{612}-Pro^{613} and Gln^{634}-Pro^{635} peptide bonds. **(B)-(D)** Fractional populations of the V5α species having one Xaa-Pro bond in cis-conformation. Isomerizing Pro residues are highlighted in orange. The wtV5α and dmV5α data are shown in black and green, respectively. The position of Pro residues is indicated with arrows. Residues with quantifiable populations are underlined. In **(C)**, the mutation site T638E is highlighted in red. The data for the turn motif Thr(Glu)^{638}-Pro^{639}-Pro^{640} are shown with filled bars.

Representative data are shown in Figure 12A for the cis- and trans-conformations of P613 and P635.

V5α has a total of eight Pro residues highlighted in Figure 12B-D. We determined that six of them are either involved in (P612, P613, P635, P639, and P666) or influenced by (P640) the cis-trans isomerization processes. For the two isolated Pro residues, P635 and P666, the most abundant conformers with a population of $\gtrsim$ 90% correspond to the trans Gln^{634}-Pro^{635} and His^{665}-Pro^{666} peptide bonds. The average populations of cis-conformers are 9 (10)% and 8 (8)%, for the wtV5α (dmV5α), respectively. The data for individual residues are given in Figure 12C and Figure 12D.

The other four prolines occur as consecutive proline pairs, Pro^{612}-Pro^{613} and Pro^{639}-Pro^{640}. Each pair could potentially give rise to four possible conformations due to cis-trans isomerization. We identified a total of three sets of cross-peaks for the residues that bracket the Pro^{612}-Pro^{613} segment. Based on the $\Delta(C\beta\text{-}C\gamma)$ values of P613, they correspond to the trans-, cis-, and trans- conformations of the Pro^{612}-Pro^{613} peptide bond, with the populations of the latter two given in Figure 12B. The isomerization state of Gln^{611}-Pro^{612} cannot be determined directly because Pro^{613} does not have an N-H group. However, extensive thermodynamic data on unstructured peptides[116] suggest that the "cis-cis" conformation of Gln^{611}-Pro^{612}-Pro^{613} would be the least populated of the four possible conformations. Therefore, we assigned the three V5α species to "trans-trans" (80%), "trans-cis" (12%), and "cis-trans" (8%) conformers of the Gln^{611}-Pro^{612}-Pro^{613} segment; the populations are comparable in the wtV5α and dmV5α.

In contrast to the Pro^{612}-Pro^{613} pair, the conformational exchange behavior of the Pro^{639}-Pro^{640} segment that immediately follows the turn motif, T638, differs between wtV5α and dmV5α. In both V5α constructs, we identified two conformers: major and minor. Based on the Δ(Cβ-Cγ) values of P640, both conformers have a trans Pro^{639}-Pro^{640} peptide bond. Using the same thermodynamic considerations as above, we assigned the major conformer to the "trans-trans" and the minor conformer to the "cis-trans" conformations of the $Thr(Glu)^{638}$-Pro^{639}-Pro^{640} segment. The average population of the minor species increases from 8% in the wtV5α to 13% in the dmV5α (Figure 12C, right).

The shift of the equilibrium towards the cis peptidyl-prolyl bond in the phosphorylation-mimicking variant is likely a property of the local amino acid context of V5 rather than a general consequence of introducing a negative charge. Indeed, studies of model pentapeptides revealed that having Xaa = Glu instead of Thr does not alter the population of the cis Xaa-Pro bond, (9.0% versus 9.4% at pH6).[116] In another peptide study, phosphorylation of the Thr residue slowed down the rate of cis-trans isomerization compared to that of the Thr-Pro, but did not produce a systematic change in the population of the cis-isomers.[117] The conformational preferences of the Thr^{638}-Pro^{639} bond may play a role in the Pin1-mediated down-regulation of PKCα. Pin1 is a peptidyl-prolyl isomerase that, according to the recently proposed model[45], docks onto the hydrophobic motif of V5 and catalyzes the cis-trans isomerization of turn motif, $pThr^{638}$-Pro^{639}. In this model, the trans conformer of the $pThr^{638}$-Pro^{639} peptidyl-prolyl bond in the agonist-activated PKC is potentially more susceptible to dephosphorylation

and ubiquitin-mediated degradation than the cis conformer. Our NMR data provide direct evidence of the existing equilibrium between the cis- and trans- conformers of the turn motif in V5α. Structural characterization of the Pin1-V5α complex is required to determine the molecular basis of V5α-Pin1 interaction and its dependence on the conformation of the pThr^{638}-Pro^{639} bond.

V5α binds to DPC micelles and acquires partial α-helical structure

To determine the propensity of V5α to partition into membrane-mimicking hydrophobic environment, we conducted NMR experiments on both variants in the presence of dodecylphosphocholine (DPC) micelles. DPC micelles were chosen as a membrane-mimicking medium because it worked well for the two peripheral membrane domains of PKCα, C1B[38,118] and C2.[119] Unexpectedly, the NMR HSQC spectrum of wtV5α changed dramatically upon addition of DPC micelles (Figure 13A), resulting in significant cross-peak shifts for all but the most N-terminal amino acids. The changes in cross-peak positions are accompanied by changes in the peak line-widths, indicating that wtV5α binds to the micelles.

The same pattern of spectral changes was observed for dmV5α, as shown in Figure 14A. The backbone resonances of wtV5α and dmV5α complexed to DPC micelles were then assigned using triple-resonance NMR experiments and subjected to CSP analysis using the DPC-free chemical shifts as references. The residue-specific Δ values of wtV5α (Figure 13B) are small for the first 15 amino acids, up to the start of the NFD motif at position 625.

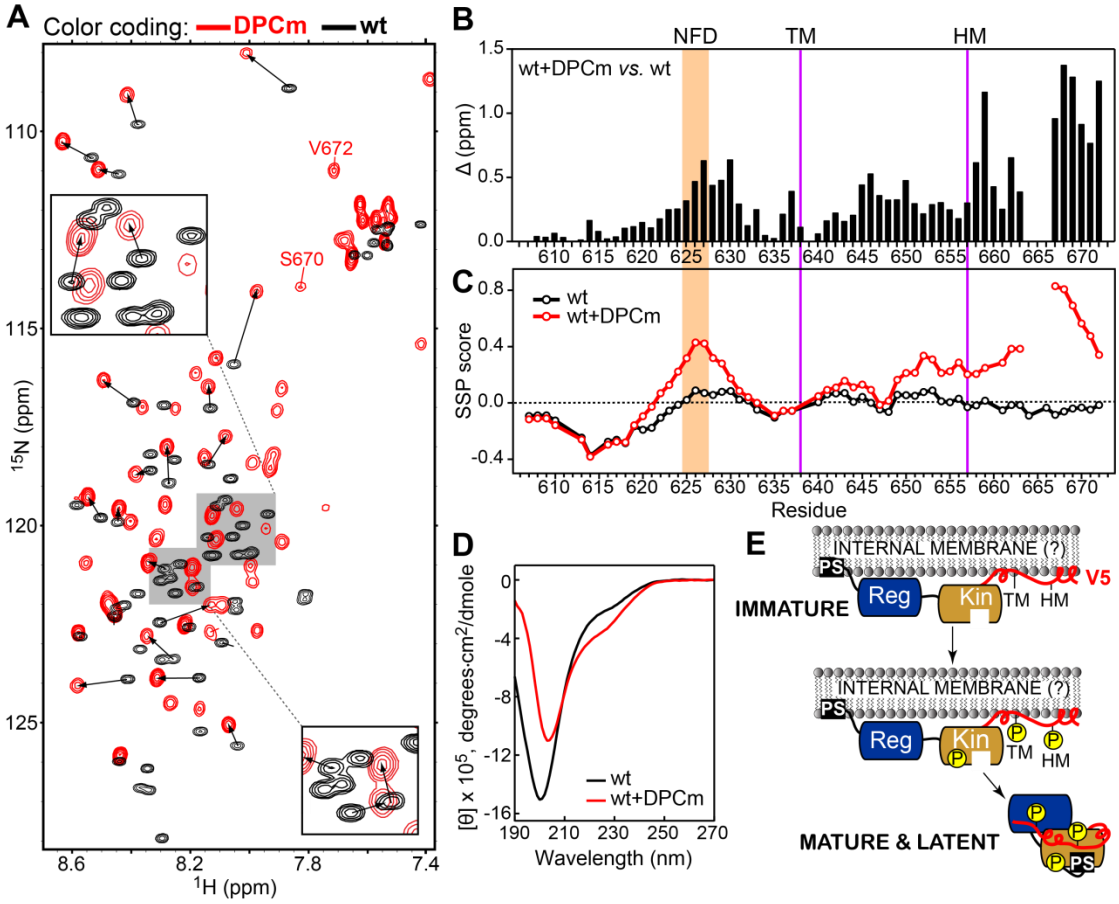

Figure 13. wtV5α associates with DPC micelles (DPCm) and acquires partial α-helical structure. (A) Overlay of the ^{15}N-^{1}H HSQC spectra of wtV5α (black) and wtV5α/DPCm (red). HS673 stands for homoserine lactone, which is the C-terminal residue generated upon CNBr cleavage of the $(His)_6$-tag from V5α. **(B)** Chemical shift perturbation analysis of the wtV5α/DPCm and wtV5α pair. Residues having an incomplete set of chemical shifts are listed in Experimental Procedures. **(C)** SSP scores plotted as a function of the primary structure. **(D)** Circular dichroism spectra of wtV5α domains in the presence (red) and absence (black) of DPC micelles. **(E)** Potential role of V5 as a membrane anchor. Reg and Kin are the regulatory and kinase domains, respectively. The regulatory domain comprises the tandem C1A and C1B domains, commonly referred to as C1, and the C2 domain. PS stands for the pseudo-substrate region. V5α is shown in red.

The chemical shifts of the NFD-containing region (residues 625-634) are significantly perturbed, as well as the region between the TM and HM. Downstream of HM, Δ values increase further reaching the largest values at the C-terminus. Two residues, 664 and 665, are broadened beyond detection indicating a presence of a chemical exchange process that is intermediate on the NMR chemical shift timescale.

Calculated SSP values of the micelle-associated wtV5α, calculated based on Cα and Cβ chemical shifts, are plotted against the primary structure in Figure 13C. The micelle-free wtV5α data are also shown for comparison. According to the SSP data analysis, V5α acquires higher propensity to form helical structures in two regions upon binding to DPC micelles. The first region is the NFD motif, where the SSP score reaches a maximum value of 0.43. The second region is the last one-third of the V5α domain starting from residue 649. The helical propensity increases along the polypeptide backbone reaching the maximum of 0.83 at residue 667, and then decreases to 0.34 at the C-terminus. Our findings are further corroborated by the circular dichroism data that we collected for both V5α variants in the presence of DPC micelles. The CD spectrum of micelle-bound wtV5α is overlaid with the DPC-free spectrum in Figure 13D. The negative signal at 200nm becomes larger and shifted, indicating formation of more structured elements globally. The shoulder region between 220 and 230 nm becomes more prominent, indicating an increase in the helical structure content. Estimation by the CONTIN[108,109] software package produces a ~two-fold increase in the regular α-helical structure content, from 4 to 9%, compared to the micelle-free wtV5α.

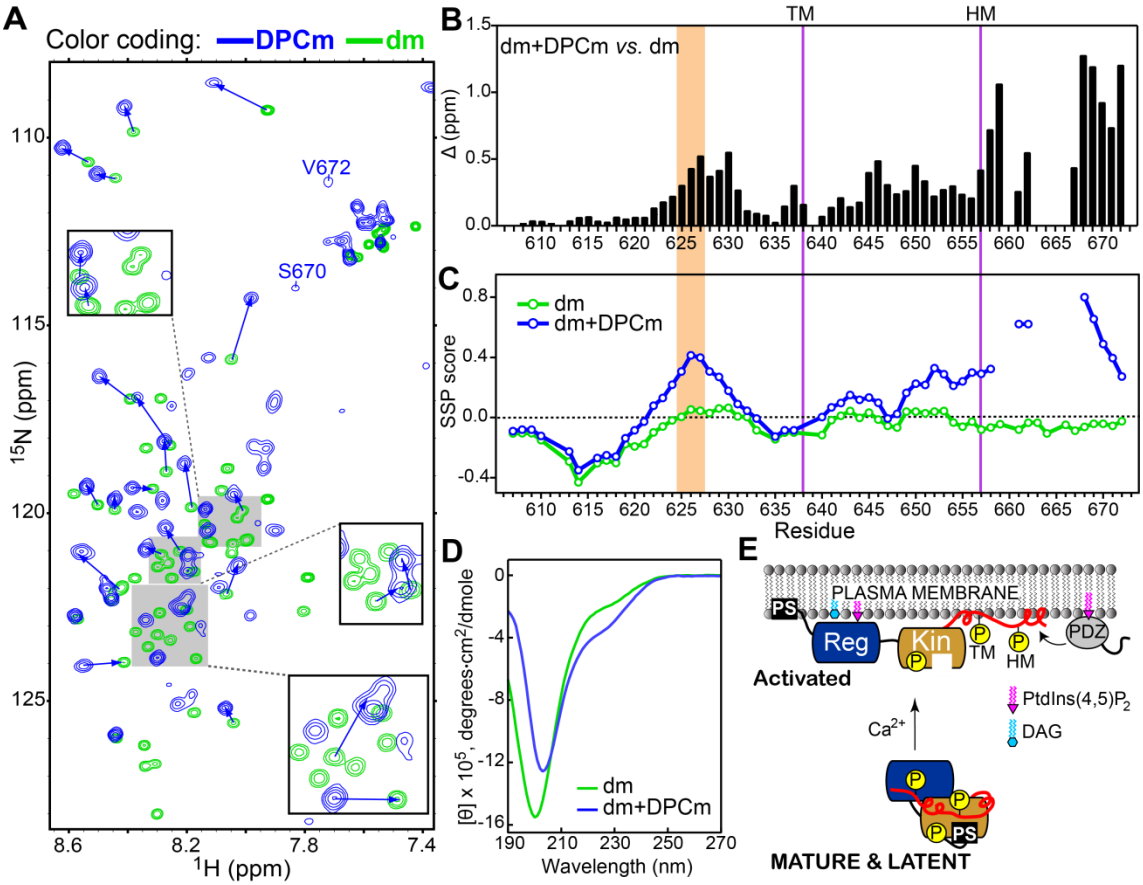

Figure 14. dmV5α binds to DPC micelles (DPCm) and acquires partial α-helical structure. **(A)** Overlay of the ^{15}N-^{1}H HSQC spectra of dmV5α (green) and dmV5α/DPCm (blue) collected at 11.7 Tesla. The DPC concentration is 100 mM. The cross-peaks are labeled according to the residue identity and number. HS673 stands for homoserine lactone, which is the C-terminal residue generated upon CNBr cleavage of the $(His)_6$-tag from V5α. **(B)** Chemical shift perturbation analysis of the dmV5α and dmV5α/DPCm pair. Residues having an incomplete set of chemical shifts are listed in Experimental Procedures. Purple vertical lines indicate the turn and hydrophobic motifs. The NFD motif is shaded. **(C)** SSP scores plotted as a function of the primary structure. Compared to the micelle-free dmV5α, the helical propensity increases for the NFD motif and the surrounding region, the region between the TM and HM, and the most C-terminal amino acid stretch. **(D)** CD spectra of dmV5α in the presence (blue) and absence (green) of DPC micelles. **(E)** Proposed model for activated PKCα interacting with PDZ domain containing signaling proteins. PtdIns(4,5)P_2 and diacylglycerol (DAG) lipid molecules are as indicated in the insert.

The β-structure content remains unchanged for wtV5α. Micelle-associated dmV5α shows a similar pattern of chemical shift perturbations, SSP scores, and CD spectrum (Figure 14).

V5α interacts weakly with LUVs in two modes

In light of our work with DPC micelles, we seek to understand if V5α would interact with bilayer type of membrane mimetics. Liposomes are commonly used bilayer membrane mimetics, which mimics the basic environment of biological cellular membranes. However, they are large in sizes and tumble significantly slower to be detectable using solution NMR methods. For example, the LUVs we use have a size distribution centered at 100nm, which has an estimated molecular weight of >60.8MDa. Therefore, we reason that the crosspeaks of LUV-associated V5α will be broadened completely beyond detection. By comparing the ^{15}N-^{1}H HSQC spectra of V5α in the absence and presence of LUVs (POPC/POPS/PIP_2 89:10:1 molar ratio), there are no significant chemical shift changes on the V5α cross-peaks (Figure 15). There are three possible scenarios associated with the identical chemical shifts: (1) there is no interaction between V5α and the LUVs; (2) there is interaction, but the exchange process between free V5α and an invisible "dark" state is slow in NMR chemical shift timescale; or (3) the exchange process can be fast or intermediate, with a very small population of LUV-bound V5α contributing to undetectable chemical shift perturbations.

By measuring R_2 values of the amide ^{1}H both in the absence and presence of LUVs, we observe an overall increase of R_2 by 0.32 ± 0.01 s^{-1} with the addition of LUVs

(Figure 16B). This value of increase is small but significant, indicating a minor interaction. This can be attributed to the relatively low concentration of LUVs (20mM lipids correspond to 2μM of liposomes) or a relatively low binding affinity. By close inspection of the ΔR_2 along the sequence (Figure 16B), there are regions that have decreased R_2 values in the presence of LUVs, especially residues around the HM (644-663). This observation indicates a more complicated system than a simple two-state exchange between monomer V5α and LUV-bound V5α. In the simple two-state exchange case, R_2 is typically increased close to uniform across the protein sequence.[120]

Since the average value of ΔR_2 is overall $<1\ s^{-1}$, we could not use the dark-state saturation transfer based experiments to reliably probe residue-specific information about LUV interaction.[121] Instead, we utilize paramagnetic relaxation enhancement (PRE) experiments to investigate this case. PRE methods are sensitive for even low population of weak interactions. We first use 5-doxyl-PC doped LUVs (see Experimental procedures), to probe the interaction between V5α and LUVs. The resulting Γ_2 rates (i.e. change in R_2) by comparing the paramagnetic LUVs containing sample and the V5α only sample display a complex pattern (Figure 16C). For example, the N-terminal region (residues 610-615) and the hydrophobic motif region (residues 651-658) have slightly negative Γ_2 rates, while most other residues have positive Γ_2 rates. The positive Γ_2 rates at NFD region (residues 623-631) and C-terminal region (residues 665-672) match well with the micelle-induced association (Figure 16A, C). The overall average Γ_2 value is $0.14 \pm 0.16\ s^{-1}$. This small Γ_2 value is probably due to that the binding interface between LUVs and V5α is restricted to the headgroup region.

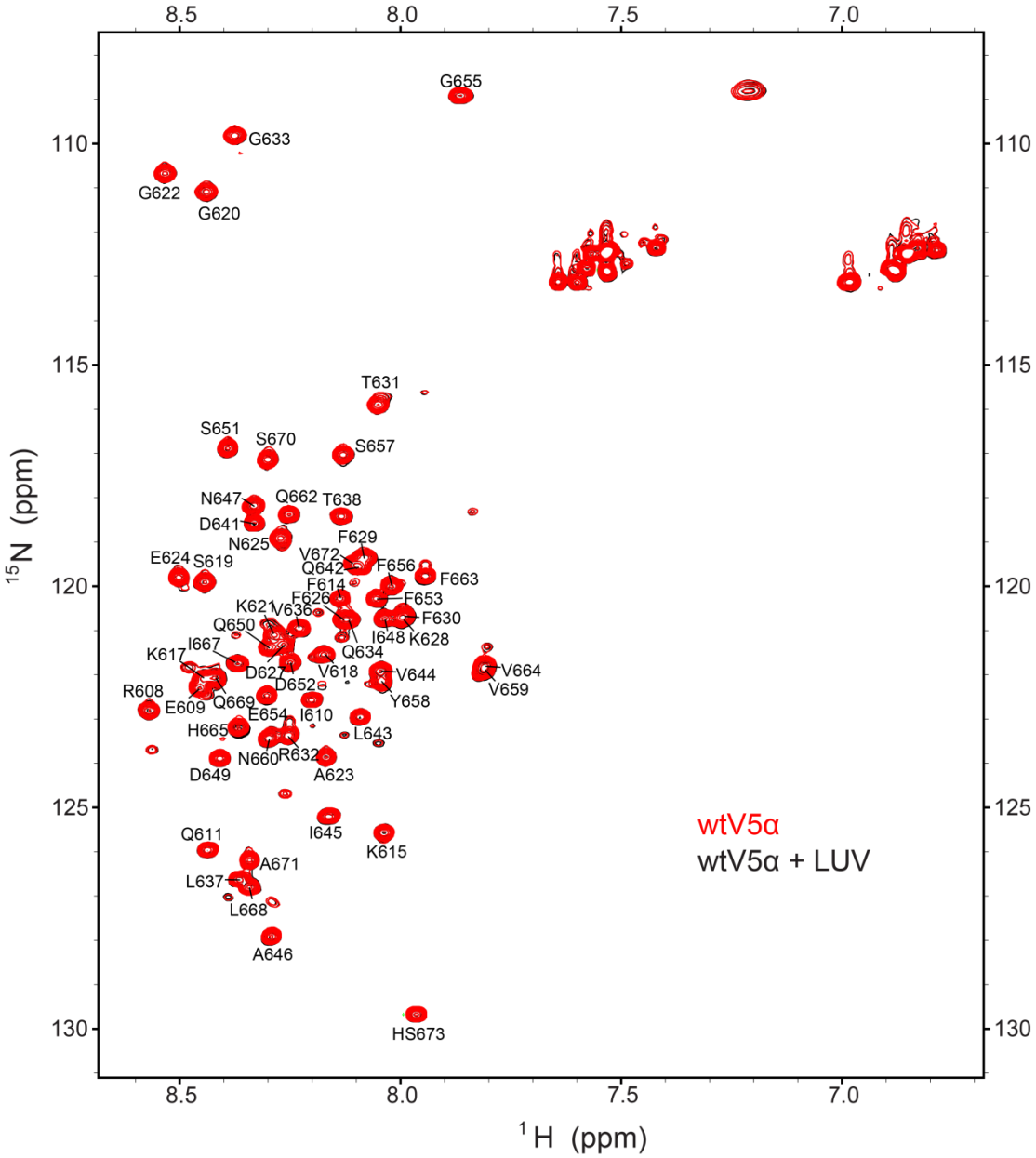

Figure 15. HSQC spectral overlay of wtV5*α* without (red) and with (black) the addition of bilayer membrane mimetic LUVs. The lipid components of the LUVs used are POPC, POPS, and PIP_2 with a ratio of 89:10:1. Total lipid concentration was 20mM. Backbone resonance identities are labeled next to the cross-peaks or with a line directing the labels.

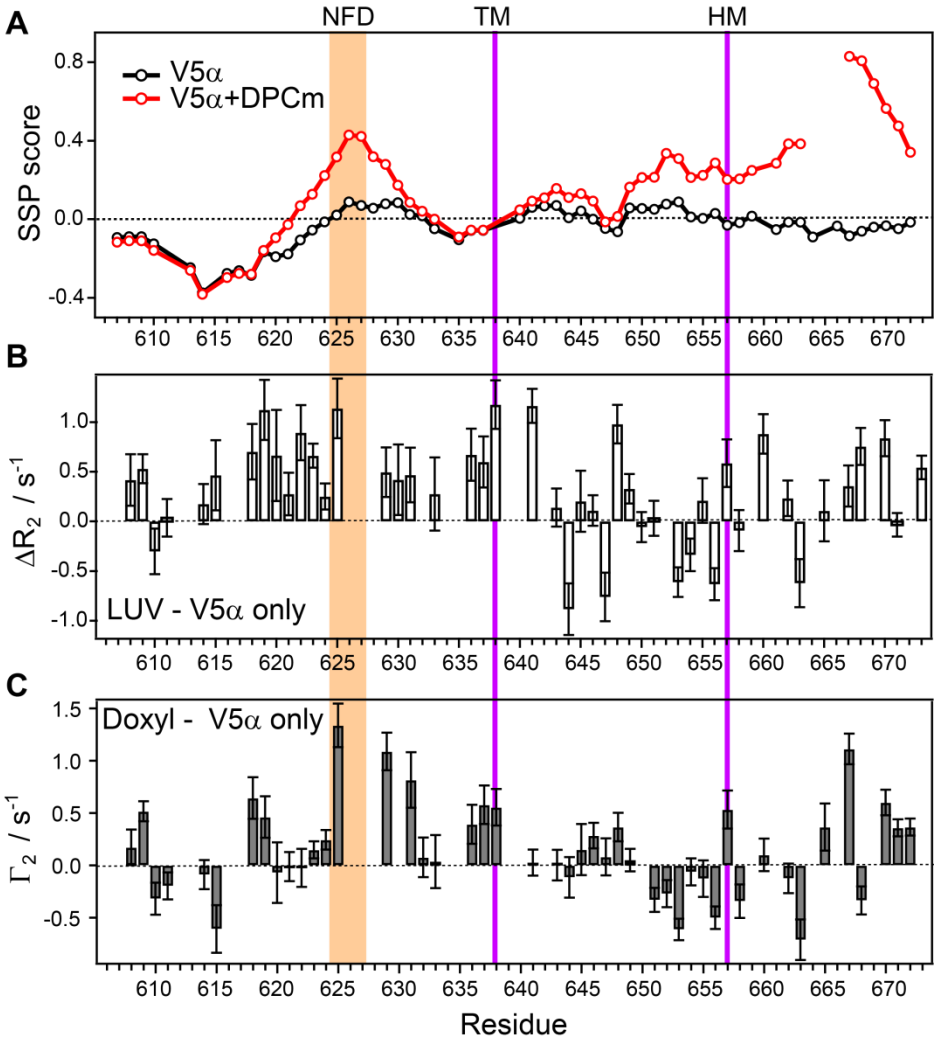

Figure 16. wtV5α interaction with LUVs probed by 5-doxyl-PC induced PRE. **(A)** SSP scores plotted as a function of the primary structure of the wtV5α/DPC micelles and wtV5α experiments. **(B)** The calculated ΔR_2 of wtV5α in the presence and absence of LUVs. **(C)** Γ_2 rates induced by paramagnetic doxyl-LUV. The reference is wtV5α only sample.

The amino acid composition of V5α is largely charged with some scattered hydrophobic residues, displaying amphiphilic properties. In other words, all interacting V5α residues

are probably far away from the hydrophobic core of LUVs where the doxyl groups are located. This could explain the relatively small Γ_2 values induced by the doxyl-LUVs.

In order to further investigate the potential interaction of V5α with the headgroup region of LUVs, we use Mn(II)-coated LUVs.[122] It was previously shown that when negatively charged lipids are incorporated into LUVs, sub-stoichiometric Mn^{2+} ions spontaneously coat the surface of LUVs with relatively high affinity.[122] By using the Mn(II)-coated LUVs, we observe large positive Γ_2 rates for the NFD region and the HM region in which helical conformation was induced upon micelle binding (Figure 17). We then added Mn^{2+} to V5α in the absence of LUVs, to look at broadening due to direct Mn^{2+} binding instead of Mn(II)-coated LUV interactions. This is illustrated in Figure 17, where NFD region is not broadened by solution Mn^{2+} ions. HM region is broadened by solution Mn^{2+} ions, but a different set of residues are affected when comparing to the Mn(II)-coated LUV experiment (Figure 17C, D). This indicates that the HM region broadened by Mn(II)-coated LUV is a result of membrane binding, instead of simply metal binding to the negatively charged HM residues.

From the above data, we conclude that V5α also interacts with bilayer membrane mimetics. The interaction between V5α and LUVs is probably weak but significant. The regions affected by interaction with LUVs are overall similar to those affected by DPC micelles, but the effect was more pronounced with micelles than LUVs. This is likely due to the more exposed hydrophobic environment of micelles compared to the well-packed bilayer of LUVs.

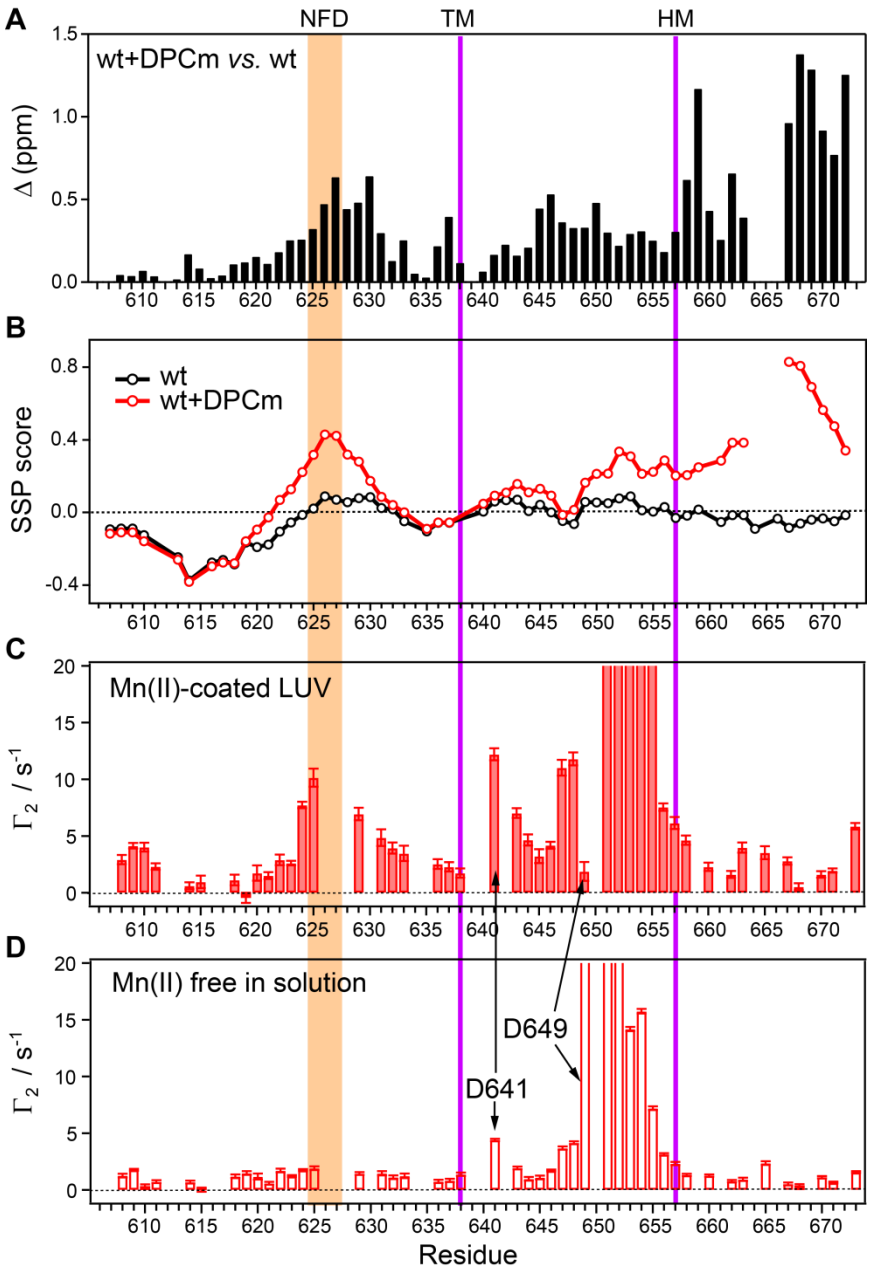

Figure 17. wtV5α interaction with bilayer membrane LUVs probed by Mn^{2+} induced PRE. (A) Chemical shift perturbation analysis of the wtV5α/DPCm and wtV5α pair. **(B)** SSP scores plotted as a function of the primary structure. **(C)** Γ_2 rates which reports on PRE induced by Mn(II)-coating of LUV. The reference is diamagnetic LUV containing sample. **(D)** Γ_2 rates which reports on PRE induced by Mn^{2+} ions in solution. The reference is wtV5α sample in the absence of metal.

Interestingly, we observed a slowly formed conformation of V5α, when checking the LUV added samples in a period of 22 hours (Figure 18). This slowly induced change of an intrinsically disordered region or a disordered peptide upon membrane interaction has been observed previously, with noted examples for membrane penetrating peptides forming pores[123] and Aβ peptide aggregation induced by membrane binding.[124]

Discussion of results

Immature, or newly synthesized, PKC is not phosphorylated. It has been shown that immature PKC partitions some into the detergent-soluble membrane fraction of the cell[24] and loosely associates with the membrane; the nature of the membrane compartment (internal membranes or plasma membrane) is not known. The current thinking in the field is that immature PKC is tethered to the membranes via the pseudo-substrate region[125] and weak cofactor-free interactions of the C1 and C2 domains.[83] Together, these domains make up the entire N-terminal half of the enzyme, as shown in Figure 7A. The propensity of wtV5α to partition into the hydrophobic membrane-mimicking environment suggests that it can potentially serve as a membrane anchor in immature PKCα, as illustrated in our model (Figure 13E). In this model, not only the N-terminal regulatory domain and the pseudo-substrate regions are tethered to the membrane, but also the V5 domain, which provides the anchoring point at the C terminus of the enzyme. The binding affinity is probably weak, as illustrated with our LUV experiments.

.

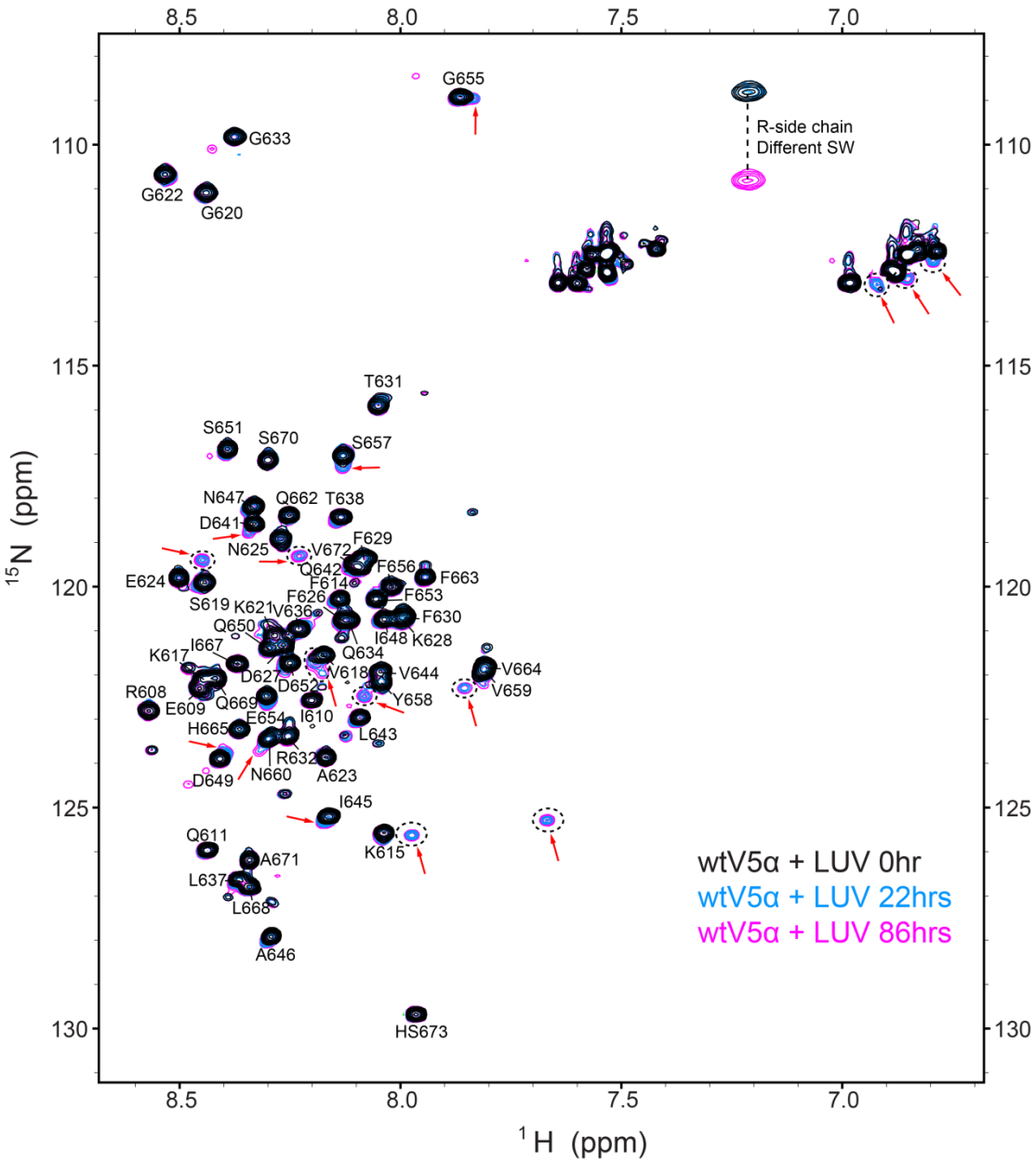

Figure 18. HSQC spectral overlay of wtV5α with the addition of LUVs (black) and after incubation. The 22hrs spectrum (cyan) was acquired after 22 hours incubation at 25 ℃. The 86hrs spectrum (magenta) was acquired for additional 64 hours incubation at 4 ℃. The resonances that appeared after incubation are marked with red arrows, combined with dashed line circles if resolved better. The very different resonance at ^{1}H 7.211ppm is from Arg side-chains, where the 86hrs spectrum has a larger ^{15}N spectral width resulting in a different folded ^{15}N chemical shift position. Backbone resonance identities are labeled next to the cross-peaks or with a line directing the labels.

This is in agreement with two studies showing that the association of newly synthesized, immature PKCs with membranes are of low affinity and can translocate to plasma membrane upon PDBu stimulation.[24,126]

The maturation process involves three ordered phosphorylation reactions, with two phosphorylation sites residing on the conserved hydrophobic and turn motifs, respectively.[83] It is well established that, upon maturation, majority of PKCα localizes in the cytosol.[24] In the cytosol, it adopts a compact latent form, in which the pseudo-substrate region is involved in the auto-inhibitory interactions with the active site of the kinase, as shown in Figure 13E.[127]

What could be the driving force for the mature (i.e. phosphorylated) V5α to disengage completely from the membrane and associate with the N-terminal lobe of the kinase? We speculate that this process is driven by the hydrogen-bonding and electrostatic interactions between the phosphate groups of TM and HM and the residues of the N-terminal lobe of the kinase. These interactions are present in several structures of PKC catalytic domains.[23,87-89] Other intramolecular interactions that differ upon phosphorylations of TM and HM could also be crucial factors, as we will illustrate later in Chapter III. Our data on dmV5α show that the overall interaction mode of V5α with zwitterionic detergent DPC is not significantly influenced by the introduction of negative charges at the HM and TM (compare Figure 13 and Figure 14). If negatively charged lipids are present in the membrane compartment where PKCα undergoes the maturation process, then the electrostatic repulsion between the phosphate groups of TM and HM

and the negatively charged lipid head-groups will also promote the dissociation of the phosphorylated V5α from the membrane.

Upon activation, the compact latent form of the enzyme releases its pseudo-substrate region from the active site of the kinase domain. This domain rearrangement is driven by the C1 and C2 domains undergoing membrane insertion in response to binding their respective cofactors, diacylglycerol (C1 domains) and Ca^{2+}/phosphatidylserine (C2 domain). The ability of the dmV5α to associate with micelles suggests that V5 can potentially function as a membrane anchor for the fully activated mature PKC, in which the N-terminal regulatory domain is membrane-associated. Such an interaction will be dependent on the lipid composition of the membrane and the availability of other V5 binding partners, such as receptors for activated C kinases. PICK1 (protein that interacts with C kinase 1) has been indicated in PKC related signaling[128], and it could potentially interact with V5 domain from PKCα specifically through a PDZ domain binding consensus sequence "-QSAV" at the extreme C-terminus.[129] Another scaffold protein DLG1 (Discs large homolog 1) was also shown to interact with PKCα through its PDZ domain, and acts as a substrate for PKCα.[130] Our data here provide a potential mechanism by which the residues preceding this PDZ consensus provides a membrane anchor for the C-terminus of V5 domain from PKCα, whereas the QSAV motif remains accessible for PDZ domain recognition (Figure 14E). This hypothesis is further supported by the PtdIns(4,5)P_2-containing membrane association of PDZ domain.[131] Upon PKCα translocating to PtdIns(4,5)P_2-enriched plasma membrane, PDZ-contained signaling proteins like PICK1 could readily interact with V5 domain by coincidence

detection. This could increase the lifetime of PKCα's membrane bound state, at the same time assist in protein-protein interactions of PKCα with its isoform-specific downstream substrates.

CHAPTER III

INTRAMOLECULAR INTERACTION BETWEEN C2 REGULATORY DOMAIN AND THE HYDROPHOBIC MOTIF OF V5 DOMAIN – STRUCTURAL AND FUNCTIONAL STUDIES

Background

Although the regulatory and catalytic domains of Protein Kinase C (PKC) isoforms contain functionally independent modules, intramolecular interactions between these domains are generally considered to be the keys to PKC regulation. Even though a complete picture connecting these interactions is lacking, many valuable studies have shed light on the potential interactions between PKC domains. In the auto-inhibited latent form of mature PKC enzymes, the pseudosubstrate (PS) region occupies the active site, located between the N- and C-lobes of the catalytic domain.[127] So far there exists no structural information for this interaction, but it is believed to be a key inhibiting physical interaction for the latent kinase. This interaction becomes destabilized upon activation of the kinase, by potentially concerted conformational changes of other regulatory domains triggered by signaling events. It is generally believed that the latent, cytosolic PKC is stabilized by autoinhibitory interactions, in addition to the PS region interacting with the active site, prior to binding of second messengers to the kinase.

One interaction suggested for stabilizing the latent conformation is the C1A–C2 interaction. The C1A–C2 interaction was detected experimentally with isolated and full-length constructs, and the identities of residues involved in this putative interaction were

inferred based on the computational docking study.[66] The other proposed main interactions are the C-terminal Variable 5 (V5) domain with both C2[47] and C1B[23] regulatory domains. The interaction between V5 and C1B is highly controversial with one study pointing out the minimal effect on the function by mutating the V5–C1B interface.[55] The potential V5–C2 interaction, on the other hand, was shown by mutagenesis to be important for the DAG-insensitivity of PKCα in the absence of calcium signaling.[47] The hydrophobic motif of V5 was shown to be critical in this potential interaction. Moreover, the importance of the V5 hydrophobic motif for Ca^{2+} sensitivity was observed in another mutagenesis study.[31] These data indicate important roles of V5 domain in both auto-inhibition and enzyme activation, but it is not yet clear what kind of interaction is involved in either process. All the potential intramolecular interactions are illustrated in Figure 19.

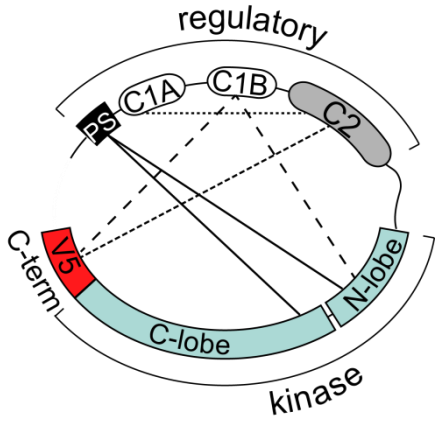

Figure 19. Schematic view of intramolecular interactions proposed for PKCα and PKCβII. PS represents the pseudosubstrate region. Figure adapted with permission from T. I. Igumenova. *Biochemistry* 2015, 54, 4953.[21]

The C-terminal V5 domains are made up of 60 to 80 amino acid segments containing two highly conserved turn and hydrophobic phosphorylation motifs (Figure 7B in Chapter II), while the extreme C-terminal residues beyond the hydrophobic motif are the least conserved sequence both in length and amino acid composition among all PKC isoenzymes. These two phosphorylation motifs of V5 domain are among the three ordered phosphorylation events required for newly-synthesized PKC enzymes to become mature and catalytically competent.[30,81] The phosphorylated mature enzymes then can be activated by association with second messengers, which are Ca^{2+} ions and diacylglycerol in the case of conventional PKCs.

We established in Chapter II that the V5 domain of PKCα is intrinsically disordered, which is consistent with its potential ability to participate in multiple intramolecular interactions. In order to overcome the intrinsic dynamics of full-length PKC, we use a "divide-and-conquer" strategy with a focus on the hydrophobic motif (HM) of the V5 domain. In this chapter, we show that the phosphorylation of the hydrophobic motif facilitates the C2–V5 interaction. Notably, this interaction is synergistically enhanced by Ca^{2+}, indicating a function of this intramolecular interaction to sensitize the C2 domain to Ca^{2+}. To investigate the molecular basis of the detected interaction, we next determined the solution structure of the C2·$(Ca^{2+})_2$·pHM complex by nuclear magnetic resonance, revealing several important electrostatic and hydrophobic interactions.

Guided by our structure, we designed full-length PKCα variants to systematically mutate the observed C2–V5 interface residues. With these variants, we verified that

both the latent conformation and C1 ligand activated membrane translocation are significantly affected. In addition, we showed that externally added V5-pHM peptide is able to activate the kinase in the absence of the C2 domain agonists. Our results indicate that the C-terminal tail of PKCα functions as an intramolecular interaction site with the C2 domain, bridging the regulation stages of PKC through potential conformational switches in response to cytosolic Ca^{2+} and anionic membrane lipids. Our proposed model may provide insights into a common regulation mechanism for other multi-domain kinases containing intrinsically disordered segments.

Experimental procedures

Protein and peptide preparation for NMR experiments

C2 domain of protein kinase Cα from R. norvegicus (residues 155-293) was expressed in E. coli and purified as previously described.[72] Uniformly ^{15}N- ([U-^{15}N]) and ^{13}C, ^{15}N-enriched ([U-^{13}C, ^{15}N]) C2 were prepared using (^{15}N, 99%) ammonium chloride and (6-^{13}C, 99%) glucose as the sole nitrogen and carbon sources, respectively. C2 samples were decalcified by incubation with 0.1 mM EDTA, followed by extensive buffer exchange into an EDTA- and Ca^{2+}-free buffer. All buffer solutions were decalcified by passing through Chelex resin (Sigma-Aldrich). For NMR-monitored binding experiments, the final buffer composition was 20 mM or 10 mM MES at pH 6.0, 8% (v/v) D_2O, and 0.02% (w/v) NaN_3. The peptides were purchased from either GenScript or Eton Bioscience. Crude peptide mixtures were purified on a C18 column using HPLC. Peptide concentration was determined from the absorbance at 280 or 205

nm; additional concentration measurements were carried out for phosphorylated peptides using a phosphate assay.[132] The molecular weight and purity of the peptides after HPLC purification were verified using MALDI-TOF mass spectrometry. The peptide stock solutions were prepared in HPLC-grade water and adjusted to pH 6.0 with ammonium hydroxide.

Insect cell expression and purification of PKCα

pBiEx1 plasmid carrying the mCer-hPKCα-mCit-FLAG gene was a generous gift of Dr. Sivaraj Sivaramakrishnan (University of Minnesota). mCer and mCit encode mCerulean and mCitrine fluorescent proteins, and they form a Förster Resonance Energy Transfer (FRET) donor-acceptor pair. Human and rat PKCα have identical amino acid sequences of their V5 domains and a single amino acid difference in the C2 domain at position 169 (Ala in human, Thr in rat), which is not part of any functional region. For recombinant PKCα expression, the mCer-hPKCα-mCit-FLAG sequence was sub-cloned into pAcGHLT-C (BD Biosciences) and pBac-1 (EMD Millipore) vectors. QuikChange site-directed mutagenesis of hPKCα was conducted using the pcDNA3 plasmid carrying the YFP-hPKCα gene to overcome challenges associated with high DNA sequence degeneracy of mCer and mCit. The mCer-hPKCα-mCit-FLAG variants were generated by replacing the wild-type gene with the mutagenic hPKCα sequence using the In-Fusion® cloning kit (Clontech). Either pAcGHLT-C or pBac-1 plasmid was co-transfected with ProGreen linearized baculovirus DNA (AB Vector) into Sf9 cells to generate recombinant baculovirus. The Sf9 cells at a density of 2.5×10^6/mL were

infected with recombinant baculovirus of high titer in a serum-free medium (Expression Systems).

The cells were cultured in suspension at 27 ℃ and harvested after 60 hours. The cell pellets were resuspended in a lysis buffer containing 50 mM Tris-HCl at pH 7.5, 1 mM EGTA, 1 mM EDTA, 3 mM $MgCl_2$, 150 mM NaCl, Halt protease inhibitor cocktail (Thermo Scientific), 1 mM PMSF, and 1% Triton X-100. The cell suspension was gently mixed on a nutator at 4 ℃ for 30 min to complete the lysis. The mCer-hPKCα-mCit-FLAG proteins in the lysate were purified using anti-FLAG M2 affinity gel (Sigma-Aldrich) according to the manufacturer's instructions. The eluted proteins were further purified from low-molecular-weight contaminants and buffer-exchanged on a 50 kDa MWCO spin concentrator (Corning). Purified proteins were analyzed by SDS-PAGE. Protein concentrations were measured with mCitrine absorbance at 516 nm with extinction coefficient of 77,000 $M^{-1}cm^{-1}$.[133]

The kinase activities of the purified mCer-hPKCα-mCit-FLAG proteins were assayed with the PepTag® non-radioactive protein kinase C assay kit (Promega) according to the manufacturer's instructions. For all activity assays mCer-hPKCα-mCit-FLAG proteins were added to a final concentration of 6 nM, which was 20ng in the reaction volume of 25μL. As a PKC activator, we used large unilamellar vesicles (LUV) consisting of 1-palmitoyl-2-oleoyl-sn-glycero-3-phosphocholine (POPC), 1-palmitoyl-2-oleoyl-sn-glycero-3-phospho-L-serine (POPS), and 1,2-dimyristoyl-sn-glycerol (DAG), all from Avanti Polar Lipids Inc. The molar ratio of the components was POPC/POPS/DAG = 65:30:5. The total lipid concentration of LUVs was 1 mM.

Activity reactions contained a final buffer of 20 mM HEPES (pH 7.4), 1 mM dithiothreitol (DTT), 1.3 mM $CaCl_2$, 10 mM $MgCl_2$ and 1 mM ATP.

For the V5-pHM peptide activating PKC experiments, separate reaction buffers were made to control Ca^{2+} and total concentration of divalent metals. The Ca^{2+}-free reactions contained a final buffer of 20 mM HEPES (pH 7.4), 1 mM DTT, 3.5 mM $MgCl_2$ and 1 mM ATP, whereas the corresponding Ca^{2+}-containing reactions had additional 1 mM $CaCl_2$. Reactions with pHM added had a final concentration of 1 mM peptide. The 10 aa version of the pHM peptide was used. PDBu was added with a stock of 5 μM in DMSO to a final concentration of 500 nM. The LUV activator had the same components as listed above. EGTA was added to a final concentration of 40μM in the Ca^{2+}-free experiment with LUV. Reactions were carried out at 30 ℃ for 30 minutes and quenched for 10 minutes at 95 ℃. The amount of phosphorylated peptide was quantified using a photon counting spectrofluorometer (ISS).

NMR-detected binding of ligands to C2

The ligand-binding experiments were conducted by adding aliquots of concentrated pHM15 (Ca^{2+}) stock solutions to apo and Ca^{2+}-bound (pHM15-bound) [U-^{15}N] C2 domain. The protein concentration in the NMR samples ranged from 80 to 100 μM. Ca^{2+} stock solutions were prepared from 1.0 M standard calcium chloride solution (Fluka Analytical). For each ligand concentration, [^{15}N-^{1}H] HSQC spectra were collected at 25 ℃ on Varian INOVA spectrometers operating at the Larmor ^{1}H frequencies of 500 MHz or 600 MHz. For the chemical shift perturbation (CSP) and

binding curve analysis, the residue-specific chemical shift change between any given pair of C2 states was calculated as follows:

$$\Delta = \sqrt{(\Delta\delta_H)^2 + (0.152 \times \Delta\delta_N)^2} \quad \textbf{3.1}$$

where $\Delta\delta_H$ and $\Delta\delta_N$ are the residue-specific differences in ^1H and ^{15}N chemical shifts, respectively. The binding curves were constructed by plotting Δ against total ligand concentration. The dissociation constants K_d for the pHM15 binding to C2 were determined by fitting the binding curves with the single-site equation:

$$\Delta = \Delta_{max} \frac{P_0 + L_0 + K_d - \sqrt{(P_0 + L_0 + K_d)^2 - 4P_0L_0}}{2P_0} \quad \textbf{3.2}$$

where $\Delta\delta_{max}$, P_0 and L_0 are the chemical shift change at complete saturation, total protein concentration and total ligand concentration, respectively. The dissociation constants K_d for Ca^{2+} binding to C2 were acquired by fitting the binding curves with the modified Hill equation[134] to account for the moderate cooperativity of Ca^{2+} binding:

$$\Delta = \Delta_{max} \frac{\left(L_0 - \left(P_0 + L_0 + K_d - \sqrt{(P_0 + L_0 + K_d)^2 - 4P_0L_0}\right)/2\right)^n}{K_d^n + \left(L_0 - \left(P_0 + L_0 + K_d - \sqrt{(P_0 + L_0 + K_d)^2 - 4P_0L_0}\right)/2\right)^n} \quad \textbf{3.3}$$

where n is the Hill coefficient. This equation assumes that 2 Ca^{2+} ions bind to C2 with the same affinity.

NMR experiments for structure validation, resonance assignment, and structural restraints

We used lanthanide (Ln^{3+})-induced pseudocontact shift (PCS) values to assess the structure of the pHM-complexed C2. The peptide pHM corresponds to a highly

soluble 10 amino acid version of the hydrophobic motif, Ac-DQSDFEGFpSY-NH_2. The complexes of [U-^{15}N,^{13}C] C2 with Ln^{3+} (Ln=La, Tb, and Tm) were prepared by combining equimolar amounts of C2 and $LnCl_3$ (Sigma Aldrich) dissolved in HPLC-grade water. In the pHM-containing sample, the concentration of pHM was 600 μM and the concentration of the C2·Ln^{3+} complexes ranged from 40 to 60 μM. [^{15}N-^{1}H] HSQC spectra were collected at 25 ℃ on Avance III spectrometers (Bruker Biospin) operating at ^{1}H Larmor frequencies of 500 and 600 MHz. The PCS values were determined by subtracting the residue-specific ^{1}H and ^{15}N C2 chemical shifts of La^{3+}-containing diamagnetic complexes from those of Tm^{3+}-and Tb^{3+}-containing paramagnetic complexes. The resonance assignment of diamagnetic C2·La^{3+} spectra was done by comparison with the previously assigned spectrum of single Pb^{2+}-bound C2.[72] The resonance assignment of the paramagnetic C2 spectra was done iteratively as implemented in Numbat,[135] using the Pb^{2+}-complexed structure of C2 (PDB ID 3TWY).

Two NMR samples, with either C2 or the hydrophobic motif peptide in molar excess, were prepared for the structural characterization of the C2·Ca^{2+}·pHM complex. Sample 1 contained 0.89 mM [U-^{13}C, ^{15}N] C2, 2.23 mM $CaCl_2$, and 2 mM pHM. Sample 2 contained 1.47 mM [U-^{13}C, ^{15}N] C2, 3.75 mM $CaCl_2$, and 0.6 mM pHM. The final buffer conditions after the preparation of the C2·Ca^{2+}·pHM complex were 6.7 mM MES at pH 6.0, 67 mM KCl, 8% (v/v) D_2O and 0.02% (w/v) NaN_3. All NMR data were collected at 23 ℃ using Avance III NMR instruments (Bruker Biospin) operating at the ^{1}H Larmor frequencies of 500, 600, and 800 MHz, the latter two equipped with a cryogenically cooled probe. For sample 1, the resonances of backbone ^{1}H, ^{13}C and ^{15}N

atoms of the pHM-complexed C2 were assigned using 2D [^{15}N-^{1}H] HSQC, 3D HNCO,[93] 3D HN(CA)CO[94] and 3D HNCACB[93] experiments. The resonances of side-chain ^{13}C and ^{1}H atoms were assigned using 2D [^{13}C-^{1}H] HSQC, 3D CC(CO)NH,[95] 3D H(CCO)NH,[136] 3D HCCH-TOCSY,[137] 3D HCCH-COSY[138] and 3D ^{15}N-TOCSY-HSQC[139] experiments. The resonances of aromatic ^{1}H atoms were assigned with 2D aro-[^{13}C-^{1}H] HSQC and 3D aro-HCCH-TOCSY experiments.

The NOE restraints for calculating the structure of C2 were obtained from the 3D ^{13}C-edited NOESY-HSQC and ^{15}N-edited NOESY-HSQC experiments[139-141] conducted on sample 1. Inter-molecular C2-pHM NOE restraints were obtained from 2D [F2] ^{15}N, ^{13}C-filtered NOESY, 3D [F1] ^{15}N,^{13}C-filtered NOESY-^{15}N-HSQC, and 3D [F1] ^{15}N, ^{13}C-filtered NOESY-^{13}C-HSQC spectra.[142] The inter-molecular origin of these cross-peaks was verified using 2D [F1] ^{15}N, ^{13}C-filtered NOESY and 2D [F1, F2] ^{15}N,^{13}C-filtered NOESY experiments.[143] The ^{1}H atoms of the C2-bound pHM in sample 2 were assigned with 2D [F1, F2] ^{15}N, ^{13}C-filtered TOCSY and 2D [F1, F2] ^{15}N,^{13}C-filtered NOESY spectra; the latter was used to obtain the NOE restraints for the calculation of the pHM structure. The mixing time for all NOESY experiments was 120 ms. All NMR data were processed using NMRPipe.[144] The analysis and all-atom assignments were performed with Sparky.[145]

Calculation of NMR structures and assembly of the ternary complex

Automated NOE assignment, calculation of Ca^{2+}-bound C2 structure in the context of the C2•Ca^{2+}•pHM complex, and its refinement in explicit solvent was carried

out using ARIA software (version 2.3).[146] The ^{1}H-^{1}H distance restraints were determined from the volumes of cross peaks in the 3D NOESY spectra. Hydrogen bonds were identified based on the ^{1}H-^{2}D exchange rates of amide ^{1}H atoms. Dihedral angles were predicted by TALOS+[147] using a complete set of ^{15}N, ^{13}C′, $^{13}C^{\alpha}$, $^{13}C^{\beta}$, $^{1}H^{\alpha}$ and $^{1}H^{N}$ chemical shifts. Metal coordination restraints in the range of 2.1-2.5 Å between the Ca^{2+} ions and the coordinating oxygens of C2 were also included. We also carried out the structure calculation and refinement of C2 without Ca^{2+} restraints and obtained essentially identical ensemble of structures albeit with more variability in the loop regions. The structure of the C2-bound pHM was calculated using 100 NOE restraints obtained from the 2D [F1, F2] ^{15}N,^{13}C-filtered NOESY spectrum. After refinement in explicit solvent, the 20 lowest energy structures were selected for the final NMR ensembles and validated by PROCHECK-NMR.[148]

The model of the C2•Ca^{2+}•pHM complex was generated using HADDOCK 2.2 software.[149,150] To generate initial structures for rigid-body docking, all combinations of Ca^{2+}-bound C2 and pHM structures were drawn from their respective NMR ensembles. The unambiguous distance restraints consisted of 29 intermolecular NOEs between the ^{1}H atoms of C2 and pHM, and 12 metal ion-oxygen restraints for the two Ca^{2+} ions bound to C2. The ambiguous restraints were based on the extent of ^{1}H and ^{15}N chemical shift perturbations experienced by the C2 residues as a result of pHM binding. The "active" residues of C2 were defined as those having CSP values at least one standard deviation above the mean and an all-atom surface accessibility of > 50%, determined using Naccess.[151] All pHM peptide residues were treated as "passive". The calculations

generated 6000/400/400 models for the rigid body docking, semi- and fully- flexible simulated annealing, and explicit solvent refinement stages. The final 400 models were subjected to cluster analysis, as described in Daura et al.[152] The interface RMSD cutoff of 3.0 Å was used to generate the clusters. To assess the influence of the initial pHM conformation on the final structure of the complex, extended and α-helical peptide conformations with the dihedral angles (φ, ψ) of (-139 °, -135 °) and (-60 °, -45 °), respectively, were generated and used for docking.

The HADDOCK models for full-length PKCα and PKCβII were docked with the set unambiguous and ambiguous intermolecular restraints from the C2–pHM experiments. In addition, pHM intramolecular NOEs were incorporated for the PKCα docking. For the full-length PKCα docking, input structures are kinase domain crystal structure from PDB ID 3IW4 and C2 domain solution structure from this study, respectively. For the full-length PKCβII modeling, both kinase domain and C2 domain structures are from crystal structure PDB ID 3PFQ. The calculations generated 1000/200/200 models for the rigid body docking, semi- and fully- flexible simulated annealing, and explicit solvent refinement stages. The final 200 models were subjected to cluster analysis, as described in Daura et al.[152] The interface RMSD cutoff of 7.5 Å was used to generate the clusters. The intermolecular restraints used for all three HADDOCK modeling are listed in Table 1. Cluster analysis results for C2–pHM docking are summarized in Table 2 and Table 3. Cluster analysis results for full-length PKCα and PKCβII docking are lists in Table 4.

Table 1. Distance restraints used for HADDOCK modeling

	C2–pHM and full-length PKCα		Full-length PKCβII	
Interdomain restraints				
	C2	V5	C2	V5
Unambiguous 4.0 -2.2 +2.5 Å	W 247 Hε1	G 655 Hα	W 247 Hε1	G 658 Hα
		F 656 Hα		F 659 Hα
		F 656 Hβ		F 659 Hβ
		F 656 Hε		F 659 Hε
		F 656 Hδ		F 659 Hδ
		Y 658 H		F 661 H
		Y 658 Hα		F 661 Hα
		NH_2/V 659 H		V 662 H
a	W 247 Hζ2	pS 657 Hβ		
		G 655 Hα		
		F 656 Hβ		
	W 247 Hη2	pS 657 Hβ		
	W 247 Hδ1	pS 657 Hβ		
	N 253 H	F 653 Hδ	N 253 H	F 656 Hδ
	K 197 Hε	F 653 Hα	K 197 Hε	F 656 Hα
		F 653 Hε		F 656 Hε
		F 653 Hδ		F 656 Hδ
	R 252 Hδ	F 653 Hα	R 252 Hδ	F 656 Hα
		F 653 Hε		F 656 Hε
		F 653 Hδ		F 656 Hδ
	R 252 Hγ	F 653 Hδ	R 252 Hγ	F 656 Hδ
	R 252 Hα	F 656 Hδ	R 252 Hα	F 659 Hδ
	R 252 Hβ	F 656 Hδ	R 252 Hβ	F 659 Hδ
	K 199 Hε	F 653 Hα	K 199 Hε	F 656 Hα
		F 653 Hδ		F 656 Hδ
	K 209 Hγ	F 653 Hε	K 209 Hγ	F 656 Hε
	K 211 Hε	F 656 Hα	K 211 Hε	F 659 Hα
		F 656 Hε		F 659 Hε
	T 214 H	F 656 Hε	T 214 H	F 659 Hε
Ambiguous 2.0 -2.0 +0.0 Å	K 209	All passive	K 209	All passive
	W 247		W 247	
	T 250		T 250	
	T 251		T 251	
	R 252		R 252	
	N 253		N 253	
Ca^{2+} coordination				
	2.30 -0.2 +0.2 Å		Original crystallographic distances with -0.2 +0.2 Å	
	C2	calcium	C2	calcium
	D 187 Oδ1	1	D 187 Oδ1	1
	D 187 Oδ2		D 187 Oδ2	
	D 193 Oδ2		D 193 Oδ2	
	D 246 Oδ1		D 246 Oδ1	

Table 1. Continued

C2	calcium	C2	calcium
D 248 Oδ1 W 247 O	1	D 248 Oδ1 W 247 O	1
M 186 O D 187 Oδ1 D 246 Oδ2 D 248 Oδ1 D 248 Oδ2 D 254 Oδ2	2	M 186 O D 187 Oδ1 D 246 Oδ2 D 248 Oδ1 D 248 Oδ2 D 254 Oδ2	2
		D 248 Oδ2 S 251 Oγ D 254 Oδ1 D 254 Oδ2 R 252 O	3

a. Restraints colored blue are specific to C2–pHM docking

The NMR resonance assignments and structure coordinates are deposited in BioMagResBank/PDB under accession numbers/entry codes: 26016/2NCE (C2), 26017/2NCF (C2·$(Ca^{2+})_2$·pHM complex).

Steady-state fluorescence spectroscopy

The steady-state fluorescence emission spectra of purified mCer-hPKCα-mCit-FLAG proteins were recorded at 25 °C on a photon counting spectrofluorimeter (ISS) using the excitation wavelength of 430 nm and the detection range of 450–650 nm. The excitation and emission slit widths were set to 8 nm. The cuvettes were coated with Sigmacote (Sigma-Aldrich) to minimize protein adsorption on the walls. Protein samples with concentrations ranging from 7 to 50 nM were prepared in a decalcified buffer containing 20 mM HEPES at pH 7.4, 100 mM KCl, and 5 mM β-mercaptoethanol.

Table 2. Cluster statistics of C2–pHM HADDOCK docking with RMSD cutoff of 3.0 Å

Cluster rank	Cluster population	HADDOCK score (a.u.) (based on best 10)	RMSD from overall lowest energy structure (Å)	iRMSD from the average structure of each cluster (Å)	E_{vdw} (kcal/mol)	E_{elec} (kcal/mol)	E_{AIR} (kcal/mol)	E_{desolv} (kcal/mol)
1	166	-133.8 ±4.4	1.4 ±0.7	1.4 ±0.7	-35.1 ±7.5	-378.2 ±75.1	48.7 ±47.3	6.5 ±4.9
2	134	-103.4 ±2.6	2.2 ±0.2	1.1 ±0.5	-33.0 ±6.0	-349.7 ±57.9	78.9 ±21.1	11.1 ±5.2
5	21	-96.1 ±4.3	2.0 ±0.3	1.0 ±0.6	-29.7 ±6.8	-320.9 ±45.6	42.3 ±27.5	2.7 ±5.9
4	22	-96.0 ±4.0	2.3 ±0.1	0.6 ±0.1	-31.9 ±3.1	-356.8 ±26.4	45.0 ±8.8	8.5 ±3.7
3	43	-85.2 ±4.9	1.7 ±0.2	1.9 ±0.4	-37.8 ±3.9	-184.4 ±46.4	32.4 ±36.8	-1.5 ±4.4
6	8	-58.0 ±7.9	2.1 ±0.2	0.9 ±0.4	-28.2 ±3.3	-174.4 ±41.6	83.2 ±21.0	-3.2 ±5.6

Table 3. Intermolecular energies and violation analysis for all clusters of C2–pHM HADDOCK docking

Cluster rank	Cluster population	Buried Surface Area (Å^2)	E_{inter}[a.] (based on best 10) (kcal/mol)	E_{inter} (kcal/mol)	E_{NOE} unambiguous only (kcal/mol)	Violations > 0.5 Å	Violations > 0.3 Å
1	166	1109.0 ±98.1	-528.0 ±35.6	-364.6 ±101.4	3.4 ±5.1	0.9 ±1.2	0.9 ±1.2
2	134	1099.1 ±69.9	-383.6 ±25.8	-303.9 ±57.6	7.2 ±2.1	1.8 ±0.5	1.8 ±0.5
5	21	961.2 ±43.9	-333.7 ±28.2	-308.4 ±41.9	2.2 ±3.5	0.6 ±0.9	0.8 ±0.8
4	22	1101.7 ±40.8	-362.4 ±23.2	-343.6 ±30.2	4.1 ±1.1	1.0 ±0.0	1.0 ±0.0
3	43	1076.3 ±40.8	-221.6 ±25.9	-189.8 ±25.2	2.4 ±2.8	0.8 ±0.9	0.8 ±0.9
6	8	876.4 ±84.7	-119.4 ±52.8	-119.4 ±52.8	8.0 ±2.8	1.6 ±0.7	1.6 ±0.7

a. $E_{inter} = E_{NOE}$(all restraints) + E_{vdw} + E_{elec}

Table 4. Cluster statistics of full-length PKCα and βII HADDOCK docking with RMSD cutoff of 7.5 Å

Cluster rank	**Cluster population**	**HADDOCK score (a.u.) (based on best 10)**	**RMSD from overall lowest energy structure (Å)**	**iRMSD from the average structure of each cluster (Å)**	**E_{NOE} unambiguous only (kcal/mol)**	**Violations > 0.5 Å**	**Violations > 0.3 Å**
PKCα							
1	151	-123.5 ± 5.2	1.9 ± 1.0	2.3 ± 1.5	15.9 ± 7.2	2.6 ± 1.2	2.9 ± 1.3
3	12	-105.7 ± 12.8	4.4 ± 0.5	2.1 ± 1.4	12.0 ± 7.8	2.6 ± 1.2	3.0 ± 1.4
2	18	-89.1 ± 10.8	5.3 ± 0.4	1.2 ± 1.1	8.3 ± 7.4	1.8 ± 1.4	2.1 ± 1.6
4	10	-77.5 ± 22.5	10.9 ± 1.2	2.6 ± 1.2	11.0 ± 6.2	2.9 ± 1.9	3.6 ± 2.2
5	4	-76.8 ± 11.1	6.2 ± 1.0	1.6 ± 1.0	18.1 ± 7.4	4.5 ± 2.2	5.3 ± 2.0
PKCβII							
1	200	-124.2 ± 7.4	0.9 ± 0.3	0.9 ± 0.3	38.2 ± 3.9	4.4 ± 1.0	5.8 ± 1.5

FRET efficiency was calculated as the ratio of peak intensities corresponding to the emission maxima of mCit at 525 nm and mCer at 475 nm. To obtain the reference fluorescence spectra of mCit and mCer in the absence of intramolecular interactions, wild-type mCer-hPKCα-mCit-FLAG was subjected to limited proteolysis with endoproteinase Lys-C (Thermo Scientific) that leaves the fluorescent proteins intact. The reaction was carried out at 30 ℃ at a protein to Lys-C ratio of 20:1 (w/w). The fluorescence spectrum was acquired 30 minutes after initiating the reaction. The completeness of the cleavage reaction was verified using SDS-PAGE.

Membrane translocation experiments[*]

Human YFP-PKCα was generated by sub-cloning PKCα into pcDNA3 with YFP at the N-terminus. Membrane-targeted CFP[34] has been previously described. All variants were generated by QuikChange™ site-directed mutagenesis. The pan anti-phospho-PKC activation loop antibody was previously described.[153] The anti-PKCα (610108) antibody was from BD Transduction Laboratories. The anti-phospho-PKCα/PKCβ turn motif (9375S) and the pan anti-phospho-PKC hydrophobic motif (9371S) antibodies were from Cell Signaling Technology. The anti-α-Tubulin (T6074) antibody was from Sigma-Aldrich. PDBu was purchased from Calbiochem.

COS7 cells were cultured in DMEM (Cellgro) containing 10% fetal bovine serum (Atlanta Biologicals) and 1% penicillin/streptomycin (Gibco) at 37 ℃ in 5%

[*] Membrane translocation experiments and FRET imaging were conducted by J. A. Callendar from Dr. A. C. Newton's Lab at University of California, San Diego.

CO2. Transient transfections were carried out using jetPRIME (PolyPlus Transfection) for ~24 hrs prior to analysis. Cells were lysed in 50 mM Tris pH 7.4, 1% Triton X-100, 50 mM NaF, 10 mM $Na_4P_2O_7$, 100 mM NaCl, 5 mM EDTA, 1 mM Na_3VO_4, 1 mM PMSF, 50 μg/mL Leupeptin, 1 μM Microcystin, 1 mM DTT, and 2 mM Benzamidine. Whole cell lysates were analyzed by SDS-PAGE and immunoblotting via chemiluminescence on a FluorChemQ imaging system (ProteinSimple). For PDBu-induced translocation experiments, cells were treated with 200 nM PDBu.

FRET imaging and analysis

Cells were imaged as described previously.[154] COS7 cells were co-transfected with the indicated YFP-tagged PKC and plasma membrane-targeted CFP. Cells were rinsed once with and imaged in Hanks' balanced salt solution containing 1 mM Ca^{2+}. Images were acquired on a Zeiss Axiovert microscope (Carl Zeiss Microimaging, Inc.) using a MicroMax digital camera (Roper-Princeton Instruments) controlled by MetaFluor software (Universal Imaging, Corp.). Using a 10% neutral density filter, CFP, YFP, and FRET images were obtained every 7 or 15 seconds. YFP emission was monitored as a control for photo bleaching and to ensure that overexpressed PKC levels were equal in all experiments. Base-line images were acquired for ≥ 2 min before PDBu addition and data were normalized to the baseline FRET ratios. Data are plotted as the average ± S.E.M. of this normalized FRET ratio for n > 20 cells from at least 3 independent experiments.

The membrane translocation data were modeled phenomenologically, using a pseudo-first-order kinetic process. The FRET-detected translocation curves, with baseline FRET ratios normalized to 1, were fit using the following equation:

$$y = 1.0 + A(1 - e^{-kt}) \quad \textbf{3.4}$$

where y is the FRET ratio; k is the sum of the on- and off- rate constants, (k_{on} + k_{off}); A is the steady-state FRET ratio that reflects the amount of translocated protein and is ~ (1 + k_{off} / k_{on})$^{-1}$. For variants that showed non-saturatable behavior, we have added a linear term, D×t, to describe the time dependence.

Results

Phosphorylation of the hydrophobic motif enhances its interaction with C2

We first investigated whether the isolated hydrophobic motif of V5 domain interacts with the Ca^{2+}-sensing C2 domain in solution. We designed four peptides to probe this potential interaction (Figure 20B). The unphosphorylated peptide uHM mimics the state of hydrophobic motif in the immature (i.e., unphosphorylated) kinase; S657E has the phospho-mimicking amino acid in place of the phosphorylated Ser657; pHM is the phosphorylated HM representing its state in the mature kinase; and SCB is the scrambled version of uHM with the same overall charge and amino acid identities. The binding of peptides to Ca^{2+}-complexed [U-^{15}N] enriched C2 domain was monitored using ^{1}H-^{15}N hetero-nuclear single-quantum coherence (HSQC) experiments.

In all four cases, we observed changes in the ^{1}H and ^{15}N chemical shifts of several C2 amide groups, indicating that their electronic environment changed as a result

of peptide binding (Figure 20B). A full scale spectral overlay is shown in Figure 21. Because essentially the same subset of C2 residues is affected, the peptides likely interacted with the same site on C2. The SCB and pHM peptides caused the smallest and largest chemical shift changes of the C2 resonances, respectively. The final concentrations of C2 and peptides used in the experiments as shown in Figure 20B were identical. Therefore, we can use the extent of chemical shift perturbation to qualitatively evaluate the affinity of peptides to C2, which gives us the following order: pHM > S657E > uHM > SCB.

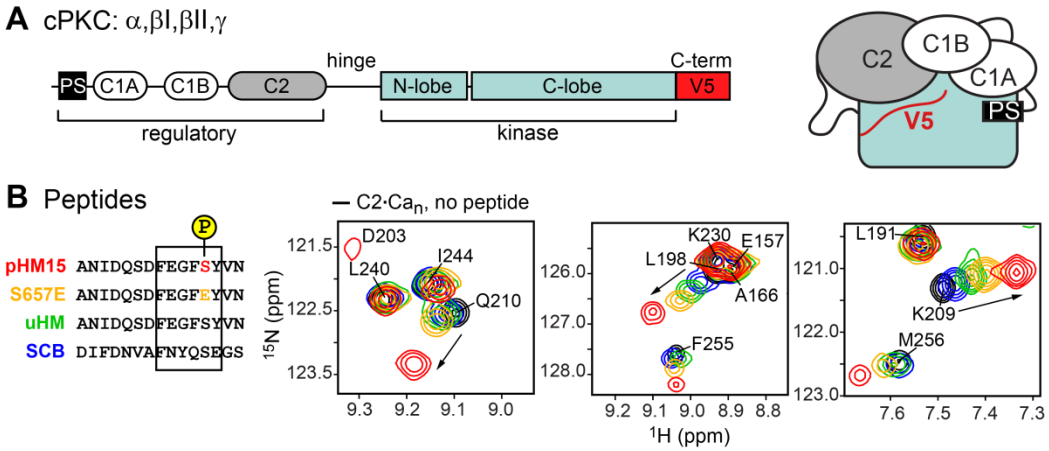

Figure 20. Host protein context and interactions between C2 and V5 domains. **(A)** Domain sub-structure of conventional PKC isoenzymes and schematic representation of the inactive form. The Ca^{2+}-sensing C2 and C-terminal V5 domains are shown in gray and red, respectively; PS is the pseudo-substrate region. **(B)** Expansions of ^{15}N-^{1}H HSQC spectra of Ca^{2+}-bound C2 domain ($C2{\cdot}Ca_n$, n=2,3), in the absence (black) and presence of four V5-derived peptides: pHM15 (red), S657E (gold), uHM (green), and SCB (blue). The changes in cross-peak positions indicate the changes in electronic environment of the backbone N-H groups of C2 due to binding.

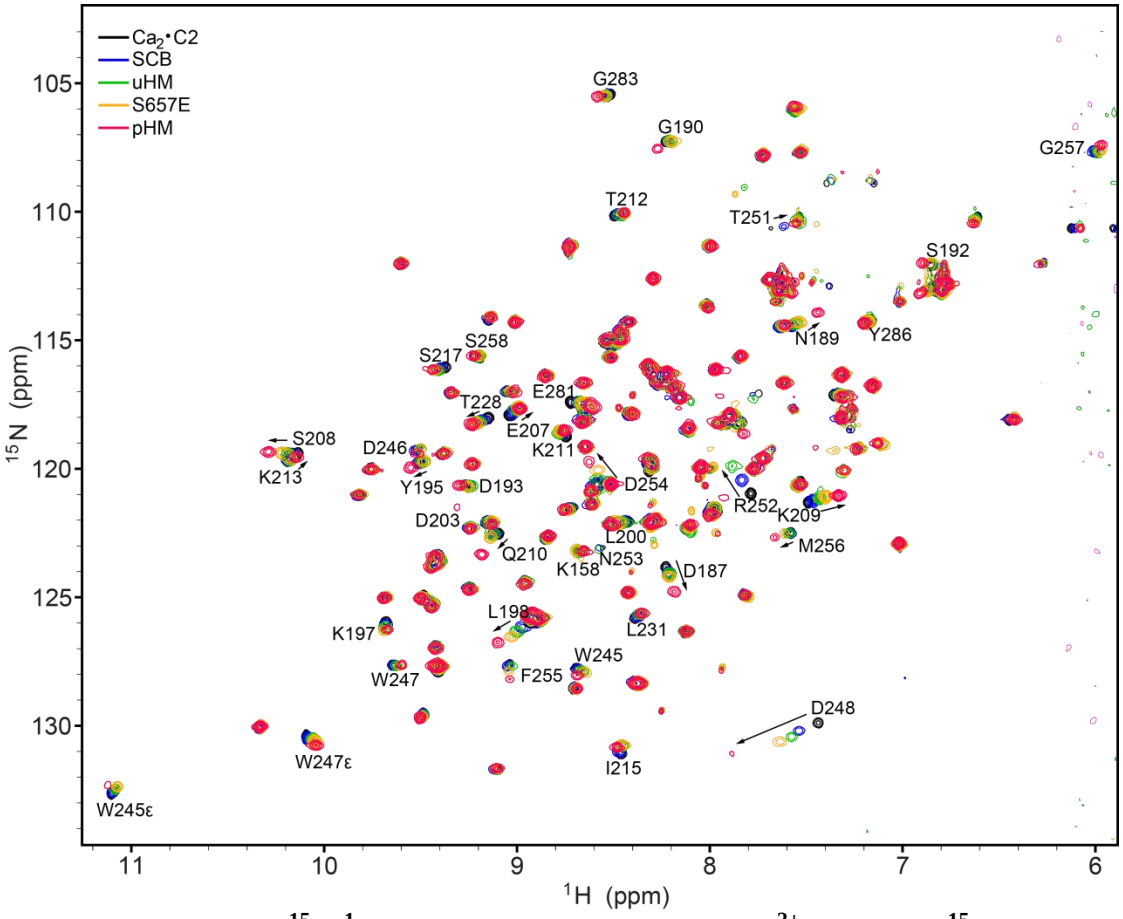

Figure 21. Full-scale ^{15}N-^{1}H HSQC spectra overlay of Ca^{2+} bound [U-^{15}N] C2 domain, in the absence or presence of four HM peptides: SCB, uHM, S657E and pHM. The color coding of spectra are indicated by the legend in the left top corner of the figure. Arrows indicate a qualitative trend of increasing binding affinity.

Electrostatic contacts make a significant contribution to this interaction, based on the observation that the peptide with a scrambled amino acid sequence can still bind to C2, albeit with a reduced affinity compared to uHM. We conclude that the phosphorylation of the hydrophobic motif enhances its interactions with C2. For all subsequent studies,

we use the pHM peptide to represent the hydrophobic motif of the C-terminal V5 domain.

Synergy between Ca^{2+} and hydrophobic motif

Ca^{2+} binding to the C2 domain is the first step of the PKC activation process. We used solution NMR to determine the effect of Ca^{2+} on the interactions of the hydrophobic motif with C2. The concentration of pHM15 in the sample containing either [U-^{15}N] apo C2 or C2·Ca_n varied from zero to 1.5 mM. The ^{1}H-^{15}N HSQC spectra were collected at each concentration of pHM15 and overlaid to identify C2 residues that had experienced chemical shift perturbations due to interactions with the peptide. For both C2 states, a significant number of C2 residues showed changes in their N-H chemical shifts (Figure 22A, B). The cross-peaks of the C2 species follow a smooth trajectory as a result of increasing pHM15 concentration, indicating that the binding process is fast on the NMR chemical shift timescale irrespective of the state of metal ligation.

We applied chemical shift perturbation (CSP) analysis to identify the C2 regions affected by the interactions with the hydrophobic motif. CSP values Δ were calculated between a pair of C2 states containing no peptide and 1.5 mM pHM15, and plotted against the amino acid sequence of C2 (Figure 22C). While the magnitude of chemical shift changes in the apo C2 (Figure 22C, bottom panel) is smaller than that of C2·Ca_n (Figure 22C, top panel), the overall pattern is quite similar. We conclude that Ca^{2+} binding does not significantly change the interaction mode of C2 with HM.

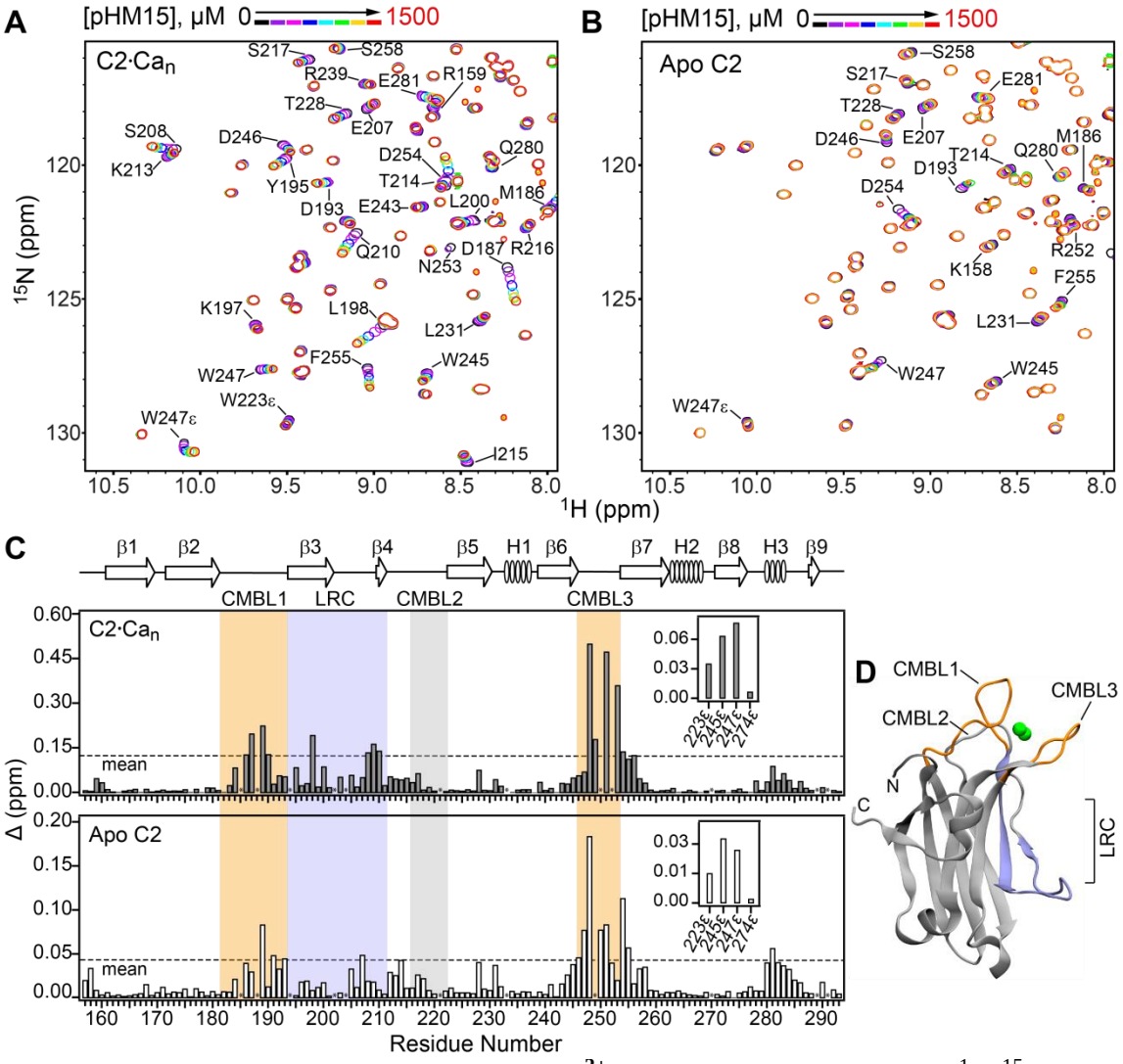

Figure 22. pHM interacts with apo and Ca^{2+}-bound C2. Expansions of ^{1}H-^{15}N HSQC spectra of [U-^{15}N] apo C2 **(A)** and C2·Ca$_n$ **(B)** showing the effect of increasing pHM15 concentration [pHM15]. The spectra are overlaid and color-coded according to [pHM15]. The N-H groups of C2 whose chemical shift changes as a result of binding are labeled. **(C)** Chemical shift perturbations Δ due to pHM15 binding for all spectrally resolved residues of C2·Ca$_n$ (top panel) and apo C2 (bottom panel). Residue-specific Δ values were calculated using spectra with zero and 1.5 mM [pHM15] for apo C2 (top panel) and C2·Ca$_n$ (bottom panel). Asterisks indicate residues that are either prolines or broadened/not spectrally resolved. The inserts show chemical shift perturbations for the indole side chain amine groups of the four Trp residues. **(D)** Crystal structure of the C2 domain complexed to two Ca^{2+} ions (PDB ID: 1DSY). CMBLs and LRC stand for Ca^{2+}- and membrane-binding loops and lysine-rich cluster, respectively. Ca^{2+} ions are shown as green spheres.

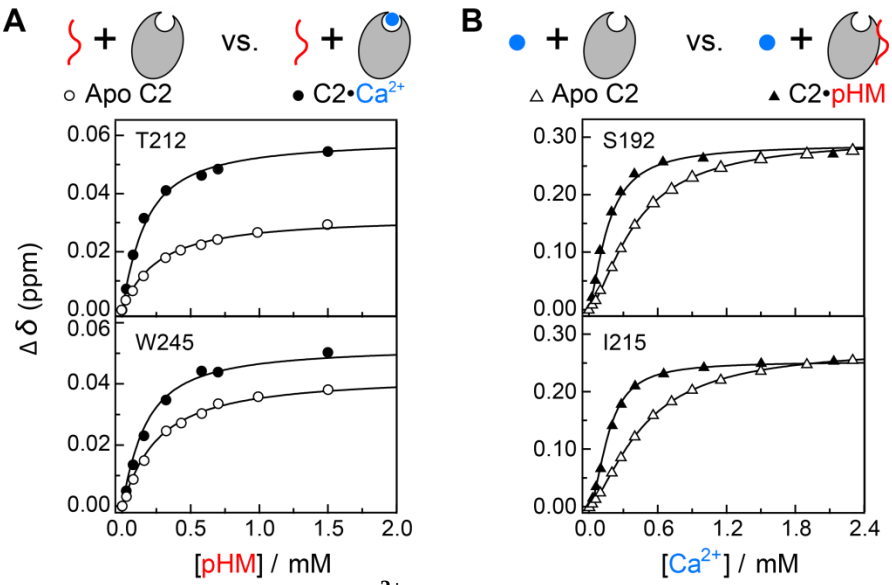

Figure 23. Synergistic action of Ca^{2+} and hydrophobic motif. (A) Representative binding curves of pHM15 to apo C2 (open circles) and C2·Ca_n (filled circles). **(B)** Representative binding curves of Ca^{2+} to apo C2 (open triangles) and C2·Ca_n (filled triangles). In both cases, the affinity of one ligand is enhanced in the presence of the other.

The crystal structure of the Ca^{2+}-bound C2 provides a structural context for interpreting the observed chemical shift perturbations. The C2 domain has two major functional regions, the Ca^{2+}- and membrane-binding loops (CMBLs) and the lysine-rich cluster (LRC). CMBL1 and CMBL3 provide oxygen-containing ligands for Ca^{2+} ions that bridge the protein and negatively charged groups of anionic phospholipids. LRC is the interaction site of the C2 domain with a signaling lipid PtdIns(4,5)P_2. The CSP data show that the regions affected by the interactions with the hydrophobic motif include the major functional elements of C2, namely CMBL1, CMBL3, and LRC, plus the C-terminal helix H3. A similar pattern of chemical shift perturbations was previously

observed in the NMR studies of PtdIns(4,5)P_2-C2 interactions, suggesting that the hydrophobic motif and PtdIns(4,5)P_2 bind to the same C2 site.

To determine the affinity of pHM15 to C2, we constructed binding curves using the chemical shifts of all responsive residues that fall into the fast-exchange regime. We found that Ca^{2+} increases the affinity of C2 to the hydrophobic motif ~2.0-fold, based on the K_d values of 120 ± 4 μM and 203 ± 6 μM for the Ca^{2+}-bound and apo C2, respectively (Figure 23A). We then conducted a converse experiment, where we measured the affinity of the C2 domain to Ca^{2+} in the absence and presence of pHM15 (Figure 23B). The presence of pHM15 decreased the Ca^{2+} K_d approximately 3-fold, from 356 ± 9 μM to 126 ± 4 μM, while the Hill coefficient increased from 1.3 to 1.5. In summary, our data demonstrate that both apo and Ca^{2+}-complexed C2 domains interact with the hydrophobic motif of the C-terminal V5 domain in solution. A clear synergy between Ca^{2+} and pHM15 is manifested in the mutual enhancement of their respective affinities to the C2 domain.

Structural characterization of the C2·$(Ca^{2+})_2$·pHM complex

To dissect the structural basis of the interactions between C2 and the hydrophobic motif, we prepared a complex consisting of Ca^{2+}-bound C2 and a 10-residue pHM peptide. pHM has a higher solubility and slightly higher affinity to Ca^{2+}-complexed C2 compared to its 15-residue variant, with a K_d of 105 ± 2 μM. As a first step, we determined the structure of the C2 domain in the context of the complex using NMR spectroscopy.

Table 5. NMR-based restraints and structure refinement statistics.	
NOE restraints	
total	2689
ambiguous	520
unambiguous	2169
intra (|i-j|=0)	618
medium (0<|i-j|<5)	786
long (|i-j|≥5)	765
hydrogen bonds	33
dihedral angles (Φ, Ψ)	210
Ca^{2+}/ligands	12
average no. of violations	
NOE > 0.3 Å	1.4 ± 0.9
NOE > 0.5 Å	0.3 ± 0.6
dihedral angles > 5 °	0.0
mean rmsd from ideal geometry	
bond length (Å)	0.004 ± 0.0001
bond angle (°)	0.5 ± 0.01
impropers (°)	1.4 ± 0.09
rmsd values from the mean (Å)	
secondary structure (backbone)	0.4 ± 0.07
secondary structure (heavy)	0.8 ± 0.08
all heavy atoms	1.4 ± 0.1
Ramachandran analysis (PROCHECK)	
most-favored region, %	80.8
additionally allowed region, %	18.5
generously allowed region, %	0.4
disfavored region, %	0.3

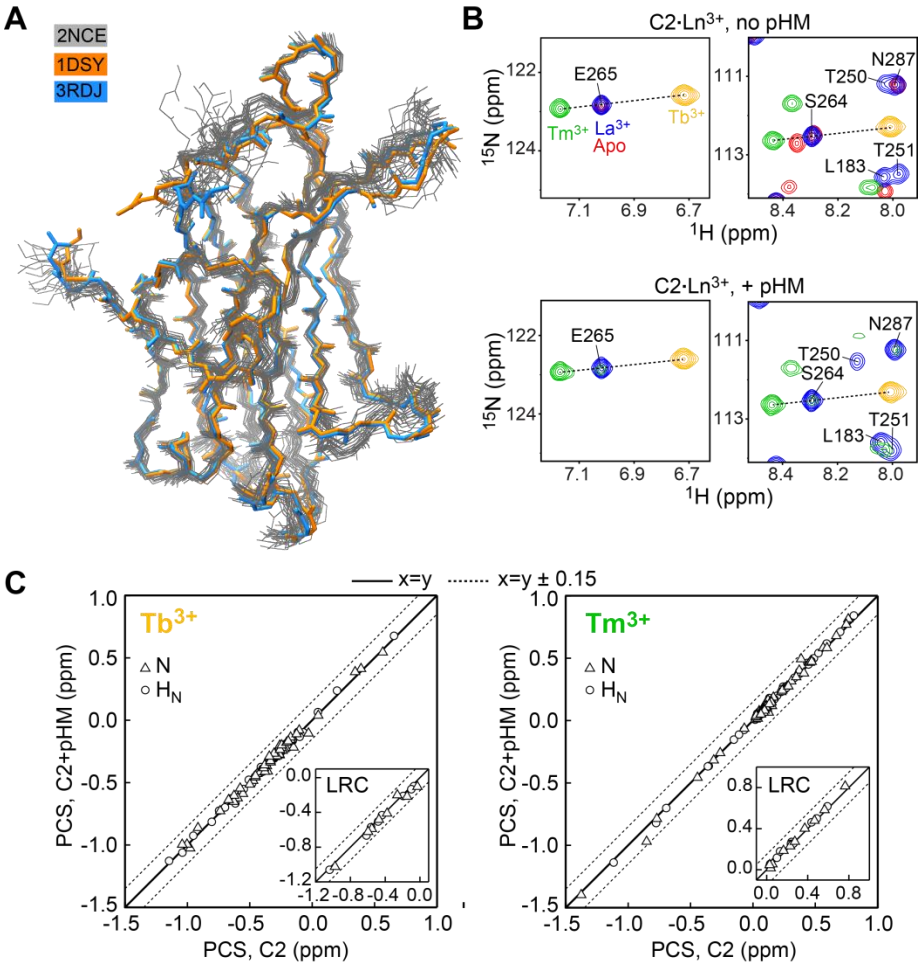

Figure 24. pHM binding does not significantly affect the backbone conformation of C2 domain. **(A)** Backbone superposition of the C2·$(Ca^{2+})_2$ NMR ensemble (2NCE, gray) in the pHM complex with the crystal structures of the apo- (3RDJ, blue) and Ca^{2+}-complexed C2 (1DSY, orange). **(B)** Expansions of the ^{15}N-^{1}H HSQC spectra showing Ln^{3+}-induced pseudocontact shifts of C2·Ln^{3+} in the absence and presence of 15-fold molar excess of pHM. The corresponding correlation plot of the PCS values is given in **(C)**. The inset shows the PCS correlation data for the LRC residues; LRC is the interaction site of pHM with C2. The solid lines are x = y, whereas dashed lines are x = y ± 0.15; ± 0.15 is a typical uncertainty of the PCS measurements.

The experimental restraints included NOE intensities, dihedral angles, hydrogen bonds, and metal ion-oxygen coordination restraints for two Ca^{2+} ions (Table 5). Superposition of the solution NMR ensemble of C2·$(Ca^{2+})_2$ onto the crystal structures of apo (3RDJ) and Ca^{2+}-bound C2 (1DSY) C2 produced the backbone RMSD value of 1.1 ±0.1 Å for both (Figure 24A). This indicates that the structure of C2 does not significantly change upon binding with pHM. It is evident from the inspection of the NMR structural ensemble that the CMBL3 and the loop region between strands β3-β4 of the lysine-rich cluster show more variability than the other C2 regions. This is due to a lower number of restraints in these regions, which are highly dynamic in the complex.

To establish if the structures of pHM-free and complexed C2 are similar in solution, we compared the ^{1}H and ^{15}N pseudo-contact shifts (PCS), which are induced by paramagnetic lanthanides. Lanthanide-induced PCSs are sensitive reporters of protein structure through their dependence on polar coordinates of NMR-active nuclei in the coordinate frame of the magnetic susceptibility tensor, $\Delta\chi$. The C2 domain binds one Ln^{3+} ion with high affinity. The binding site coincides with the high-affinity Pb^{2+} binding site that we previously characterized. This was established based on the near-identity of ^{1}H and ^{15}N chemical shifts, and slow exchange behavior in the spectra of single Ln^{3+}- and Pb^{2+}-complexed C2. We chose two paramagnetic lanthanide metal ions, Tb^{3+} and Tm^{3+} that have relatively large $\Delta\chi$. They also have opposite signs of axial and rhombic $\Delta\chi$ components (Figure 24B). The PCS values were calculated as the difference between the chemical shifts in the paramagnetic and diamagnetic complexes of C2. To ensure that the majority of C2 is in the pHM-bound form, we used samples

with a 15-fold molar excess of pHM over C2. For both Tb^{3+} and Tm^{3+}, we observed an excellent correlation between the backbone PCS values of C2 residues—including those that belong to the LRC—in the absence and presence of pHM (Figure 24C). These results indicate the similarity of the C2 backbone conformation in the pHM-free and pHM-bound forms.

The next step was to determine the conformation of pHM in the C2·$(Ca^{2+})_2$·pHM complex. A separate NMR sample was prepared that had C2 in molar excess with respect to pHM. This sample was used to ensure that ≥ 90% of pHM was in the C2-complexed form. We obtained the intra-peptide NOEs from the [^{15}N,^{13}C]-filtered 2D ^{1}H-^{1}H NOESY spectrum of the complex. We detected no long-range NOEs in the spectrum of the bound pHM. Except for the changes associated with the increase in the rotational diffusion correlation time due to the complex formation, there were no drastic differences between the NOE patterns of the free and C2-bound pHM. This indicates that pHM does not undergo any significant conformational change upon C2 binding. The structural ensemble of pHM, which was calculated using 58 intra-residue and 41 medium-range NOEs, revealed moderate conformational variability with a backbone RMSD of 1.9±0.5 Å. The NMR ensembles of Ca^{2+}-bound C2 and pHM were then used to generate the structural model of the complex.

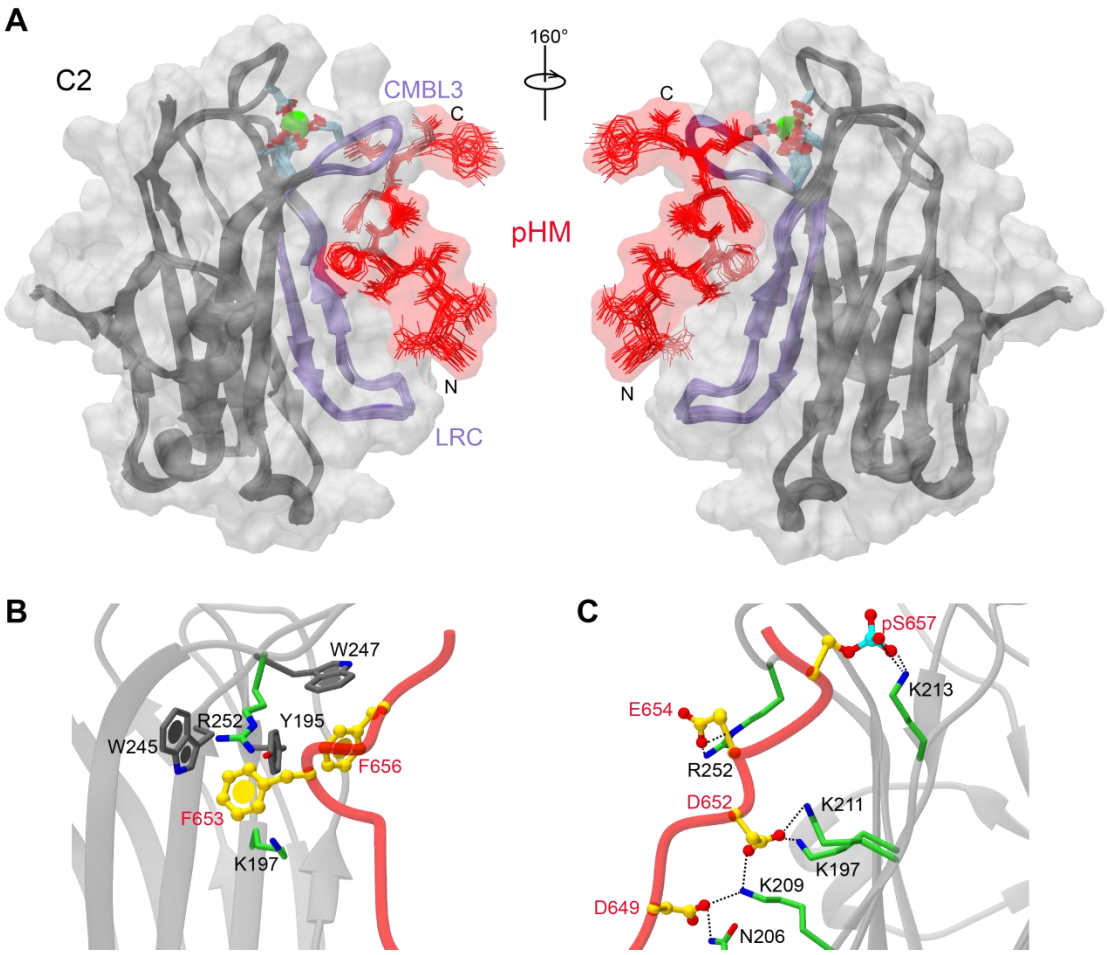

Figure 25. The C2-pHM interface is stabilized by electrostatic and aromatic interactions. (A) 20 top-ranking structures of the C2·$(Ca^{2+})_2$·pHM complex with pHM and LRC/CMBL3 highlighted in red and purple, respectively. Ca^{2+} ions are represented with green spheres. The interface of the complex is stabilized by aromatic **(B)** and electrostatic **(C)** interactions. The charged/polar and aromatic side-chains of C2 are shown in green and dark gray, respectively; all pHM side chains are colored gold. The interacting residues are labeled with red (pHM) and black (C2) fonts.

C2·(Ca^{2+})$_2$·pHM complex is stabilized by electrostatic and aromatic interactions

To obtain structural restraints for the C2·(Ca^{2+})$_2$·pHM complex, we conducted isotope-filtered/edited NOESY experiments that produced 29 inter-molecular NOEs between the C2 and pHM. These NOEs were used as unambiguous restraints in the docking and refinement protocol, as implemented in HADDOCK 2.2/CNS 1.3. The other type of restraints was the chemical shift perturbations of the ^{15}N and $^{1}H_N$ of C2 due to pHM binding; those were incorporated as ambiguous restraints. The 400 structures of the C2·(Ca^{2+})$_2$·pHM complex produced during the final refinement step consistently have the pHM interacting with the concave face of C2 that bears the LRC region. Some conformational variability is observed only for the N-terminal part of pHM that comprises residues 649–651. This is due to a lack of unambiguous restraints in this region, as most inter-molecular NOEs were observed for the C-terminal and middle parts of pHM. The most populated cluster 1 contained 41.5 % of the structures and also had the lowest average inter-molecular interaction energy among the six clusters. The 20 lowest-energy structures of the C2·(Ca^{2+})$_2$·pHM complex also belong to cluster 1 and form a tight ensemble with an all-residue backbone RMSD of 0.41 ± 0.05 Å.

The top-ranking structures of C2·(Ca^{2+})$_2$·pHM illustrate the interaction mode between the hydrophobic motif and C2 domain (Figure 25A). pHM binds to the concave face of the C2 domain, and makes contact with two major functional elements: the LRC region and the calcium binding loop CMBL3. The conformation of pHM is extended, with the N-terminus pointing towards the loop between strands β3 and β4 of the LRC and the C-terminus pointing towards CMBL3. The C2-pHM interface is stabilized by

electrostatic and aromatic interactions (Table 6). Electrostatic interactions involve salt bridges between the negatively charged sidechains of the pHM residues and the positively charged sidechains of the C2 domain. For example, Lys197, Lys209 and Lys 211 form a salt bridge with the sidechain of Asp652, while Lys213 forms a salt bridge with the phosphoryl oxygens of Ser657 (Figure 25C). Two phenylalanine residues of the hydrophobic motif, 653 and 656, are involved in ring stacking interactions with the aromatic residues of C2: Y195, Trp245, and Trp247 (Figure 25B).

Table 6. Analysis of the C2-pHM interface

	C2 residue /atom	V5 residue /atom	Distance (Å)
Electrostatic			
salt bridges	K213/Nζ	pS657/O3P	2.6
	K213/Nζ	pS657/O2P	2.8
	R252/Nη2	E654/Oε1	2.8
	R252/Nε	E654/Oε1	3.0
	K209/Nζ	D652/Oδ2	2.7
	K197/Nζ	D652/Oδ2	2.9
	K211/Nζ	D652/Oδ2	4.1[b]
	K209/Nζ	D649/Oδ2	2.7
	N206/Nδ2	D649/Oδ2	2.7
Aromatic			
ring stacking	Y195/Cε	F656/Cζ	3.4[a]
weak H-bond	Y195/OH	F653/Cδ	3.8
ring stacking	W247/Cδ2	F656/Cδ	3.6[a]
ring stacking	W245/Cγ	F653/Cε	3.8[a]
cation-π	R252/Nε	F653/Cδ	3.4
cation-π	K197/Nζ	F653/Cε	3.7

[a] Representative distances are given to illustrate the proximity of the aromatic rings
[b] 11/20 structures of the ensemble have this distance smaller than 2.8 Å. In the other 9 structures K211 is forming a H-bond with the backbone carbonyl of G655.

The cation-π interactions between Lys197, R252 and the aromatic ring of Phe653 additionally stabilize the interface. All residues listed in Table 6, with the exception of Asn206, are conserved among the conventional PKC isoenzymes.

Residues at the C2–V5 interface contribute to stabilization of the auto-inhibited conformation

The next step was to determine the role of C2-V5 interactions in maintaining the auto-inhibited conformation of PKC. Guided by the structural information about the C2·$(Ca^{2+})_2$·pHM complex, we designed mutations that target electrostatic and aromatic interactions at the C2–V5 interface (Table 7). The mutations were introduced into the full-length PKCα construct fused with a FRET pair of fluorescent proteins: mCer at the N-terminus and mCit at the C-terminus. To assess the effect of these mutations on the conformation of inactive PKCα, we conducted intra-molecular steady-state FRET experiments *in vitro*, using mCer-PKCα-mCit-FLAG variants purified from Sf9 cells. All PKCα variants were kinase-active (Table 7). The activity assays were conducted with endogenous activators, Ca^{2+} and diacylglycerol, incorporated into phosphatidylserine-containing large unilamellar vesicles.

Steady-state FRET experiments were conducted in the absence of PKC activators. Representative fluorescence spectra of PKCα variants illustrate the magnitude of the FRET response (Figure 26A). The "no-FRET" control spectrum (black trace) was collected for the wild-type protein, which was subjected to partial proteolysis that left mCit and mCer intact.

Table 7. Mutated residues in each construct and their kinase activities relative to WT.

Variant	*C2*	*V5*	*Kinase Activity*[a]
WT			1.00 ± 0.12
S657A		S657A	1.19 ± 0.10
K213A	K213A		0.62 ± 0.17
D652A		D652A	0.31 ± 0.09
DS		D652A/S657A	0.81 ± 0.16
KKRDS	K197A/K209A/R252A	D652A/S657A	0.42 ± 0.04
D652K		D652K	1.10 ± 0.09
KK	K209E/K211E		0.74 ± 0.07
DKK	K209E/K211E	D652K	0.42 ± 0.11
YW	Y195A/W247A		0.20 ± 0.02
FYYW	Y195A/W247A	F656A/Y658A	0.13 ± 0.03
F656A		F656A	0.22 ± 0.01

[a] Performed in the presence of POPC:POPS:DAG=(65:30:5) LUVs. All activities are scaled relative to WT proteins.

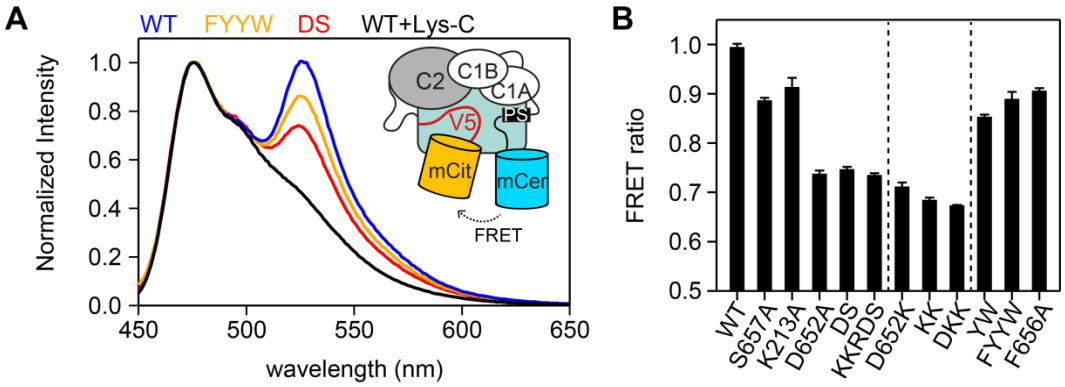

Figure 26. Destabilization of the autoinhibited PKCα conformation by targeted mutagenesis at the C2–V5 interface. (A) Fluorescence emission spectra of WT, FYYW variant, DS variant and the Lys-C treated WT. The inset schematic on the left depicts the mCer-PKCα-mCit-FLAG construct used for *in vitro* fluorescence measurements of autoinhibited PKCα. **(B)** The FRET ratio ± SEM of WT and all variants are from at least three independent experiments. The dashed lines group the variants the same as in Table 7.

In the spectrum of the intact wild-type PKCα (blue trace), the intensity of mCit emission peak at 525 nm increases due to FRET between the protein termini. The fluorescence spectra of two PKCα variants, D652A/S657A and Y195A/W247A/F656A/Y658A, illustrate the decrease in FRET efficiency due to perturbations of electrostatic and aromatic interactions at the interface.

The FRET data, presented as acceptor/donor intensity ratios, show that all PKCα variants have lower FRET efficiencies compared to the wild-type protein (Figure 26B). The data are divided into three groups, according to the type/specifics of the targeted interaction. To probe the contribution of electrostatic interactions, we disrupted two salt bridges by mutating charged residues to an alanine. The S657A and its K213A variants showed similar values of FRET ratios, ~0.9, compared to 1 in the wild type. The other salt bridge involves Asp652 that interacts with the lysines of the LRC. Mutation of D652 to either alanine or lysine decreased the FRET ratio to 0.74 or 0.71, respectively. A similar result was obtained for the DS variant where both negatively charged amino acids of the V5, phosphorylated Ser657 and Asp652, were replaced with alanine.

The charge reversal of the Asp652 interacting partners, Lys209 and Lys211, in the KK PKCα variant produced an even lower FRET ratio of 0.69. A simultaneous charge reversal of Asp652 and Lys209/Lys211 in the DKK variant generated a FRET ratio that was comparable to what we observed in the individual charge reversal variants D652K and KK. These data indicate that the wild type-like conformation of auto-inhibited PKCα is not fully recovered by a simple charge reversal of the interacting

sidechains. Mutations involving aromatic residues generated a more moderate decrease in FRET ratios compared to those observed in Asp652 variants. A surprising finding was that a mutation of a single aromatic amino acid in the hydrophobic motif, Phe656, was sufficient to produce a FRET ratio comparable to that of the S657A variant.

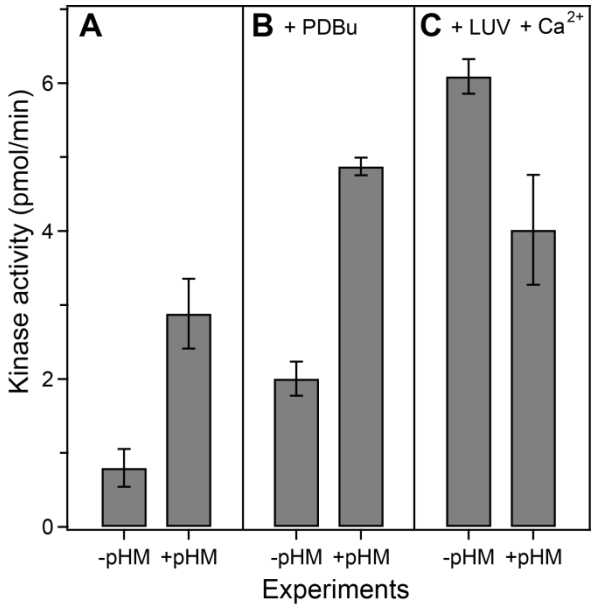

Figure 27. pHM activates PKCα under various conditions. (A) Basal activities of mCer-hPKCα-mCit-FLAG in the absence of lipid ligand, with and without pHM peptide added. **(B)** Activities in the presence of 500nM PDBu, with and without pHM peptide added. **(C)** Activities in the presence of LUV (POPC/POPS/DAG = 65/30/5 mole %) and 1mM Ca^{2+}, with and without pHM peptide added. All activities are averaged for at least three independent experiments, with ±STD.

In summary, our fluorescence data indicate that conserved PKCα residues at the C2–V5 interface contribute to the stabilization of the auto-inhibited conformation of the enzyme. It should be noted that while FRET data provide a general (and motionally

averaged) view of the PKCα conformation, they do not directly report on the exposure of membrane binding sites.

pHM activates PKCα under various conditions

In an effort to further demonstrate the autoinhibited role of the observed C2–V5 interface, we measured kinase activities of the wild-type mCer-hPKCα-mCit-FLAG protein in the absence and presence of the pHM peptide. If the C2–V5 interaction contributes to autoinhibition, we would expect a competition by the externally added pHM peptide with the intra-molecular pHM site, which would destabilize the closed conformation to increase kinase activity. This is indeed what we see: the basal activity is increased significantly 3.6-fold by pHM peptide in the absence of Ca^{2+} (Figure 27A).

We further tested the kinase activities in the presence of PDBu, which binds the C1 domains with high affinity. PDBu alone activates the kinase some (2.00 ± 0.23 pmol/min with the quantity of kinase added, see Experimental procedures) (Figure 27A, B), which is consistent with previous findings.[2] We also see a further activation of 2.4-fold by the addition of pHM peptide. This is consistent with pHM destabilizing the autoinhibited conformation of the kinase, which results in a higher exposure of C1 domains to PDBu binding. The activities in the presence of LUVs and Ca^{2+} are much higher than the equivalent PDBu conditions, consistent with C2 domain binding PtdSer-containing membranes in a Ca^{2+}-dependent manner. However, we observed an inhibiting effect of pHM peptide with Ca^{2+} and LUVs (Figure 27C). This could be explained by pHM occupying the LRC of C2 to prevent C2 associating with LUVs. It is worth

mentioning that with the pHM peptide alone, the kinase activity is already 47% of the fully activated state (LUV and Ca^{2+}) (Figure 27A, C). In the absence of Ca^{2+}, PDBu and pHM together can activate the kinase to 80% of the fully activated power (Figure 27B, C).

In summary, the pHM peptide is able to activate the full-length kinase under various conditions, with the largest enhancing effects seen in the absence of PKC agonists. This is consistent with our model where the C2–pHM interface contributes predominantly to the closed, autoinhibited conformation of the latent kinase.

Altered membrane translocations of PKCα by targeted mutagenesis at the C2-V5 interface

To investigate the effects of mutating C2–V5 interface on the activation of PKCα, we used a different FRET pair setup to measure membrane translocation in mammalian cells. This part of the work was done in collaboration with Julia Callender and Dr. Alexandra Newton at UC-San Diego. The experimental setup is shown in Figure 28A, where YFP was fused to the N-terminus of PKCα, and CFP is anchored on the plasma membrane through fused signal sequences for myristoylation and palmitoylation. All variants still retain a significant amount of phosphorylation at the turn motif (Figure 28B pT638 panel). Two variants, FYYW and F656A, display a noticeable decrease in the turn motif phosphorylation, and an undetectable phosphorylation at the activation loop (Figure 28B pT497 panel).

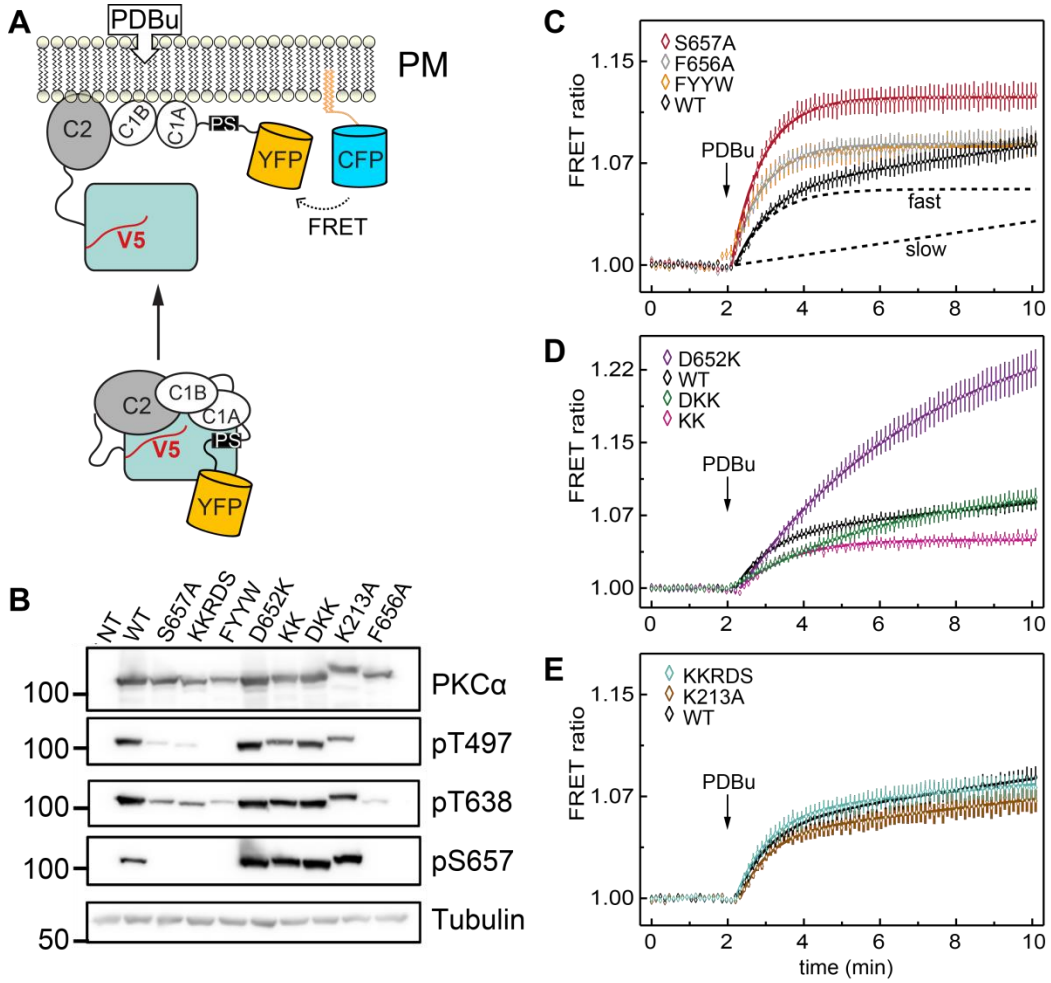

Figure 28. Altered membrane translocations of PKCα by targeted mutagenesis at the C2–V5 interface. (A) Schematic diagram showing the experimental setup for monitoring the YFP-tagged PKCα membrane translocation to plasma membrane (PM) containing myristoylated/palmitoylated CFP used in (C-E). **(B)** Western blot displaying the cell lysates transfected with the YFP-PKCα constructs. The primary antibodies used for each panel are listed on the right. **(C-E)** FRET ratio changes (mean ± SEM) displaying PDBu induced PKCα plasma membrane translocation of WT and variants S657A, FYYW and F656A in (C); D652K, KK and DKK in (D), and the rest of the variants in (E). Figure credits: J. A. Callendar and A. C. Newton panel (B); T. I. Igumenova panels (C-E).

This indicates that the variants containing Phe656 mutation are correctly phosphorylated by PDK-1 in the cell, but are more susceptible to phosphatases due to more open conformations. The lack of signal for S657A, KKRDS variants at hydrophobic motif, is due to the mutation (Figure 28B pS657 panel). It is hard to determine the phosphorylation states at hydrophobic motif for the FYYW and F656A variants. The Phe656 mutation may affect antibody binding; because the pS657 antibody was commercially produced by immunizing animals with a synthetic phosphopeptide corresponding to residues surrounding Ser660 of human PKCβII including the Phe residue (see Experimental procedures for source of antibody).

The change in FRET ratio upon PDBu addition exclusively reports on membrane translocation to the plasma membrane (PM). It is worth noting that the PM contains a majority of cellular PtdIns(4,5)P_2, which is the ligand for the LRC of C2 domain. PDBu is an analogue of the natural ligand DAG, and it binds much tighter than DAG to the C1 domains of PKC. Ca^{2+} concentrations in the cells were kept at basal level in these experiments, since mutations on the C2–V5 interface would also affect the overall affinity for Ca^{2+} and the following Ca^{2+}-dependent membrane binding. Thus, the membrane translocation data here relies in part on the exposure of C1 domains in each construct. Other factors also play a role in modulating the membrane translocation, since the system is quite complex as described in the following text.

The kinetics of membrane translocation of the wild-type YFP-PKCα construct is biphasic upon PDBu stimulus (Figure 28C, black). The wild-type FRET ratio trace can be fit very well with a combination of "fast" and "slow" functions (Figure 28C, dashed

lines). In a previous study where both YFP-tagged PKCα and PKCβII were tested, YFP-PKCβII seems to translocate with a single exponential kinetics.[155] The single exponential kinetics of YFP-PKCβII indicates that the biphasic behavior of YFP-PKCα is not likely due to an intrinsic biphasic behavior of the YFP upon membrane translocation of the fusion protein. A more possible interpretation for the biphasic behavior is that there is an intermediate PKCα conformation, in addition to the fully-closed conformation, existing in the cell. This intermediate conformation responds to PDBu stimulation much faster than the fully-closed conformation. The possible intermediate conformations are: (1) a "pre-DAG" membrane-associated conformation which is partially open,[156] (2) a dimer conformation pre-formed at plasma membrane[157] and (3) a dephosphorylated conformation. The "pre-DAG" conformation is the most likely one. The dimer conformation was proposed to be induced by the presence of Ca^{2+}/PMA or Ca^{2+}/PS/DAG.[157] The dephosphorylated conformation for WT PKCα is induced by prolonged stimulus of PDBu but not DAG.[45,158] The maximum time window here is 10 min, which should not cause active dephosphorylated conformation at the moment of PDBu addition. In addition, the western blots showed that the phosphorylation levels at pT497 and pT638 for wild-type PKCα were high, and that of pS657 was also significant (Figure 28B). The "pre-DAG" and dimer conformations were both investigated in the case of PKCα, explaining potential isoform discrepancy from PKCβII.

In the frame of the mostly likely scenario, i.e., the faster-responding intermediate conformation corresponds to the partially open "pre-DAG" conformation, the variants

can be categorized into three groups. The first group consists of variants S657A, F656A and FYYW as shown in Figure 28C. Their membrane translocation traces contain only a "fast" stage compared to the wild-type. This indicates that these three variants completely disrupted the fully-closed conformation of the kinase, resulting in only the intermediate conformation in the cell. The equations for fitting the apparent rate constants are shown in the Experimental Procedure section. It is important to note that the apparent rate constant is the sum of forward and reverse rates ($k_{app} = k_{on} + k_{off}$, where k_{on} is the pseudo first-order rate constant, assuming the simplest model in which available membrane ligands far exceeds the amount of cytosolic protein). When comparing the fitted apparent rate constants for these three variants to the "fast" stage of wild-type, the variants are still translocating faster than the intermediate of wild-type (Table 8). This is consistent with our hypothesis that HM is involved in stabilizing the compact form.

Table 8. Apparent membrane translocation rates for wild-type and variants.

Variant	Components	Step	k_{app} (min^{-1})
WT	2	fast	1.10 ± 0.06
		slow	$(4.10 \pm 0.26) \times 10^{-3}$
S657A	1	fast	1.20 ± 0.04
F656A	1	fast	1.22 ± 0.05
FYYW	1	fast	1.28 ± 0.03
D652K	1	slow	0.20 ± 0.01
KK	1	fast	0.77 ± 0.03
DKK	1	slow	0.22 ± 0.01
K213A	2	fast	1.11 ± 0.03
		slow	$(2.48 \pm 0.15) \times 10^{-3}$
KKRDS	2	fast	1.32 ± 0.07
		slow	$(3.32 \pm 0.19) \times 10^{-3}$

The second group consists of D652K, KK and charge-reversal DKK variants. D652K mutation results in high total translocation levels compared to all variants tested in this work. A high translocation level of D652K is consistent with a large k_{off}/k_{on} ratio (fraction of protein translocated at steady state equals $1/(1+K_d)$, where $K_d = k_{off}/k_{on}$). It is unlikely that D652K mutation affects the off-rate, because it is potentially not in the membrane-binding part of the kinase. Therefore, high total translocation levels are due to an increased *kon* value, which would be consistent with the destabilization of the inactive conformation.

The translocation trace of D652K appears to contain only one component (Figure 28D). It is possible that the Asp652 to Lys mutation interferes with the formation of the intermediate conformation existing in wild-type protein. In this case, the D652K variant only has one conformation in the cell, which is similar to the fully-closed conformation of wild-type. However, the apparent translocation rate of the D652K variant is much faster than the "slow" rate of wild-type (Table 8). This is still consistent with a more open mature conformation by mutating residue Asp652.

In the DKK variant, the apparent rate is the same as in D652K (Table 8). This means that the sum of k_{on} and k_{off} is the same for both. However, the steady-state translocation level of DKK is lower, indicating an increase in the ratio k_{off}/k_{on}. If k_{off} in DKK goes up compared to D652K, this should be accompanied by a decrease of k_{on}. Decrease in k_{on} in DKK is consistent with the stabilization of the inactive conformation by simultaneous charge reversal of D652 and the LRC residues. However, it does not exhibit the biphasic behavior of wild-type protein. In the KK variant, the apparent rate

goes up to 0.77 min^{-1} but the steady-state levels are smaller compared to D652K (Table 8 and Figure 28D). This is consistent with an increase the k_{off}/k_{on} ratio compared to D652K. It is likely due to the effect of an increased k_{off}, which previously occurred in mutations of positively charged residues near this region.[61,63]

The last group consists of K213A and KKRDS variants. Their translocation kinetics are similar to wild-type in the sense of biphasic behavior (Figure 28E). The K213A variant seems to increase the k_{off}/k_{on} ratio slightly compared to wild-type behavior. This is consistent with an increased k_{off} as seen for the KK variant (see above). However, the change is small due to the fact that LRC has a high density of positive charges and can still interact with pSer657 in the variant. The KKRDS variant increases the apparent rate for the "fast" stage compared to the wild-type. However, it has a similar steady-state translocation level to the wild-type behavior. This is consistent with a simultaneous increase of both k_{off} and k_{on}.

Discussion of results

We present here the solution structural model of the ternary C2·$(Ca^{2+})_2$·pHM complex, which unveils the first atomic details of the C2–V5 intramolecular interaction of PKCα. The interacting interface of the complex structure involves both electrostatic and hydrophobic residues from C2 and V5. All interacting residues are highly conserved throughout conventional PKCs.

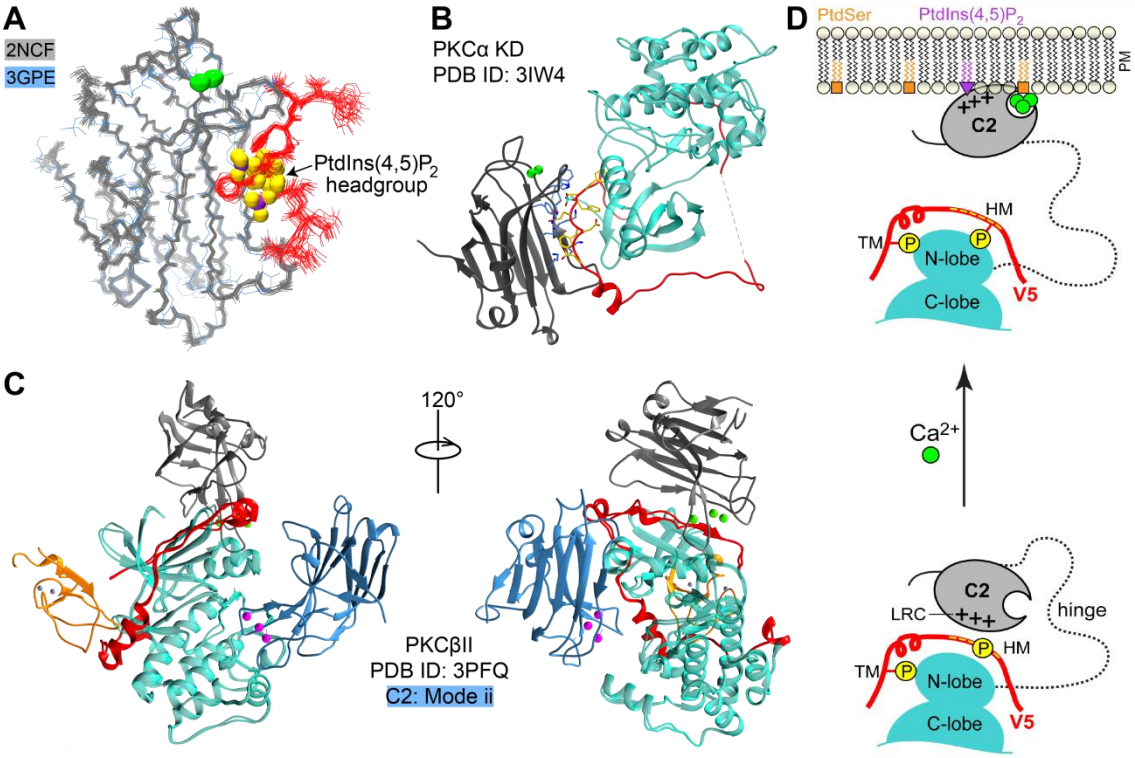

Figure 29. Model for the calcium-sensitizing and autoinhibitory roles of C2–V5 interaction during PKCα activation. (A) Overlay of binding sites between the pHM and PtdIns(4,5)P_2. The PtdIns(4,5)P_2 headgroup-associated crystal structure is PDB ID: 3GPE. Atoms of pHM peptide are colored red, and PtdIns(4,5)P_2 headgroup is colored gold with purple phosphorus atoms. **(B)** HADDOCK model of C2–V5 interaction using the crystal structure of PKCα kinase domain (PDB ID: 3IW4) and the solution structure of C2 domain determined in this work. C2 domain is colored dark grey, V5 domain is in red and the rest of kinase domain is colored cyan. **(C)** HADDOCK model of C2–V5 interaction using the crystal structure of PKCβII (PDB ID: 3PFQ), overlaid with the "Mode ii" of the original crystal structure.[23] C2 domains are colored dark grey in the HADDOCK model, and blue in the "Mode ii" model. **(D)** Model depicting the dual roles of C2–V5 interaction during PKCα activation. The C2–V5 interaction is enhanced by the phosphorylation of hydrophobic motif upon maturation, which contributes largely to the closed conformation of cytosolic, autoinhibitory PKCα. The same interaction alters the electrostatic potential of C2 domain such that the calcium binding affinity is enhanced during activation. Interaction between C2 lysine-rich cluster with PtdIns(4,5)P_2 on the plasma membrane displaces V5-pHM and leads to maximum activation of PKCα. Panel D figure credit: T. I. Igumenova.

Among the V5 residues involved in this interaction, Asp652 is identical in PKCγ and is a Glu in PKCβI and PKCβII; Phe653 and Phe656 are identical throughout all four cPKCs; and the conserved phosphorylation residue Ser657 is identical in PKCβI and PKCβII, and is Thr in PKCγ (Figure 7B in Chapter II). All C2 residues on the interacting interface are identical throughout cPKCs, with the exception of Asn206. Since Asp649 is located on the edge of the interface, and the N-terminus is not restrained well when inspecting the whole HADDOCK pool of 400 structures, we concluded that the interaction involving Asp649 and Asn206 does not play an indispensable role.

This structural model is validated by the functional impact of mutating the residues at the C2–V5 interacting interface guided by the same structure. From the FRET ratios of purified autoinhibited proteins, we concluded that all the charged and hydrophobic residues contribute in concert to the interaction. We also observed an unambiguous activating effect of externally added pHM peptide on the wild-type full kinase. From the membrane translocation studies, we concluded that the mutation of the Phe656/pSer657 dual from HM of V5 both significantly increased the k_{on} to plasma membrane upon PDBu stimulation. The Asp652 centered interaction disrupts the biphasic behavior of the wild-type protein, potentially resulting in a faster membrane-translocating mature conformation. Taken together, the C2–V5 interface described here plays a pivotal role in maintaining the closed conformation of the autoinhibited kinase, in which the membrane-binding sites of C1 domains are masked by intra-molecular interactions.

Another role of C2–V5 interaction, which seems contradictory from the autoinhibitory aspect, is to sensitize the calcium binding to the C2 domain by lowering the overall electrostatic potential of C2. This is seen here by our extensive in vitro investigation of the interplay between pHM and Ca^{2+} ligands to C2 domain. A similar effect was also seen previously with PtdIns(4,5)P_2 enhancing the binding affinity of the C2 domain to Ca^{2+} and Pb^{2+}. As observed with the structural overlay of our complex structure to the PtdIns(4,5)P_2 bound C2 crystal structure (Figure 29A), the Asp652 centered interactions masks the PtdIns(4,5)P_2 binding site for C2. From these, we infer that the C2–V5 interaction presented here is crucial for PtdIns(4,5)P_2 selectivity of cPKCs.

In order to visualize the C2–V5 interaction described here in the context of full-length cPKCs, we modelled the interaction with the crystal structures of PKCα and PKCβII, using the same set of inter-molecular restraints derived from our solution C2·$(Ca^{2+})_2$·pHM complex. The LRC concave of C2 domain contacts extensively the HM of V5 for both cases (Figure 29B, C), whereas the CMBLs of C2 remains solvent exposed and Ca^{2+} accessible. In a superimposed comparison of the previously proposed C2–kinase model[23,55] and our docked model (Figure 29C), C2 domain is rotated around the tip of the beta3-4 loop towards V5-HM in our model for 161 °. Both models are validated by mutagenesis studies, and support the importance of LRC from the C2 domain as well as the HM from the V5 domain. However, our data that the externally added pHM peptide effectively activates the kinase support the HM as an interacting partner for C2. Since the hinge linker between the C2 and N-lobe of the kinase domain

consists of about 43 amino acids, the C2 domain in theory can sample around the entire kinase domain with a large degree of freedom. Thus these two models present a delicate illustration of the potential conformational plasticity relating to the C2 domain at different stages of kinase regulation. Given the extent and conservation of interacting residues in our model, as well as the functional aspect of Ca^{2+} and PtdIns(4,5)P_2 interactions, we think that the C2-V5 interaction described herein resembles closely the conformation between the initial Ca^{2+} binding event and C2 association with the PtdIns(4,5)P_2-containing plasma membrane. The reason this interaction was not observed in the intermediate state of PKCβII crystal structure could be due to the intrinsically dynamic properties of the entire V5 region preventing the formation of stable crystal packing. In our docked model with full kinase domains of PKCα and PKCβII, no extra interaction is observed between C2 domain and residues of kinase domain other than V5-HM. Thus the C2–V5 interaction probably does not provide much further stabilization of V5 conformation.

We propose a model of cPKC activation by second messengers pertaining to the C2–V5 interaction described here (Figure 29D). The phosphorylated HM of V5 masks the LRC of C2 domain in the auto-inhibited conformation of PKC prior to the upstream signaling event leading to an increase of cytosolic calcium concentration. The altered electrostatic potential of the C2 domain assists in acute response for calcium binding by interacting with the HM. Once calcium ions are bound to the CMBLs of C2, the C2 domain is now capable of associating with the PtdSer lipid headgroup through completion of the calcium coordination sphere (to be discussed in Chapter V). However,

the HM of V5 remains associated with C2 domain until a search for PtdIns(4,5)P_2 headgroup is successful, replacing the HM from LRC and leading to a full release of C2 domain. The C2–V5 interaction here plays both calcium-sensitizing and autoinhibitory roles. Once fully activated, the C2–V5 interaction probably contributes to the recycling of the kinase when the calcium concentration is decreased. Alternatively, V5-HM was shown important for Pin1 peptidyl-propyl isomerase dependent down-regulation,[45] which according to our model would only be accessible to Pin1 when V5-HM is displaced by PtdIns(4,5)P_2 (to be discussed in Chapter IV).

Caution needs to be taken when interpreting the significance of our docked models with PKCα and PKCβII, since C1A and C1B domains are not included. The exact placement of these two domains in the full-length kinase is still largely elusive. It is worth noting that neither our C2–V5 model nor the previously proposed C2–kinase model supports the intra-molecular interaction between C1B domain and the NFD region of V5 domain, due to the limited length of the C1B–C2 linker. To discern the locations of C1 domains and the order of actions relative to the C2 domain conformations discussed in this work, future research is required investigating intra-molecular interactions involving C1 domains. However, our study certainly illustrates the atomic-level information about the significant contribution from the HM of V5 domain to both auto-inhibition and activation of cPKC. Although the interacting residues between C2–V5 are conserved within cPKCs, the V5 region is highly variable throughout all PKC isozymes. The information provided here could shed light on designing therapeutic

agents targeting the C2–V5 interaction, in order to up- or down-regulate kinase activities specific to conventional PKC isoforms.

CHAPTER IV

INTERMOLECULAR INTERACTION BETWEEN V5 DOMAIN AND PEPTIDYL-PROLYL ISOMERASE PIN1 REVEALS NON-CANONICAL BINDING SITE AND NON-CATALYTIC MECHANISM.

Background

As discussed in Chapter II and III, the C-terminal V5 domain is intrinsically disordered and interacts with the Ca^{2+}-dependent membrane-binding C2 domain within the same PKCα molecule. In addition to these characteristics, the V5 domain has also been implicated in potential intermolecular interaction with the peptidyl-prolyl isomerase Pin1 by Abrahamsen et al.[45] This study revealed that the proteasome-dependent down-regulation of conventional PKC isoforms is controlled by the peptidyl-prolyl isomerase Pin1. The authors proposed a model in which conventional PKCs directly interact with Pin1; this interaction facilitates dephosphorylation of PDBu-stimulated conventional PKCs and leads to down-regulation through ubiquitination and proteasome-dependent degradation. This chapter focuses on understanding the molecular basis of Pin1 interaction with the C-terminal V5 domain.

Pin1 is a eukaryotic peptidyl-prolyl isomerase, which belongs to the parvulin sub-family.[159] It contains two domains each possessing a distinct structure and function: (1) a type IV WW domain that preferentially binds phosphorylated-(Ser/Thr)-(Pro) (referred to as pS/T-P in the following text) motifs and (2) a PPIase domain that catalyzes proline *cis-trans* isomerization of the same motif (Figure 30A).

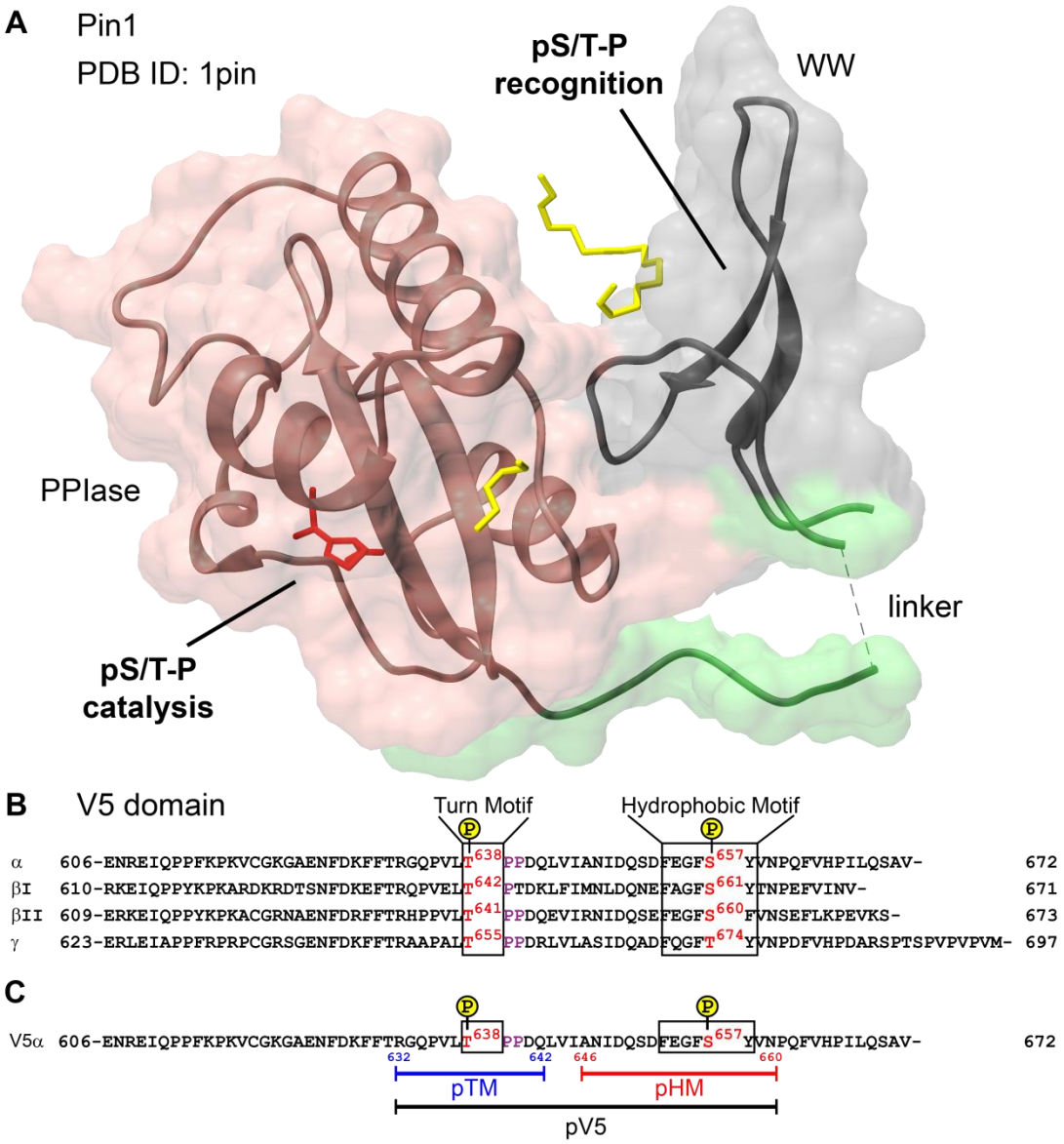

Figure 30. The two proposed binding partners: Pin1 protein and the V5 domain from conventional PKCs. (A) Crystal structure of full-length Pin1 protein is displayed in both ribbon and surface representations (PDB ID: 1PIN). Surface of the WW domain is dark gray, the PPIase domain is salmon, and the linker is green. The PEG molecule (gold) and the AlaPro dipeptide (red) from the crystal structure are shown to indicate pS/T-P motif binding sites. **(B)** Sequence alignment is shown for the V5 domain from conventional PKC isoforms. Turn and hydrophobic motifs are shown in the boxes, with phosphorylation sites indicated. Proline residues in the turn motif are highlighted with purple fonts. **(C)** Sequences of phosphorylated peptides used in this study are indicated. The pTM, pHM and pV5 peptides are highlighted with blue, red and black lines, respectively.

The two domains of Pin1 both recognize the pS/T-P motif, but for several known Pin1 targets the WW domain has been observed to have significantly higher substrate affinity than the PPIase domain.[160] The substrate selectivity of Pin1 is unique among the PPIase family, which allows it to modulate protein interactions following the phosphorylation events during kinase signaling.[161] Due to these features, Pin1 plays a role in various key signaling pathways and has been associated with many human diseases such as neurodegenerative diseases and cancers.[162-164]

The molecular mechanism of the Pin1 function is not well understood. This is due to three main challenges. The first challenge has to do with the linker between the two domains of Pin1, which is long and flexible. The linker length between the two domains is 16~18 amino acids, calculated from the last amino acid of WW domain folded core Pro37[165,166] to Arg54, Val55 or Arg56, the first amino acid of β4 defined in PDB ID 1NMV, 1F8A or 1PIN, respectively. This relatively long and solvent-exposed linker allows a large degree of freedom for the linker itself, and consequently, the conformational flexibility of the full protein. This can be visualized by inspecting the large conformational deviations in the Pin1 NMR structural ensemble (PDB ID 1NMV), and a lack of inter-domain NOE in the same study.[167] The NMR structural ensemble is shown in Figure 31, with the flexible linker highlighted. Although the domain interaction is probably weak in solution, numerous studies have provided information on the change of conformational sampling between the two domains upon ligand binding. It was proposed that domain interactions of Pin1 could affect substrate recognition.[168] Another study observed transient and intricate open and closed conformations of Pin1

under various conditions.[169] A most recent mutagenesis study indicated an auto-inhibiting role of domain interactions in the case of the pCdc25C substrate.[170] These studies together demonstrated the complexity of the ligand binding mode due to the large domain flexibility of Pin1.

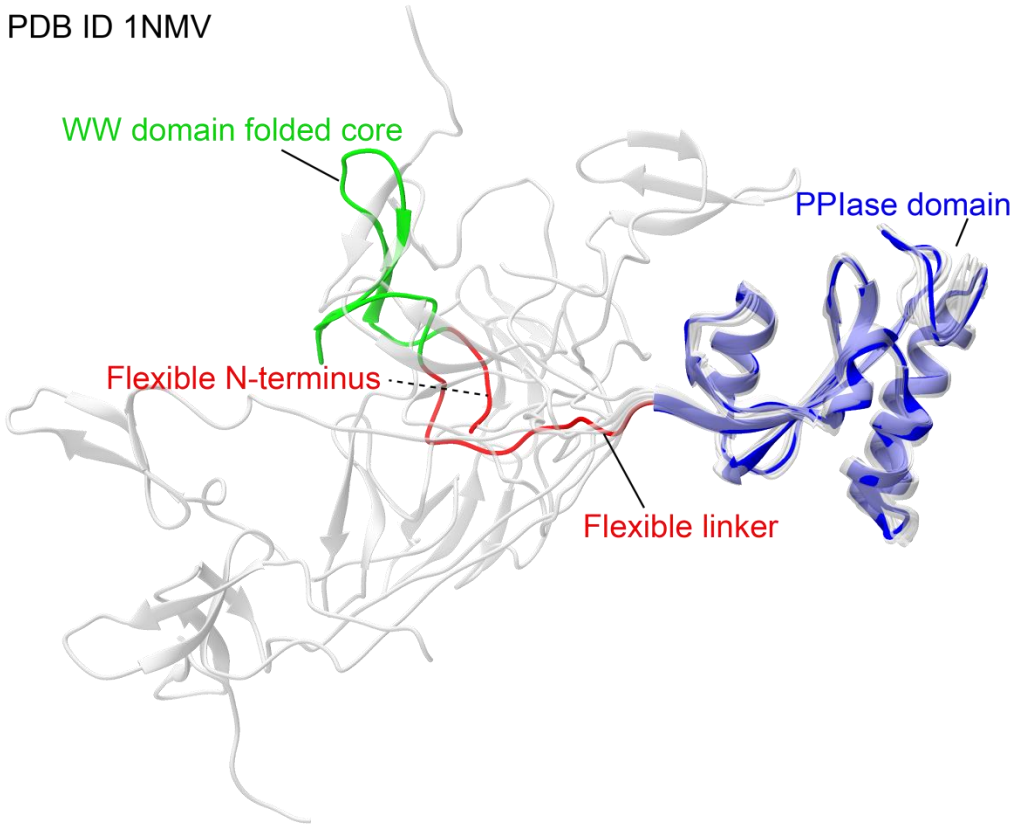

Figure 31. The large conformational flexibility of the two domains visualized in the NMR structural ensemble of Pin1 (PDB ID 1NMV). The first structure in the ensemble is selected to illustrate the domain compositions, and the rest of structures are colored gray. The folded core of the WW domain is colored green; the PPIase domain is blue; the flexible N-terminus and the flexible inter-domain linker are red.

The second challenge to understanding the Pin1 function is related to the mechanism of the Pin1 catalysis. The PPIase domain of Pin1 catalyzes the *cis-trans* isomerization of the substrate peptidyl-prolyl bond. The two main proposed mechanisms for this process are: (1) nucleophilic addition by the enzyme thiol of Cys113 at the carbonyl carbon of phosphorylated residue, which is supported by the apparent pH dependence of enzymatic activity;[159] (2) twisting the amide bond out of conjugation by hydrogen bonding to the prolyl nitrogen, which is supported by normal 2 °KIE (kinetic isotope effect) on the phosphorylated residue and inverse 2 °KIE on the proline residue.[171] Each mechanism has a crystal structure of Pin1 as a support, but the twisted amide mechanism seems to be more favored due to a similar mechanism of other PPIase proteins.

The third challenge is the role of catalysis in the Pin1 function. Despite the catalyzing function of its PPIase domain, Pin1 has been proposed to play a non-catalytic role especially in the cytoplasm of the cell.[172] In this study, mutations of the phosphate binding loop on the PPIase domain had a negative effect on Pin1 binding to some target proteins; however, this did not apply to the mutation of the potential active site residue Cys113.[172] Even though the Cys113 was thought to be associated with the nucleophilic catalytic mechanism, which still remains controversial, this information still reveals importance of the PPIase-substrate binding in addition to the catalytic activity. On the other hand, a quite significant number of known Pin1 substrates contain a pS/T-P-P sequence, with an additional proline at the +1 position. The −1 and 0 positions by convention refer to the phosphorylated serine/threonine (pS/T) and the first proline (P)

residues, respectively. NMR experiments of Tau protein indicated that the pS/T-P-P sequence interacted preferentially to the WW domain.[173,174] Two other Pin1 target proteins were also indicated to be PPIase domain independent.[175,176] In addition, various Pin1 target proteins contain more than one binding site, suggesting potential multi-valent protein-protein interactions. However, it is not clear yet how the non-catalytic aspect of Pin1 relates to its cellular function and regulation due to limited information.

It is worth mentioning that since the PPIase domain has a weak affinity and catalytic activity towards the pS/T-P motifs, the only structures of a PPIase domain bound to a longer peptide were co-crystalized with peptide inhibitors.[177] With all aspects of Pin1 complexity in mind, we seek to understand the molecular mechanism relating to the Pin1-mediated down-regulation process of conventional PKCs. In the model of Abrahamsen et al., Pin1 was proposed to bind the hydrophobic motif (HM) of the V5 domain and catalyze the proline isomerization of the turn motif (TM).[45] However, the sequence in the hydrophobic motif of the V5 domain lacks a proline following the phosphorylated serine residue (Figure 30B), raising the question as to why this non-canonical site is essential for Pin1 binding. On the other hand, the turn motifs of PKCα, βII and γ isoforms have an additional proline residue that immediately follows the conventional isomerization site, i.e., p(Thr)-(Pro)-(Pro). It is not clear whether or not the turn motif of these isoenzymes is an efficient substrate for Pin1 catalysis. In addition to the above questions, the proposed interaction between V5 and Pin1 involves four potential players: TM and HM of the V5 domain; the WW domain and the PPIase

domain of Pin1 (Figure 30). Unfortunately, the mode of Pin1–V5 interaction could be complicated by all the possible binding combinations.

In this chapter, we demonstrate the binding preferences of Pin1 to V5 with a "divide-and-conquer" approach. We first isolated the four basic interaction elements to investigate protein-protein interactions. We then assembled the full-length Pin1 and V5 motifs to obtain the whole picture. We also showed that the TM of V5 from PKCα is not an efficient substrate for the PPIase activity of Pin1. These results provided valuable insights into the first step of conventional PKCs down-regulation mediated by Pin1, which could assist in developing strategies for isoform-specific regulation of PKC. The study herein is, to our knowledge, the first detailed characterization of a cooperative multivalent Pin1 interaction containing both a non-catalytic site and a non-canonical site for Pin1.

Experimental procedures

Plasmid construction

The human Pin1 (residue 1–163 full length, codon-optimized DNA sequence) construct was cloned into a pET-SUMO vector (Invitrogen). Isolated WW domain (1–50) and PPIase domain (41–163) constructs were generated by QuikChange™ site-directed mutagenesis using the original pET-SUMO-Pin1 plasmid as a template.

Protein and peptide purification

The human Pin1 (residue 1–163 full length) construct was transformed in *E.coli* BL21(DE3) cells for overexpression. The isolated WW domain and PPIase domain have significant leaky expression in the regular BL21(DE3) cells before addition of IPTG, so instead BL21(DE3)pLysS cells are used for expressing isotope-enriched proteins. For natural abundance proteins, cell cultures were grown to OD_{600} value of 0.6 and induced with 0.5 mM IPTG for 4–5 hrs at 37 ℃. For ^{15}N-enriched (^{13}C,^{15}N-enriched) proteins, we used the resuspension method of Marley et al.[92] with M9 minimal media containing 1 g/L of $^{15}NH_4Cl$ and natural abundance glucose (1 g/L $^{15}NH_4Cl$ and 3 g/L ^{13}C-D-glucose) (Cambridge Isotopes). In the case of isotope-enriched preparations, the protein expression was induced for 15 hrs at 15 ℃ for regular BL21(DE3) cells, or 5 hrs at 37 ℃ for BL21(DE3)pLysS cells.

The cells were harvested by centrifugation (30 min, 4,000 rpm at 4 ℃) and lysed by sonication in a buffer containing 20 mM Tris-HCl, 0.5 M NaCl, 5 mM imidazole and 10 mM βME at pH 7.5. The His_6-tagged SUMO-$Pin1_{[fl,\ WW\ or\ PPIase]}$ fusion proteins were purified using a HisTrap™ HP Ni affinity column (GE Healthcare Life Sciences). The fractions containing fusion protein were buffer exchanged on a HiPrep 26/10 column (GE Healthcare Life Sciences) into a cleavage buffer containing 20 mM Tris-HCl, 0.15 M NaCl at pH 8.0. Tag-free $Pin1_{[fl,\ WW\ or\ PPIase]}$ proteins were obtained by cleaving the fusion proteins for 30 minutes with His_6-tagged SUMO protease at room temperature, followed by another Ni affinity purification step to remove SUMO and SUMO protease. The purified proteins were further buffer exchanged with a 5 kDa MWCO membrane

concentrator (Sartorius Vivaspin) for full-length Pin1 or the isolated PPIase domain, or a 3kDa MWCO membrane concentrator (Sartorius Vivaspin) for the isolated WW domain, into freshly made final NMR buffer containing 10 mM d4-imidazole, pH 6.6, 100 mM KCl, 1mM TCEP, 8% D_2O, and 0.02% NaN_3. The purity of $Pin1_{[fl, WW or PPIase]}$ proteins was evaluated using SDS-PAGE. The concentrations were measured with A280 nm with the corresponding extinction coefficients: full-length Pin1 20,970 $M^{-1}cm^{-1}$, isolated WW domain 13,980 $M^{-1}cm^{-1}$, and isolated PPIase domain 6,990 $M^{-1}cm^{-1}$. The molecular weights of purified proteins were verified by MALDI-TOF mass spectrometry.

The peptides were purchased from Eton Bioscience, with acetylation and amidation at the N- and C-termini, respectively. Amino acid sequences of peptides used in this study are shown in Figure 30C. The pTM-P640A is a single alanine substitution peptide at the P640 position of pTM peptide. Crude peptide mixtures were purified on a C18 column using HPLC. The buffers used for HPLC were: A 5 mM NH_4HCO_3 in HPLC-grade water and B 5 mM NH_4HCO_3 in 82% HPLC-grade acetonitrile and 18% HPLC-grade water. Linear gradients from 0–20%, 0–30%, 10–30%, 10–40% buffer B were used to purify pTM-P640A, pTM, pHM and pV5 peptides, respectively. The molecular weight and purity of the peptides after HPLC purification were verified using ESI mass spectrometry. The peptide stock solutions were prepared in HPLC-grade water and adjusted to pH 6.6 with ammonium hydroxide. Stock concentrations of purified phosphorylated peptide were measured using a phosphate assay.[132]

NMR-monitored binding experiments and resonance assignments

The peptide-binding experiments were conducted by adding aliquots of concentrated peptide stock solutions to [U-^{15}N] Pin1 full-length protein or isolated WW domain protein. The protein concentration in the NMR samples ranged from 90 to 100 μM. For each ligand concentration, [^{15}N-^{1}H] HSQC spectra were collected at 25 ℃ on Bruker Avance III spectrometers operating at the Larmor ^{1}H frequencies of 600 MHz or 800 MHz. For the chemical shift perturbation (CSP) and binding curve analysis, the residue-specific chemical shift change between any given pair of Pin1 (or WW) states was calculated as follows:

$$\Delta = \sqrt{(\Delta\delta_H)^2 + (0.152 \times \Delta\delta_N)^2} \qquad \textbf{4.1}$$

where $\Delta\delta_H$ and $\Delta\delta_N$ are the residue-specific differences in ^{1}H and ^{15}N chemical shifts, respectively. The binding curves were constructed by plotting Δ against total ligand concentration. Residues with Δ values above the mean value for all residues were selected to determine binding affinities. The dissociation constants K_d for the peptides binding to Pin1 or WW domain were determined by fitting the binding curves with the single-site equation:[134]

$$\Delta = \Delta_{max} \frac{P_0 + L_0 + K_d - \sqrt{(P_0 + L_0 + K_d)^2 - 4P_0L_0}}{2P_0} \qquad \textbf{4.2}$$

where $\Delta\delta_{max}$, P_0 and L_0 are the chemical shift change at complete saturation, total protein concentration and total ligand concentration, respectively.

To evaluate dissociation constants with two binding sites, a two-site equation is used:

$$\Delta = \Delta_{max} \frac{P_0 + L_0 - A + K_{d1} - \sqrt{(P_0 + L_0 - A + K_{d1})^2 - 4P_0(L_0 - A)}}{2P_0}$$

$$A = \frac{P_0 + L_0 + K_{d2} - \sqrt{(P_0 + L_0 + K_{d2})^2 - 4P_0 L_0}}{2} \quad \textbf{4.3}$$

where K_{d1} and K_{d2} are the dissociation constants for the two binding sites, respectively.

Assignment of Pin1 residues was carried out with a sample containing 1.5 mM [U-^{13}C, ^{15}N] full-length Pin1 protein, dissolved in the final NMR buffer (*vide supra*). Backbone resonances of ^{1}H, ^{13}C and ^{15}N were assigned with experiments 2D [^{15}N-^{1}H] HSQC, 3D HNCACB,[93] 3D CBCA(CO)NH,[93] 3D HNCO,[93] and verified with 3D CC(CO)NH[95] and 3D H(CCO)NH[136] experiments. Resonances of WW domain residues were transferred from the assignments of full-length Pin1 and verified with 3D ^{15}N-edited NOESY-HSQC[139-141] spectrum with a sample containing 1 mM [U-^{15}N] WW domain.

Assignment of Pin1 residues saturated with pV5 peptide was carried out with a sample containing 1 mM [U-^{13}C, ^{15}N] full-length Pin1 protein and 1.25 mM pV5 peptide. 3D CBCA(CO)NH[93] spectrum was collected for this purpose. All assignment experiments were carried out at 25 ℃ on a Varian VNMRS spectrometer operating at the Larmor ^{1}H frequencies of 600 MHz, or on Bruker Avance III spectrometers operating at the Larmor ^{1}H frequencies of 600 MHz or 800 MHz.

Assignments of the pTM and pV5 peptides were carried out at 25 ℃ with 2D NOESY,[178,179] 2D TOCSY[180] and 2D ROESY[181] experiments collected on Bruker Avance III spectrometers, operating at the Larmor ^{1}H frequencies of 500 MHz or 800 MHz. The NOE mixing time was kept at 500 ms. The TOCSY spectra were collected

with 80 ms mixing time. The ROE spin-lock duration was 240 ms, corresponding to a 2 kHz field at a low power of 0.06 W. Additional verifications were performed by comparing protein chemical shifts with our assignments of full-length dmV5α as described in Chapter II. The pTM peptide assignments were further verified by collecting a natural abundance [^{15}N-^{1}H] HSQC spectrum.

NMR EXSY experiments and data analysis

Observations of exchange cross-peaks were done by collecting 2D NOESY and ROESY spectra. NOE mixing time and ROE spin-lock duration are the same as specified above. One sample consisted of 2 mM pTM peptide in the presence of 50 μM fresh proteins (full-length Pin1 or isolated PPIase domain). The other sample consisted of 1.53 mM pV5 peptide in the presence of 90 μM fresh full-length Pin1 protein. Spectra in the absence of Pin1 or PPIase proteins did not exhibit exchange cross-peaks.

Exchange spectroscopy (EXSY) experiments of pTM peptide were carried out at 25 ℃ with 2D NOESY at exchange mixing times of 40, 70, 100, 200 (×2), 300, 400 and 500 (×2) ms. For pTM peptide, the exchange rate constant, k_{EXSY}, was estimated by fitting the intensity ratios as following:[182,183]

$$\frac{I_{tc}}{I_{cc}} = \frac{k_{ct}(1 - e^{-k_{EXSY}t})}{k_{tc} + k_{ct}e^{-k_{EXSY}t}} \qquad \textbf{4.4}$$

where $k_{EXSY} = k_{ct} + k_{tc}$, I_{tc} is the intensity of the exchange cross-peak from *trans* to *cis*, I_{cc} is the intensity of the diagonal peak for the *cis* conformation, k_{ct} (k_{tc}) is the rate constant from *cis* to *trans* (*trans* to *cis*), and *t* is the mixing time of each experiment. The

intensity of *trans* diagonal resonance was not included due to an overlap with an adjacent diagonal resonance.

Results

Hydrophobic motif is a non-canonical interaction site for Pin1

The amino acid sequence of the hydrophobic motif (HM) from PKCα has a tyrosine immediately following the phosphorylated-serine residue, rendering it a non-canonical interaction site for Pin1 if the proposed interaction[45] does exist (Figure 30B). In order to address this, we started out to investigate if the proposed interaction between the PKCα and Pin1 can occur with the isolated phosphorylated-HM (pHM). The isolated WW domain of Pin1 was first tested since a target-recognizing role is generally considered for this domain. With the addition of the pHM peptide, we observed unambiguous chemical shift perturbations of the isolated WW domain residues monitored by NMR HSQC experiments (Figure 32). The time scale of the binding event overall is in the fast exchange regime, allowing us to plot and fit the binding curves to extract an accurate dissociation constant value. The global fitting of 13 responsive amino acids (Equation **4.2**) generated a dissociation constant K_d of 1006 ± 9.33 μM. Representative binding curves are shown in Figure 34A. This indicates a direct interaction between the pHM and the isolated WW domain of Pin1, albeit with a relatively weak binding affinity.

We next tested binding between the full-length Pin1 and the pHM peptide. Unexpectedly, we observed chemical shift perturbations (CSP) on both WW domain and

PPIase domain residues of Pin1 upon increasing concentration of the pHM peptide, indicating potential interactions of the pHM peptide with both domains (Figure 33). The binding curves of WW domain residues globally fit to a dissociation constant K_d of 893 ± 13.7 μM (Figure 34B), whereas global fitting of the PPIase domain residues generated a dissociation constant K_d of 772 ± 7.33 μM (Figure 34C).

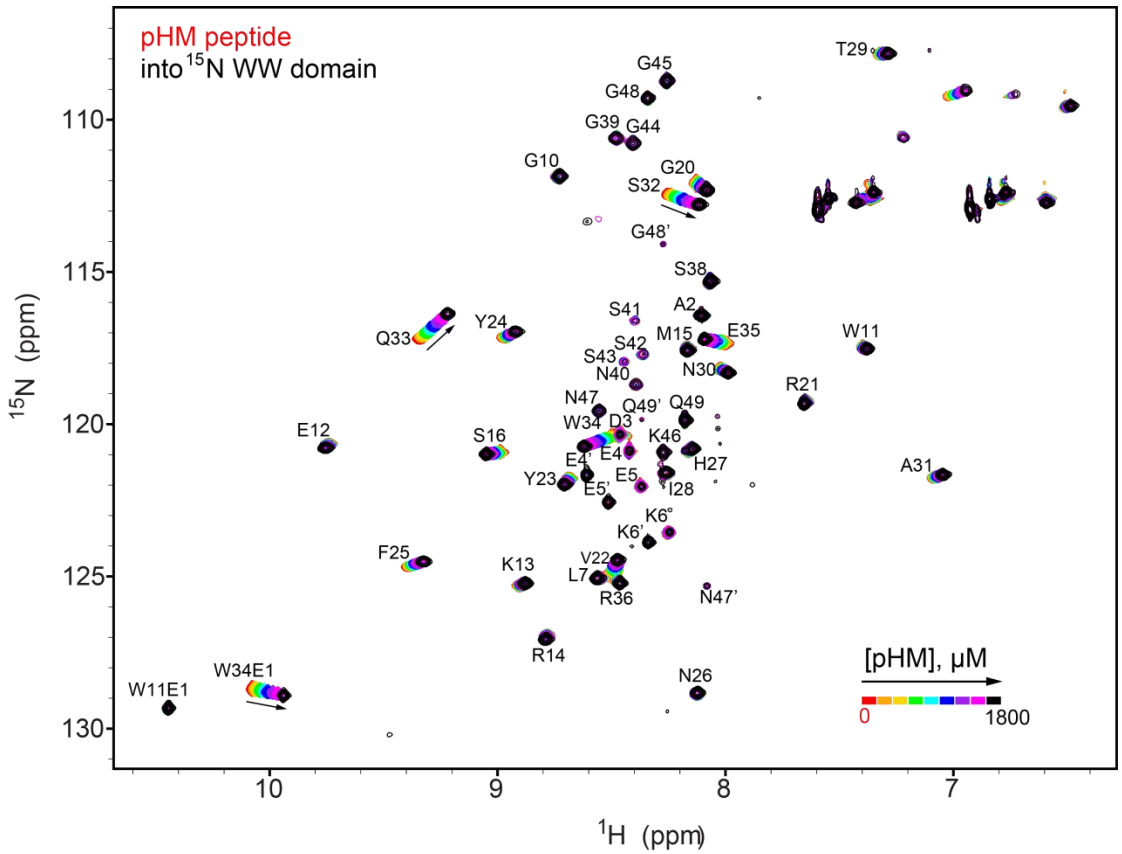

Figure 32. The pHM peptide interacts with isolated WW domain from Pin1 detected by NMR. [^{15}N-^{1}H] HSQC spectra of [U-^{15}N] enriched isolated WW domain (residue 1-50) of Pin1 with increasing concentration of the pHM peptide are shown as an overlay. The color coding of each spectrum with increasing pHM peptide concentrations is indicated as insert in the bottom right corner.

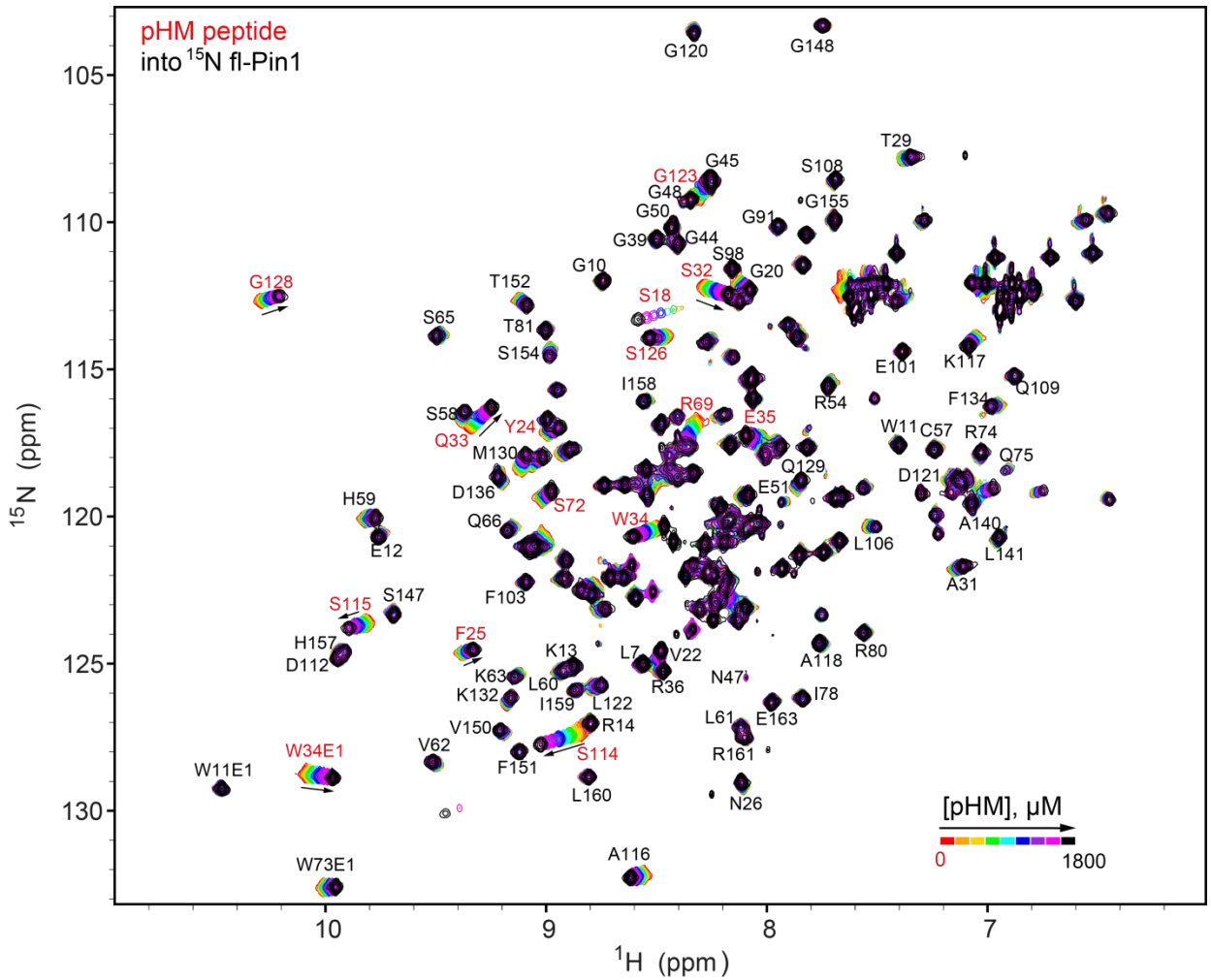

Figure 33. The pHM peptide interacts with full-length Pin1 detected by NMR. [^{15}N-^{1}H] HSQC spectra of [U-^{15}N] enriched full-length Pin1 with increasing concentration of the pHM peptide are shown as an overlay. The color coding of each spectrum with increasing pHM peptide concentrations is indicated as insert in the bottom right corner.

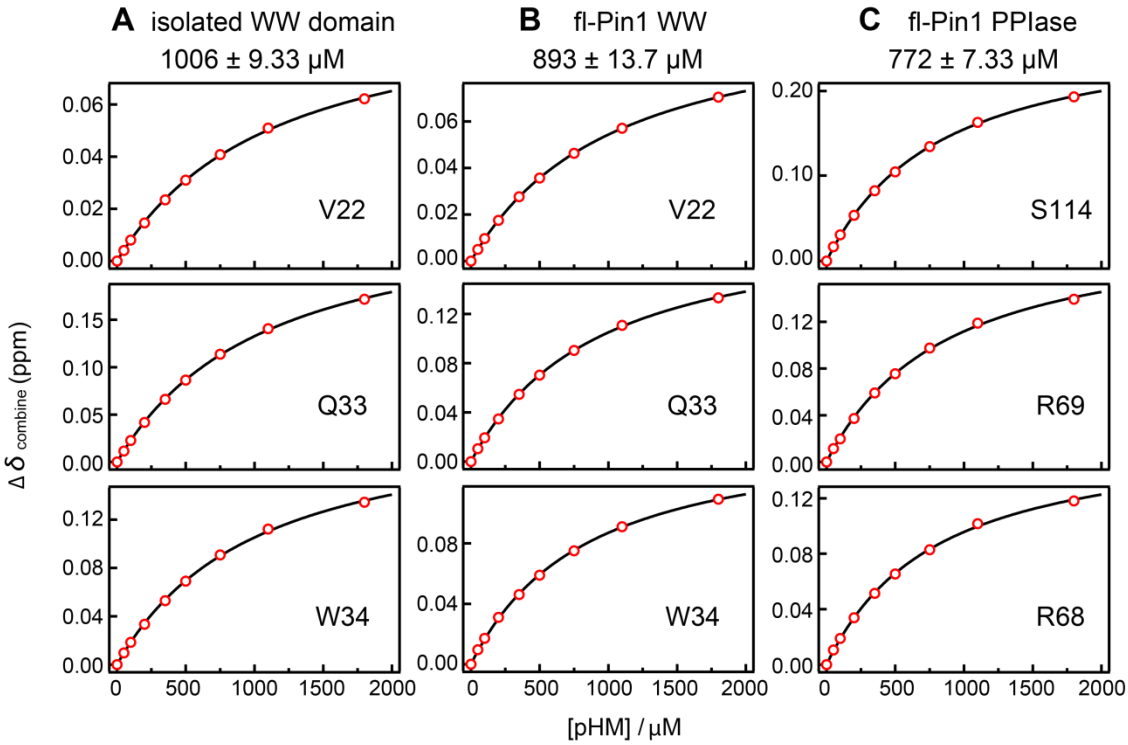

Figure 34. The pHM peptide interacts with the isolated WW domain and both domains of full-length Pin1 with a similar affinity. Representative NMR-detected pHM binding curves are shown for the isolated WW domain experiment **(A)**, the full-length Pin1 experiment with residues from the WW domain **(B)** and PPIase domain **(C)**. All solid lines are global fitting results.

Both apparent affinities are similar to the binding affinity of pHM to the isolated WW domain (K_d = 1006 ± 9.33 μM), with the affinity of PPIase domain being slightly higher than WW domain in the context of full-length Pin1.

It is worth mentioning that CSP indicates a change in the chemical environment of the atom in question. Thus, CSP herein may not necessarily reflect a direct binding. Due to the high similarity of CSP patterns between the isolated WW domain experiment and the WW domain residues in the full-length Pin1 experiment, we are certain that the pHM peptide directly interacted with the WW domain in both experiments (Figure 35).

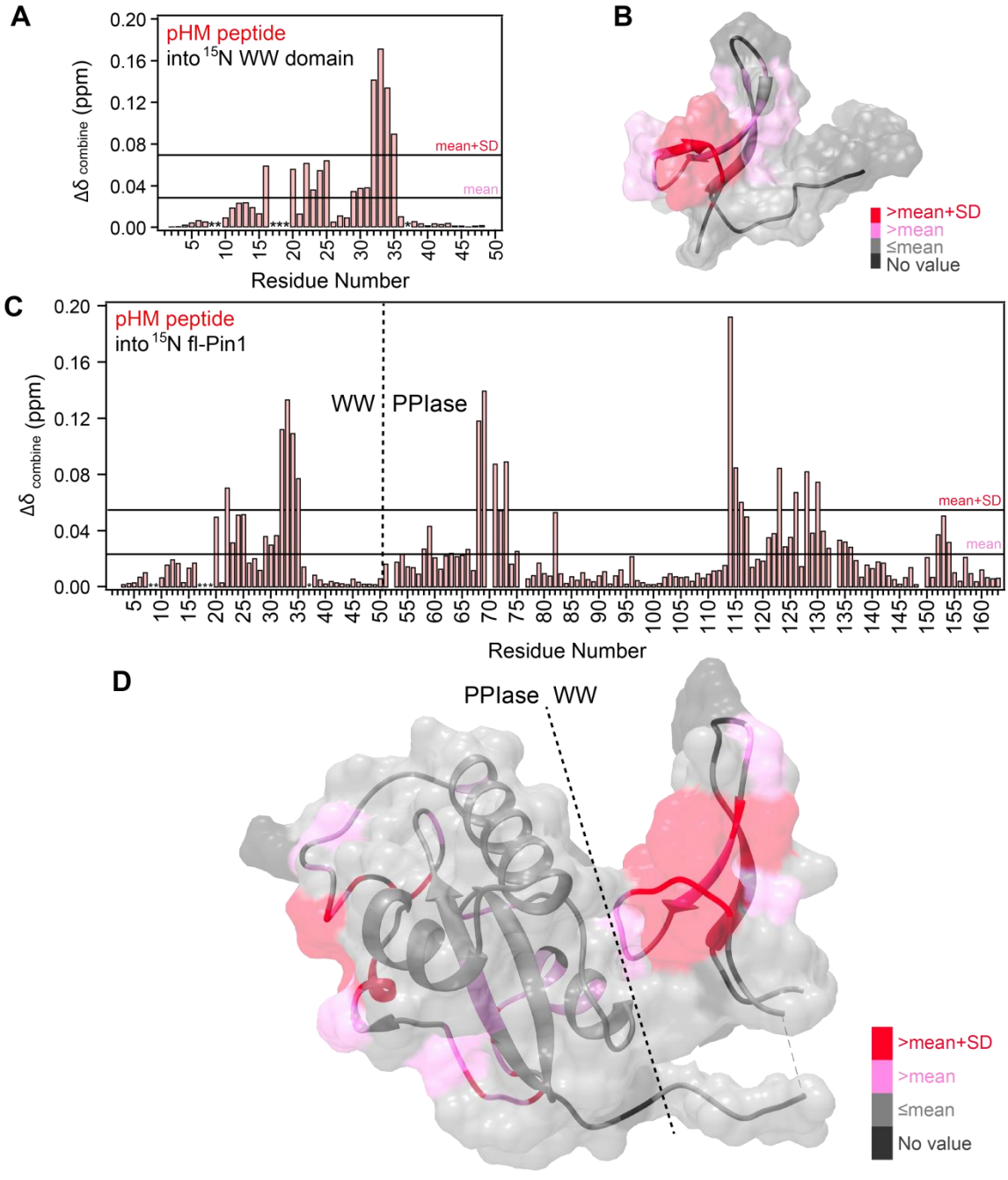

Figure 35. Chemical shift perturbation analysis of the pHM binding experiments. **(A)** Combined chemical shift perturbation (CSP) of the isolated WW domain with 18-fold molar excess of pHM peptide vs. no peptide is plotted against residue number. Residues with no CSP values are prolines, residues broadened beyond detection and residues that are not spectrally resolved. **(B)** The CSP values are mapped onto the isolated WW domain structure (PDB ID 2M8I)**.** (C) Combined CSP of the full-length Pin1 pHM-binding experiment and **(D)** mapped on the Pin1 structure (PDB ID 1PIN)**.**

However, the CSP of PPIase domain residues can be an indirect effect of WW–pHM interaction. Although given the similar scale of CSP values between the two Pin1 domains responding to pHM addition (Figure 35B), we believe that the PPIase residues are more likely responding to a direct binding event with a similar affinity to the WW domain binding event. An additional support is that the identities of PPIase responding residues match well with the previously indicated phosphorylated peptide binding pocket.[159,170] Further control experiment is required with isolated PPIase domain in order to fully verify this.

With the above discussion, we think of the isolated pHM peptide interaction with the full-length Pin1 as two independent binding events: pHM–WW and pHM–PPIase. The two apparent K_ds shown in Figure 34 are extracted from fitting the binding curves with the single-site equation (**4.2**). However, with two independent binding sites of similar affinity, we are slightly underestimating the affinities due to a depleted pool of free ligand concentration for one site while the other is occupied. The extent of underestimation is evaluated with a two-site equation (**4.3**), with one K_d fixed at various values and extract the other K_d extracted with global fitting. From the evaluation results shown in Table 9, we conclude that the overestimation of K_d is about 14% for the WW site and about 11% for the PPIase site. Since the overestimation is minor, we will use K_d values from fitting with the single-site equation (**4.2**) to compare with those from the pTM and pV5 peptides (*vide infra*) for consistency.

Table 9. Evaluation of the pHM–Pin1 binding curves with two-site equation

Equation	WW residues		PPIase residues	
	K_d / μM	Hold K_d / μM	K_d / μM	Hold K_d / μM
Single Site	893 ± 13.7		772 ± 7.33	
		PPIase		WW
Two Sites	800 ± 12.0	1000	692 ± 6.33	1000
	779 ± 11.6	772	684 ± 6.23	893
	769 ± 11.5	684	674 ± 6.10	769

Turn motif specifically associates with the WW domain over the PPIase domain

The turn motif (TM) from PKCα, βII and γ contains consecutive proline residues following the phosphorylated threonine. According to previous studies on Tau protein, the pT^{231}-P-P site of Tau was shown to be a WW domain specific interaction site.[173,174,184] Phosphorylation sites with consecutive proline residues from peroxisome proliferator-receptor γ (PPARγ) and CREB-regulated transcriptional coactivator 2 (CRTC2) were also shown responsible for interaction with Pin1.[175,176] In order to see if the TM from the three conventional PKC isoforms (α, βII and γ) is a WW domain specific interaction site, we first took the isolated phosphorylated-TM (pTM) and tested binding with the isolated WW domain monitored by NMR. With this experiment, we observed significant chemical shift perturbations with a much tighter association of pTM to the isolated WW domain than the pHM peptide. This is manifested by both the fast-to-intermediate behavior for most responding resonances on the NMR exchange

timescale (Figure 36) and the globally fitted dissociation constant K_d of 25.2 ± 0.215 μM (Figure 38A). The binding affinity of the isolated pTM was 40-fold tighter than the isolated pHM associated with the isolated WW domain. This was surprising to us since the HM was attributed a more critical role in the peptide array experiment in Abrahamsen et al.[45]

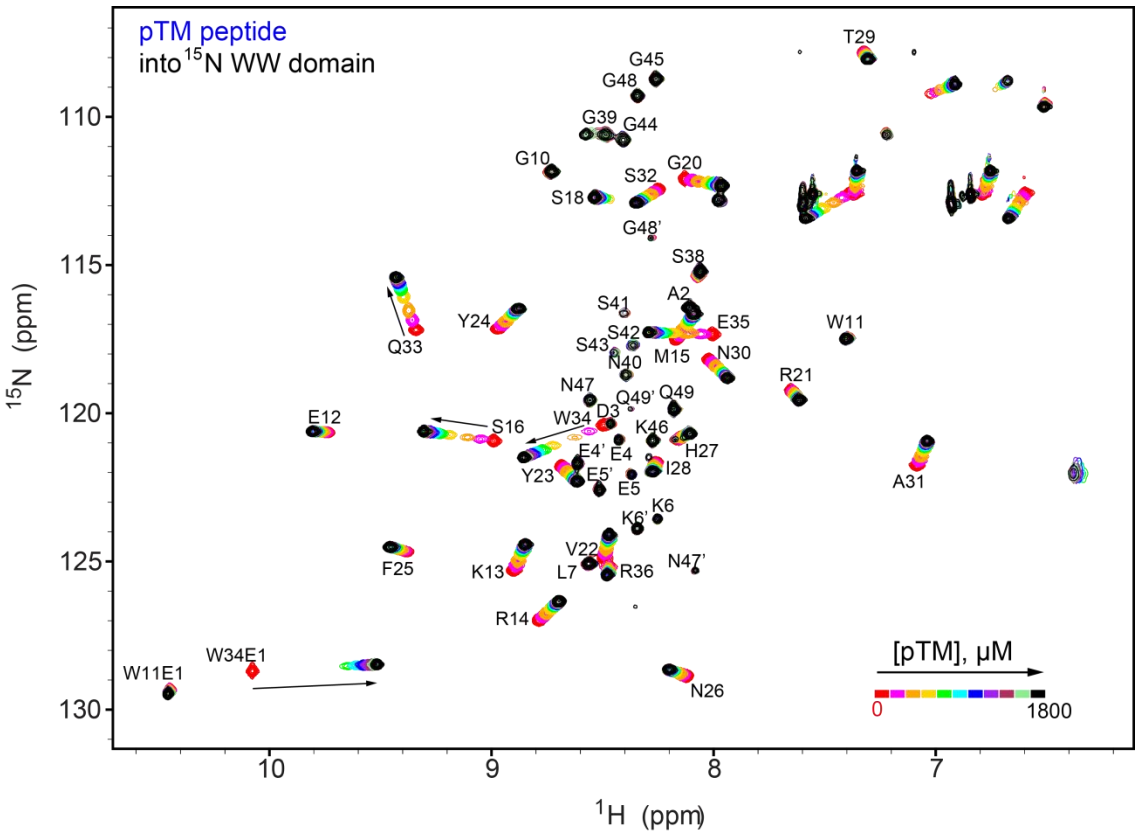

Figure 36. The pTM peptide interacts with isolated WW domain from Pin1 detected by NMR. [^{15}N-^{1}H] HSQC spectra of [U-^{15}N] isolated WW domain of Pin1 with increasing concentration of the pTM peptide are shown as an overlay. The color coding of each spectrum with increasing pTM peptide concentrations is indicated as insert in the bottom right corner.

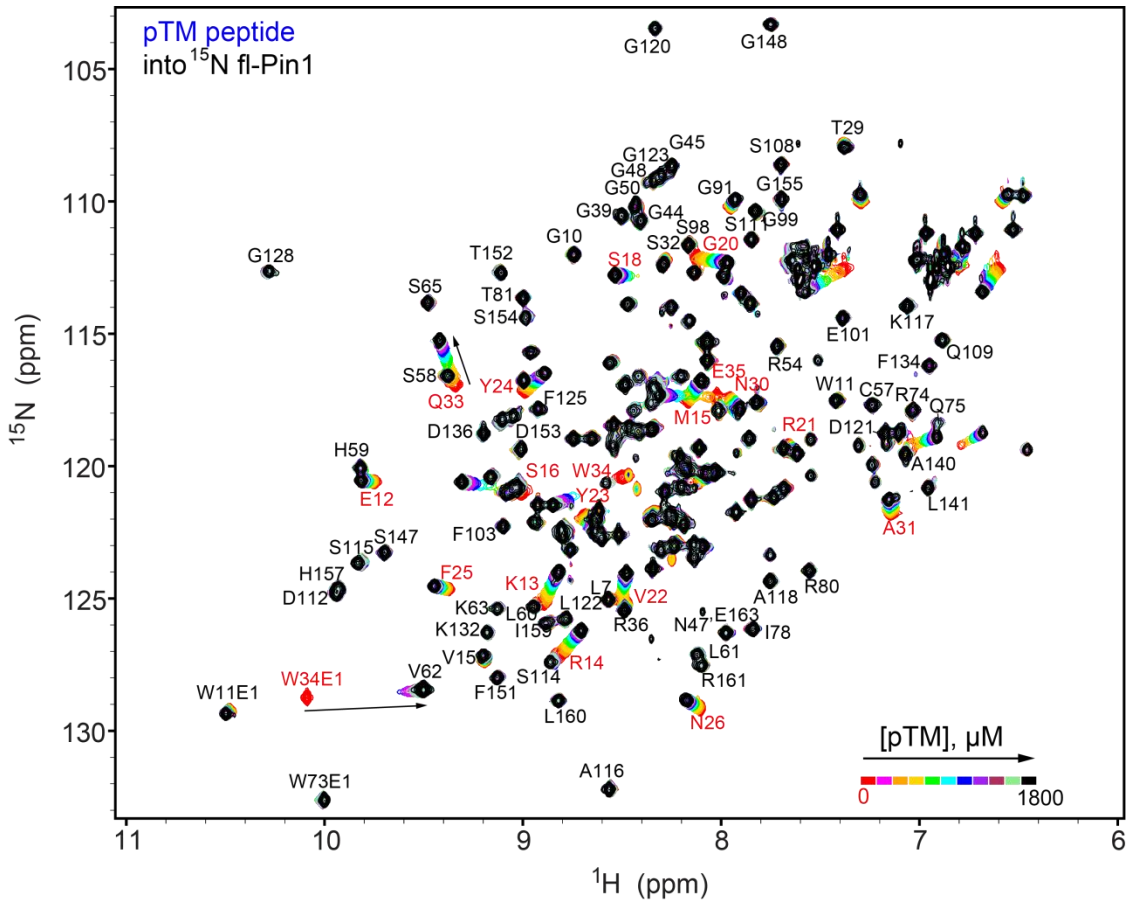

Figure 37. The pTM peptide interacts with full-length Pin1 detected by NMR. [^{15}N-^{1}H] HSQC spectra of [U-^{15}N] full-length Pin1 with increasing concentration of the pTM peptide are shown as an overlay. The color coding of each spectrum with increasing pTM peptide concentrations is indicated as insert in the bottom right corner.

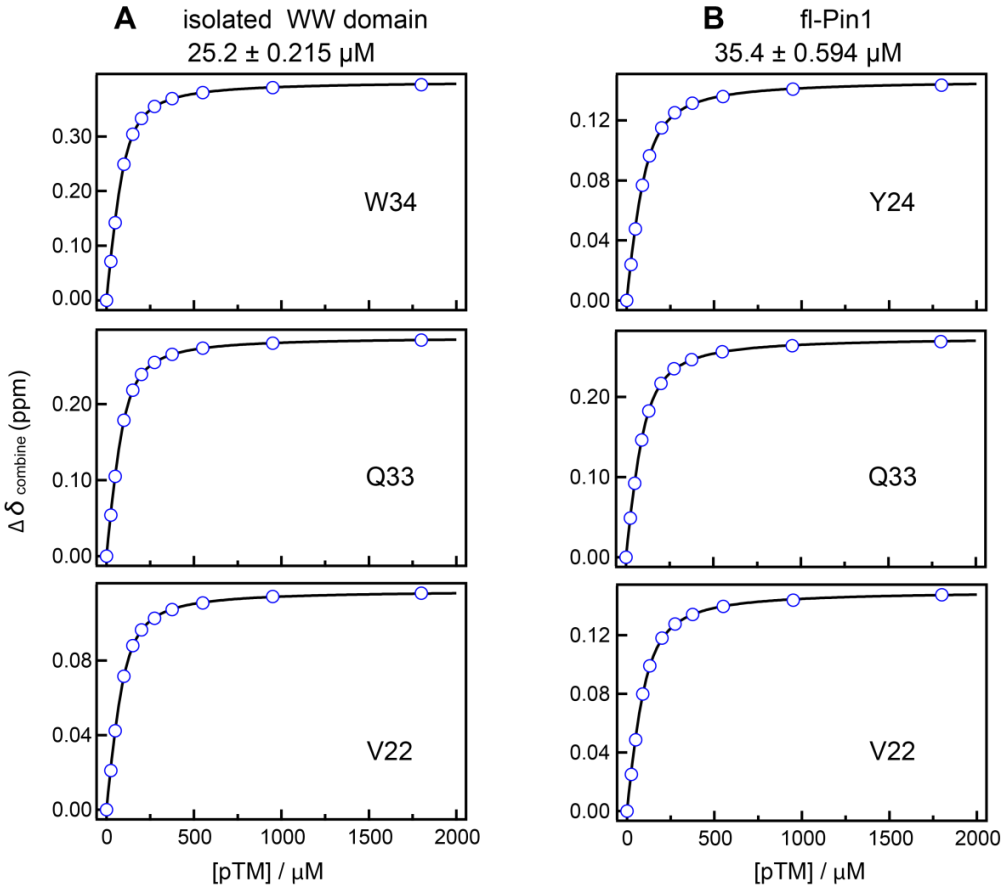

Figure 38. The pTM peptide interacts with the isolated WW domain and the WW domain residues of full-length Pin1 with similar affinity. Representative NMR-detected pTM binding curves are shown for the isolated WW domain experiment **(A)** and the WW domain residues of the full-length Pin1 experiment **(B)**. All solid lines are global fitting results.

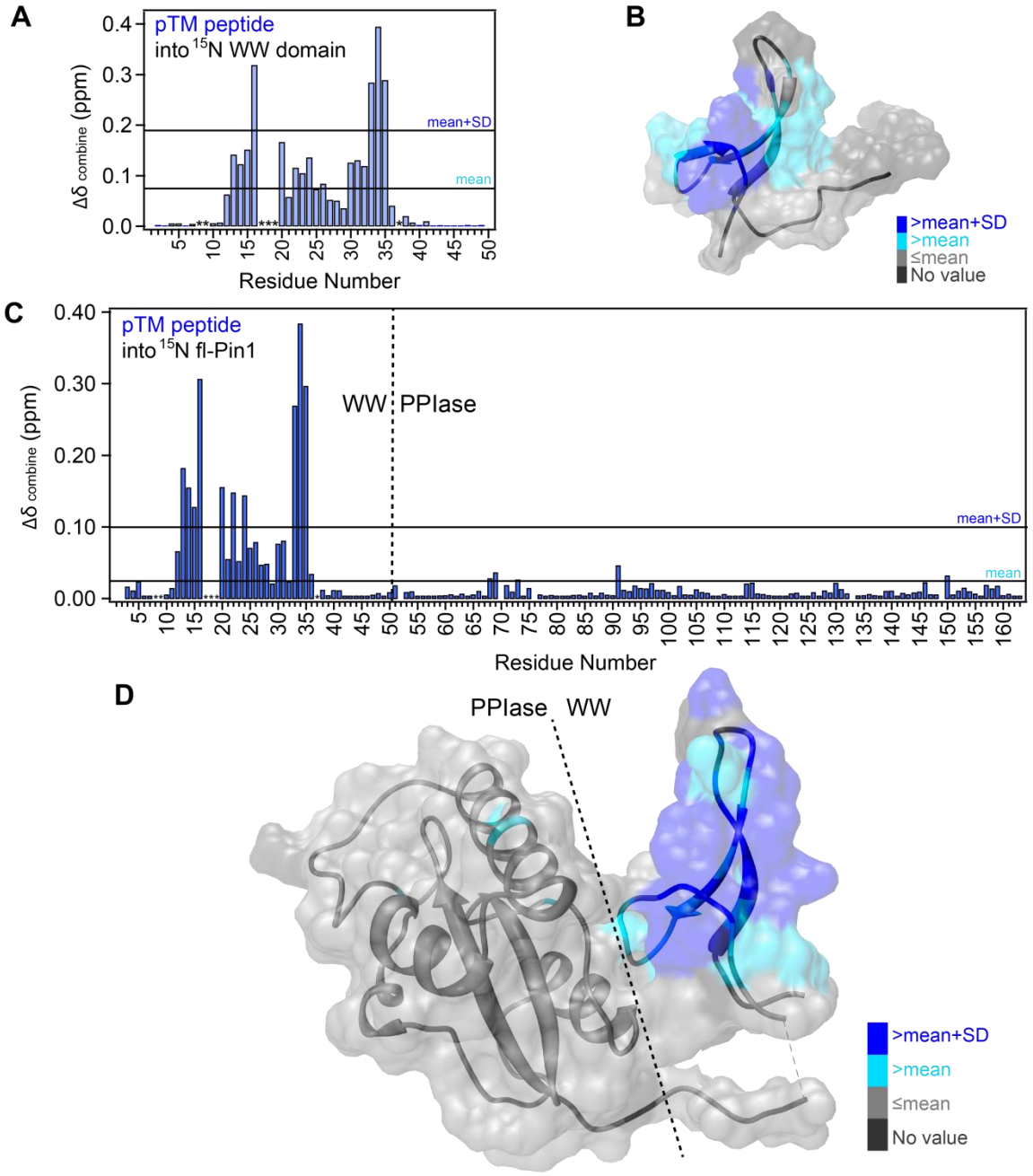

Figure 39. Chemical shift perturbation analysis of the pTM binding experiments. **(A)** Combined chemical shift perturbation (CSP) of the isolated WW domain with 18-fold molar excess of pTM peptide vs. no peptide is plotted against residue number. Residues with no CSP values are prolines, residues broadened beyond detection and residues that are not spectrally resolved. **(B)** The CSP values are mapped onto the isolated WW domain structure (PDB ID 2M8I)**.** (C) Combined CSP of the full-length Pin1 pTM-binding experiment and **(D)** mapped on the Pin1 structure (PDB ID 1PIN)**.**

We next performed binding experiments of pTM peptide to the full-length Pin1. Similar to the perturbation pattern of the isolated WW domain experiment, we observed pTM perturbing the WW domain residues within the full-length Pin1 protein (Figure 39). Both the resonance shifts and globally fitted K_d (35.4 ± 0.594 μM) were similar to those of the isolated WW domain experiment (compare Figure 36, Figure 37 and Figure 38). However, very little CSP was observed for the PPIase domain residues (Figure 39C). This result supports the previously proposed argument that p(Thr/Ser)-Pro-Pro motif could interact exclusively with the WW domain.[172] We cannot rule out the existence of any interaction between pTM and the PPIase domain with these data. The interaction could occur with a very low affinity or could cause minimal CSP.

In order to address if there is an interaction between the pTM peptide and the PPIase domain, we looked closely at the residues that responded slightly to the addition of peptide. Despite the small CSP values, we calculated mean and standard deviation of CSP for the PPIase domain residues in the binding experiment of the pTM peptide to full-length Pin1. For the residues perturbed above (mean + STD) within PPIase domain residues, we observed two types of response by inspecting the individual binding curves. Group 1 residues responded in concert with the WW domain residues to the pTM binding event, with individual K_d fitted to values close to the globally fitted K_d of 35.4 μM for WW domain residues. Group 2 residues have their binding curves displaying linear response within the range of the peptide concentrations we tested, potentially due to a much weaker binding affinity. The identities of the residues and individual K_d are shown in Table 10.

Interestingly, when looking at the two groups of residues on the crystal structure, we found that Group 1 residues are located at the domain interface of the crystal structure (Figure 40). Group 2 residues, on the contrary, map to the substrate binding pocket of PPIase domain (Figure 40). We think that Group 1 residues respond to the same pTM–WW binding event, potentially due to a change in domain interactions triggered by the WW domain associating with the pTM peptide. Group 2 residues likely represent a very weak binding site for pTM. We could not obtain the affinity of this group because of the limitations of the protein and peptide concentrations tested. We roughly estimate that the K_d of this weak binding event is larger than 3 mM.

Table 10. Two groups of PPIase residues in response to pTM binding to Pin1

Group	*Residue*	K_d / μM
1	E51	39.3 ± 4.28
	G91	32.0 ± 2.30
	Q94	35.3 ± 2.11
	K97	54.0 ± 4.79
	D102	40.9 ± 2.20
	M146	29.2 ± 3.37
	V150	42.5 ± 1.72
	H157	137 ± 68.0
	I159	25.0 ± 2.51
2	R68	>3000
	R69	
	S71	
	W73	
	S114	
	S115	
	M130	

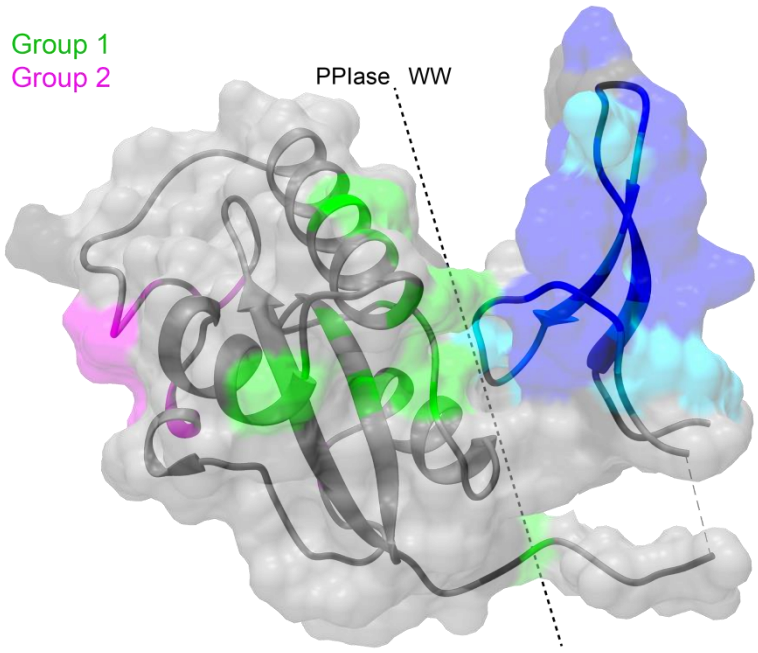

Figure 40. Two groups of PPIase residues responding to addition of pTM mapped on the crystal structure of Pin1. Group 1 and 2 residues are colored green and magenta, respectively. The WW domain residues are colored the same as in Figure 39D to represent the direct pTM–WW binding interface.

Turn motif is not an efficient catalytic substrate for Pin1 due to the consecutive prolines

For the previously known Pin1 catalytic substrates, the rate of *cis–trans* isomerization was significantly accelerated by Pin1 catalysis. With Pin1 catalysis, the exchange between *cis* and *trans* conformations of the substrate could be directly observed with NMR experiments including a mixing time for chemical exchange.[185] To test if the pTM is a catalytic substrate for the peptidyl-prolyl isomerase activity, we collected the NOESY spectrum of the isolated pTM peptide in the presence of Pin1 with a 500 ms mixing time. In the NOESY spectrum, we unambiguously observed and assigned (see Experimental procedures) all four conformations of the pT^{638}-P^{640}-P^{641} motif due to the two peptidyl-prolyl bonds, corresponding to *trans/trans*, *cis/trans*,

trans/cis and *cis/cis* conformations, respectively (Figure 41). The two *cis* and *trans* conformations of the Q^{634}-P^{635} site were also assigned (Figure 41). Under these conditions, we did not observe any detectable exchange cross-peak from any combinations of the four conformations from the pT^{638}-P^{640}-P^{641} motif (Figure 42). The absence of exchange cross-peak indicates a lack of catalysis or inefficient catalysis. This is in agreement with the proposed non-catalytic role for Pin1 targets with consecutive proline residues.

To our surprise, we detected weak but unambiguous exchange cross-peaks between the *trans* and the *cis* Q^{634}-P^{635} conformations in the presence of Pin1 (Figure 42). No exchange cross-peaks were observed in the absence of Pin1 under identical experimental conditions. Even though glutamine is not negatively charged, we think the non-specific catalysis herein is due to the similarity between the side-chains of glutamine and glutamate, which has been extensively used as a phosphorylation mimic for measuring Pin1 catalytic activity.[186] These data also demonstrated the existence of an interaction between the isolated pTM and the PPIase domain. The NOESY spectrum of the pTM peptide in the presence of the isolated PPIase domain is highly similar to that of the full-length Pin1, confirming that the non-specific catalysis towards the Q^{634}-P^{635} site is due to a direct weak pTM–PPIase domain interaction. This weak interaction is probably what we observed for the Group 2 residues with a K_d larger than 3 mM (Figure 40). Using ^{1}H-^{1}H EXSY experiments, we estimated the k_{EXSY} of Pin1 catalyzed Q^{634}-P^{635} isomerization to be 4.05 ± 0.143 s^{-1}. The fitting results are shown in Table 11. This

catalyzed exchange rate is slower than most other human Pin1 substrates ranging from 10–87 s^{-1} tested under similar concentrations.[170,183,187,188]

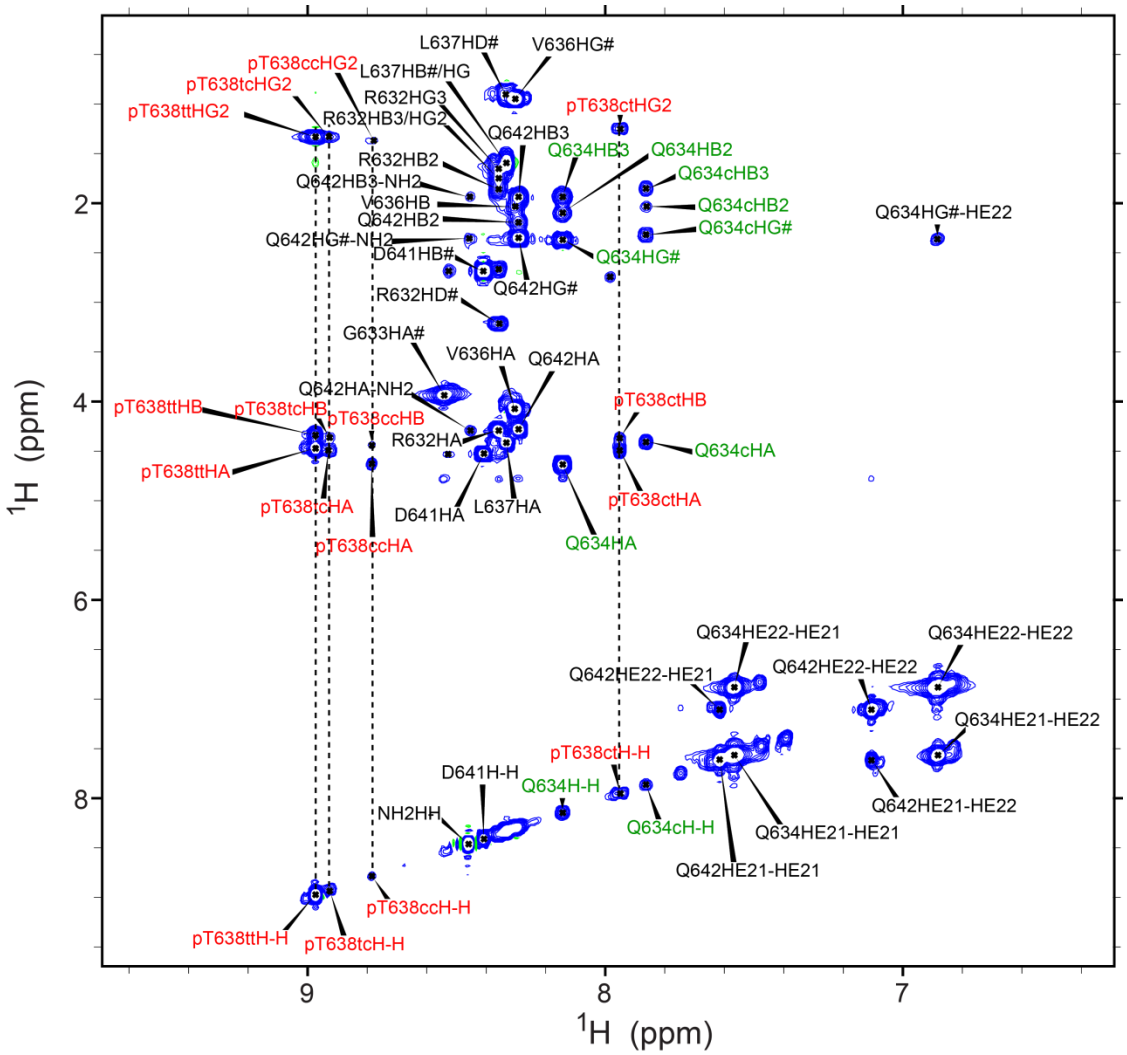

Figure 41. The amide region of TOCSY spectrum showing assignments of pTM peptide. The four conformations of the pT^{638}-P^{639}-P^{640} motif are highlighted with red fonts and dashed lines showing connections. The two Q^{634}-P^{635} conformations are highlighted with green fonts.

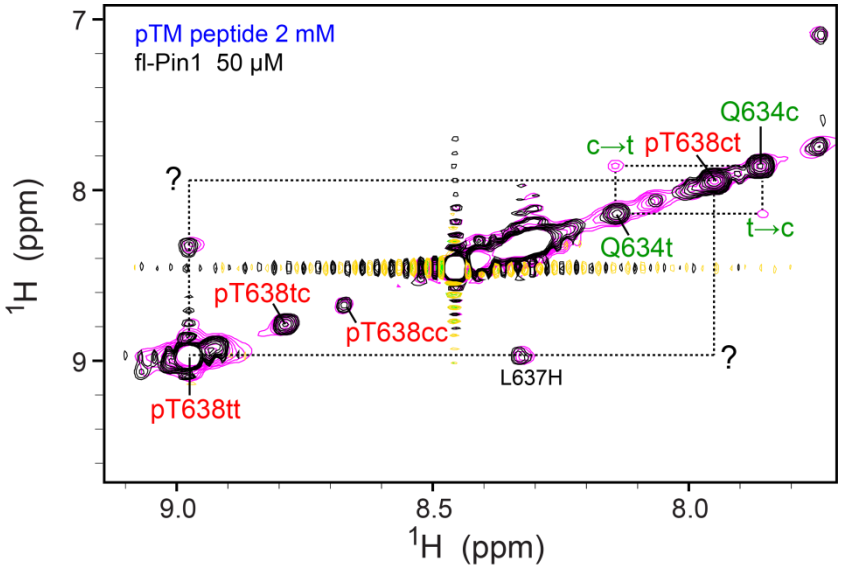

Figure 42. Expansion of NOESY spectrum showing exchange cross-peaks for the non-specific Q^{634}-P^{635} site on pTM peptide. The spectrum colored in magenta was collected with a sample containing the catalytic amount (50µM) of full-length Pin1 protein added to 2 mM pTM peptide. As a control, the spectrum in black was collected with a sample containing only 2mM pTM peptide. The four conformations of the pT^{638}-P^{639}-P^{640} motif are highlighted with red fonts. The two Q^{634}-P^{635} conformations are highlighted with green fonts. Cross-peak positions expected for chemical exchange are shown with dashed lines.

Table 11. Pin1-catalysed *cis* to *trans* (*k*ct) and *trans* to *cis* (*k*tc) isomerization rates of pTM peptide Q^{634}-P^{635} site

	+ Pin1 (s^{-1})		
	*k*ct	*k*tc	*k*EXSY
Itc/Icc	0.667 ±0.0153	3.38 ±0.142	4.05 ±0.143

In order to see if the proline residue at +1 position is the key to the inefficient catalysis observed, we tested a pTM-P640A peptide with an alanine substituting the +1

proline while keeping the rest of the pTM peptide identical. Exchange cross-peaks were exhibited between the *cis* and *trans* conformations of the pT^{638}-P^{639} bond of the pTM-P640A peptide under identical experimental conditions (Figure 43). The Q^{634}-P^{635} exchange cross-peaks originated from non-specific catalysis were still present for the pTM-P640A peptide. However, the intensity ratio of the pT^{638}-P^{639} bond exchange cross-peak versus diagonal I_{ct}/I_{cc} is 22-fold larger than that of Q^{634}-P^{635} exchange cross-peak, whereas the I_{tc}/I_{tt} is comparable for both. This indicates a much more efficient catalysis for the pT^{638}-P^{639} bond by Pin1 than the Q^{634}-P^{635} bond in the pTM-P640A peptide. Spectrum of the pTM-P640A peptide in the absence of Pin1 did not show any exchange cross-peak.

Pin1 interaction with pV5 reveals specific binding mode

After understanding how the isolated pTM and pHM interact with the two domains of Pin1, we went on and tested Pin1 interaction with a bisphosphorylated pV5 peptide covering the amino acid sequence from residue 632–660 of V5 domain with both pTM and pHM sites included. From the [^{15}N-^{1}H] HSQC spectral overlay with increasing concentrations of pV5 peptide (Figure 44), we observed distinct resonance shift patterns of the WW domain and PPIase domain residues within the full-length Pin1 protein. The WW domain residues shift upon interacting with pV5 with directions and amplitudes highly similar to the binding experiment with isolated pTM peptide (comparing Figure 37 with Figure 44). On the contrary, the directions and amplitudes of the PPIase domain residues shifts are similar to the binding experiment with isolated pHM peptide (comparing Figure 33 with Figure 44).

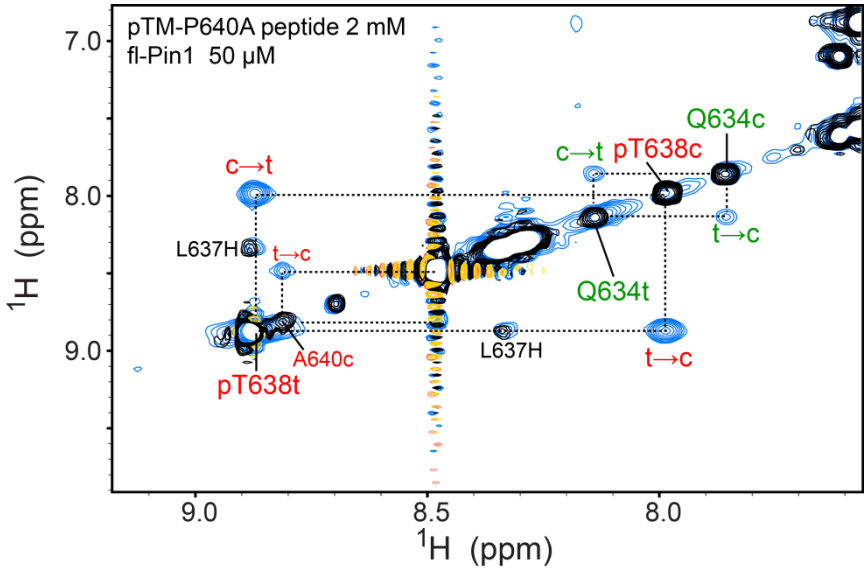

Figure 43. Expansion of NOESY spectrum showing exchange cross-peaks for both the pT^{638}-P^{640} and the non-specific Q^{634}-P^{635} site on pTM-P640A peptide. The blue spectrum was collected with a sample containing a catalytic amount (50µM) of full-length Pin1 protein added to 2 mM pTM-P640A peptide. As a control, the spectrum in black was collected with a sample containing only 2mM pTM-P640A peptide. The four conformations of the pT^{638}-P^{639}-P^{640} motif are highlighted with red fonts. Exchange peak for A^{640} is also shown in red fonts. The two Q^{634}-P^{635} conformations are highlighted with green fonts. Cross-peak positions expected for chemical exchanges are shown with dashed lines.

In addition, we calculated CSP of Pin1 residues upon interacting with the pV5 peptide as shown in Figure 44A. The CSP plot pattern matches well when comparing to an overlay of the CSP plots from isolated pTM and pHM experiments (Figure 44B). From these data, we concluded that the interaction between full-length Pin1 and the pV5 peptide is comprised of two unambiguous sub-interactions: pTM interacting with WW domain and pHM interacting with PPIase domain.

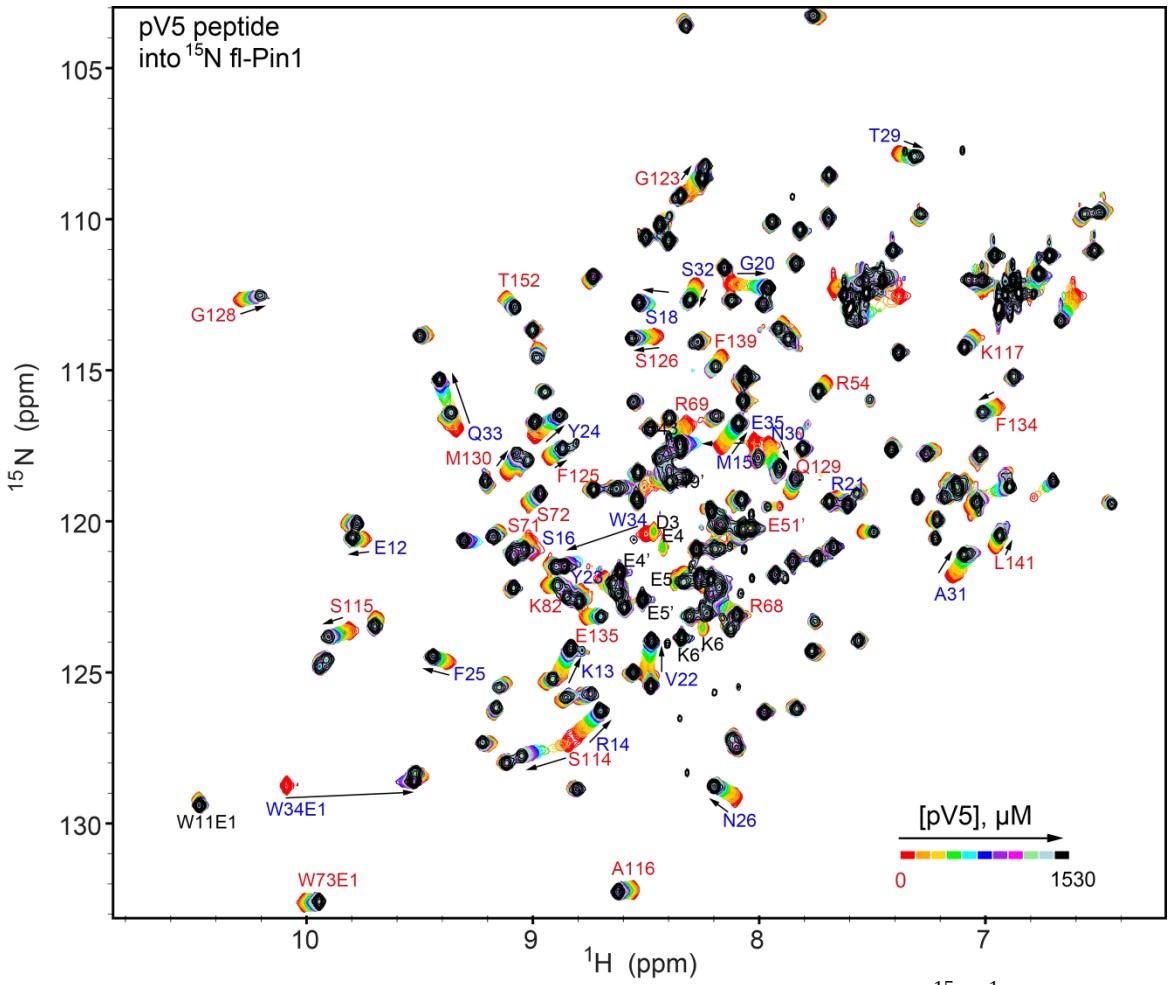

Figure 44. The pV5 peptide interacts with full-length Pin1 detected by NMR. [^{15}N-^{1}H] HSQC spectra overlay of [U-^{15}N] full-length Pin1 with an increasing pV5 concentration. The color coded legend shows the increasing concentrations. Residues are labeled blue and red corresponding to pTM–WW and pHM–PPIase sub-interactions, respectively.

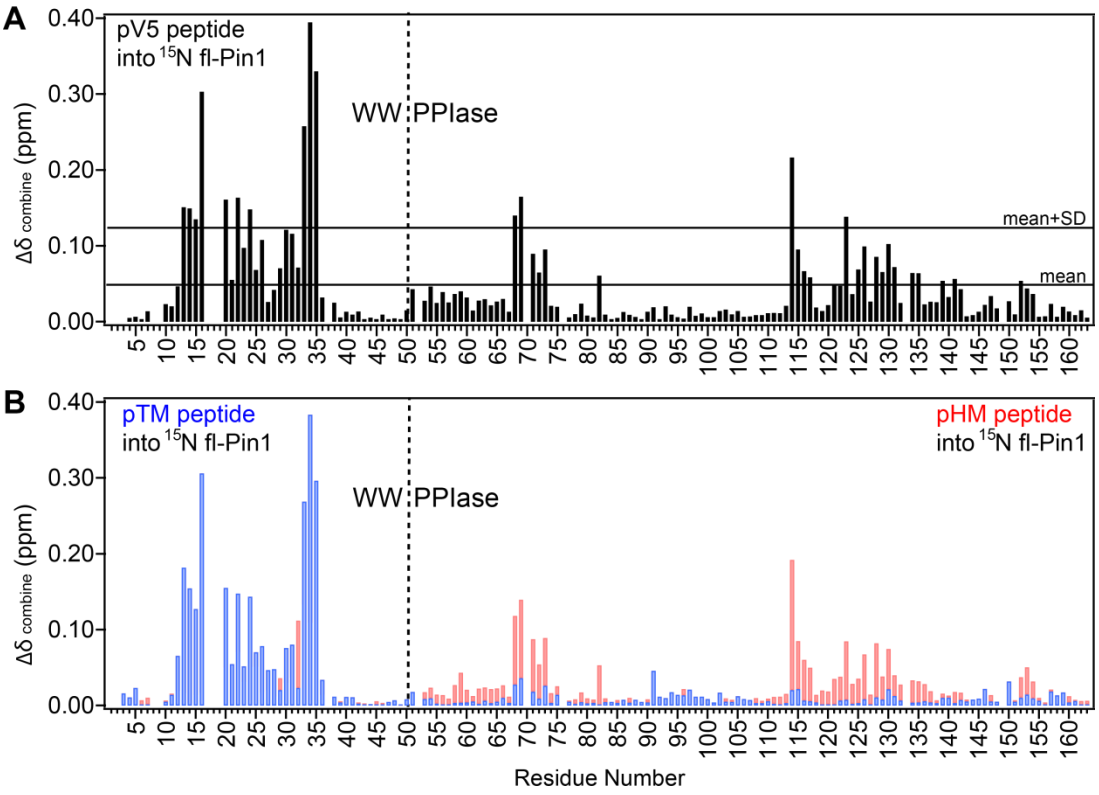

Figure 45. Chemical shift perturbations reveal specific binding mode between full-length Pin1 and the pV5 peptide. **(A**) Combined chemical shift perturbations (CSP) of full-length Pin1with 17-fold molar excess of pV5 peptide vs. no peptide are plotted against residue number. **(B)** Overlay of CSP from the full-length Pin1 binding experiments with isolated pTM peptide (blue) and pHM peptide (red). CSP values are the same as in Figure 39C and Figure 35C, respectively.

Most of the Pin1 resonances responding to pV5 interaction still displayed fast behavior on the NMR exchange timescale, with a few WW domain resonances exhibiting fast-to-intermediate exchange. The only exceptions are that both the Trp34 backbone N-H and side-chain Nε1-Hε1 resonances showed slow exchange behavior, which was the same in isolated pTM experiments. Thus, we could extract accurate

dissociation constants K_d by fitting the binding curves for fast-exchanging WW domain and PPIase domain residues in the two groups, respectively (Figure 46).

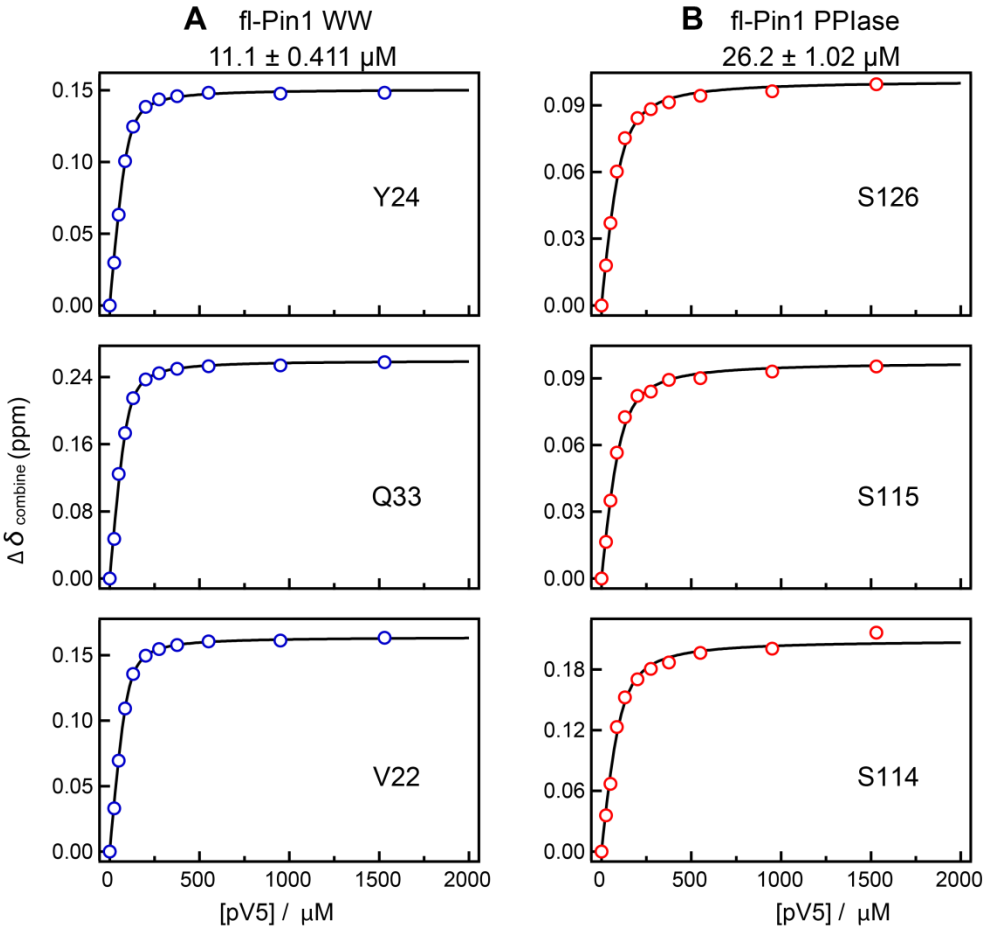

Figure 46. The pV5 peptide interacts with full-length Pin1 with avidity from the two binding sites. Representative NMR-detected pV5 binding curves are shown for full-length Pin1 experiment with **(A)** the WW domain residues and **(B)** the PPIase domain residues. All solid lines are global fitting results.

Table 12. Dissociation constants extracted from NMR binding experiments

Constructs	K_d / μM	
	WW residues	PPIase residues
pTM + WW	25.2 ± 0.215	
pTM + Pin1	35.4 ± 0.594	>3000
pHM + WW	1006 ± 9.33	
pHM + Pin1	893 ± 13.7	772 ± 7.33
pV5 + Pin1	11.1 ± 0.411	26.0 ± 1.02

The globally fitted K_d for WW domain residues interacting with the pV5 peptide was 11.1 ± 0.411 μM, which was a 3-fold decrease from the isolated pTM peptide experiment (35.4 ± 0.594 μM). The globally fitted Kd for PPIase domain residues interacting with the pV5 peptide was 26.0 ± 1.02 μM, which was a strikingly 30-fold decrease from the isolated pHM peptide experiment (772 ± 7.33 μM). All measured dissociation constants are listed in Table 12.

Pin1 interaction with pV5 diminishes the weak interaction of PPIase domain with pTM

With the highly specific interaction mode between full-length Pin1 and the pV5 peptide (*vide supra*), we asked if the weak interaction accompanied by the non-specific catalysis towards the Q^{634}-P^{635} site observed with the isolated pTM peptide would also exist for the pV5 peptide. It order to test this, we first collected full set of 2D experiments (see Experimental procedures) and assigned the pV5 peptide resonances by comparing them to three sets of prior assignments: isolated pTM assignments, isolated pHM10 assignments (Chapter III) and dmV5α assignments (Chapter II). In the NOESY spectrum of the pV5 peptide in the presence of Pin1, we did not observe any exchange

cross-peak from either the pT^{638}-P^{639}-P^{640} motif or the Q^{634}-P^{635} site (Figure 47). The weak interaction between the PPIase domain and the pTM site seemed to be diminished in the Pin1–pV5 complex. We attribute this phenomenon to the PPIase–pHM interaction enhanced through the avidity effect in the Pin1–pV5 complex. As a result, the PPIase substrate binding pocket is probably occupied by the pHM site, preventing the pTM site from another molecule of pV5 peptide to access the PPIase domain.

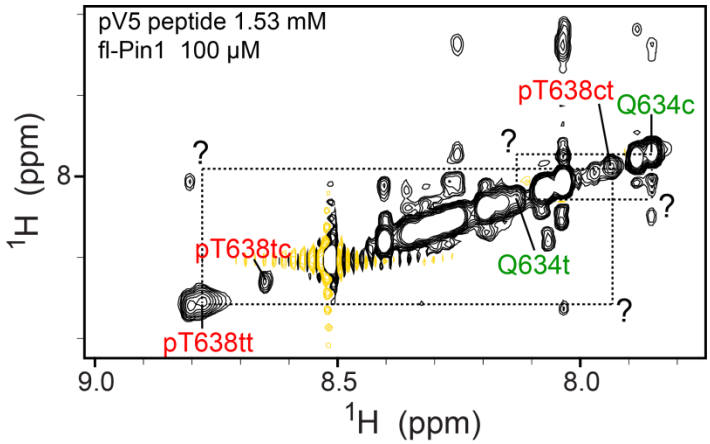

Figure 47. Expansion of NOESY spectrum showing no detectable exchange cross-peaks with pV5 peptide in the presence of full-length Pin1. The spectrum was collected with a sample containing catalytic amount (100µM) of full-length Pin1 protein added to 1.53 mM pV5 peptide. The three observed conformations of the pT^{638}-P^{639}-P^{640} motif are highlighted with red fonts. The two Q^{634}-P^{635} conformations are highlighted with green fonts. Cross-peak positions expected for chemical exchange are shown with dashed lines.

Discussion of results

Peptidyl-prolyl isomerase Pin1 is a unique member of the PPIase family, due to the fact that it adds another layer of regulation on top of a kinase signaling cascade by recognizing pS/T-P motifs. Our results indicate that Pin1 interacts directly with both

conserved phosphorylation motifs of the V5 domain from PKCα, supporting the previously suggested interaction between Pin1 and PKCα in the proteasome-dependent down-regulation process.[45] We demonstrate that the non-canonical pHM site interacts with both domains of Pin1, and binds specifically to the PPIase domain when the pTM site is also present on the same polypeptide chain. Here, we summarize and discuss our results of the Pin1–V5 interaction with highlights on the non-catalytic nature and avidity effect.

WW domain selectivity towards the pTM motif with consecutive prolines

Previous studies suggested that the pS/T-P-P Pin1 targets with consecutive prolines might interact exclusively with the WW domain,[173,174] and function in a PPIase-independent manner.[172,175,176] Several roles have been proposed for this type of potential WW domain specific sites. One proposition states that the pS/T-P-P site can function together with another pS/T-P site as a multivalent binder, such that the overall binding affinity is enhanced by the WW domain bound to the pS/T-P-P site, whereas the PPIase domain can target the pS/T-P with high specificity.[172] This could increase the efficiency of binding by preventing the simultaneous binding of WW and PPIase domains to the same site, since the PPIase domain cannot bind to the pS/T-P-P site. Since pS/T-P-P sites appear to be more prevalent in the cytosolic Pin1 targets, the other suggested role is that they could function as a reservoir (i.e., a buffer) for cytosolic Pin1 before entering the nucleus.[172] However, it was difficult to test these theories further due to limited examples of Pin1 targets containing these sites in conjunction with another binding site

and sparse knowledge regarding detailed binding measurements or molecular mechanisms.

Here in this chapter, we contribute a detailed analysis of a potential bivalent Pin1 target containing a pS/T-P-P site with consecutive prolines: the pTM site from PKCα. Chemical shift perturbation analysis of the isolated pTM binding experiment with isolated WW domain and full-length Pin1 illustrated a strong preference for pTM to interact with the WW domain over the PPIase domain. However, small but non-negligible chemical shift changes together with the non-specific catalysis towards the Q^{634}-P^{635} site in the presence of both Pin1 and isolated PPIase domain showed a weak direct interaction between pTM and the PPIase domain. The non-specific catalysis is diminished when both pTM and pHM sites are present on the same polypeptide chain in the pV5 binding experiments, supporting the role of the pS/T-P-P site in ensuring WW domain specific interaction in a multivalent system.

Under our experimental conditions, we did not observe any exchange peak for the pT^{638}-P^{639}-P^{640} (pTM) site in the presence of full-length Pin1 or isolated PPIase domain by NMR EXSY experiments. These data indicate that the pTM site is not an efficient catalytic substrate for the isomerase activity of Pin1. This is supported by a recent NMR study of Pin1–Tau interaction regarding to a pT^{231}-P-P-K-pS^{235}-P site of Tau.[188] They observed catalysis only for the pS^{235}-P bond, but not the pT^{231}-P-P bond. This could potentially be explained by a preferred binding geometry to place the pS^{235}-P site at the catalytic pocket, but herein for the pTM sequence, the Q^{634}-P^{635} site is N-terminal to the pT^{638}-P^{639}-P^{640} site instead of C-terminal like the Tau site. We attribute

the weak pTM-PPIase interaction observed here to the lack of an amide proton of the Pro640 residue, which prevents formation of an intramolecular hydrogen bond with the carbonyl oxygen of the pT638 residue. The formation of this intramolecular hydrogen bond has been suggested to help stabilize the β-turn conformation as observed in the crystal structure of Pin1 bound to a peptide inhibitor.[177] The lack of an efficient catalysis at the pTM site, on the other hand, could also be attributed to the lack of an amide proton of the P640 residue in the context of the twisted amide catalytic mechanism suggested for Pin1.[171] The formation of a five-member ring including the amide proton of the +1 residue was proposed in this mechanism, supported by another Pin1 crystal structure bound to a reduced amide and kinetic isotope effect measurements. Our hypothesis is supported by the efficient catalysis of the pT^{638}-P^{639} bond in the pTM-P640A peptide with a single alanine substitution of the +1 proline residue.

Potential interdomain communication upon pTM binding

We observed in the isolated pTM binding experiment with a full-length Pin1 that a subset of PPIase domain residues localizes on the domain interface in the Pin1 crystal structure in response to pTM–WW binding event (Figure 40). The binding curves of these residues fit to roughly the same K_d as pTM–WW binding residues (Table 10), but the scale of their chemical shift perturbations are much smaller than the pTM–WW binding residues (Figure 39). This indicates that a direct binding to these residues is unlikely. We speculate that these residues respond indirectly to the pTM–WW binding,

through a potential interdomain communication network reflecting a change in interdomain orientations or domain interactions.

Recent studies pointed out a potential negative allosteric regulation by interdomain contact in Pin1.[170] One central piece of evidence was the I28A mutation on the WW domain, which is located at the domain interface of the Pin1 crystal structure (PDB ID 1PIN). This mutant enhanced the isomerase activity towards the pCdc25C substrate when compared to wild-type Pin1.[189] Our data here support a change on the domain interface indirectly through the binding of WW domain to a WW-specific substrate pS/T-P-P site. The Group 1 residues we observed here (Figure 40) are not in direct contact with I28 in the crystal structure, but V150, M146 and E51 residues in this group are in the vicinity of I28. K97 in this group is also located on the domain interface of the crystal structure. We did not observe chemical shift changes in the Helix-4 region of PPIase domain, which was observed to be perturbed by the I28A mutation.[170] This underlies a potential substrate-dependence on the interdomain communication.

It is difficult to comment on the interdomain communication in the case of pV5 binding, since the large chemical shift perturbations that occur upon direct binding of the pHM site to the PPIase domain could have masked the changes due to interdomain communication. However, a noticeable change between the pTM induced CSP pattern and the pV5 induced CSP pattern was observed for residue G91, which was perturbed significantly in the pTM experiment but not perturbed in the pV5 experiment (Figure 45). Further characterization of the pTM and pV5 in complex with Pin1 will help to clarify the differences in interdomain communication.

Avidity from bivalent binding

Since multiple binding sites were shown to co-exist on the same Pin1 target proteins, in principle, they could enhance the interaction with Pin1 through avidity.[190] Daum et al. suggested an optimal cooperativity at a five-proline linker length for designed bivalent Pin1 binders.[191] To our knowledge there is only one characterization available regarding a bivalent Pin1 substrate with a large linker distance, which is comprised of 16 amino acids between the two phosphorylation sites.[174] In that study, a mild cooperativity was observed in the bivalent $pT^{212}/pS^{214}/pT^{231}$ Tau peptide. This chapter presents a detailed analysis of a bivalent Pin1 substrate from the V5 domain of PKCα with 18 amino acids between the two phosphorylation sites. Under the conditions tested, we found the binding affinities were clearly enhanced by bivalency 3- and 30-fold for the pTM–WW binding and pHM–PPIase binding, respectively. The 3-fold increase of pTM–WW binding affinity is similar to what was observed with the increase of the WW domain binding affinity in Smet et al. (2.3–5.4 fold), whereas the 30-fold increase of pHM–PPIase binding affinity is much more significant than the 4-fold increase observed in Smet et al.[174] We conclude that the avidity effect of pTM and pHM sites from PKCα is quite drastic, given the large linker distance between the two sites. A cause for this drastic avidity is yet to be determined.

Non-catalytic function of Pin1 during down-regulation of conventional PKCs

Using NMR experiments, we only observed a non-specific catalysis of the Q^{634}-P^{635} site when full-length Pin1 or isolated PPIase domain was added to the isolated pTM

peptide. This non-specific catalysis is diminished when pV5 peptide is used, where the pHM site is present on the same polypeptide chain as pTM. From these, we infer that Pin1 functions in a non-catalytic manner during the dephosphorylation/ubiquitination dependent down-regulation process of PKCα. The PKCα–Pin1 interaction is potentially the strongest when both pTM and pHM sites are exposed, which is likely the case for fully activated, membrane-associated PKCα (Chapter III). When only one of the two sites is exposed, Pin1 could still potentially interact weakly with V5. The structures of inactive, cytosolic and fully activated, membrane-associated forms of PKCα are still largely unknown. But based on the potential role of a pHM site in stabilizing the N-lobe of the kinase domain, which is conserved throughout AGC kinases,[192] the PKCα–Pin1 complex could have a drastically decreased kinase activity since the pHM site is associated with the PPIase domain of Pin1. This could potentially function as an acute shut-down of kinase activity as a first step of down-regulation.

Our proposed model for PKCα might also be true for PKCβII and γ, since these isoenzymes both have consecutive prolines following the phosphorylated threonine residue like PKCα. PKCβI, however, has a pT^{642}-P-T sequence for its turn motif. It is difficult to make further inferences since only PKCα and PKCβII were tested to be regulated by Pin1 in Abrahamsen et al.[45] Further binding characterization of pTM from PKCβI as well as biological investigations of βI and γ down regulations are required to clarify this.

CHAPTER V

DISCREPANCIES OF FUNCTION AND THE TERMINAL REGION OF C2 DOMAIN IN CD(II) AND CA(II) INTERACTIONS*

Background

Ca^{2+} is the physiological signaling messenger for the activation of conventional PKCs, through interactions with C2 domain. As discussed in Chapter III, C2 domain is a conditional peripheral membrane protein (CPMP) domain that undergoes membrane association in a Ca^{2+}-dependent manner, with specificity towards negatively charged phospholipids, such as phosphatidylserine (PtdSer). Although Ca^{2+} functions through changing the structure in various other calcium binding proteins (CBPs) [193-195], the crystal structures of apo and Ca^{2+} bound C2 domain from PKCα reveal minimal structural changes upon Ca^{2+} association (Figure 48A). This has prompted us to consider alternative mechanisms of Ca^{2+} binding in triggering C2-membrane association from conventional PKCs. In this chapter, we seek to understand the detailed molecular mechanism pertaining to the metal-dependent membrane association of C2 domain with a collection of NMR probes.

Previously there were two views on the role of Ca^{2+}-mediating protein-membrane interactions. One view is that Ca^{2+} increases the electrostatic potential of the membrane-

---

* Portions of this chapter have been reproduced with permission from: Krystal A. Morales, Yuan Yang, Zheng Long, Pingwei Li, Alexander B. Taylor, P. John Hart, and Tatyana I. Igumenova. Cd2+ as a Ca2+ surrogate in protein-membrane interactions: isostructural but not isofunctional. *Journal of the American Chemical Society* 2013, 135 (35), 12980-12983.

binding regions of the protein, and acts as a nonspecific "electrostatic switch" which favors the negatively charged phospholipid surface. The other view is that Ca^{2+} specifically recognizes PtdSer headgroup through the formation of coordination bonds with the carboxyl and/or phosphoryl oxygens.

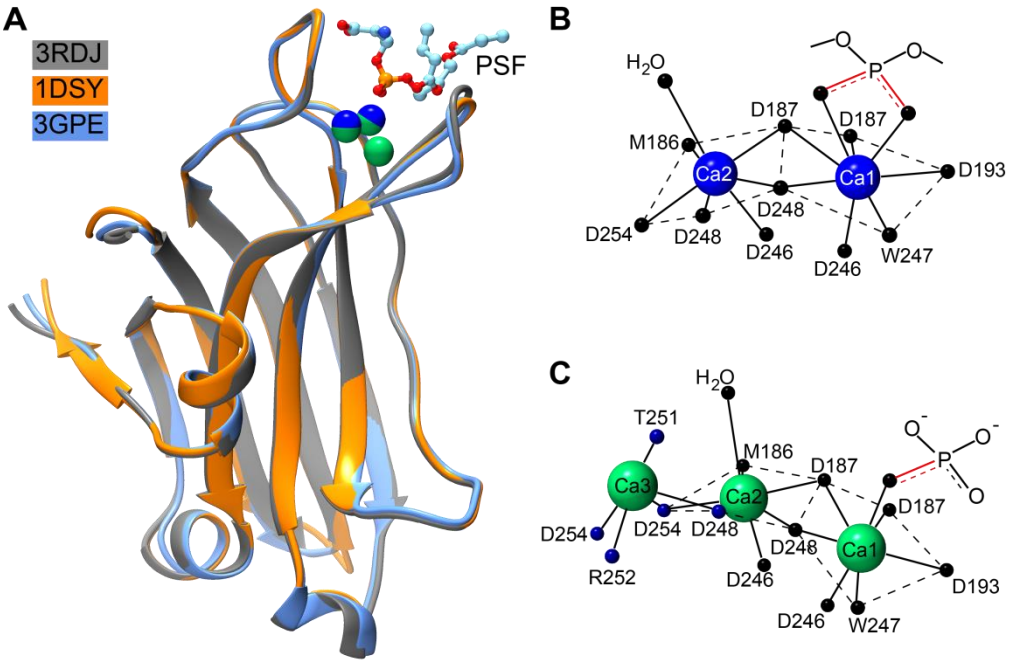

Figure 48. C2 domain from PKCα has minimal structural change upon binding Ca^{2+} and can bind two or three Ca^{2+} ions. (A) Overlay of three crystal structures of isolated C2 domain from PKCα, where PDB ID 3RDJ corresponds to apo C2 (gray), 1DSY is C2 associated with two Ca^{2+} ions and PSF molecule (orange), and 3GPE is C2 associated with three Ca^{2+} ions (blue). The PSF molecule is colored light blue with the oxygen and phosphorus atoms highlighted. **(B)** The coordination geometry of two Ca^{2+} ions from PDB ID 1DSY. All coordinating atoms are oxygens. **(C)** The coordination geometry of three Ca^{2+} ions from PDB ID 3GPE. Atoms that coordinate the third Ca^{2+} are colored blue.

The latter mechanism implies that the coordination sphere of protein-bound Ca^{2+} is dynamic: the labile water molecules coordinated by protein-bound Ca^{2+} are replaced by the lipid headgroup upon membrane association.

To test the above two mechanisms, we started out by selecting Cd^{2+} as a Ca^{2+} surrogate, due to the similarity in ionic radii (Ca^{2+} = 0.99 Å, Cd^{2+} = 0.97 Å) and the favorable NMR spectroscopic property for $^{113}Cd^{2+}$ (Spin I = 1/2). In this chapter, we compared the interactions of C2α with Ca^{2+} and Cd^{2+} with respect to the (i) structure, (ii) metal coordination geometry, (iii) affinity, (iv) metal-dependent membrane interaction, and (v) terminal region responses. We found unexpectedly that despite high affinity of Cd^{2+} to C2α and the similar coordination geometry of protein-bound Cd^{2+} and Ca^{2+}, Cd^{2+} is unable to support the membrane association of the protein domain. This is in sharp contrast with Pb^{2+}studied previously in our lab[72], which has different coordination geometry than Ca^{2+}, yet drives the C2α-membrane binding almost as well as Ca^{2+}.

From the perspective of the full-length enzymes of conventional PKCs, it is shown that a large conformational change occurs upon Ca^{2+} signaling.[69,196,197] During this conformational change, one[198] or two[155,156] C1 domains synergizes the membrane association together with C2 domain. Ca^{2+} binding to C2 is proposed to be in the first step for activation[33,69], and Ca^{2+}-dependent C2-membrane interaction is proposed to disrupt the intramolecular interactions between the C1 and C2 domains.[66] Since the structure of C2α remains identical between apo and Ca^{2+} bound states, it is thus through alternative mechanisms for C2 to propagate the signaling event to other domains. One potential mechanism is the changes in the conformational dynamics of C2 domain upon

Ca^{2+} binding. Conformational dynamics of proteins has been implicated to involve in a broad range of ligand binding events and enzymatic kinetics.[199,200] However, our knowledge about PKC regulation is still largely focused on the global structural change, with very little understanding on the local conformational dynamics of individual domains. We think it is possible that the ligand binding events are correlated to the global structural change through fine-tunings of local dynamics.

In order to answer this question, an important detail regarding C2 function is the stoichiometry of Ca^{2+} ions bound per protein molecule during a signaling event.[201,202] In the available crystal structures of C2 domain from PKCα and PKCβII, each C2 molecule was able to bind two or three equivalents of Ca^{2+} ions. The first two Ca^{2+} sites have more complete coordination geometry with six protein ligands coordinating each Ca^{2+}, comparing to the third Ca^{2+} site having five protein ligands (Figure 48B, C). We have previously shown that the first two Ca^{2+} ions bind C2 with equivalent affinities, whereas the third Ca^{2+} bind C2 with a much lower affinity.[72] Despite the apparent weak affinity for the isolated C2 domain, it was previously implicated that the third Ca^{2+} binding site can be differentially occupied in the protein-membrane complex for C2 domains from conventional PKCs.[203] The existence of a high affinity event at the membrane illustrated by isolated C2 domain indicated a potential role of the third Ca^{2+} site.[202] It is not clear yet as to a detailed understanding regarding to the effect of the third Ca^{2+} site on C2 domain. In this work, we characterized the μs-ms dynamics of isolated C2 domain as a function of Ca^{2+} with an emphasis on the third Ca^{2+} binding event. A R159G mutant which was shown in the lab to alter the exchange processes of isolated C2 was also used

as a comparison. The information acquired here together with our previous work supported a mechanism by which the third Ca^{2+} binding directly affects the conformational dynamics of the N- and C-termini regions of C2 domain. This could further assist in the destabilization of the closed kinase conformation at plasma membrane during the final stages of cPKC activation.

Experimental procedures

Materials

1-palmitoyl-2-oleoyl-sn-glycero-3-phosphocholine (POPC), 1-palmitoyl-2-oleoyl-sn-glycero-3- phospho-L-serine (POPS) were obtained from Avanti Polar Lipids (Alabaster, AL).

Sample preparation

Natural abundance, uniformly ^{15}N-enriched, uniformly $^{2}H^{13}C^{15}N$-enriched ([U-^{13}C, ^{15}N] and ~70% ^{2}H incorporation) and uniformly $^{2}H^{15}N$-enriched ([U-^{15}N] and ~70% ^{2}H incorporation) C2 domain (residues 155-293 of Protein Kinase Cα from *R. norvegicus*) was over-expressed and purified to homogeneity as previously described.[72] The R159G mutant of C2α was generated previously in the lab from wild type (WT) C2α using QuickChange™ site-directed mutagenesis. The expression and purification processes were identical to that of WT C2α. All buffers used in this study were treated with Chelex 100 resin (Sigma-Aldrich) to remove residual divalent metal ions.

NMR spectroscopy

For Cd^{2+} binding to C2α detected by NMR spectroscopy, The protein solution was prepared at the concentration of 110 μM in NMR buffer containing 10 mM 2-(N-morpholino) ethanesulfonic acid (MES) at pH = 6.0, 8% D_2O, and 0.02% NaN_3. The stock solutions of Cd(II) nitrate were prepared in the same buffer. Aliquots of Cd(II) nitrate stock solution were added stepwise to the uniformly ^{15}N-enriched C2α. The Cd^{2+}-binding and assignment experiments were conducted on a Varian Inova spectrometer operating at the Larmor ^1H frequencies of 500 and 600 MHz, respectively. The temperature in the NMR experiments was maintained at 25 °C. The resonances of Cd^{2+}-complexed C2α were assigned using: (i) 3D HNCACB experiment with ^2H decoupling[93,204] that was carried out on fractionally deuterated, [U-^{13}C,^{15}N] enriched C2α in the presence of 15-fold molar excess of Cd^{2+}, (ii) the titration behavior of the individual cross-peaks, and (iii) the previously obtained assignments of apo C2α.[72]

For the chemical shift perturbation (CSP) analysis, the overall change in chemical shift Δ was calculated between a pair of protein states as:[96]

$$\Delta = \sqrt{(\Delta\delta_H)^2 + (0.152 \times \Delta\delta_N)^2} \qquad \textbf{5.1}$$

where $\Delta\delta_H$ and $\Delta\delta_N$ are the differences between the ^1H_N and ^{15}N chemical shifts of the two states being compared.

For R_2-HE relaxation experiments[205,206] and R159G mutant HSQCs, uniformly $^2H^{15}N$-enriched C2α samples of 0.35mM and 0.16mM concentration were prepared, respectively. NMR experiments were carried out at 25 ℃ on Bruker AvanceIII spectrometer operating at a ^1H Larmor frequency of 600MHz (14.1T) equipped with

cryogenic probe. Temperature was calibrated using d4-methanol. The R_2^{HE} values were extracted by fitting to the following equation:

$$I_T = I_0 \exp(-R_2^{HE} T) \qquad \textbf{5.2}$$

where I_T and I_0 are peak heights with or without the delay T, which was 48.27ms. The errors are sample standard deviation from four repeating measurements. For Arg-HSQC one experiment was carried out at 10 ℃, with temperature calibrated with d4-methanol.

Fluorescence spectroscopy

Cd^{2+} binding to C2α was monitored using intrinsic tryptophan fluorescence of C2α. The experiments were conducted at 25°C using an ISS Phoenix spectrofluorometer. The excitation and emission slit widths were set to 4 and 8 nm, respectively. The fluorescence emission spectra were obtained in the range from 310 to 530 nm, with the excitation wavelength of 295 nm. 10 mm quartz cuvettes were coated with Sigmacote (Sigma-Aldrich) to decrease the protein adsorption on cuvette walls.

Concentrated stock solutions of Cd(II) nitrate were prepared in HPLC-grade water and titrated into the sample cuvette containing 0.5 μM C2α in 20 mM HEPES (pH 7.4) and 100 mM KCl. Prior to the start of the experiments, the buffer was treated with Chelex 100 (Sigma-Aldrich) to remove residual divalent metal ions. The reference cuvette contained 0.5 μM C2α in the same buffer. Instead of the metal ion solution, an equivalent volume of HPLC-grade water was added to the reference cuvette. The changes in tryptophan fluorescence emission upon Cd^{2+} binding were evident in the difference between the sample and reference spectra. Both the change in the emission

intensity and the shift of the emission maximum were observed over the course of the titration experiment. To quantify the Cd^{2+} binding process, we calculated the spectral center of mass (CM)[207] of the emission spectra at each metal ion concentration. The change in CM divided by the maximum observed change upon Cd^{2+} saturation of CMBL sites is proportional to the fraction of the Cd^{2+}-complexed C2α, F_{Cd}. The data were fitted with the Hill equation:

$$F_{Cd}=\frac{[M^{2+}]^{H}}{[M^{2+}]_{1/2}{}^{H}+[M^{2+}]^{H}} \qquad \textbf{5.3}$$

where H is the Hill coefficient, and $[M^{2+}]_{1/2}$ is the Cd^{2+} concentration required to yield the half-maximal CM change. The fit produced the following parameters: $H=2.9 \pm 0.3$ and $[M^{2+}]_{1/2} = 1.1 \pm 0.1$ μM. The low-affinity Cd^{2+} site is not appreciably populated at the 0.5 μM C2α concentration used in the fluorescence experiments.

Ultracentrifugation lipid-binding assays

The sucrose-loaded LUVs were prepared and the assays were carried out as previously described[72], at a total lipid concentration of 1.5 mM and C2α concentration of 5 μM. The composition of LUVs was either POPC/POPS (70:30) or POPC/POPS (80:20). An additional EDTA wash was performed to remove divalent metal ions from the LUVs, and EDTA was subsequently removed by four buffer exchanges with G-25 buffer exchange columns into final buffer of 10mM MES pH6.0 and 100mM KCl.

Results

Two types of Cd^{2+} binding sites in C2α

The Cd^{2+} binding sites in C2α were identified by solution NMR. The response of individual cross-peaks, each of which correspond to one protein backbone amide group, to increasing Cd^{2+} concentration was monitored by a series of ^{15}N-^{1}H HSQC spectra. We observed two groups of residues that respond differently to Cd^{2+} binding, as demonstrated with selected subsets in Figure 49. Group 1 residues fall into the slow-to-intermediate exchange regime on the NMR chemical-shift timescale, where the cross-peaks of the apo protein species disappear, and the metal-complexed protein species appear at their final positions and gradually build up upon Cd^{2+} saturation. Group 2 residues show fast-exchange behavior, where the cross-peak positions change smoothly upon increasing Cd^{2+} concentration. These data indicate that there are two distinguishable types of Cd^{2+} binding sites in C2α, with different binding kinetics of Cd^{2+} ions. The apparent Cd^{2+} affinities are also quite different, with group 1 and group 2 residues saturating at ~300 μM and ~4 mM Cd^{2+}, respectively.

To map the Cd^{2+} binding sites onto the structural elements of C2α, we exploited their differential Cd^{2+} affinities and conducted the chemical shift perturbation (CSP) analysis for two pairs of Cd^{2+} concentration points: 0 and 240 μM; and 240 and 4160 μM. Site 1 is mostly formed by the Ca^{2+}- and membrane-binding loops, or CMBLs (Figure 50A, shaded regions). According to the crystal structure of Ca^{2+}-complexed C2α, CMBLs provide all ligands for the binuclear Ca^{2+} site and the third Ca^{2+} site except from water molecules and external ligands (Figure 48). The CSP pattern in the low-

concentration Cd^{2+} regime is very similar to that observed previously for the binding of two Ca^{2+} ions to C2α.[72] This suggests that no less than two Cd^{2+} ions with similar affinities bind to the loop region. We used the fluorescence emission spectra of native tryptophan residues in C2α to estimate the affinity of Cd^{2+} to the high-affinity CMBL site. The shape of the binding curve indicates a significant degree of cooperativity, consistent with NMR CSP data that there are more than one metal binding for the loop region (Figure 50B).

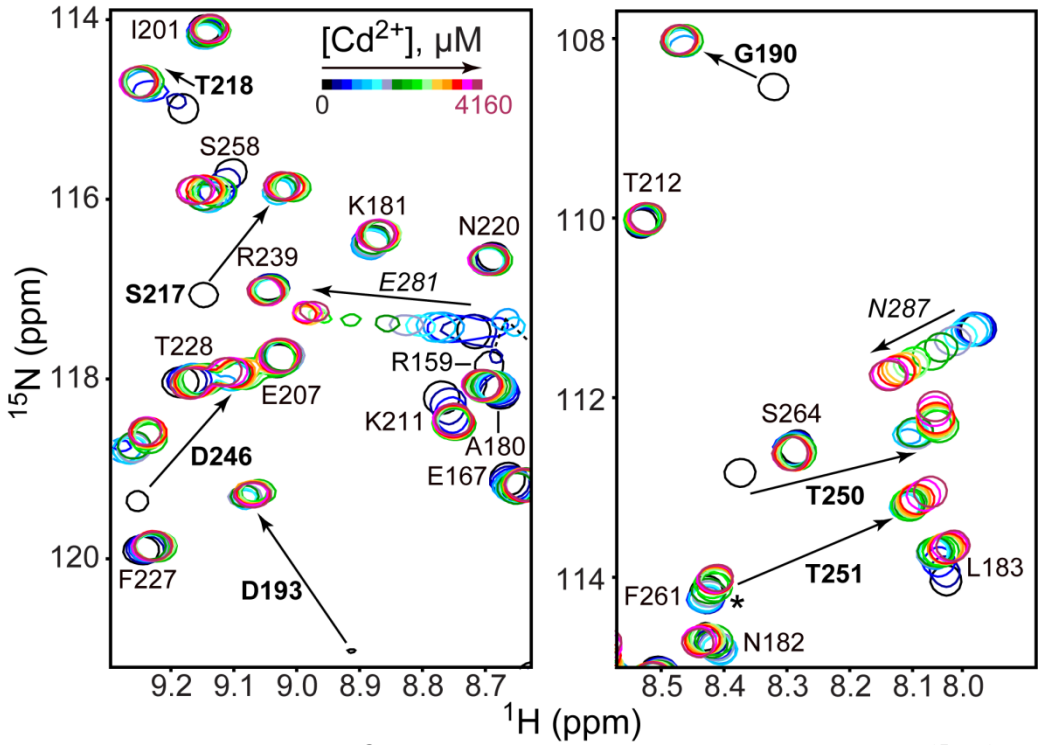

Figure 49. Two types of Cd^{2+} binding sites in C2α. Expansions of the ^{15}N-^{1}H HSQC spectra show the chemical shift changes of 110 μM C2α in response to increasing Cd^{2+} concentration. The residues of groups 1 and 2 are shown in boldface and italics, respectively. The asterisk marks the position of the apo C2α T251 cross peak, which overlaps with F261.

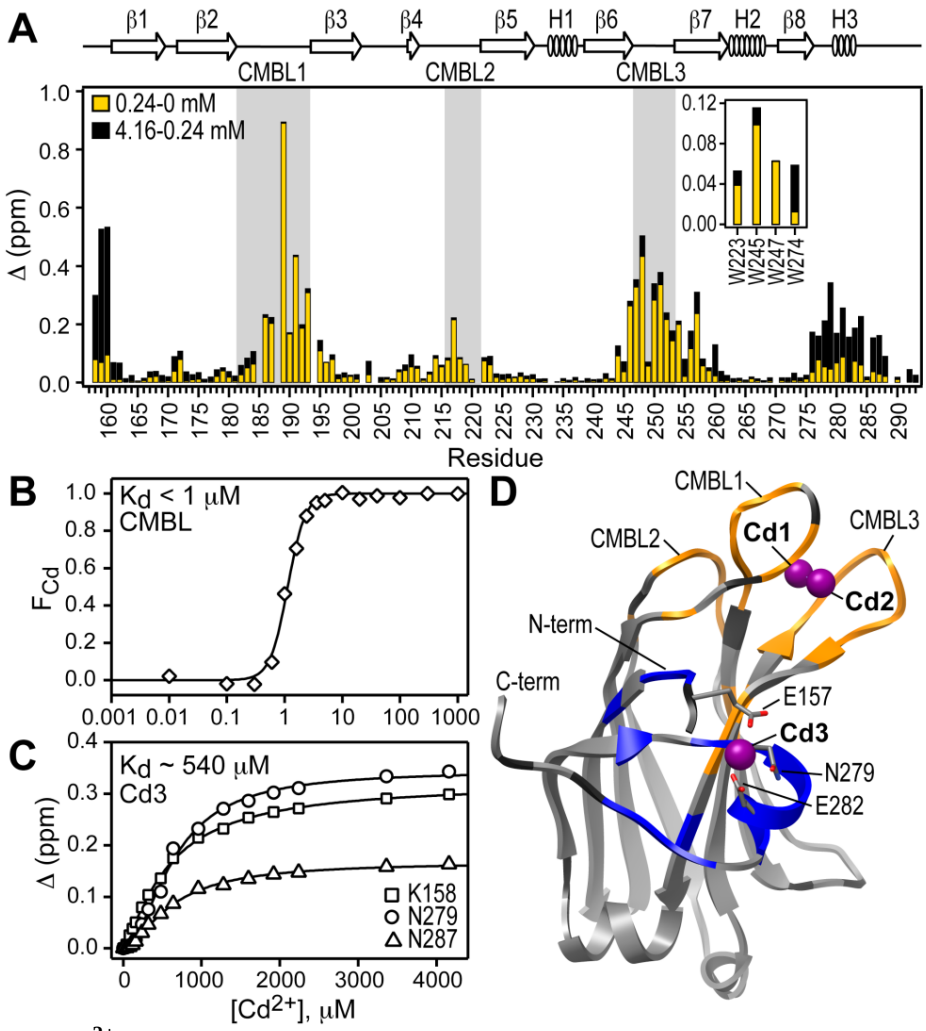

Figure 50. Cd^{2+} binds to two distinct C2α regions: CMBLs and the N-terminal /Helix3 region. (A) Chemical shift perturbation for the low- (yellow) and high-concentration (black) Cd^{2+} regimes, demonstrating the presence of two types of sites. The inset shows values for the indole N-H groups of Trp side-chains. **(B)** Fraction of the Cd^{2+}-complexed C2α, F_{Cd}, calculated using the change in the spectral center of mass of the Trp fluorescence emission spectra, plotted against Cd^{2+} concentration. **(C)** Representative NMR-detected Cd^{2+} binding curves for the N-terminal/Helix3 region. **(D)** Crystal structure of the Cd^{2+}-complexed C2α (PDB ID 4L1L). Residues that show intermediate-to-slow and fast exchange regimes upon Cd^{2+} binding are highlighted in orange and blue, respectively. Pro and residues with no data are in dark grey.

The concentration of Cd^{2+} required to achieve half-maximal binding is 1.1 ± 0.1 μM. This value can be used as an upper limit for the apparent dissociation constant K_d, given that the total concentration of C2α is comparable (0.5 μM).

The N-terminal/Helix3 region of C2α forms the low-affinity Cd^{2+} site (Figure 50A). This behavior is unique for Cd^{2+}, as the binding of Ca^{2+} to this region of C2α has not been observed. The binding curves were constructed by plotting a combined change in $^{1}H_N$ and ^{15}N chemical shifts Δ against total Cd^{2+} concentration. All curves have a slight lag period because the higher-affinity CMBL sites get populated first. This and the changes in the millisecond-timescale dynamics of the protein upon binding metal ions (K. A. Morales and T.I. Igumenova, unpublished data) make it difficult to construct an analytical function that accurately describes the binding process. To estimate the binding affinity, we simply fit the residue-specific curves individually with the Hill equation, corrected for the free ligand concentration, as described for the C2 domain of rabphilin-3A.[134] The range of apparent K_d values is 270-1100 μM, with the mean of 540 μM, which is similar to the global fitting result of 523 μM (Figure 50C). Individual fitting of all residues in the low-affinity group are shown in Figure 51. Note that the separation of the Cd^{2+} binding sites was possible, due to the different total protein concentration regimes used for the fluorescence (0.5 μM) and NMR (110 μM) experiments.

The high-affinity binding event consisting of at least two metal ions and the low-affinity binding event affecting the N-terminal/Helix3 region are in excellent agreement with the crystal structure of Cd^{2+}-complexed C2α (PDB ID 4L1L) we went on and

solved. Out of six Cd^{2+} ions bound to C2α, only three have four or more protein ligands and significant occupancy: the binuclear Cd^{2+} cluster in the CMBL region, with occupancies of 1.0 (Cd1) and 0.74 (Cd2); and Cd3 located between the N- terminal

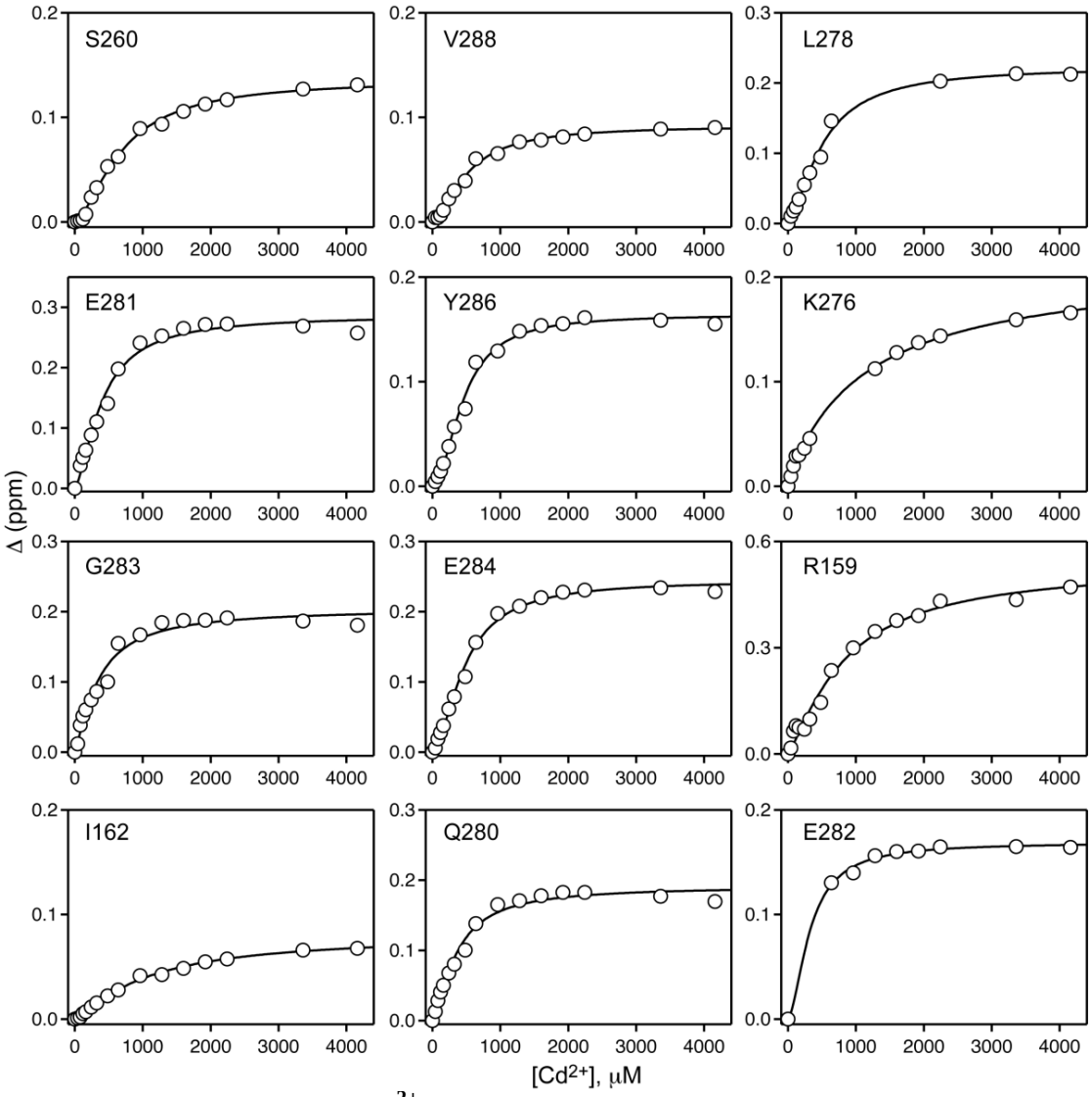

Figure 51. NMR-detected Cd^{2+}-binding curves of C2α. The solid lines represent the fits to Eq. (3) of Montaville et al..[134] Missing data points at certain Cd^{2+} concentrations indicate that the corresponding cross peak is not resolved in the HSQC spectrum.

region and Helix3, with an occupancy of 0.41 (Figure 50D and Table 13). We concluded that Cd1 and Cd2 correspond to the high-affinity sites located at CMBLs, exhibiting slow-to-intermediate exchange behavior; whereas Cd3 corresponds to the low-affinity site located at N-terminal/Helix3 region, with fast exchange behavior in NMR binding experiments.

Cd^{2+} does not support PtdSer-containing membrane association of C2α

We then seek to understand if Cd^{2+} could support membrane association of C2α with PtdSer-containing LUVs. Two types of experimental approaches were used for this purpose. One is Förster Resonance Energy Transfer (FRET) based experiments monitoring the membrane binding event with intrinsic Trp of C2α as donor of the FRET pair and dansyl-PE incorporated in LUVs as the acceptor. The other type of experiment is ultracentrifugation experiments with sucrose-loaded LUVs. The results of the FRET based membrane-binding assays (as demonstrated in Figure 3 of Morales and Yang et al.[208]) and the ultracentrifugation assays (Figure 52) both revealed that there is minimal membrane-association when Cd^{2+} is added. This is in opposite situation when comparing to Pb^{2+}, which also binds with high affinities to CMBLs of C2α but drives membrane association also as efficient as Ca^{2+}. Cd^{2+} alone neither quenches dansyl fluorescence nor associates appreciably with the PtdSer component of the LUVs under the conditions of our experiments (as described in the SI of Morales and Yang et al.[208]). We conclude that Cd^{2+} is unable to mediate the association of C2α with membranes due to the intrinsic differences of the divalent metal ion from Ca^{2+} and Pb^{2+}.

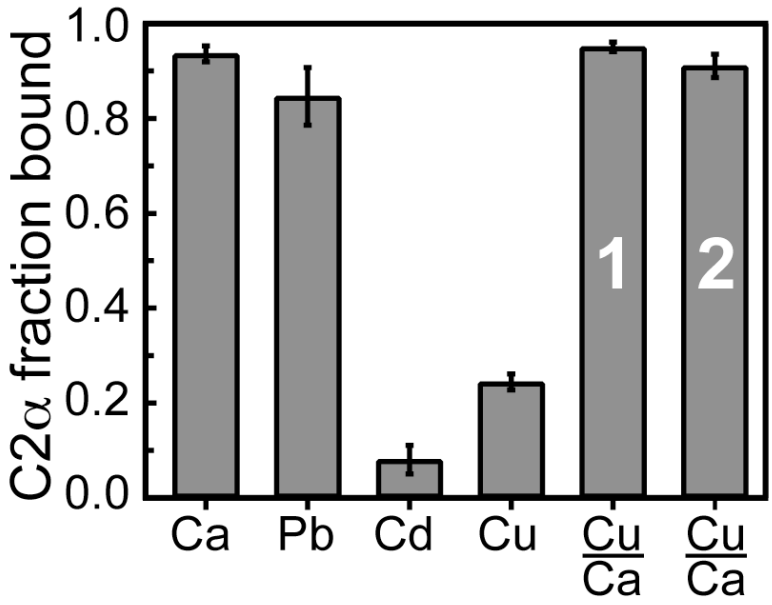

Figure 52. Fractional population of membrane-bound C2α obtained in ultracentrifugation binding assays with LUVs having 30% PtdSer component. Total concentration of metal ions was 175 μM, except for the Cu^{2+}/Ca^{2+} displacement experiments that were carried out at 12.5/175 μM (Bar 1) and 175/2450 μM (Bar 2).

The ability of metal ions to mediate membrane association does not correlate with their radii or coordination geometry when complexed to C2α

The results that Cd^{2+} cannot support C2α-membrane binding were surprising to us in two different aspects. On one hand, Pb^{2+} binds CMBLs of C2α with high affinity just like Cd^{2+}, whereas the coordination geometry of the second Pb^{2+} differs from Ca^{2+} or Cd^{2+} (Figure 53). On the other hand, Cd^{2+} (0.97Å) has a very similar radius as Ca^{2+} (0.99Å), whereas Pb^{2+} has a larger radius (1.33Å). Despite all these, Pb^{2+} drives C2α-membrane association almost as efficient as the native ligand Ca^{2+}.

We attribute this behavior to the coordination preferences of metal ions. Cd^{2+} is a soft Lewis acid[209], with preference towards soft ligands, such as thiol groups of cysteine residues.[210] Its most frequently encountered coordination number (CN) in proteins is either 4 or 6.[211] The crystal structures of Ca^{2+}-bound C2α[68] and annexin V[212] in complex with PtdSer analogs suggest that a Ca^{2+}-coordinated water molecule is replaced by either phosphoryl and/or carboxyl oxygen(s) of PtdSer upon membrane association. This may be accompanied by an expansion of the metal ion coordination sphere, as shown for Ca^{2+}-bound C2α in Figure 53. While Cd^{2+} can adopt a hepta-coordinated state when bound to C2α, the rearrangement and possible expansion of its all-oxygen coordination sphere required for PtdSer interactions may be unfavorable. In contrast, Ca^{2+} is a hard Lewis acid that favors all-oxygen coordination environment with CNs of 6-8.[213] Pb^{2+} is a borderline Lewis acid that interacts readily with oxygen-containing ligands and can adopt CNs up to 9 in proteins.[214]

This explanation correlating the ability to expand coordination sphere with membrane binding was further tested with a fourth metal ion: Cu^{2+}. Similar to Pb^{2+}, Cu^{2+} is a borderline Lewis acid, albeit with a well-documented preference for CN=4 in proteins.[211] In addition, Cd^{2+} and Cu^{2+} have been used with success as a diamagnetic-paramagnetic pair in structural studies.[215] According to elegantly measured paramagnetic relaxation enhancement effects (described in Figure 4 of Morales and Yang et al.[208]), Cu^{2+} also binds to both CMBLs and N-terminal/Helix3 region similar to Cd^{2+}. However,the N-terminal/Helix3 site populates Cu^{2+} prior to CMBLs, indicating a higher affinity of Cu^{2+} to the N-terminal/Helix3 region than the CMBLs which is with

opposite preferences to Cd^{2+}. The lipid-binding assays show that like Cd^{2+}, Cu^{2+} is not an effective mediator of protein-membrane interactions: only ~20% of Cu^{2+}-complexed C2α is membrane-bound (Figure 52). Reducing the concentration of PtdSer from 30% to 20% eliminates the membrane binding of C2α in the presence of Cu^{2+} (see Figure S10 of Morales and Yang et al.[208]).

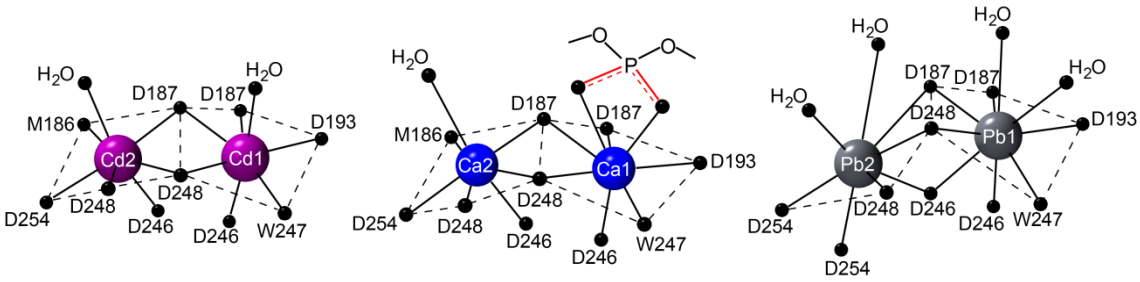

Figure 53. Comparison of the coordination geometry of Cd^{2+}, Ca^{2+} and Pb^{2+} complexed to the C2 domain from PKCα. The crystal structures used are PDB ID 4L1L, 3DSY and 3TWY, respectively. All coordinating oxygen atoms are colored black.

More interestingly, Cu^{2+} at the weaker CMBLs site could be replaced by excessive Ca^{2+}, but not the N-terminal/Helix3 site. The generated mixed species has Ca^{2+} bound to CMBLs while Cu^{2+} remained associated with the N-terminal/Helix3 site. The mixed metal-bound species associates with membrane as efficient as the Ca^{2+}-bound C2α (Figure 52). This demonstrates nicely that having a divalent metal ion bound to the N-terminal/Helix3 site does not negatively affect the C2α membrane-binding properties.

Table 13. Cd-O distances and occupancy for Cd1-3 in Cd^{2+}-complexed C2α structure

Cd1 CN[a]=7	Bond length (Å)	**Cd2** CN=7	Bond length (Å)	**Cd3** CN=6	Bond length (Å)
D187 (Oδ1)	2.57	D187 (Oδ1)	2.45	E157 (Oε2)	2.62
D187 (Oδ2)	2.52	D248 (Oδ2)	2.67	E282 (Oε2)	2.67
D193 (Oδ2)	2.35	D248 (Oδ1)	2.55	E282 (Oε1)	2.59
D248 (Oδ1)	2.40	D254 (Oδ2)	2.45	N279 (Oδ1)	3.04
D246 (Oδ1)	2.35	D246 (Oδ2)	2.34	H_2O (141)	2.84
W247 (O)	2.36	M186 (O)	2.53	H_2O (142)	2.20
H_2O (10)	2.46	H_2O (43)	2.54		
Average	2.43±0.09		2.50±0.10		2.66±0.28
Occupancy	1.00		0.74		0.41

[a]CN stands for coordination number

Table 14. Cd-O distances and occupancy for Cd4-6 in Cd^{2+}-complexed C2α structure

Cd4 CN=5	Bond length (Å)	**Cd5** CN=4	Bond length (Å)	**Cd6** CN=5	Bond length (Å)
D193 (Oδ1)	2.47	D254 (Oδ1)	2.75	E265 (Oε2)	2.38
D193 (Oδ2)	2.57	T251 (Oγ1)	2.76	E265 (Oε1)	2.92
H_2O (408)	2.37	D248 (Oδ2)	2.84	H_2O (511)	2.22
H_2O (419)	2.43	R252 (O)	2.86	H_2O (501)	2.58
H_2O (522)	2.69			H_2O (420)	2.92
Average	2.51±0.13		2.80±0.06		2.60±0.32
Occupancy	0.29		0.35		0.27

Weak Cd^{2+} sites of C2α observed in crystal structure

We were able to observe a total of six Cd^{2+} ions bound to the protein from the crystal structure of Cd^{2+}-complexed C2α. Tables summarizing all six Cd^{2+} ions are shown in Table 13 for the Cd1-3 and Table 14 for the Cd4-6, respectively. From the tables, it is apparent that Cd1-3 have significant occupancies, four or more protein ligands and six or more total coordination numbers, as comparing to Cd4-6. This is in full consistency with our solution Cd^{2+} binding studies by NMR (*vide supra*). It is worth to note that Cd4 and Cd5 both locate at the CMBLs region to form a Cd "string" via the formation of O-M-O bridges (Figure 54).

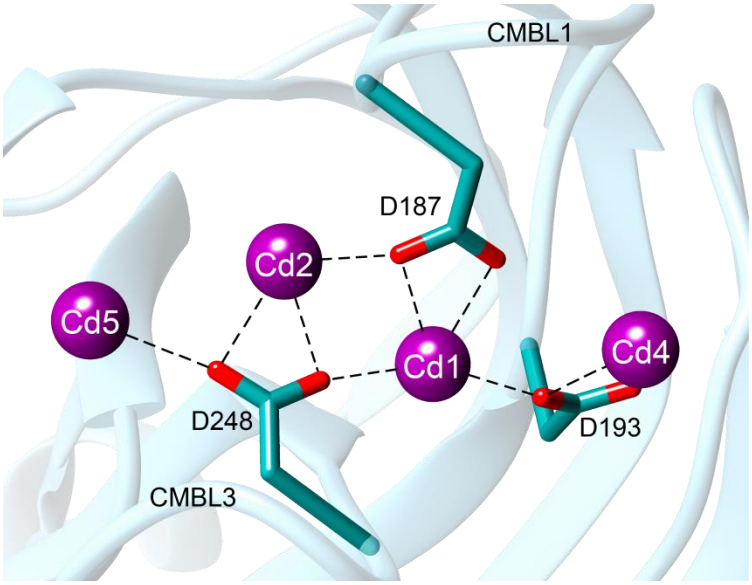

Figure 54. Cd "string" formed by Cd1, Cd2, Cd4 and Cd5 at the CMBLs region. Not all coordinating residues are shown. CMBL1 and CMBL3 are indicated.

On the other hand, Cd5 binds to the same location as the Ca3 site observed in the PDB ID 3GPE. Detailed analysis of the coordinating residues reveals that Cd5 forms the same coordination bonds as the Ca3 site (Table 13, Figure 48, Figure 53 and Figure 54), except from Cd5 having one less ligand than Ca3 (D254 Oδ2). This is again consistent with that Cd(II) and Ca(II) are isostructural, but have slightly different ligand preferences and coordination numbers.

Third Ca^{2+} binding induces μs-ms dynamics changes in C2α

After acquiring insights into the mechanism of Ca^{2+}-mediated membrane binding, the next step was to investigate the role of the third Ca^{2+} site on C2α that could relate metal-binding to the final conformational change of full-length PKC. We hypothesize that the third Ca^{2+} binding alters the conformational dynamics instead of structure. We measured amide ^{15}N R_2 values with the Hahn Echo experiments containing a single ^{15}N refocusing pulse. The R_2^{HE} values extracted from these experiments contain both spin-lattice relaxation rate R_2^0 and any existing chemical exchange rate R_{ex} on the μs-ms time scale.

Figure 55A shows the results of R_2 relaxation measurements of C2α with different concentrations of Ca^{2+}. From previous NMR studies[72] we knew that C2α associates with the first two Ca^{2+} ions with equivalent affinity of ~270μM. This allows us to estimate a saturating point for the first two Ca^{2+} ions at the protein concentration we used in the relaxation sample described in this chapter. According to the estimation, 95% of C2α is bound with the first two Ca^{2+} ions at $[Ca^{2+}]$ of 1.75mM. Therefore, only

data from high concentrations of $[Ca^{2+}] \geq 1.75$ mM are shown here in order to represent the third Ca^{2+} binding event. From the array of R_2^{HE} values (Figure 55A), it is apparent that the value of residue R159 increases dramatically upon increasing third Ca^{2+} binding. The total increase of R_2^{HE} for R159 is 9.70 ± 1.11 s^{-1} between the first and last Ca^{2+} points (1.75 mM and 87.5 mM).

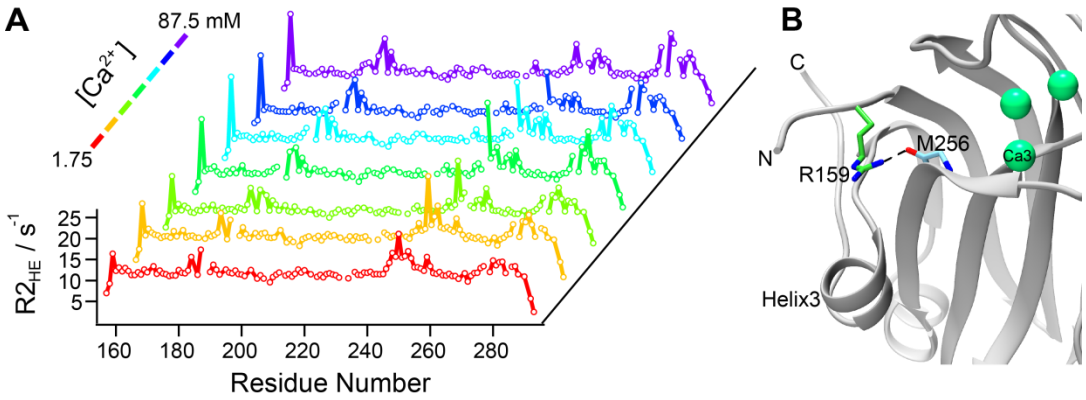

Figure 55. Third Ca^{2+} binding induces µs-ms dynamics changes in C2α. (A) Increased R_2^{HE} values of the N-terminal region by the third Ca^{2+} binding. The values plotted against residue number at increasing Ca^{2+} concentration are colored as indicated. **(B)** Hydrogen bond between R159 side-chain and the backbone carboxyl oxygen of M256 observed in crystal structure 3RDJ. The distance between nitrogen and oxygen atoms in the hydrogen bond is 2.584 Å. The locations of the Ca^{2+} are indicated by an overlay with crystal structure 3GPE.

This indicates an increased motion of R159 at µs-ms time scale. The change of R_2^{HE} at Helix3 is not as pronounced. On the contrary, CMBL1 and CMBL3 residues have decreased R_2^{HE} upon third Ca^{2+} binding. This is consistent with reduced backbone motions of CMBL1/3 residues upon formation of coordination bonds with the third Ca^{2+}. The dramatic increase of R159 motion upon addition of Ca^{2+} is not likely due to a direct

association of Ca^{2+} to the N-terminal/Helix3 region, due to two aspects: 1) we did not observe large chemical shift perturbations for the region which is the case for Cd^{2+}; 2) Ca^{2+} coordinating to this region has never been observed previously despite multiple Ca^{2+}-bound structures available in the Protein Data Bank.

In order to understand the basis of the increased motion for R159, we carefully inspected the existing crystal structures of C2α to look for potential interactions involving this residue. In all available crystal structures we analyzed, there is a hydrogen bond between the side-chain Nη1 of R159 and the backbone carbonyl oxygen of M256. This hydrogen bond is shown in Figure 55B and all bond distances analyzed are summarized in Table 15. Although crystal structures do not necessarily report on the solution state, they likely represent a thermodynamically stable conformation on the energy landscape in solution. To probe the existence of this hydrogen bond in solution, we collected ^{1}H-^{15}N HSQC spectra of wild-type and a R159G mutant of C2α with the ^{15}N carrier placed at an optimal frequency for Arg side-chain nitrogen atoms. From the spectra comparisons between wild-type and mutant (Figure 56), it is immediately apparent that there is a resonance corresponding to R159 Nη-Hη (71.6, 6.7) with a down-field shift on ^{1}H dimension comparing the other Arg Nη-Hη (71.5, 5.9). This down-field shifted resonance is not in the R159G mutant spectrum, which assisted in assigning the identity in the wild-type spectrum. At the same time, the down-field shift is consistent with a hydrogen-bonded species.

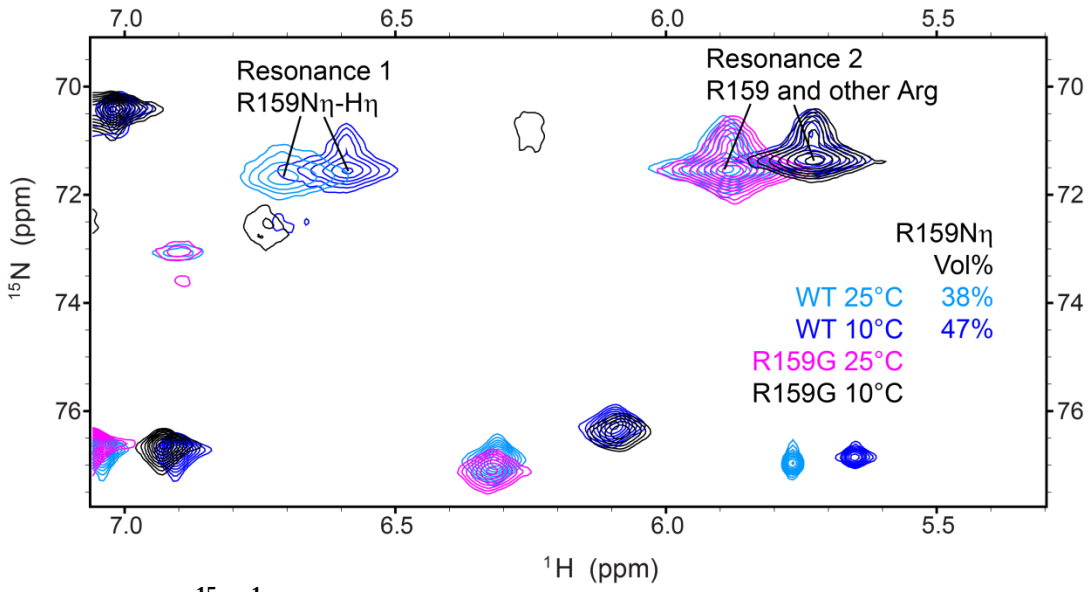

Figure 56. Arg ^{15}N-^{1}H HSQC spectral overlay of wild-type C2α and R159G mutant reveals a hydrogen-bonded species of residue R159 in the wild-type protein. The color coding of each spectrum is illustrated on the right part of the spectra, with wild-type protein spectra colored cyan (25 ℃) and blue (10 ℃), R159G mutant spectra colored magenta (25 ℃) and black (10 ℃), respectively. Resonance 1 is the hydrogen bonded species of R159, whereas Resonance 2 corresponds to all other Arg Nη-Hη and R159 species that is not hydrogen bonded. The volume percentage (Vol%) is calculated by the ratio of the peak volumes of Resonance 1 versus the sum of Resonance 1 and 2.

Table 15. Distances between R159 Nη1 and M256 O atoms

PDB ID	distance (Å)	Ligand
3RDJ	2.584	apo
1DSY	3.005	2Ca^{2+}
3GPE	2.870	3Ca^{2+}
3TWY	2.895	2Pb^{2+}
4L1L	2.969	6Cd^{2+}
4DNL	3.196	1Na^{+}
Average	2.920 ±0.201	

The population ratio of this down-field shifted resonance also increases at 10 ℃ than at 25 ℃, further confirming that this resonance corresponds to a hydrogen-bonded species which is stabilized at lower temperature.

Based on the above evidence, we infer that the increased motion of R159 residue upon third Ca^{2+} binding is related to a change in the equilibrium between hydrogen-bonded and not hydrogen-bonded species. If true, this indicates a potential role of the third Ca^{2+} binding in modulation of μs-ms motion at the slightly remoted N-terminus of C2α (Figure 55B). Given that the linker between C2 domain and the preceding C1B domain in the host enzyme PKCα is short (7 aa), the increased motion of residue R159 will potentially have an effect on the degree of freedom of the preceding C1B domain. There is a minor R_2^{HE} decrease of the baseline residues excluding residues of regions N-terminal/Helix3 and CMBL1/3. The baseline decrease is an average of $2.67 \pm 0.56\ s^{-1}$ between the first and the last Ca^{2+} points shown in Figure 55A. This minor baseline decrease is a potential result of a change in overall molecular tumbling, caused by either a change in the molecular shape or oligomerization state. The crystal structure of C2α remains identical between the two-Ca^{2+} bound state and the three-Ca^{2+} bound state (Figure 48). Therefore, we think it is more likely to be due to reduced oligomerization at lower protein concentrations for the higher [Ca^{2+}] points, as a result of dilution. The ability for C2 domain to oligomerize is further supported by the crystal structure of C2 domain from PKCβII, where the adjacent molecules form a dimer (Figure 57).

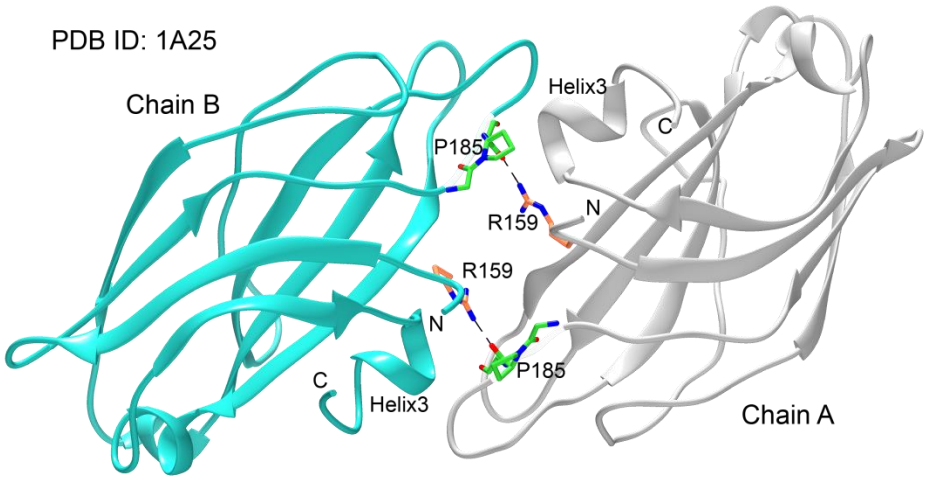

Figure 57. Homo dimer observed in crystal structure of C2 domain from PKCβII. The PDB ID is 1A25, and the two chains forming a dimer are colored cyan and grey, respectively. R159 and P185 residues forming hydrogen bonds on the dimer interface is illustrated. The Nη2-O distances are 2.401 Å and 2.428 Å for the top and bottom bonds, respectively.

R159G mutantion alters the third Ca^{2+} binding affinity

The third Ca^{2+} binding is also investigated in the R159G mutant as comparing to the wild-type C2α. Figure 58 and Figure 59 display the spectral overlay of wild-type and R159G C2α with increasing concentration of Ca^{2+}. Both constructs display a linear trajectory of resonance shifts upon populating the third Ca^{2+} bound species. The constructed binding curves fit very well with the single-site binding equation.[134] Figure 60 displays the binding curves of both wild-type and R159G mutant upon binding the third Ca^{2+} site. All solid lines displayed are global fitting results to a single-binding site equation[134], which yielded K_ds of 26.5 ± 0.8 mM for the wild-type C2α and 57.9 ± 3.3 mM for R159G mutant. This about 2-fold decrease in binding affinity indicates a role of the R159 residue in the third Ca^{2+} binding through modulating the μs-ms dynamics of

C2α. Together with the R_2^{HE} increase of R159 upon binding third Ca^{2+} (*vide supra*), we conclude that the third Ca^{2+} binding and the μs-ms dynamics of the N-terminal/Helix3 region is interconnected. This effect is likely mediated by the hydrogen-bonding network at the N-terminal/Helix3 region especially for the R159-M256 hydrogen bond.

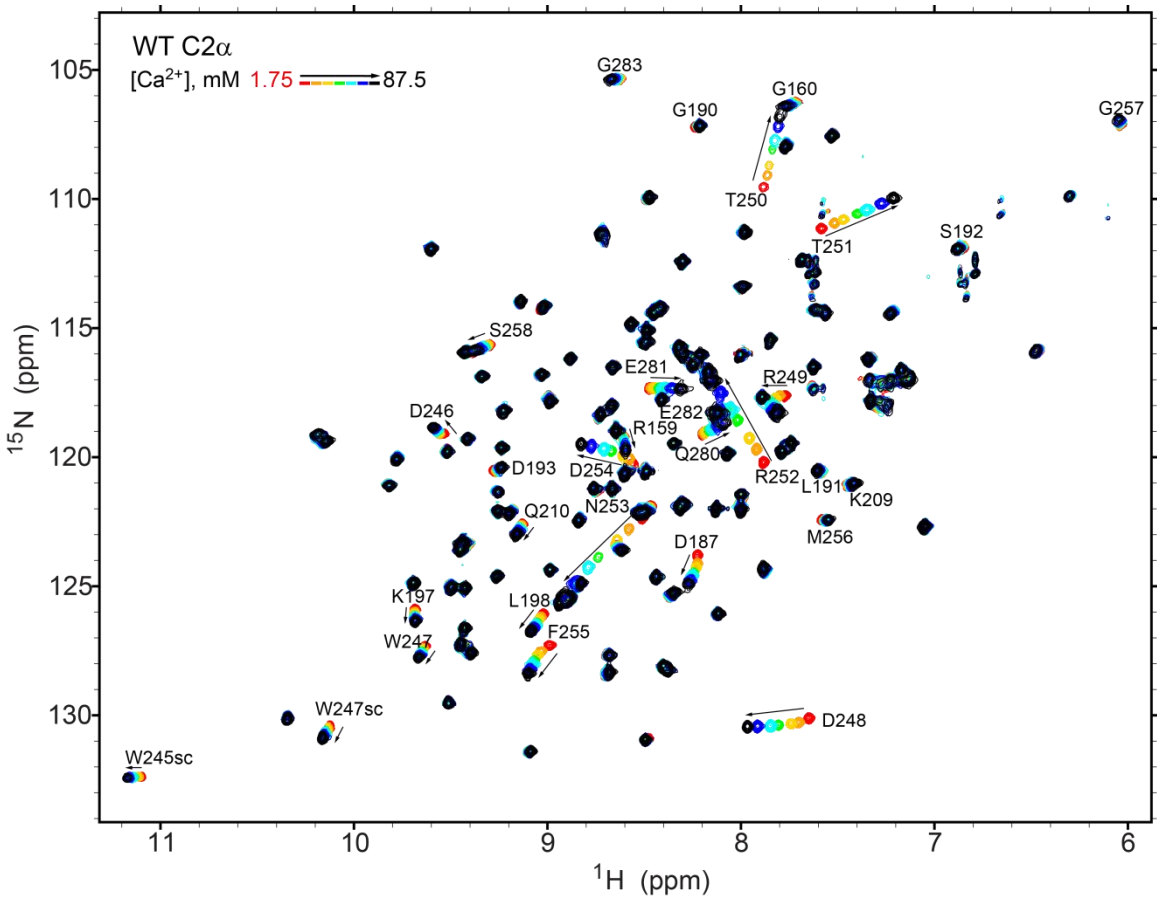

Figure 58. Spectral overlay of the wild-type C2α R_2-HE experiments without the delay T. These are essentially the same as ^1H-^{15}N HSQC experiments, and are used to extract the third Ca^{2+} binding affinity. Color coding of each spectrum is indicated at the left top corner. Only resonances with significant chemical shift perturbations are shown, with arrows indicating the direction of shifts.

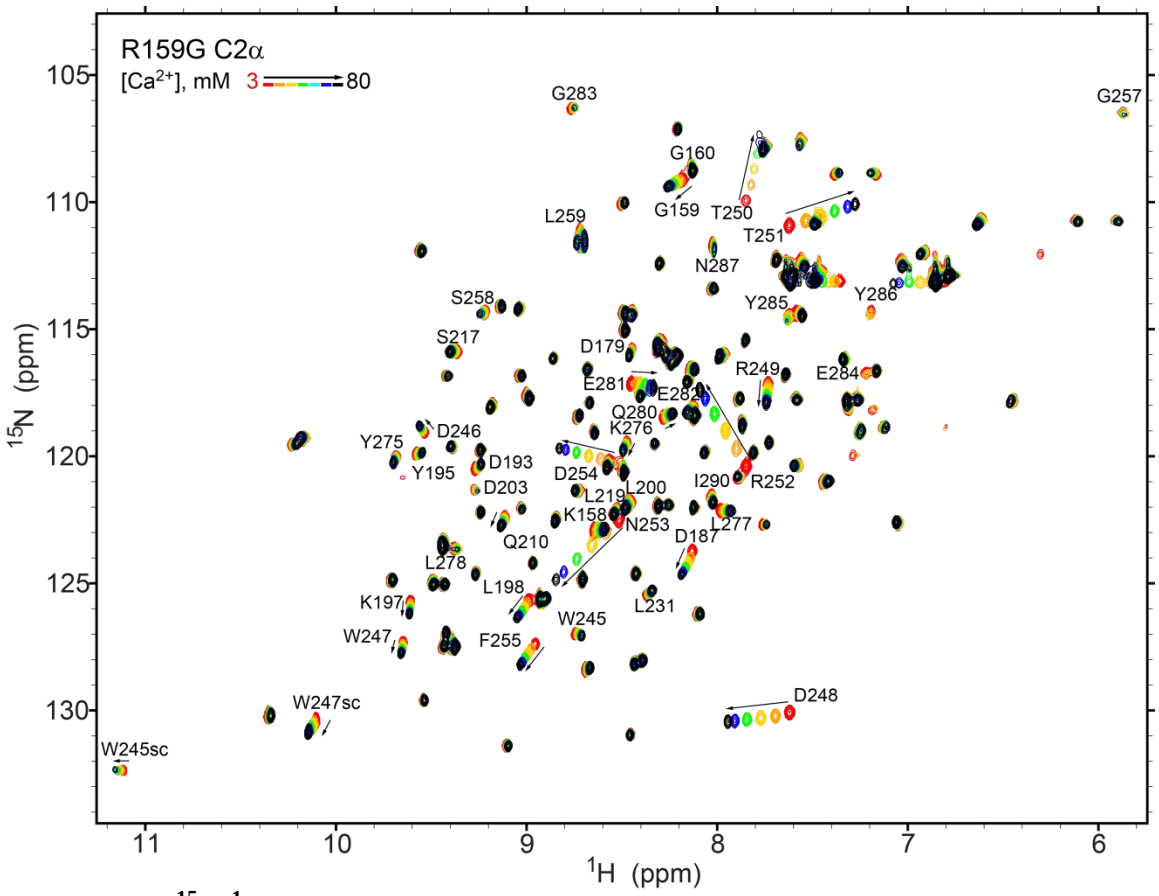

Figure 59. [^{15}N-^{1}H] HSQC pectral overlay of the R159G mutant C2α upon binding third Ca^{2+}. These are used to extract the third Ca^{2+} binding affinity. Color coding of each spectrum is indicated at the left top corner. Only resonances with significant chemical shift perturbations are shown, with arrows indicating the direction of shifts.

It is worth to mention that the effect of R159G mutation on the binding of the first two Ca^{2+} ions is not as pronounced as the third Ca^{2+}. The median of K_d for wild-type C2α binding to the first two Ca^{2+} is ~270 μM, whereas for R159G mutant the median K_d is ~301 μM. There are variations of K_d and cooperativity if individual residues are compared, reflecting a potential change in overall dynamics across the

protein by the mutation without altering the overall binding affinity for the first two Ca^{2+}.

Discussion of results

The work in this chapter provides valuable insights into the metal-dependent membrane association of C2 domain from PKCα, with specific case studies involving divalent metal ions Cd^{2+} and Ca^{2+}. Regarding to the mechanism of metal-dependent membrane association, our data clearly demonstrate that Cd^{2+}, along with two other non-native metal ions: Cu^{2+} and Pb^{2+}, can act as a general electrostatic "switch" by associating with the aspartate-rich CMBL region of C2α and neutralizing the negative charges. However, the formation of metal ion-protein complex is not sufficient to promote protein-membrane association, as demonstrated for Cd^{2+} and Cu^{2+}. We conclude that bridging interactions between a divalent metal ion and PtdSer groups are required for productive protein-membrane interactions.

Favorable spectroscopic properties and the nearly identical ionic radius have made Cd^{2+} a popular substituent of Ca^{2+}.[216] Our results show that the preferred coordination geometry of metal ions, their ability to expand the coordination sphere, and the chemical identity of protein ligands need to be taken into account when designing metal substitution studies. This is particularly important for proteins that rely on metal ions to carry out a specific function. A case in point is the C2 domains, which are the second most abundant lipid-binding domain behind the PH domains:[217] a UniProt[218]

search produced >140 different human C2-containing proteins whose function includes signal transduction and membrane trafficking.

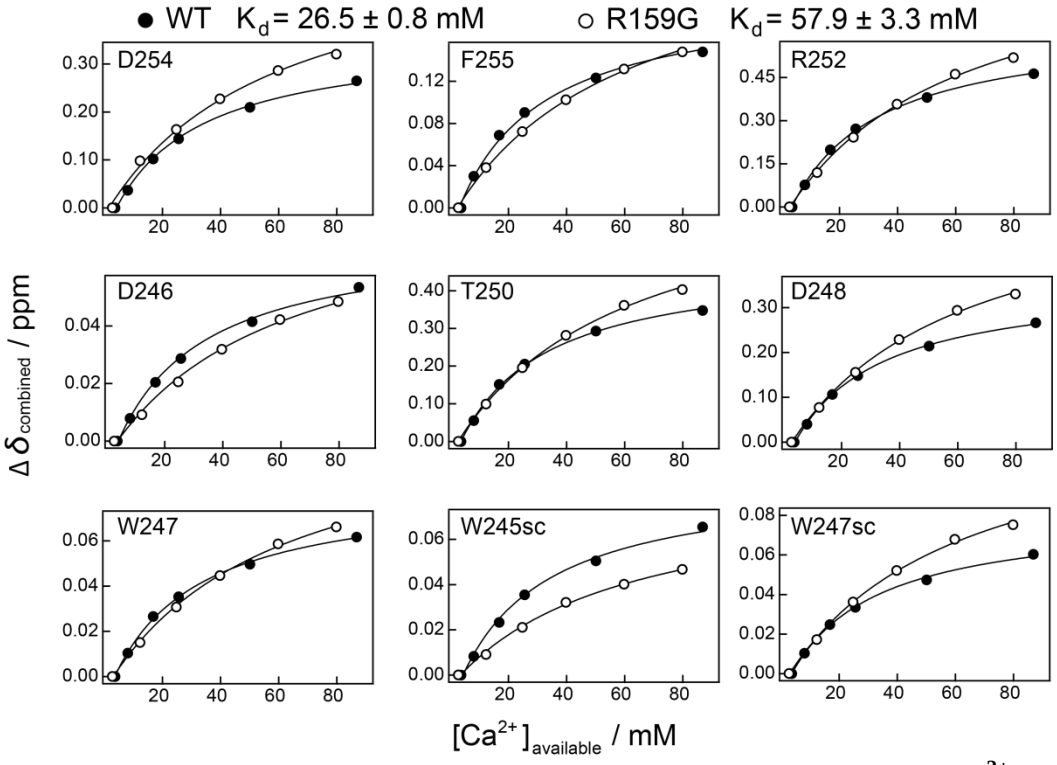

Figure 60. R159G mutation reduces the binding affinity for the third Ca^{2+} site. The binding curves for both wild-type C2α (closed symbols) and R159G mutant (open symbols) are shown in overlay. All fits are global fitting results to a single binding site equation.[134] Residue identities are shown on each graph. W245sc and W247sc refer to the imidazole side-chain Nε1-Hε1 resonances of the two trp residues on CMBL3.

Cd^{2+} is a toxic metal ion with no safe limit of exposure.[219] In our study, the affinity of Cd^{2+} to the CMBL region far exceeds the previously reported Ca^{2+} value[203] for > 30-fold. It is plausible that bioavailable Cd^{2+} can influence the function of C2-

domain containing proteins through a direct competition with Ca^{2+} for the CMBL regions. Our results demonstrate that toxic metal ions such as Cd^{2+} and Pb^{2+} can elicit very different functional responses with respect to the *in vitro* membrane binding: Pb^{2+} promotes membrane association of C2α, whereas Cd^{2+} does not. Either scenario, if occurring in the cell, would lead to the aberration in the Ca^{2+} signaling response.

We further observed a difference between the two metal ions, Cd^{2+} and Ca^{2+}, in their weak interactions with C2α beyond the first two sites. After populating the first two sites with high affinity at the CMBLs, Cd^{2+} populates a significant third binding site on the N-terminal/Helix3 region of the protein, which is absent in the case of Ca^{2+}. However, the third Ca^{2+} binding to CMBLs of C2α modulates the μs-ms dynamics of the slightly remote N-terminal/Helix3 motion potentially through a hydrogen-bonding network involving residue R159. This is further demonstrated by a 2-fold reduce in the affinity for the third Ca^{2+} by the R159G mutation which disrupts the R159-M256 hydrogen bond. These data highlight a connection between the third Ca^{2+} binding event and the μs-ms dynamics at the N-terminal/Helix3 region of C2α. The third Ca^{2+} binding was shown to be present in the PtdIns(4,5)P_2 liganded C2α structure[62], and was indicated to exist in the membrane-bound C2 domains from all conventional PKCs.[203] Given that the N-terminus of C2 domain connects to the preceding C1B domain through a short linker, we infer that third Ca^{2+} binding to C2 domain could trigger a more open conformation of conventional PKCs through potential alteration of the linker μs-ms motions. On the other hand, since Cd^{2+} populates a binding site at the N-terminal/Helix3 region with residues E157, E282 and N279, Cd^{2+} could also affect the motions of the

C1B-C2 linker through direct weak binding. Further studies including the interactions between the C1B-C2 two-domain construct and full-length PKC constructs with Cd^{2+} and Ca^{2+} are required to provide a more complete understanding on this subject.

CHAPTER VI

SUMMARY AND FUTURE DIRECTIONS

Summary and perspectives

Protein kinase C (PKC) isoenzymes have been identified as promising treatment targets for numerous human diseases, due to their central role in a broad range of cellular signaling pathways.[12] However, the current understanding of PKC regulation is not sufficient to achieve isoenzyme specific modulations by therapeutic agents. One of the main challenges in the field is to acquire atomic level information that could serve as a foundation to better understand the molecular mechanisms of PKC function and to address the fine differences between isoenzymes within PKC family. Towards this goal, the work conducted in this dissertation focuses the C-terminal V5 domain, a critical regulator for PKC function and isoenzyme-specific cellular localization, of which structural information was largely missing.

Chapter I provided the first successful expression and purification of the isolated V5 domain from PKCα with sufficient quantity for structural studies. We showed by combined spectroscopic methods that V5 domain is intrinsically disordered, with minor secondary structural propensities. This immediately explains the missing structural information prior to this study, since disordered proteins and protein domains generally exhibit large flexibility which prevents them to be visualized by crystallography and other structural approaches. On the other hand, the intrinsically disordered properties of V5 domain potentially allow highly adaptive protein-protein interactions with multiple

targets, which is one of the commonly suggested functions for disordered proteins and protein domains during cell signaling.[112,220] This is consistent with the large number of intermolecular domains, upstream kinases, scaffold proteins, molecular chaperone and other regulating proteins proposed to bind V5. In addition, the phosphorylation mimetic mutant was found to not affect the structural properties of V5 domain, suggesting alternative mechanisms for the PKC conformational change upon the phosphorylation events other than a change of V5 structure during the kinase maturation process.

The propensities of the isolated V5 domain from PKCα to interact and partition into hydrophobic environments were also unveiled in this work using detergent micelles as a membrane mimetic. We further tested this propensity with bilayer membrane mimetic LUVs. The interaction seems to be weaker with bilayer membrane as compared to micelles, consistent with the overall weak affinity of endogenous newly synthesized PKC to membranes. Using sensitive paramagnetic relaxation enhancement techniques, we observed similar regions of V5 interacting with bilayer membrane mimetic LUVs to those observed in micelle experiments. A slowly built-up species of V5 in the presence of LUVs over a time course of days suggested an additional interaction mode between V5 and bilayer membrane.

Chapter III and IV investigated the intramolecular and intermolecular interactions of PKC involving the V5 domain as implicated in previous functional studies. In Chapter III, direct evidence of the intramolecular C2–V5 interaction from PKCα was presented. This same interaction was shown to enhance the calcium binding affinity of the C2 regulatory domain, which would potentially decrease the concentration

of calcium needed to activate PKCα in cells. We determined the ternary C2•Ca^{2+}•V5-pHM complex structural model in solution, which showed overlapping binding sites between V5-pHM and PtdIns(4,5)P_2 on the C2 regulatory domain. Guided by the structure, mutations were designed to disrupt the observed C2–V5 interface in full-length PKCα construct. These mutations were shown to affect both autoinhibited conformation of the latent full-length PKCα and the membrane translocation kinetics upon phorbol ester PDBu stimulus in live cells. These data together with other studies suggested a potential conformational plasticity in the intramolecular binding site of the C2 domain. A fine-tuning and intricate regulation mechanism through the phosphorylated hydrophobic motif of V5 domain was described to be both autoinhibitory and activating at the same time.

Chapter IV provided a detailed analysis of V5 domain from PKCα as a bivalent binder for the peptidyl-prolyl isomerase Pin1. Several novel insights were contributed to both PKC field and Pin1 field. As a non-canonical Pin1 site, the hydrophobic motif of V5 domain was observed to interact with both domains of Pin1. On the other hand, the turn motif was found to be a WW domain specific interaction site and an inefficient substrate for Pin1 catalysis of peptidyl-prolyl bond *cis-trans* isomerization. When both turn and hydrophobic motifs are present on the same polypeptide chain, the interaction mode between Pin1 and bisphosphorylated V5 is highly specific: the turn motif interacts with the WW domain and the hydrophobic motif interacts with the PPIase domain. The binding affinities were shown to be enhanced significantly in the bivalent binding when comparing to the isolated motifs. These data illustrated a mechanism of Pin1–V5

interaction during the dephosphorylated/ubiquination dependent down-regulation process of conventional PKCs (with a potential exception for PKCβ).

We further investigated the reason why the phosphorylated turn motif is not an efficient substrate or interaction site for the PPIase domain. An unexpected non-specific catalysis was observed for the Q^{634}-P^{635} site in the presence of full-length Pin1 or the isolated PPIase domain. We demonstrated that this non-specific catalysis is due to a direct weak interaction between the phosphorylated turn motif and the substrate binding pocket of the PPIase domain. We attributed this phenomenon to the similarity between Gln and Glu residue, which is an effective phosphorylation mimic for Pin1. On the other hand, we hypothesized that the lack of amide proton for the +1 proline is the key to the lack of catalysis or binding. Indeed, a peptide with an alanine substitution at the +1 proline position while keeping the rest of the phosphorylated turn motif peptide identical exhibited efficient catalysis by Pin1 under the same experimental conditions.

Although the non-specific catalysis towards Q^{634}-P^{635} site still existed in the alanine substituted peptide, the full pV5 peptide did not display any efficient catalysis. This indicates that the nature of Pin1–V5 interaction during down-regulation of conventional PKC isoenzymes (α, βII and γ) is non-catalytic. In addition, we observed potential interdomain communication upon Pin1 interacting with the isolated phosphorylated turn motif. This could contribute in part to the significant avidity for the bivalent binding between full-length Pin1 and the bisphosphorylated V5 domain.

In Chapter V, we dissected the roles of divalent metal ion during the metal-dependent membrane interaction of the C2 regulatory domain. Specifically, cadmium

was used as a calcium structural surrogate. The coordination geometries of cadmium at the calcium membrane binding loops of C2 domain were shown to be identical to calcium. However, cadmium was not able to support C2–membrane interaction. This was further compared with lead and copper. Divalent lead has a much larger ionic radius than calcium, and was shown previously in the lab to have a different coordination geometry at the second metal-binding site from calcium.[72] Despite of that, lead was shown to support C2–membrane interaction almost as efficient as calcium. Divalent copper is similar to cadmium regarding to their limited coordination numbers generally observed, and could not support C2–membrane binding just like cadmium in this study. Taken together, we attributed the ability of divalent metal ions to support membrane association to the ability to expand their coordination sphere to oxygen atoms of phospholipids on top of the protein ligands, rather than the radius or protein-ligated coordination geometry. This is the first time to our knowledge where a "bridging" mechanism is verified directly through combined bioinorganic and membrane binding analysis.

A third binding site at the N-terminus/Helix3 region was observed for cadmium and copper. However, the third calcium binding site is located at the loop region of C2 from PKCα. Although not directly interacting, we observed a change of dynamics at the N-terminus/Helix3 region on the microsecond to millisecond timescale in response to the third calcium binding. This effect was attributed to the hydrogen bond network at the N-terminus/Helix3 region as shown by disrupting one hydrogen bond with the R159G mutation. This mutation did not significantly affect the first two calcium binding

affinities, but reduced the cooperativity slightly between the first two calcium binding events and reduced the binding affinity of the third calcium binding by two fold. Given the short linker length between C2 domain and the preceding C1B domain, as well as previously indicated increased third calcium binding by association with negatively charged membrane, these findings suggest a potential connection between the third calcium binding to the conformational change of full-length cPKCs upon membrane binding.

Future directions

This dissertation provided characterization and direct evidence for the multi-functional properties of the intrinsically disordered C-terminal V5 domain from conventional PKCs. The intramolecular and intermolecular interactions described here of V5 domain with both C2 regulatory domain and peptidyl-prolyl isomerase Pin1 illustrated the critical roles of V5 domain at all stages of PKC regulation with atomic level details. However, this is only the first step towards acquiring a full understanding of how V5 domain controls PKC life cycle. Many questions remain to be answered. We now know that the isolated V5 domain is intrinsically disordered and presents large conformational flexibility wrapping around the N-lobe of the catalytic domain in crystal structures. This property may be changed under different regulation stages. For example, the two phosphorylation sites on V5 domain were suggested to be autophosphorylation sites for conventional PKCs. In order for this to happen, the two unphosphorylated motifs may be interacting with the active site located between the N-

and C-lobes of the kinase core. The phosphorylation events are then concerted with intramolecular interactions in an unknown order resulting in a closed conformation of the mature kinase.

The Pin1 mediated down-regulation of PKC is shown in this dissertation to be non-catalytic with avidity from bivalent binding for at least three out of four isoenzymes in the conventional PKC subfamily. The source of the observed avidity will be determined by future experiments. A structural model is yet to be determined for this bivalent Pin1–V5 complex. The effect of dephosphorylation for both V5 motifs on the Pin1–V5 binding is still not clear. Future experiments with full-length enzyme could test the sequence of action to see which V5 motif interacts first with Pin1, and what kind of initial changes could occur to Pin1. Since the *cis-trans* isomerizations of V5 are not altered by Pin1 for these PKC isoenzymes, another conformational change may occur to the full-length PKC upon Pin1 interaction that will eventually lead to dephosphorylation and ubuiquitination of PKC. Perhaps the non-catalytic V5–Pin1 interaction mediates other protein-protein interactions with phosphatases or ubiquitination pathway proteins. Since the turn motif of PKCβI is potentially an efficient substrate for Pin1 catalysis, it could be regulated by Pin1 through a different mechanism. It also remains to be investigated if other Pin1 targets in the cell containing non-catalytic or non-canonical sites would share a common mechanism as observed in this study.

Finally, other functional elements of the C-terminal V5 domain remain to be studied. The propensities of V5 domain from PKCα to interact with hydrophobic environment could relate to PDZ-domain interaction via the C-terminal QSAV motif ,

which is unique for PKCα. This could be further investigated to test α-isoform specific regulations. Functions of the highly conserved NFD motif and the N-terminal PPXXP sites of V5 domain are still largely unexplored. Since interpretations of functional studies through mutagenesis are currently limited by the lack of full-length PKC structures, biophysical studies with individual V5 elements will provide valuable insights for understanding regulation mechanisms of PKC.

Protein kinase C has been a significant cell regulator and a challenging kinase system since its discovery almost forty years ago. However, the functional significance of intrinsically disordered proteins and protein domains in eukaryotes only emerged within the past twenty years. We hope the results and approaches in this dissertation would assist in future understanding of regulations not only for PKC, but also the abundance of eukaryotic proteome containing disordered regions.

REFERENCES

(1) Inoue, M.; Kishimoto, A.; Takai, Y.; Nishizuka, Y. *Journal of Biological Chemistry* **1977**, *252*, 7610.

(2) Castagna, M.; Takai, Y.; Kaibuchi, K.; Sano, K.; Kikkawa, U.; Nishizuka, Y. *Journal of Biological Chemistry* **1982**, *257*, 7847.

(3) Rosse, C.; Linch, M.; Kermorgant, S.; Cameron, A. J. M.; Boeckeler, K.; Parker, P. J. *Nature Reviews Molecular Cell Biology* **2010**, *11*, 103.

(4) Reyland, M. E. *Frontiers in Bioscience* **2009**, *14*, 2386.

(5) Ali, A. S.; Ali, S.; El-Rayes, B. F.; Philip, P. A.; Sarkar, F. H. *Cancer Treatment Reviews* **2009**, *35*, 1.

(6) Konopatskaya, O.; Poole, A. W. *Trends in Pharmacological Sciences* **2010**, *31*, 8.

(7) Liu, Q.; Molkentin, J. D. *Journal of Molecular and Cellular Cardiology* **2011**, *51*, 474.

(8) Palaniyandi, S. S.; Sun, L.; Batista Ferreira, J. C.; Mochly-Rosen, D. *Cardiovascular Research* **2009**, *82*, 229.

(9) Ferreira, J. C. B.; Mochly-Rosen, D.; Boutjdir, M. *Frontiers in bioscience (Scholar edition)* **2012**, *4*, 532.

(10) Sun, M.-K.; Alkon, D. L. *Pharmacology & Therapeutics* **2010**, *127*, 66.

(11) Nelson, T. J.; Sun, M.-K.; Hongpaisan, J.; Alkon, D. L. *European Journal of Pharmacology* **2008**, *585*, 76.

(12) Mochly-Rosen, D.; Das, K.; Grimes, K. V. *Nature Reviews Drug Discovery* **2012**, *11*, 937.

(13) de Barry, J.; Liegeois, C. M.; Janoshazi, A. *Experimental Gerontology* **2010**, *45*, 64.

(14) Goldberg, M.; Steinberg, S. F. *Biochemical Pharmacology* **1996**, *51*, 1089.

(15) Bittova, L.; Stahelin, R. V.; Cho, W. *Journal of Biological Chemistry* **2001**, *276*, 4218.

(16) Moscat, J.; Diaz-Meco, M. T. *Embo Reports* **2000**, *1*, 399.

(17) Suzuki, A.; Akimoto, K.; Ohno, S. *Journal of Biochemistry* **2003**, *133*, 9.

(18) Krishnamurthy, K.; Wang, G.; Silva, J.; Condie, B. G.; Bieberich, E. *Journal of Biological Chemistry* **2007**, *282*, 3379.

(19) Isakov, N.; Altman, A. *Frontiers in Immunology* **2013**, *4*.

(20) Ivey, R. A.; Sajan, M. P.; Farese, R. V. *Journal of Biological Chemistry* **2014**, *289*, 25021.

(21) Igumenova, T. I. *Biochemistry* **2015**, *54*, 4953.

(22) Steinberg, S. F. *Physiological Reviews* **2008**, *88*, 1341.

(23) Leonard, T. A.; Rozycki, B.; Saidi, L. F.; Hummer, G.; Hurley, J. H. *Cell* **2011**, *144*, 55.

(24) Sonnenburg, E. D.; Gao, T.; Newton, A. C. *Journal of Biological Chemistry* **2001**, *276*, 45289.

(25) Newton, A. C. *Chemical Reviews* **2001**, *101*, 2353.

(26) Keranen, L. M.; Dutil, E. M.; Newton, A. C. *Current Biology* **1995**, *5*, 1394.

(27) Le Good, J. A.; Ziegler, W. H.; Parekh, D. B.; Alessi, D. R.; Cohen, P.; Parker, P. J. *Science* **1998**, *281*, 2042.

(28) Chou, M. M.; Hou, W. M.; Johnson, J.; Graham, L. K.; Lee, M. H.; Chen, C. S.; Newton, A. C.; Schaffhausen, B. S.; Toker, A. *Current Biology* **1998**, *8*, 1069.

(29) Dong, L. Q.; Zhang, R. B.; Langlais, P.; He, H. L.; Clark, M.; Zhu, L.; Liu, F. *Journal of Biological Chemistry* **1999**, *274*, 8117.

(30) Edwards, A. S.; Faux, M. C.; Scott, J. D.; Newton, A. C. *Journal of Biological Chemistry* **1999**, *274*, 6461.

(31) Edwards, A. S.; Newton, A. C. *Journal of Biological Chemistry* **1997**, *272*, 18382.

(32) Gao, T. Y.; Toker, A.; Newton, A. C. *Journal of Biological Chemistry* **2001**, *276*, 19588.

(33) Oancea, E.; Meyer, T. *Cell* **1998**, *95*, 307.

(34) Violin, J. D.; Zhang, J.; Tsien, R. Y.; Newton, A. C. *Journal of Cell Biology* **2003**, *161*, 899.

(35) Tanimura, A.; Nezu, A.; Morita, T.; Hashimoto, N.; Tojyo, Y. *Journal of Biological Chemistry* **2002**, *277*, 29054.

(36) Johnson, J. E.; Giorgione, J.; Newton, A. C. *Biochemistry* **2000**, *39*, 11360.

(37) Dries, D. R.; Gallegos, L. L.; Newton, A. C. *Journal of Biological Chemistry* **2007**, *282*, 826.

(38) Stewart, M. D.; Morgan, B.; Massi, F.; Igumenova, T. I. *Journal of Molecular Biology* **2011**, *408*, 949.

(39) Jaken, S.; Parker, P. J. *Bioessays* **2000**, *22*, 245.

(40) Churchill, E. N.; Qvit, N.; Mochly-Rosen, D. *Trends in Endocrinology and Metabolism* **2009**, *20*, 25.

(41) Csukai, M.; Mochly-Rosen, D. *Pharmacological Research* **1999**, *39*, 253.

(42) Dorn, G. W.; Souroujon, M. C.; Liron, T.; Chen, C. H.; Gray, M. O.; Zhou, H. Z.; Csukai, M.; Wu, G. Y.; Lorenz, J. N.; Mochly-Rosen, D. *Proceedings of the National Academy of Sciences of the United States of America* **1999**, *96*, 12798.

(43) Ron, D.; Luo, J. H.; Mochlyrosen, D. *Journal of Biological Chemistry* **1995**, *270*, 24180.

(44) Hansra, G.; Garcia-Paramio, P.; Prevostel, C.; Whelan, R. D. H.; Bornancin, F.; Parker, P. J. *Biochemical Journal* **1999**, *342*, 337.

(45) Abrahamsen, H.; O'Neill, A. K.; Kannan, N.; Kruse, N.; Taylor, S. S.; Jennings, P. A.; Newton, A. C. *Journal of Biological Chemistry* **2012**, *287*, 13262.

(46) Lum, M. A.; Pundt, K. E.; Paluch, B. E.; Black, A. R.; Black, J. D. *Journal of Biological Chemistry* **2013**, *288*, 13093.

(47) Stensman, H.; Larsson, C. *Journal of Biological Chemistry* **2007**, *282*, 28627.

(48) Ammendrup-Johnsen, I.; Thorsen, T. S.; Gether, U.; Madsen, K. L. *Biochemistry* **2012**, *51*, 586.

(49) Stebbins, E. G.; Mochly-Rosen, D. *Journal of Biological Chemistry* **2001**, *276*, 29644.

(50) Gao, T. Y.; Newton, A. C. *Journal of Biological Chemistry* **2002**, *277*, 31585.

(51) Becker, K. P.; Hannun, Y. A. *Journal of Biological Chemistry* **2004**, *279*, 28251.

(52) Chalfant, C. E.; Mischak, H.; Watson, J. E.; Winkler, B. C.; Goodnight, J.; Farese, R. V.; Cooper, D. R. *Journal of Biological Chemistry* **1995**, *270*, 13326.

(53) Gokmen-Polar, Y.; Fields, A. P. *Journal of Biological Chemistry* **1998**, *273*, 20261.

(54) DeVries, T. A.; Neville, M. C.; Reyland, M. E. *Embo Journal* **2002**, *21*, 6050.

(55) Antal, C. E.; Callender, J. A.; Kornev, A. P.; Taylor, S. S.; Newton, A. C. *Cell Reports* **2015**, *12*, 1252.

(56) Gao, T.; Newton, A. C. *Journal of Biological Chemistry* **2006**, *281*, 32461.

(57) Frodin, M.; Antal, T. L.; Dummler, B. A.; Jensen, C. J.; Deak, M.; Gammeltoft, S.; Biondi, R. M. *Embo Journal* **2002**, *21*, 5396.

(58) Adwan, T. S.; Ohm, A. M.; Jones, D. N. M.; Humphries, M. J.; Reyland, M. E. *Journal of Biological Chemistry* **2011**, *286*, 35716.

(59) Moravcevic, K.; Oxley, C. L.; Lemmon, M. A. *Structure* **2012**, *20*, 15.

(60) Rizo, J.; Sudhof, T. C. *Journal of Biological Chemistry* **1998**, *273*, 15879.

(61) Scott, A. M.; Antal, C. E.; Newton, A. C. *Journal of Biological Chemistry* **2013**, *288*, 16905.

(62) Guerrero-Valero, M.; Ferrer-Orta, C.; Querol-Audi, J.; Marin-Vicente, C.; Fita, I.; Gomez-Fernandez, J. C.; Verdaguer, N.; Corbalan-Garcia, S. *Proceedings of the National Academy of Sciences of the United States of America* **2009**, *106*, 6603.

(63) Manna, D.; Bhardwaj, N.; Vora, M. S.; Stahelin, R. V.; Lu, H.; Cho, W. *Journal of Biological Chemistry* **2008**, *283*, 26047.

(64) Landgraf, K. E.; Malmberg, N. J.; Falke, J. J. *Biochemistry* **2008**, *47*, 8301.

(65) Medkova, M.; Cho, W. H. *Journal of Biological Chemistry* **1999**, *274*, 19852.

(66) Stahelin, R. V.; Wang, J. Y.; Blatner, N. R.; Raftner, J. D.; Murray, D.; Cho, W. H. *Journal of Biological Chemistry* **2005**, *280*, 36452.

(67) Murray, D.; Honig, B. *Molecular Cell* **2002**, *9*, 145.

(68) Verdaguer, N.; Corbalan-Garcia, S.; Ochoa, W. F.; Fita, I.; Gomez-Fernandez, J. C. *Embo Journal* **1999**, *18*, 6329.

(69) Medkova, M.; Cho, W. W. *Journal of Biological Chemistry* **1998**, *273*, 17544.

(70) Bouton, C.; Frelin, L. P.; Forde, C. E.; Godwin, H. A.; Pevsner, J. *Journal of Neurochemistry* **2001**, *76*, 1724.

(71) Sun, X. Y.; Tian, X. T.; Tomsig, J. L.; Suszkiw, J. B. *Toxicology and Applied Pharmacology* **1999**, *156*, 40.

(72) Morales, K. A.; Lasagna, M.; Gribenko, A. V.; Yoon, Y.; Reinhart, G. D.; Lee, J. C.; Cho, W.; Li, P.; Igumenova, T. I. *Journal of the American Chemical Society* **2011**, *133*, 10599.

(73) Edwards, A. S.; Newton, A. C. *Biochemistry* **1997**, *36*, 15615.

(74) Griner, E. M.; Kazanietz, M. G. *Nature Reviews Cancer* **2007**, *7*, 281.

(75) Kheifets, V.; Mochly-Rosen, D. *Pharmacological Research* **2007**, *55*, 467.

(76) Kim, J.; Thorne, S. H.; Sun, L.; Huang, B.; Mochly-Rosen, D. *Oncogene* **2011**, *30*, 323.

(77) Kim, J.; Choi, Y.-L.; Vallentin, A.; Hunrichs, B. S.; Hellerstein, M. K.; Peehl, D. M.; Mochly-Rosen, D. *Cancer Research* **2008**, *68*, 6831.

(78) Ferreira, J. C. B.; Boer, B. N.; Grinberg, M.; Brum, P. C.; Mochly-Rosen, D. *Plos One* **2012**, *7*.

(79) Ferreira, J. C. B.; Koyanagi, T.; Palaniyandi, S. S.; Fajardo, G.; Churchill, E. N.; Budas, G.; Disatnik, M.-H.; Bernstein, D.; Brum, P. C.; Mochly-Rosen, D. *Journal of Molecular and Cellular Cardiology* **2011**, *51*, 980.

(80) Palaniyandi, S. S.; Batista Ferreira, J. C.; Brum, P. C.; Mochly-Rosen, D. *Journal of Cellular and Molecular Medicine* **2011**, *15*, 1769.

(81) Parekh, D. B.; Ziegler, W.; Parker, P. J. *Embo Journal* **2000**, *19*, 496.

(82) Solodukhin, A. S.; Kretsinger, R. H.; Sando, J. J. *Cellular Signalling* **2007**, *19*, 2035.

(83) Newton, A. C. *Biochemical Journal* **2003**, *370*, 361.

(84) Facchinetti, V.; Ouyang, W.; Wei, H.; Soto, N.; Lazorchak, A.; Gould, C.; Lowry, C.; Newton, A. C.; Mao, Y.; Miao, R. Q.; Sessa, W. C.; Qin, J.; Zhang, P.; Su, B.; Jacinto, E. *Embo Journal* **2008**, *27*, 1932.

(85) Ikenoue, T.; Inoki, K.; Yang, Q.; Zhou, X.; Guan, K.-L. *Embo Journal* **2008**, *27*, 1919.

(86) Behn-Krappa, A.; Newton, A. C. *Current Biology* **1999**, *9*, 728.

(87) Takimura, T.; Kamata, K.; Fukasawa, K.; Ohsawa, H.; Komatani, H.; Yoshizumi, T.; Takahashi, I.; Kotani, H.; Iwasawa, Y. *Acta Crystallographica Section D-Biological Crystallography* **2010**, *66*, 577.

(88) Grodsky, N.; Li, Y.; Bouzida, D.; Love, R.; Jensen, J.; Nodes, B.; Nonomiya, J.; Grant, S. *Biochemistry* **2006**, *45*, 13970.

(89) Messerschmidt, A.; Macieira, S.; Velarde, M.; Badeker, M.; Benda, C.; Jestel, A.; Brandstetter, H.; Neuefeind, T.; Blaesse, M. *Journal of Molecular Biology* **2005**, *352*, 918.

(90) Xu, Z. B.; Chaudhary, D.; Olland, S.; Wolfrom, S.; Czerwinski, R.; Malakian, K.; Lin, L.; Stahl, M. L.; McCarthy, D. J.; Benander, C.; Fitz, L.; Greco, R.; Somers, W. S.; Mosyak, L. *Journal of Biological Chemistry* **2004**, *279*, 50401.

(91) Wagner, J.; von Matt, P.; Sedrani, R.; Albert, R.; Cooke, N.; Ehrhardt, C.; Geiser, M.; Rummel, G. a.; Stark, W.; Strauss, A.; Cowan-Jacob, S. W.; Beerli, C.;

Weckbecker, G.; Evenou, J.-P.; Zenke, G.; Cottens, S. *Journal of Medicinal Chemistry* **2009**, *52*, 6193.

(92) Marley, J.; Lu, M.; Bracken, C. *Journal of Biomolecular Nmr* **2001**, *20*, 71.

(93) Muhandiram, D. R.; Kay, L. E. *Journal of Magnetic Resonance Series B* **1994**, *103*, 203.

(94) Clubb, R. T.; Thanabal, V.; Wagner, G. *Journal of Magnetic Resonance* **1992**, *97*, 213.

(95) Grzesiek, S.; Anglister, J.; Bax, A. *Journal of Magnetic Resonance Series B* **1993**, *101*, 114.

(96) Schumann, F. H.; Riepl, H.; Maurer, T.; Gronwald, W.; Neidig, K.-P.; Kalbitzer, H. R. *Journal of Biomolecular Nmr* **2007**, *39*, 275.

(97) Farrow, N. A.; Muhandiram, R.; Singer, A. U.; Pascal, S. M.; Kay, C. M.; Gish, G.; Shoelson, S. E.; Pawson, T.; Formankay, J. D.; Kay, L. E. *Biochemistry* **1994**, *33*, 5984.

(98) Farrow, N. A.; Zhang, O. W.; Formankay, J. D.; Kay, L. E. *Biochemistry* **1995**, *34*, 868.

(99) Farrow, N. A.; Zhang, O. W.; Szabo, A.; Torchia, D. A.; Kay, L. E. *Journal of Biomolecular Nmr* **1995**, *6*, 153.

(100) Peng, J. W.; Wagner, G. *Journal of Magnetic Resonance* **1992**, *98*, 308.

(101) Peng, J. W.; Wagner, G. *Biochemistry* **1992**, *31*, 8571.

(102) Iwahara, J.; Tang, C.; Clore, G. M. *Journal of Magnetic Resonance* **2007**, *184*, 185.

(103) Kuliopulos, A.; Walsh, C. T. *Journal of the American Chemical Society* **1994**, *116*, 4599.

(104) Bornancin, F.; Parker, P. J. *Journal of Biological Chemistry* **1997**, *272*, 3544.

(105) Bornancin, F.; Parker, P. J. *Current Biology* **1996**, *6*, 1114.

(106) Uversky, V. N.; Li, J.; Souillac, P.; Millett, I. S.; Doniach, S.; Jakes, R.; Goedert, M.; Fink, A. L. *Journal of Biological Chemistry* **2002**, *277*, 11970.

(107) Greenfield, N. J. *Nature Protocols* **2006**, *1*, 2876.

(108) Provencher, S. W.; Gloeckner, J. *Biochemistry* **1981**, *20*, 33.

(109) Sreerama, N.; Woody, R. W. *Analytical Biochemistry* **2000**, *287*, 252.

(110) Dyson, H. J.; Wright, P. E. *Chemical Reviews* **2004**, *104*, 3607.

(111) Marsh, J. A.; Singh, V. K.; Jia, Z.; Forman-Kay, J. D. *Protein Science* **2006**, *15*, 2795.

(112) Wright, P. E.; Dyson, H. J. *Current Opinion in Structural Biology* **2009**, *19*, 31.

(113) Bai, Y. W.; Chung, J.; Dyson, H. J.; Wright, P. E. *Protein Science* **2001**, *10*, 1056.

(114) Jarymowycz, V. A.; Stone, M. J. *Chemical Reviews* **2006**, *106*, 1624.

(115) Schubert, M.; Labudde, D.; Oschkinat, H.; Schmieder, P. *Journal of Biomolecular Nmr* **2002**, *24*, 149.

(116) Reimer, U.; Scherer, G.; Drewello, M.; Kruber, S.; Schutkowski, M.; Fischer, G. *Journal of Molecular Biology* **1998**, *279*, 449.

(117) Schutkowski, M.; Bernhardt, A.; Zhou, X. Z.; Shen, M. H.; Reimer, U.; Rahfeld, J. U.; Lu, K. P.; Fischer, G. *Biochemistry* **1998**, *37*, 5566.

(118) Stewart, M. D.; Cole, T. R.; Igumenova, T. I. *Journal of Biological Chemistry* **2014**, *289*, 27653.

(119) Yang, Y.; Morales, K. A.; Stewart, M. D.; Igumenova, T. I. In *eMagRes*; John Wiley & Sons, Ltd: 2015; Vol. 4.

(120) Fawzi, N. L.; Ying, J.; Ghirlando, R.; Torchia, D. A.; Clore, G. M. *Nature* **2011**, *480*, 268.

(121) Fawzi, N. L.; Ying, J.; Torchia, D. A.; Clore, G. M. *Nature Protocols* **2012**, *7*, 1523.

(122) Su, Y.; Mani, R.; Hong, M. *Journal of the American Chemical Society* **2008**, *130*, 8856.

(123) Karal, M. A.; Alam, J. M.; Takahashi, T.; Levadny, V.; Yamazaki, M. *Langmuir* **2015**, *31*, 3391.

(124) Bokvist, M.; Grobner, G. *Journal of the American Chemical Society* **2007**, *129*, 14848.

(125) Mosior, M.; McLaughlin, S. *Biophysical Journal* **1991**, *60*, 149.

(126) Gould, C. M.; Kannan, N.; Taylor, S. S.; Newton, A. C. *Journal of Biological Chemistry* **2009**, *284*, 4921.

(127) House, C.; Kemp, B. E. *Science* **1987**, *238*, 1726.

(128) Baron, A.; Deval, E.; Salinas, M.; Lingueglia, E.; Voilley, N.; Lazdunski, M. *Journal of Biological Chemistry* **2002**, *277*, 50463.

(129) Staudinger, J.; Lu, J. R.; Olson, E. N. *Journal of Biological Chemistry* **1997**, *272*, 32019.

(130) O'Neill, A. K.; Gallegos, L. L.; Justilien, V.; Garcia, E. L.; Leitges, M.; Fields, A. P.; Hall, R. A.; Newton, A. C. *Journal of Biological Chemistry* **2011**, *286*, 43559.

(131) Zimmermann, P.; Meerschaert, K.; Reekmans, G.; Leenaerts, I.; Small, J. V.; Vandekerckhove, J.; David, G.; Gettemans, J. *Molecular Cell* **2002**, *9*, 1215.

(132) Rouser, G.; Fleischer, S.; Yamamoto, A. *Lipids* **1970**, *5*, 494.

(133) Shaner, N. C.; Steinbach, P. A.; Tsien, R. Y. *Nature Methods* **2005**, *2*, 905.

(134) Montaville, P.; Coudevylle, N.; Radhakrishnan, A.; Leonov, A.; Zweckstetter, M.; Becker, S. *Protein Science* **2008**, *17*, 1025.

(135) Schmitz, C.; Stanton-Cook, M. J.; Su, X. C.; Otting, G.; Huber, T. *Journal of Biomolecular NMR* **2008**, *41*, 179.

(136) Montelione, G. T.; Lyons, B. A.; Emerson, S. D.; Tashiro, M. *Journal of the American Chemical Society* **1992**, *114*, 10974.

(137) Kay, L. E.; Xu, G. Y.; Singer, A. U.; Muhandiram, D. R.; Formankay, J. D. *Journal of Magnetic Resonance Series B* **1993**, *101*, 333.

(138) Bax, A.; Clore, G. M.; Driscoll, P. C.; Gronenborn, A. M.; Ikura, M.; Kay, L. E. *Journal of Magnetic Resonance (1969)* **1990**, *87*, 620.

(139) Marion, D.; Driscoll, P. C.; Kay, L. E.; Wingfield, P. T.; Bax, A.; Gronenborn, A. M.; Clore, G. M. *Biochemistry* **1989**, *28*, 6150.

(140) Marion, D.; Kay, L. E.; Sparks, S. W.; Torchia, D. A.; Bax, A. *Journal of the American Chemical Society* **1989**, *111*, 1515.

(141) Zuiderweg, E. R. P.; Fesik, S. W. *Biochemistry* **1989**, *28*, 2387.

(142) Zwahlen, C.; Legault, P.; Vincent, S. J. F.; Greenblatt, J.; Konrat, R.; Kay, L. E. *Journal of the American Chemical Society* **1997**, *119*, 6711.

(143) Iwahara, J.; Wojciak, J. M.; Clubb, R. T. *Journal of Biomolecular NMR* **2001**, *19*, 231.

(144) Delaglio, F.; Grzesiek, S.; Vuister, G. W.; Zhu, G.; Pfeifer, J.; Bax, A. *Journal of Biomolecular NMR* **1995**, *6*, 277.

(145) Goddard, T. D.; Kneller, D. G. **2008**.

(146) Rieping, W.; Habeck, M.; Bardiaux, B.; Bernard, A.; Malliavin, T. E.; Nilges, M. *Bioinformatics* **2007**, *23*, 381.

(147) Shen, Y.; Delaglio, F.; Cornilescu, G.; Bax, A. *Journal of Biomolecular NMR* **2009**, *44*, 213.

(148) Laskowski, R. A.; Rullmann, J. A. C.; MacArthur, M. W.; Kaptein, R.; Thornton, J. M. *Journal of Biomolecular NMR* **1996**, *8*, 477.

(149) De Vries, S. J.; van Dijk, A. D. J.; Krzeminski, M.; van Dijk, M.; Thureau, A.; Hsu, V.; Wassenaar, T.; Bonvin, A. *Proteins-Structure Function and Bioinformatics* **2007**, *69*, 726.

(150) Dominguez, C.; Boelens, R.; Bonvin, A. *Journal of the American Chemical Society* **2003**, *125*, 1731.

(151) Hubbard, S. J.; Thornton, J. M. **1993**.

(152) Daura, X.; Gademann, K.; Jaun, B.; Seebach, D.; van Gunsteren, W. F.; Mark, A. E. *Angewandte Chemie-International Edition* **1999**, *38*, 236.

(153) Dutil, E. M.; Toker, A.; Newton, A. C. *Current Biology* **1998**, *8*, 1366.

(154) Gallegos, L. L.; Kunkel, M. T.; Newton, A. C. *Journal of Biological Chemistry* **2006**, *281*, 30947.

(155) Antal, C. E.; Violin, J. D.; Kunkel, M. T.; Skovso, S.; Newton, A. C. *Chemistry & Biology* **2014**, *21*, 459.

(156) Ziemba, B. P.; Li, J.; Landgraf, K. E.; Knight, J. D.; Voth, G. A.; Falke, J. J. *Biochemistry* **2014**, *53*, 1697.

(157) Swanson, C. J.; Ritt, M.; Wang, W.; Lang, M. J.; Narayan, A.; Tesmer, J. J.; Westfall, M.; Sivaramakrishnan, S. *Journal of Biological Chemistry* **2014**, *289*, 17812.

(158) Lum, M. A.; Barger, C. J.; Hsu, A. H.; Leontieva, O. V.; Black, A. R.; Black, J. D. *Journal of Biological Chemistry* **2016**, *291*, 6331.

(159) Ranganathan, R.; Lu, K. P.; Hunter, T.; Noel, J. P. *Cell* **1997**, *89*, 875.

(160) Verdecia, M. A.; Bowman, M. E.; Lu, K. P.; Hunter, T.; Noel, J. P. *Nature Structural Biology* **2000**, *7*, 639.

(161) Rudrabhatla, P.; Pant, H. C. *Journal of Alzheimers Disease* **2010**, *19*, 389.

(162) Pastorino, L.; Ma, S. L.; Balastik, M.; Huang, P.; Pandya, D.; Nicholson, L.; Lu, K. P. *Journal of Alzheimers Disease* **2012**, *30*, 277.

(163) Zheng, H. W.; You, H.; Zhou, X. Z.; Murray, S. A.; Uchida, T.; Wulf, G.; Gu, L.; Tang, X. R.; Lu, K. P.; Xiao, Z. X. J. *Nature* **2002**, *419*, 849.

(164) Tun-Kyi, A.; Finn, G.; Greenwood, A.; Nowak, M.; Lee, T. H.; Asara, J. M.; Tsokos, G. C.; Fitzgerald, K.; Israel, E.; Li, X.; Exley, M.; Nicholson, L. K.; Lu, K. P. *Nature Immunology* **2011**, *12*, 733.

(165) Wintjens, R.; Wieruszeski, J. M.; Drobecq, H.; Rousselot-Pailley, P.; Buee, L.; Lippens, G.; Landrieu, I. *Journal of Biological Chemistry* **2001**, *276*, 25150.

(166) Kowalski, J. A.; Liu, K.; Kelly, J. W. *Biopolymers* **2002**, *63*, 111.

(167) Bayer, E.; Goettsch, S.; Mueller, J. W.; Griewel, B.; Guiberman, E.; Mayr, L. M.; Bayer, P. *Journal of Biological Chemistry* **2003**, *278*, 26183.

(168) Jacobs, D. M.; Saxena, K.; Vogtherr, M.; Bernado, P.; Pons, M.; Fiebig, K. M. *Journal of Biological Chemistry* **2003**, *278*, 26174.

(169) Matena, A.; Sinnen, C.; van den Boom, J.; Wilms, C.; Dybowski, J. N.; Maltaner, R.; Mueller, J. W.; Link, N. M.; Hoffmann, D.; Bayer, P. *Structure* **2013**, *21*, 1769.

(170) Wang, X.; Mahoney, B. J.; Zhang, M.; Zintsmaster, J. S.; Peng, J. W. *Structure* **2015**, *23*, 2224.

(171) Mercedes-Camacho, A. Y.; Mullins, A. B.; Mason, M. D.; Xu, G. G.; Mahoney, B. J.; Wang, X.; Peng, J. W.; Etzkorn, F. A. *Biochemistry* **2013**, *52*, 7707.

(172) Innes, B. T.; Bailey, M. L.; Brandl, C. J.; Shilton, B. H.; Litchfield, D. W. *Frontiers in Physiology* **2013**, *4*.

(173) Smet, C.; Sambo, A. V.; Wieruszeski, J. M.; Leroy, A.; Landrieu, I.; Buee, L.; Lippens, G. *Biochemistry* **2004**, *43*, 2032.

(174) Smet, C.; Wieruszeski, J. M.; Buee, L.; Landrieu, I.; Lippens, G. *Febs Letters* **2005**, *579*, 4159.

(175) Fujimoto, Y.; Shiraki, T.; Horiuchi, Y.; Waku, T.; Shigenaga, A.; Otaka, A.; Ikura, T.; Igarashi, K.; Aimoto, S.; Tate, S.-i.; Morikawa, K. *Journal of Biological Chemistry* **2010**, *285*, 3126.

(176) Nakatsu, Y.; Sakoda, H.; Kushiyama, A.; Ono, H.; Fujishiro, M.; Horike, N.; Yoneda, M.; Ohno, H.; Tsuchiya, Y.; Kamata, H.; Tahara, H.; Isobe, T.; Nishimura, F.; Katagiri, H.; Oka, Y.; Fukushima, T.; Takahashi, S.-I.; Kurihara, H.; Uchida, T.; Asanoa, T. *Journal of Biological Chemistry* **2010**, *285*, 33018.

(177) Zhang, Y.; Daum, S.; Wildemann, D.; Zhou, X. Z.; Verdecia, M. A.; Bowman, M. E.; Luecke, C.; Hunter, T.; Lu, K.-P.; Fischer, G.; Noel, J. P. *Acs Chemical Biology* **2007**, *2*, 320.

(178) Macura, S.; Ernst, R. R. *Molecular Physics* **1980**, *41*, 95.

(179) Kumar, A.; Ernst, R. R.; Wuthrich, K. *Biochemical and Biophysical Research Communications* **1980**, *95*, 1.

(180) Braunschweiler, L.; Ernst, R. R. *Journal of Magnetic Resonance* **1983**, *53*, 521.

(181) Bax, A.; Davis, D. G. *Journal of Magnetic Resonance* **1985**, *63*, 207.

(182) Palmer, A. G.; Kroenke, C. D.; Loria, J. P. *Nuclear Magnetic Resonance of Biological Macromolecules, Pt B* **2001**, *339*, 204.

(183) Pastorino, L.; Sun, A.; Lu, P. J.; Zhou, X. Z.; Balastik, M.; Finn, G.; Wulf, G.; Lim, J.; Li, S. H.; Li, X. J.; Xia, W. M.; Nicholson, L. K.; Lu, K. P. *Nature* **2006**, *440*, 528.

(184) Lu, P. J.; Wulf, G.; Zhou, X. Z.; Davies, P.; Lu, K. P. *Nature* **1999**, *399*, 784.

(185) Landrieu, I.; De Veylder, L.; Fruchart, J. S.; Odaert, B.; Casteels, P.; Portetelle, D.; Van Montagu, M.; Inze, D.; Lippens, G. *Journal of Biological Chemistry* **2000**, *275*, 10577.

(186) Gemmill, T. R.; Wu, X. Y.; Hanes, S. D. *Journal of Biological Chemistry* **2005**, *280*, 15510.

(187) Namanja, A. T.; Wang, X. J.; Xu, B.; Mercedes-Camacho, A. Y.; Wilson, B. D.; Wilson, K. A.; Etzkorn, F. A.; Peng, J. W. *Journal of the American Chemical Society* **2010**, *132*, 5607.

(188) Eichner, T.; Kutter, S.; Labeikovsky, W.; Buosi, V.; Kern, D. *J Mol Biol* **2016**, *428*, 1760.

(189) Wilson, K. A.; Bouchard, J. J.; Peng, J. W. *Biochemistry* **2013**, *52*, 6968.

(190) Mammen, M.; Choi, S. K.; Whitesides, G. M. *Angewandte Chemie-International Edition* **1998**, *37*, 2755.

(191) Daum, S.; Luecke, C.; Wildemann, D.; Schiene-Fischer, C. *Journal of Molecular Biology* **2007**, *374*, 147.

(192) Yang, J.; Cron, P.; Thompson, V.; Good, V. M.; Hess, D.; Hemmings, B. A.; Barford, D. *Molecular Cell* **2002**, *9*, 1227.

(193) Kuboniwa, H.; Tjandra, N.; Grzesiek, S.; Ren, H.; Klee, C. B.; Bax, A. *Nature Structural Biology* **1995**, *2*, 768.

(194) Nowakowski, M.; Ruszczynska-Bartnik, K.; Budzinska, M.; Jaremko, L.; Jaremko, M.; Zdanowski, K.; Bierzynski, A.; Ejchart, A. *Biochemistry* **2013**, *52*, 1149.

(195) Wang, L.; Yang, X.; Li, S.; Wang, Z.; Liu, Y.; Feng, J.; Zhu, Y.; Shen, Y. *Embo Journal* **2014**, *33*, 594.

(196) Orr, J. W.; Newton, A. C. *Journal of Biological Chemistry* **1994**, *269*, 8383.

(197) Orr, J. W.; Keranen, L. M.; Newton, A. C. *Journal of Biological Chemistry* **1992**, *267*, 15263.

(198) Koenig, B.; Dinitto, P. A.; Blumberg, P. M. *Journal of Cellular Biochemistry* **1985**, *29*, 37.

(199) Daniel, R. M.; Dunn, R. V.; Finney, J. L.; Smith, J. C. *Annual Review of Biophysics and Biomolecular Structure* **2003**, *32*, 69.

(200) Kern, D.; Zuiderweg, E. R. P. *Current Opinion in Structural Biology* **2003**, *13*, 748.

(201) Ochoa, W. F.; Corbalan-Garcia, S.; Eritja, R.; Rodriguez-Alfaro, J. A.; Gomez-Fernandez, J. C.; Fita, I.; Verdaguer, N. *Journal of Molecular Biology* **2002**, *320*, 277.

(202) Nalefski, E. A.; Newton, A. C. *Biochemistry* **2001**, *40*, 13216.

(203) Kohout, S. C.; Corbalan-Garcia, S.; Torrecillas, A.; Gomez-Fernandez, J. C.; Falke, J. J. *Biochemistry* **2002**, *41*, 11411.

(204) Yamazaki, T.; Lee, W.; Arrowsmith, C. H.; Muhandiram, D. R.; Kay, L. E. *Journal of the American Chemical Society* **1994**, *116*, 11655.

(205) Hahn, E. L. *Physical Review* **1950**, *80*, 580.

(206) Palmer, A. G.; Skelton, N. J.; Chazin, W. J.; Wright, P. E.; Rance, M. *Molecular Physics* **1992**, *75*, 699.

(207) Lopes, D. H. J.; Chapeaurouge, A.; Manderson, G. A.; Johansson, J. S.; Ferreira, S. T. *Journal of Biological Chemistry* **2004**, *279*, 10991.

(208) Morales, K. A.; Yang, Y.; Long, Z.; Li, P.; Tayo, A. B.; Hart, P. J.; Igumenova, T. I. *Journal of the American Chemical Society* **2013**, *135*, 12980.

(209) Pearson, R. G. *Journal of the American Chemical Society* **1963**, *85*, 3533.

(210) Chakraborty, S.; Kravitz, J. Y.; Thulstrup, P. W.; Hemmingsen, L.; DeGrado, W. F.; Pecoraro, V. L. *Angewandte Chemie-International Edition* **2011**, *50*, 2049.

(211) Rulisek, L.; Vondrasek, J. *Journal of Inorganic Biochemistry* **1998**, *71*, 115.

(212) Swairjo, M. A.; Concha, N. O.; Kaetzel, M. A.; Dedman, J. R.; Seaton, B. A. *Nature Structural Biology* **1995**, *2*, 968.

(213) Kirberger, M.; Wang, X.; Deng, H.; Yang, W.; Chen, G.; Yang, J. J. *Journal of Biological Inorganic Chemistry* **2008**, *13*, 1169.

(214) Kirberger, M.; Yang, J. J. *Journal of Inorganic Biochemistry* **2008**, *102*, 1901.

(215) Jensen, M. R.; Hansen, D. F.; Ayna, U.; Dagil, R.; Hass, M. A. S.; Christensen, H. E. M.; Led, J. J. *Magnetic Resonance in Chemistry* **2006**, *44*, 294.

(216) Armitage, I. M.; Drakenberg, T.; Reilly, B. In *Cadmium: From Toxicity to Essentiality*; Sigel, A., Sigel, H., Sigel, R. K. O., Eds. 2013; Vol. 11, p 117.

(217) Cho, W.; Stahelin, R. V. *Biochimica Et Biophysica Acta-Molecular and Cell Biology of Lipids* **2006**, *1761*, 838.

(218) The UniProt Consortium *Nucleic Acids Research* **2012**, *40*, D71.

(219) Thevenod, F.; Lee, W.-K. In *Cadmium: From Toxicity to Essentiality*; Sigel, A., Sigel, H., Sigel, R. K. O., Eds. 2013; Vol. 11, p 415.

(220) Wright, P. E.; Dyson, H. J. *Nature Reviews Molecular Cell Biology* **2015**, *16*, 18.